
Dynamics and self-organization of
membrane-bound minimal actin
and actomyosin cortices based on
ezrin-PtdIns[4,5]P₂ linkage

Dissertation

for the award of the degree

Doctor rerum naturalium

of the Georg-August-Universität Göttingen

within the doctoral program

IMPRS for Physics of Biological and Complex Systems

submitted by

Nils Laurin Liebe

from Hannover

Göttingen 2022

Members of the thesis committee

Prof. Dr. Claudia Steinem
Institute of Organic and Biomolecular Chemistry
Georg-August-Universität Göttingen

Prof. Dr. Sarah Köster
Institute of X-Ray Physics
Georg-August-Universität Göttingen

Prof. Dr. Silvio O. Rizzoli
Department of Neuro- and Sensory Physiology
Georg-August-Universität Göttingen

Further members of the examination board

apl. Prof. Dr. Burkhard Geil
Institute of Physical Chemistry
Georg-August-Universität Göttingen

Prof. Dr. Jörg Enderlein
III. Physical Institute, Biophysics/Complex Systems
Georg-August-Universität Göttingen

Jun.-Prof. Dr. Nadja A. Simeth
Institute of Organic and Biomolecular Chemistry
Georg-August-Universität Göttingen

Date of oral examination

11.04.2022

Declaration

I, Nils Laurin Liebe,

hereby certify that my doctoral thesis entitled “Dynamics and self-organization of membrane-bound minimal actin and actomyosin cortices based on ezrin-PtdIns[4,5]P₂ linkage” has been written independently and with no other sources and aids than quoted.

Göttingen 2022

(Date)

(Nils Laurin Liebe)

ABSTRACT. The cellular cortex is a thin actin layer attached to the cytoplasmatic plasma membrane leaflet of mammalian cells. Through a complex interaction with hundreds of actin binding proteins (ABPs), controlling e.g. the cortex organization and dynamics, the cortical actin network is a key regulator of cell morphogenesis, shape and motility. A crucial property associated with these functions is the direct membrane attachment by linker-proteins such as ezrin/radixin/moesin (ERM).

The high complexity of the cortical actin network impedes the characterization of individual component properties and functions *in vivo*. Thus, a biomimetic minimal actin cortex (MAC) composed of solid-supported lipid bilayers, the constitutively active ezrin mutant T567D, and pre-polymerized filamentous actin (F-actin) was utilized to model the actin cortex plasma membrane linkage in a minimal component system. The impact of *in vivo* mimicking conditions such as the plasma membrane lipid composition, branched actin filaments and a crowded media was investigated in terms of the MAC organization and membrane attachment. It was demonstrated that the amount of membrane-bound ezrin and F-actin not only increases with higher concentrations of the ezrin receptor lipid L- α -phosphatidylinositol-4,5-bisphosphate (PtdIns[4,5]P₂), but also significantly in the presence of 1-palmitoyl-2-oleoyl-*sn*-glycero-3-phospho-L-serine (POPS), which resembles the composition of the cytoplasmatic plasma membrane leaflet. In addition, it was shown that a methyl cellulose crowded media, mimicking the cytoplasm density, increases the amount of membrane-bound F-actin. Growing amounts of membrane-bound F-actin could further be shown to dictate both single F-actin organization and MAC architecture, switching from single to bundled filaments and entangled to nematic ordered MACs. In comparison to this unbranched actin, it could be revealed that the amount of membrane-bound F-actin is reduced by a co-polymerization with the actin related protein 2/3 complex, although dense 3D networks could be formed in solution.

Atomic force microscopy indentation experiments on freestanding pore-spanning membranes (f-PSMs) revealed a reduced lateral membrane tension and a viscoelastic force response of f-PSMs with biomimetic attached MACs.

Analyzing the reorganization of membrane-bound minimal actomyosin cortices as a function of the ezrin-PtdIns[4,5]P₂ linkage and membrane composition, revealed that a lipid composition of 1-2 mol% PtdIns[4,5]P₂ and 17 mol% POPS, resembling the inner plasma membrane leaflet, promotes the MAC contractility. These findings highlight that lipids which do not directly interact with the actin cortex, such as POPS, requires consideration in the design of actomyosin studies.

Contents

1	Introduction	1
1.1	The cellular cytoskeleton network	1
1.2	Actin	2
1.3	The actin cortex	7
1.4	Actin cortex model systems	10
2	Scope of thesis	13
3	Materials and methods	15
3.1	Materials	15
3.1.1	Lipids	15
3.1.1.1	Receptor Lipids	15
3.1.1.2	Matrix Lipids	16
3.1.2	Fluorophores	17
3.1.2.1	Lipid coupled fluorophores	17
3.1.2.2	Protein staining fluorophores	19
3.2	Proteins and biochemical methods	21
3.2.1	Ezrin T567D isolation	21
3.2.1.1	Plasmid transformation	21
3.2.1.2	Heterologous protein expression	22
3.2.1.3	Cell lysis and protein purification	23
3.2.1.4	Sodium dodecyl sulfate polyacrylamide gel electrophoresis (SDS-PAGE)	24
3.2.2	Skeletal rabbit muscle myosin II isolation	27
3.2.3	Determination of Protein Concentration	30
3.2.4	Protein labeling	31
3.2.4.1	G-actin labeling with ATTO 594-NHS-ester	32
3.2.4.2	Myosin II labeling with DyLight® 488-NHS-ester	33
3.3	Preparative methods	34
3.3.1	Vesicle preparation	34
3.3.1.1	Small unilamellar vesicles	34
3.3.1.2	Giant unilamellar vesicles	35
3.3.2	Artificial membrane preparation	36
3.3.2.1	Solid supported lipid bilayers	36

3.3.2.2	Pore-spanning membranes	37
3.3.3	Filamentous actin polymerization	38
3.3.4	Preparation of minimal actin cortices	39
3.3.4.1	Solid supported minimal actin cortice preparation	39
3.3.4.2	Pore spanning minimal actin cortice preparation	40
3.3.5	Reorganization of minimal actin cortices by myosin II	41
3.4	Biosensing techniques	43
3.4.1	Reflectometric interference spectroscopy	43
3.5	Biophysical methods	48
3.5.1	Fluorescence microscopy	48
3.5.1.1	Confocal laser scanning microscopy	48
3.5.1.2	Airyscan technique	51
3.5.1.3	Fluorescence recovery after photobleaching (FRAP)	53
3.5.1.4	Total internal reflection fluorescence microscopy	55
3.5.2	Atomic force microscopy	60
3.5.2.1	Principal of atomic force microscopy	60
3.5.2.2	Force distance curves	62
3.5.2.3	Lateral membrane tension determination	63
3.5.2.4	Experimental procedure	64
3.6	Data evaluation	66
3.6.0.1	<i>Tube filter</i> analysis and network skeletonization	66
3.6.0.2	Nematic order parameter	68

4 Results 71

4.1	Minimal actin cortex self-organization on lipid bilayers	71
4.1.1	The minimal actin cortex	72
4.1.2	Characterization of F-actin binding to solid supported lipid bilayers as a function of the PtdIns[4,5]P ₂ content	75
4.1.3	Minimal actin cortices under cellular mimicking conditions.	79
4.1.3.1	Characterization of actin binding to solid supported bilayers with the crowding agent methyl cellulose as a function of PtdIns[4,5]P ₂ content	79
4.1.3.2	Branched MAC's with the Arp2/3-VCA complex	83
4.1.3.3	Influence of POPS on the minimal actin cortex architecture	88

4.2	Dynamics of membrane-bound minimal actomyosin cortices	95
4.2.1	Single filament motion in actomyosin networks	95
4.2.2	Contractility of membrane-bound actomyosin networks	99
4.3	Mechanical properties of membrane-bound minimal actin cortices	107
5	Discussion	113
5.1	Reciprocal interaction of the membrane-actin cortex linkage	113
5.1.1	Membrane composition dependent F-actin attachment and self-organization	113
5.1.2	Influence of actin cortex binding on lipid membrane dynamics	122
5.2	Impact of cellular mimicking conditions on the actin cortex self-organization	125
5.2.1	Influence of the crowding agent methyl cellulose	125
5.2.2	Influence of the actin binding protein Arp2/3	126
5.3	Membrane-bound actomyosin contractility	130
5.4	Membrane attachment of biomimetic MACs alters the mechanical properties of pore-spanning membranes	136
6	Conclusion	139
7	Bibliography	141
A	Appendix	165
A.1	List of Figures	165
A.2	List of Tables	169
A.3	Nematic order parameter: director field window-size determination and utilized parameters	170
A.4	RIfS control experiments for POPS	171
A.5	Particle image velocimetry analysis	172
A.6	Pore spanning membranes	173
A.6.1	Alexa Fluor™ 633 phalloidin control experiments	173
A.6.2	Length-dependent binding of F-actin to pore-spanning membranes	174
A.6.3	Overview of tested parameters for the PSM attachment of minimal actin cortices	175
A.7	SOAX parameters	177
A.8	Abbreviations and symbols	178

A.9 Chemicals and consumables	182
A.10 Devices and software	185

1 Introduction

1.1 The cellular cytoskeleton network

Cells are the basic building blocks of tissues and organs. Since they are subject to continuous structural changes due to growth, movement or external forces, cells must be able to maintain their characteristic shape while simultaneously adapting dynamically. In animal cells, this pivotal property is controlled by the cytoskeleton network.^[1] The cytoskeleton of mammalian cells is mainly composed of three different filament classes, which are microtubules (MTs), intermediate filaments (IFs) and actin filaments (AFs).^[2]

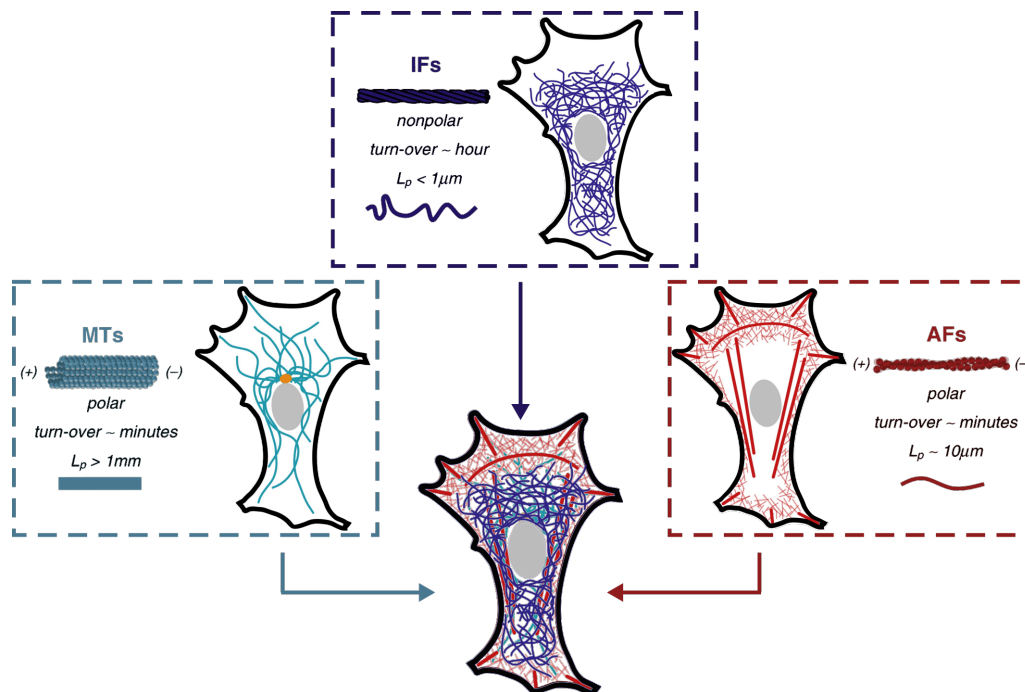


Figure 1.1: Schematic illustration of the cellular cytoskeleton. Localization and filament structure of microtubules (MTs, cyan), intermediate filaments (IFs, blue) and actin filaments (AFs, red). Figure modified from HUBER et al.^[3]

Although each filament class exhibits a defined localization within the cell, as schematically depicted in figure 1.1, the three classes have been shown to interact both directly via cross-linker and steric interactions (cf. figure 1.1, bottom) or indirectly via gene regulation and biochemical signaling pathways.^[3] While the overall cell mechanics and dynamics are determined by these interactions, the mechanical characteristics of the individual cytoskeletal subsystems are determined

by the respective filament organization.^[1,3,4] MTs (cf. figure 1.1, cyan) are polar and composed of 13 protofilaments formed by the head-to-tail alignment of α - and β -tubulin.^[5] These hollow filaments exhibit fast (dis)-assembly rates, however MTs are in comparison to ITs and AFs rigid, due to their large persistence length (l_p) of up to 5 mm.^[4] In contrast, IFs (cf. figure 1.1, blue) encompass a large group of about 70 proteins, which all form highly flexible ($l_p < 1 \mu\text{m}$)^[4] and nonpolar filaments with turn-over rates of hours.^[1,3] AFs (cf. figure 1.1, red), instead, are semi-flexible, since their filament length of 10-20 μm ^[6,7] (determined *in vitro*) is approximately equal to their l_p of 10-18 μm ^[8,9]. This semi-flexible filament character combined with a fast turnover and the localisation in the cell periphery causes AFs to be a key regulator of cell migration, morphology and division.^[1,4,10]

1.2 Actin

The monomeric actin protein (G-actin, $M = 42 \text{ kDa}$) consists of around 374 amino acids, forming a single polypeptide chain. While each known eukaryotic organism express at least a single actin protein, the general actin structure is highly conserved, shown e.g. a 94 % conservation between human cells and the yeast *Saccharomyces cerevisiae*.^[11] Mammalian cells express six different actin isoforms, with three smooth muscle α -isoforms (α_{skeletal} , α_{cardiac} , α_{vascular}) and the two non-muscle isoforms β and γ .^[12] G-actin itself is small globular protein with a size of approximately $55 \times 55 \times 35 \text{ \AA}$ and composed of two main domains: the large α - and small β -domain, which are also called outer and inner domain (cf. figure 1.2 A).^[13] These two can be further subdivided into the subdomains (SD) 1 - 4, with SD 1 - 2 constituting the small domain and SD 3 - 4 forming the large domain.^[14] Through the structural construction of the large and small domain to each other G-actin exhibits two clefts.^[13,14] The cleft between the subdomains 1 - 3 is composed of mainly hydrophobic amino acid residues and referred to as the hydrophobic cleft or target-binding cleft. This cleft contains the binding site for several regulatory actin binding proteins (ABPs) such as gelsolin.^[13,15] However, the hydrophobic cleft is not to be confused with the hydrophobic plug between SD 3 - 4 (cf. figure 1.2 B), which is an essential component of the interaction between individual G-actin monomers inside of filamentous actin (F-actin).^[11] Polymerizing G-actin into F-actin requires the binding of adenosine

triphosphate (ATP) and associated divalent cations (e.g. Mg^{2+}) to the second cleft (nucleotide cleft) in between SD 2-4.

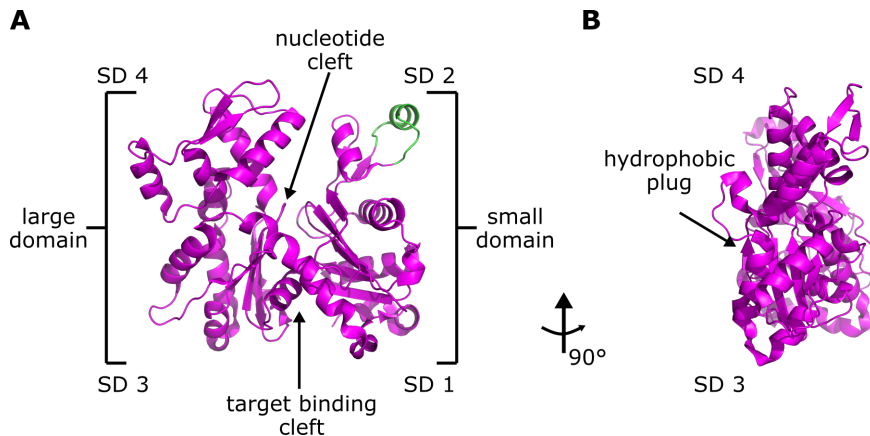


Figure 1.2: Exemplary crystal structure of G-actin. Frontal (A) and lateral (B) views of the G-actin crystal structure with the DNase I-binding loop (D-loop) in SD 2 highlighted in green. Images were generated by means of PDB (*1J6Z*)^[16] and the software PyMOL Molecular Graphics.

KORN et al. showed, that ATP-bound G-actin is capable to polymerize only above a certain critical concentration (*in vitro* $\sim 0.1 \mu M$)^{[17], [18]} According to the authors model, actin polymerization is initialized by the assembling of ATP-G-actin into a trimer nucleus (nucleation phase, cf. figure 1.3 A). The binding of a further monomers subsequently leads to fast elongation on both filament ends (elongation phase, cf. figure 1.3 A). Due to the head-to-tail monomer organization within actin filaments, schematically depicted in figure 1.3 C, and the resulting structural polarity, F-actin exhibits two distinct ends which are referred to as barbed- (+) and pointed-ends (-).^[11,19,20] Further, the polymerization leads to a twist of the large and small domain with respect to each other ($\sim 20^\circ$)^[21], inducing the hydrolysis of the actin bound ATP to ADP and P_i . While the ATP hydrolysis within F-actin occurs at fast rates of $\sim 0.3 s^{-1}$, the P_i release from ADP- P_i -actin is slowed down by two orders of magnitude.^[11,22] Both, the enhanced ATP- and ADP- P_i -actin stability compared to ADP-actin and the structural polarity contribute to an up to 10-fold increased polymerization at the barbed-end (+).^[20,23] Decreasing concentrations of unbound ATP-G-actin during continuing polymerization lead to reduced elongation rates at both ends. In this state the predominant polymerization at the barbed-end and the predominant depolymerization at the pointed-end are equal, leading to no net filament growth at a constant net flow of actin monomers (*steady-state* phase, cf. figure 1.3 A).^[18,20] Due to this flow, the *steady-state* is also called actin

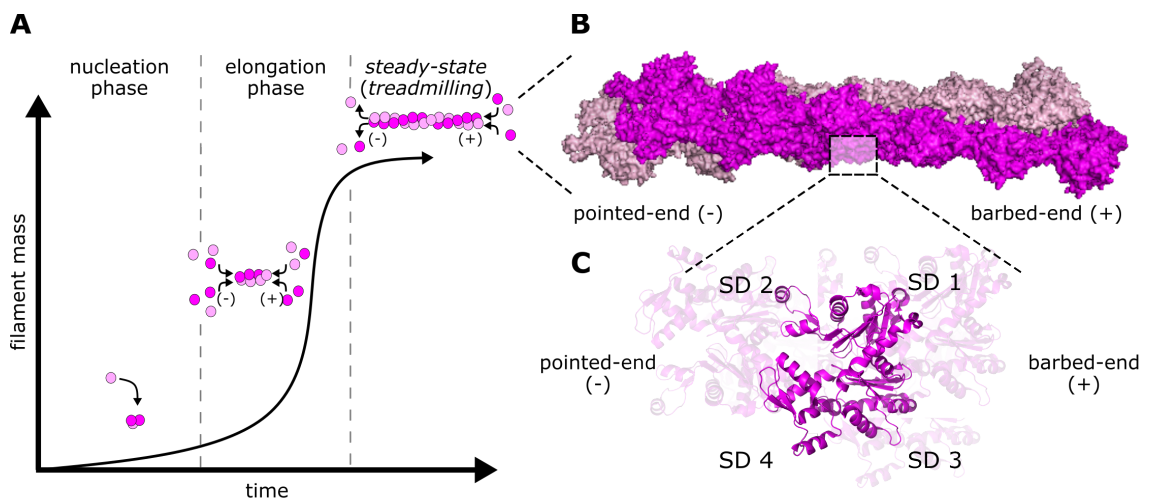
treadmilling.^[24]

Figure 1.3: Schematic illustration of the time-dependent actin polymerization and F-actin structure. **A:** Proposed actin polymerization model by KORN et al., showing the actin nucleation, elongation and *steady-state (treadmilling)* phases of F-actin. **B:** Illustration of the right-handed F-actin helix, showing the two left-handed single strands (magenta, light rose) and filament polarity with the barbed- (+) and pointed-ends (-). **C:** Representation of the head-to-tail organization of actin filaments, with SD 2 and 4 facing towards the pointed- and SD 1 and 3 towards to barbed-end. G-(1J6Z)^[16] and F-actin structure (3G37)^[25] were generated by means of PDB and the software PyMOL Molecular Graphics.

Cryo-electron microscopy revealed, that F-actin is composed of two left-handed actin chains, forming a right-handed helix (cf. figure 1.3 B).^[26] The F-actin helix exhibits a diameter of around 5 - 7 nm and repeats after 36 nm respectively 13 actin monomers with a rise of 2.76 nm per monomer.^[13,27,28] Within the F-actin, monomers interact with the two lateral opposing (lower and upper opposing) and the two longitudinally neighbouring actin monomers.^[20] An important longitudinal interaction appears between the in SD 2 located D-loop (cf. figure 1.2 A, highlighted in green) and the target binding cleft between SD 1 - 3.^[13] The lateral contact of a respective actin monomer with the upper and lower opposite neighboring actins is mediated by the hydrophobic plug between SD 3 - 4 (cf. figure 1.2 B). The hydrophobic plug connects the SD 2 of the lower and SD 3 of the upper opposing neighbours.^[20]

Non-muscle cells show a total actin concentration of 50 - 200 μM .^[29] Since *in vitro* these high concentration would lead to fast and spontaneous actin polymerization, cells have to control actin nucleation and F-actin assembly/disassembly. For this purpose, the cell possesses a broad spectrum of actin binding proteins (APBs) controlling

the F-actin polymerization. One of the most abundant APBs in eukaryotic cells is profilin. Profilin regulates the actin homeostasis by binding to the barbed-end of unpolymerized G-actin in the cytoplasm and preventing the actin nucleation.^[20,29] Furthermore, the profilin bound to G-actin barbed-ends inhibits the elongation at the F-actin pointed-end.^[29,30] Beside the nucleation control, ABPs such as the heterodimeric actin capping protein restrict F-actin elongation by binding specifically to the barbed-end.^[31] Other barbed-end specific ABPs, such as gelsolin, do not regulate elongation rates, but lead to severing of actin filaments.^[29]

Beside the regulation of single filament dynamics, ABPs are of fundamental importance for the architecture and organization of actin structures in cells. Figure 1.4 illustrates a number of the elementary cellular actin structures that are formed and coordinated by ABPs. For the macroscopic actin organization, cross-linking ABPs are of central importance. Cross-linkers are capable to connect polymerized F-actin, as they exhibit two individual actin binding sides.^[29] The distance between these binding sides determine the cross link distance of the respective proteins, ranging from a few nanometers up to 160 nm.^[8,32] Cross-linkers with a small cross-link distance, such as fascin or fimbrin, lead to a dense bundling of actin filaments. Parallel bundles of F-actin are present in filopodia of migrating cells or hair-cells (cf. figure 1.4 A).^[8] In addition to parallel actin bundles, anti-parallel ordered filaments occur in stress fibers, which are thick bundles of actin and the motor protein myosin II (cf. figure 1.4 C).^[33] Within this fiber, ~ 10 -20 actin filaments are anti-parallel cross-linked via the cross-linker α -actinin. Stress fibers are associated with focal adhesion sites and fulfill a key role in cell adhesion and motility.^[34] In contrast to bundling, cross-linkers, such as filamin, exhibiting a large cross-link range generate interconnected F-actin networks, such as the lamellipodia at the front of motile cells (cf. figure 1.4 C).^[8,29] The lamellipodium is a dense, nearly 2-dimensional, actin protrusion driven by the polymerization of branched actin filaments. Actin branching is controlled via the actin-related-protein 2/3 complex (Arp2/3).^[33] Arp2/3 is heptameric protein complex composed of the actin-related proteins Arp2/Arp3 and five supporting units (ArpC1-5).^[35] By binding to pre-existing "mother" filaments and activation via nucleating-promoting factors (NFPs) like the verprolin-homologous protein (WAVE), Arp2/3 is capable to polymerize new "daughter" filaments (branches) at a defined angle of $\sim 70^\circ$ (cf. figure 1.4 C).^[8,33] In addition to the lamellipodium, Arp2/3 is also localized in the actin cortex (cf. figure 1.4 A), which will be reviewed in more detail below.^[33]

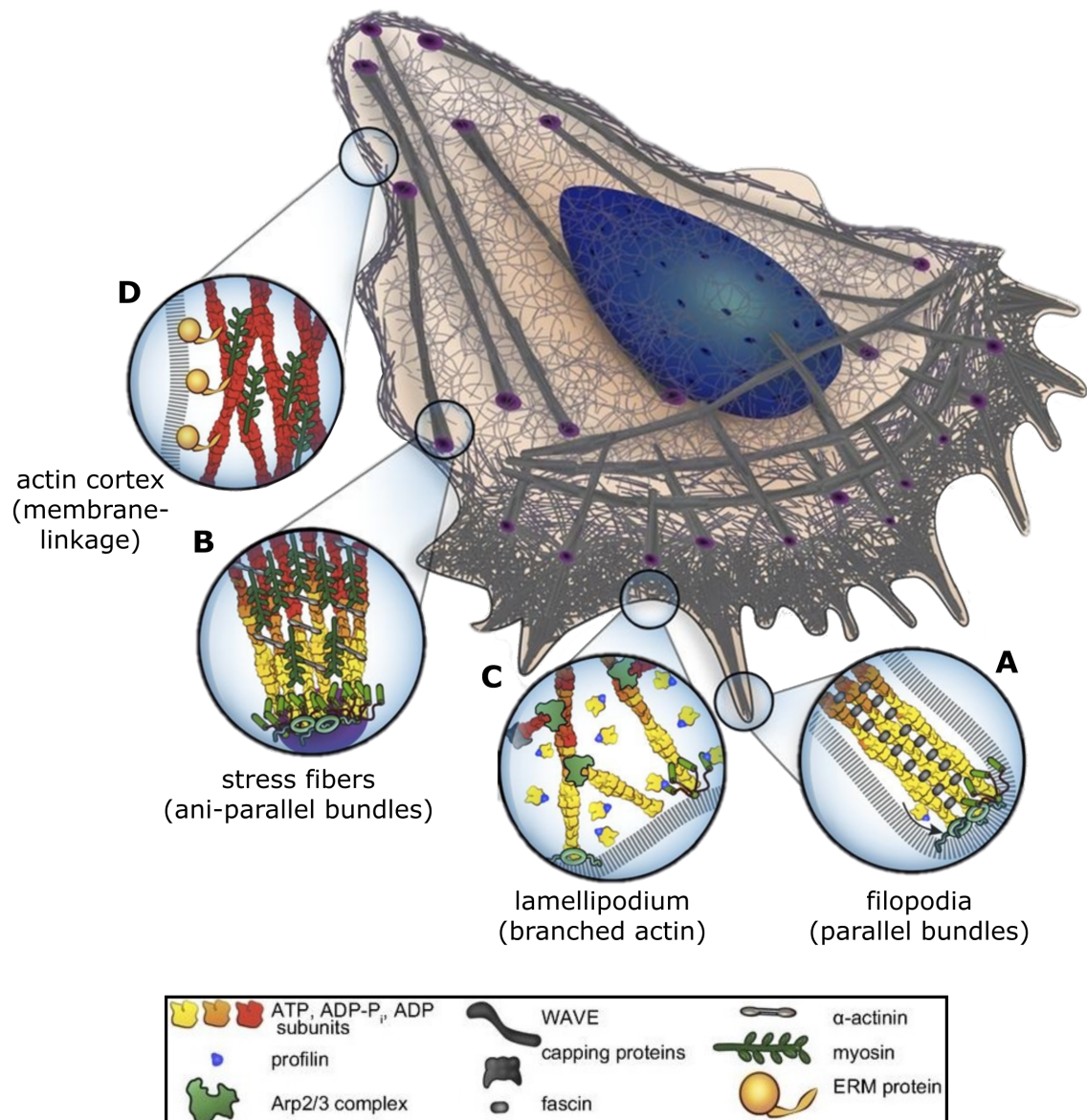


Figure 1.4: Cellular actin localization and organization. Schematic illustration of the *in vivo* actin architecture regulated by specific actin binding proteins. **A:** Filopodia formed by parallel organized F-actin bundled via the cross-linker fascin. **B:** Stress fibers of anti-parallel cross-linked actin filaments and associated α -actinin and myosin II. **C:** Lamellipodium formed by Arp2/3 branched actin filaments. **D:** Myosin II associated contractile actin cortex, linked to the plasma membrane via ERM-proteins. Figure modified from BLANCHOIN et al. [35]

1.3 The actin cortex

The actin cortex is a thin actin layer located at the cytoplasmic plasma membrane leaflet of the most mammalian cells (cf. figure 1.4 D).^[10] Within the cortex, actin is associated with more than hundred different ABPs.^[10,36] While cortical actin nucleation has been shown to be controlled via Arp2/3^[37] and several formins^[38,39], cross-linkers such as, fascin, filamin and α -actinin, form a dens interconnected actin network with a mesh size of 20-250 nm^[8,40] and a thickness of around 200 nm^[41].^[33] Actin filaments are organized both, parallel and perpendicular to the plasma membrane with the generally isotropic architected network.^[33] An important characteristic of the actin cortex is the direct membrane-attachment via linker-proteins such as myosin I motors or the ezrin/radixin/moesin (ERM) proteins.^[10,42]

The three members of the ERM-family are evolutionary highly conserved and share an amino acid sequence identity of over 70%.^[43] In mammals, the ERM-proteins show a tissue specific expression, with moesin being enriched in endothelial cells and radixin within hepatocytes. In contrast, epithelial cells exhibit a predominate expression of ezrin.^[44] The structure and function of the individual ERM domains will be described in the following based on ezrin. Ezrin is composed of a single polypeptide chain forming three characteristic domains: the N-terminal N-ERMAD domain (N-terminal ezrin-radixin-moesin associated domain), a long α -helical region and the C-terminal C-ERMAD domain (cf. figure 1.5 A).^[44] The N-ERMAD, which is also referred to as FERM domain (Four-point one, ezrin, radixin, moesin)^[42], is the membrane-binding domain of ezrin formed by around 300 amino acids. As illustrated in figure 1.5 B, N-ERMAD is composed of three subdomains (F1-3) forming a cloverleaf-like structure.^[43] N-ERMAD is linked via the \sim 170 amino acids containing α -helical region and a small linker to C-ERMAD.^[44] C-ERMAD is composed of \sim 80 amino acids, exhibiting the F-actin binding site within the last 34 amino acid residues.^[44] In cells ezrin is present in two conformational states, a closed (inactive) and opened (active) conformation.^[43] The closed conformation results from the interaction of N- and C-ERMAD within a single ezrin monomer or between two monomers (dimerization), masking the F-actin binding site (cf. figure 1.5 C I). For the transition from inactive to active, a two-step mechanism has been proposed.^[44-46] The first step, includes the binding of N-ERMAD to L- α -phosphatidylinositol-4,5-bisphosphate (PtdIns[4,5]P₂) (cf. figure 1.5 C II). PtdIns[4,5]P₂ is a negatively charged lipid, which is enriched

in the inner plasma membrane (PM) leaflet and accounts for 1 - 2 mol% of the total PM-lipids.^[47] The PtdIns[4,5]P₂ binding induces a conformational change of the associated N- and C-ERMAD, enabling a phosphorylation of the threonine residue at position 567.^[43] After phosphorylation ezrin transitions from the closed into the open conformation, as the negative charged induced by phosphorylation leads to repulsive interactions between N- and C-ERMAD.^[43] As schematically depicted in figure 1.5 C III, the opened ezrin is capable to link the actin cortex to the membrane.

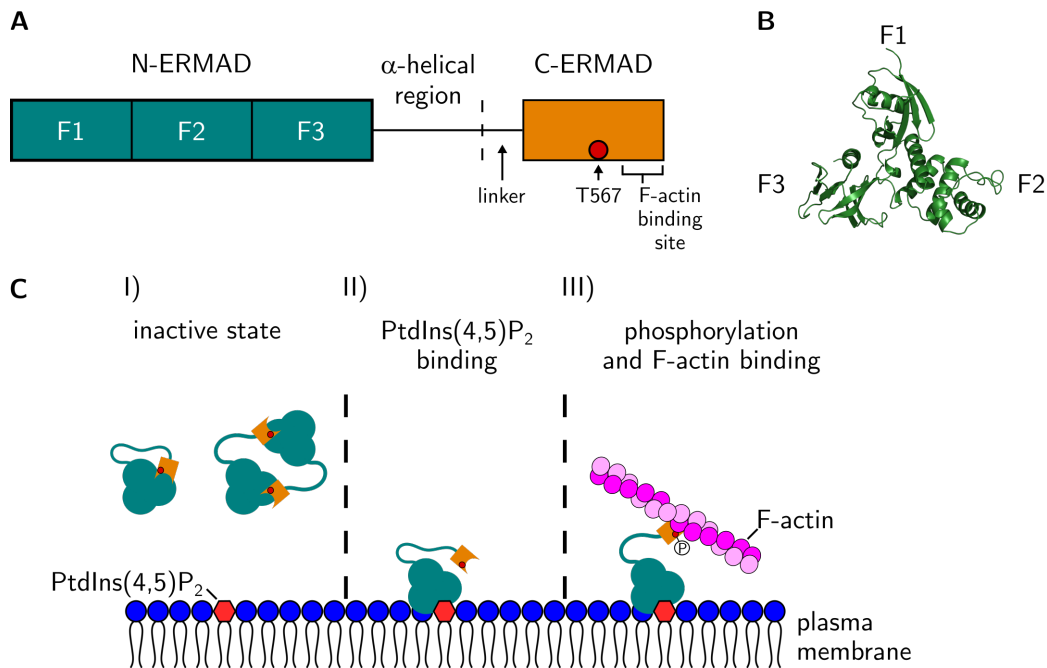


Figure 1.5: Schematic illustration of the ezrin domains and two-step activation. **A:** Ezrin domain organization: N-terminal ezrin-radexin-meosin associated domain (N-ERMAD, green) with the subunits F1-3, α -helical region, small linker segment and C-terminal ERM domain (C-ERMAD, orange) with the highlighted threonine at position 567 (T567, red circle) and the F-actin binding site. **B:** N-ERMAD crystal structure showing the cloverleaf-like organization of the subunits F1-3. **C:** (I) Inactive (closed) conformation of ezrin and two-step activation process (II-III) with the initial binding to PtdIns[4,5]P₂ (II) followed by a phosphorylation of T567 leading to full activation (III). In the opened (active conformation) ezrin is capable of linking the actin-cortex to the plasma membrane. N-ERMAD crystal structure of human ezrin (*1NI2*)^[48] was generated by means of PDB and the software PyMOL Molecular Graphics. Figure partly adapted from FEHON et al.^[44]

Another important protein which is associated with the cellular actin cortex is the motor protein myosin II. Myosin II is a hexameric protein complex composed of two heavy chains, containing the N-terminal motor domain and a long α -helical tail domain, two regulatory light chains and two essential chains.^[10,49] Myosin II

molecules assemble by the formation of a coil-coil structure between the α -helical tail domains.^[49] By a tail-to-tail assembly in a parallel and anti-parallel manner, several myosin II hexamers are capable to form bipolar myofilaments.^[50-52] In non-muscle cells, these myofilaments are composed of around 30 myosin II hexamers with a size of ~ 300 nm, while the general assembly process is controlled by the phosphorylation of the regulatory light chains.^[49,53] Myosin II is capable of binding F-actin via the N-terminal motor domain at the presumed main binding sites at the actin subdomains SD 1 and SD 3.^[20,54] By hydrolysing ATP, myosin II moves specifically towards the barbed-end of the bound actin filament.^[49,55] Since the actin cortex is a dense isotropically organized actin mesh, myofilaments are capable to reorganize the actin cortex by contraction.^[10,56] As the actin cortex is directly linked to the plasma membrane, network contraction and arising cortical tension are propagated towards the membrane, determining the cellular plasma membrane tension.^[10] The myosin II induced cortical tension is further dependent on the local actin cortex organization^[10] and membrane-cortex-linkage^[57]. Plasma membrane tension gradients have been shown to regulate cell shape during migration, cell division and cellular processes such as membrane trafficking^[58] and exocytosis^[59].^[10]

The high complexity of the cellular actin cortices impedes a determination of individual components impacting the dynamics and organization of membrane associated actin networks. Therefore, *in vitro* bottom up approaches of minimal actin cortices (MACs) were established over the recent years.^[60]

1.4 Actin cortex model systems

Since the cellular actin cortex is associated with motor proteins, such as myosin II, and hundreds of different actin binding proteins, biomimetic minimal actin cortices (MACs) have been evolved over the past decades to decipher functions and identify fundamental components.^[60] MACs are based on bottom up approaches, starting with the minimal set of components and increasing the system complexity over time. First approaches towards biomimetic minimal actin cortices were made via the charge mediated attachment of F-actin layers to the inside of GUVs (cf. figure 1.6 A I).^[61,62]

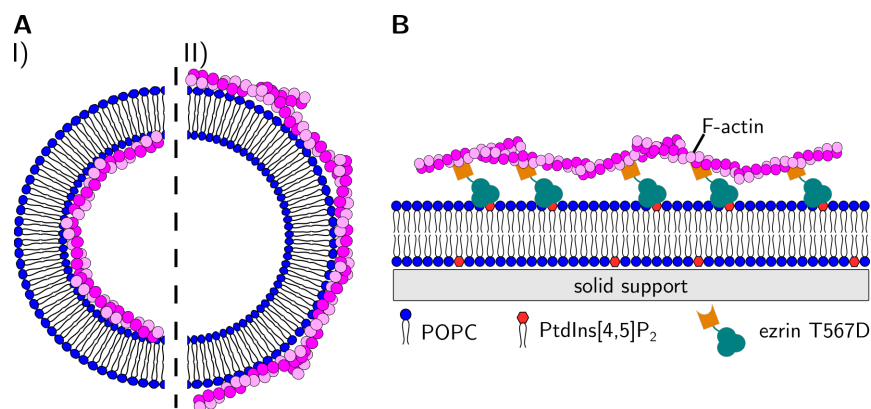


Figure 1.6: Schematic illustration of different approaches for minimal actin cortices (MACs). **A:** Exemplary illustration of three dimensional MACs on the in- (I) and outside (II) of GUVs. **B:** Illustration of a two-dimensional MAC on a solid supported lipid bilayer linked via the constitutively active ezrin mutant T567D. Figure adapted from SCHÖN et al.^[60]

While three dimensional model systems of in- or outside actin coated GUVs (cf. figure 1.6 A I/II) have been proven to be valid systems for the investigation of actin related mechanical properties^[63-67] and the polymerization behavior of encapsulated actin^[62,68], two dimensional (2D) MACs allow a more precise analysis of actin network organization and filament dynamics (cf. figure 1.6 B).^[60] These membrane-bound 2D MACs, based on solid supported bilayers, have been formed in various studies using in most instances artificial membrane-linkages. VOGEL et al. utilized biotin-neutravidin interactions to generate contractile actin-myosin II (actomyosin) networks on solid supported membranes. The authors were able to show, that F-actin contraction was accompanied by an actin filament fragmentation, which is also referred to as buckling and breaking.^[69] Similar observations were made by

GANZINGER et al., using a less artificial membrane-cortex linkage via a histidine-tagged VCA-domain and Ni-NTA-DGS receptor lipids, inducing Arp2/3 branched actin polymerization on solid supported membranes.^[70] Beside actin fragmentation, the authors were able to highlight the impact of myosin II on the actin turnover, as actomyosin cortices were characterized by a dynamic *steady-state* resulting from myosin II fragmentation/contraction and simultaneous actin polymerization. Similar to this approach, KÖSTER et al. utilized Ni-NTA-DGS receptor lipids and membrane-actin linkers constructed from variable histidine-tagged proteins and the F-actin binding domain of ezrin to generate contractile actomyosin cortices.^[71] The authors were able to reveal, that the contraction length scale of membrane-bound actomyosin networks is determined by the F-actin network organization, while actin network contraction is capable to modulate the membrane architecture.

Recently, NÖDING et al., as well as SCHÖN et al., developed a physiological minimal actin cortex by attaching pre-polymerized F-actin via the receptor lipid PtdIns[4,5]P₂ and the constitutively active ezrin mutant T567D to solid supported membranes (1.6 B).^[60,72] The point mutation in ezrin at position 567, from threonine to aspartic acid, induces a negative charge and leads to a pseudo-phosphorylation and a constitutively activated ezrin.^[73] While NÖDING et al. revealed that both, MAC organization and viscoelasticity are determined by the membrane concentration of the physiological receptor lipid PtdIns[4,5]P₂, SCHÖN et al. were able to highlight the dynamics of the ezrin-PtdIns[4,5]P₂ linkage, as the architecture of preformed MACs could be altered via cross-linkers.^[60,72]

2 Scope of thesis

One of the most important structures of mammalian cells is the cytoskeleton, which forms an intracellular network by a complex interaction of various proteins, providing both mechanical stability and high dynamics. A key component of this network is the actin cortex which is involved in the regulation of cell shape and processes such as exocytosis. The actin cortex itself is a thin layer of filamentous actin (F-actin), linked to the inner plasma membrane of mammalian cells by proteins of the ERM (ezrin/radixin/moesin) family. The actin cortex organization and dynamics such as contractility are regulated by hundreds of actin-binding proteins (ABPs), making this thin actin sheet a remarkably complex protein network.

Since the high complexity of this cortical actin network impedes the characterization of individual component properties and functions on the actin cortex *in vivo*, various bottom up approaches have been developed to detangle the complex interrelationships. In this work, biomimetic minimal actin cortices (MACs) composed of a solid-supported membrane, the ERM protein mutant ezrin T567D, and pre-polymerized F-actin will be utilized to model the attachment of the actin cortex to the plasma membrane in a minimal component system. In a first step, the MAC organization and membrane attachment will be investigated for various concentrations of the ezrin receptor lipid L- α -phosphatidylinositol-4,5-bisphosphate (PtdIns[4,5]P₂). Starting from this minimal system, the complexity of the MAC will be increased. For this purpose, the influences of biomimicking conditions, such as plasma membrane lipid composition or branched actin filaments, will be investigated in terms of MAC organization and membrane attachment. The acquired knowledge will then be used to establish biomimetic actomyosin cortices. The final aim is to investigate the dynamic contraction of membrane-bound actin cortices by bipolar myofilaments in dependence on parameters such as the ezrin-PtdIns[4,5]P₂ linkage. To reveal how the membrane-attachment of a biomimetic MAC alters the mechanical properties of the underlying lipid bilayer, pore-spanning membranes with ezrin-PtdIns[4,5]P₂ linked F-actin networks are to be established and probed via AFM-indentation experiments.

3 Materials and methods

3.1 Materials

3.1.1 Lipids

In this thesis model membranes were used to mimic and study the plasma membrane. Therefore artificial bilayers were prepared out of various receptor and matrix lipid mixtures to investigate their impact on the formation and reorganization of minimal actin cortices. For fluorescence microscopic examinations the membranes were additionally doped with lipid coupled fluorophores.

3.1.1.1 Receptor Lipids

Receptor lipids represent only a minor portion of the overall lipid composition, however, as a target for protein binding they enable the specific interaction of proteins with the lipid bilayer. Therefore receptor lipids play an important role, e.g. in the specific adsorption of proteins on membranes.

In the present thesis, the receptor lipid L- α -phosphatidylinositol-4,5-bisphosphate (PtdIns[4,5]P₂) was used. PtdIns[4,5]P₂ carries a negatively charged phosphorylated inositol headgroup, which serves as binding target for cytoskeletal linker-proteins like the ERM-protein ezrin (cf. chapter 1.3).^[74,75] For the experiments performed in this thesis, a natural PtdIns[4,5]P₂ mixture (*Avanti*[®], Alabaster, AL, USA), extracted from pork brains, was used. Crucial fatty acids within the lipid extract are stearoylic and arachidonoylic acid (figure 3.1, C₄₇H₉₄N₃O₁₉P₃, $M_{av} = 1096.36 \text{ g mol}^{-1}$).

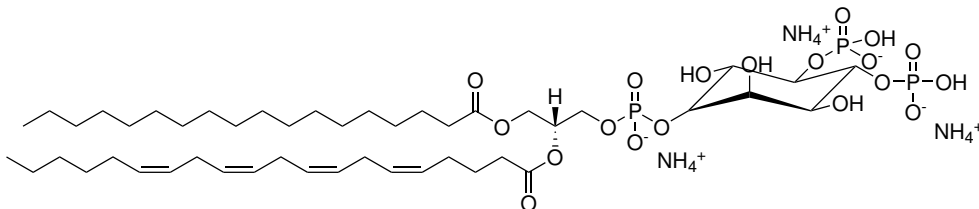
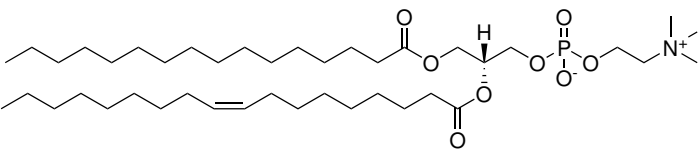
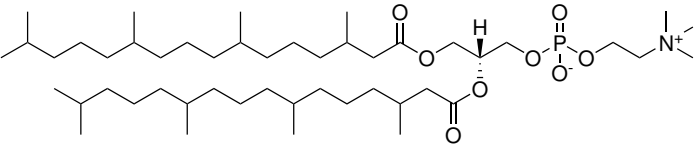
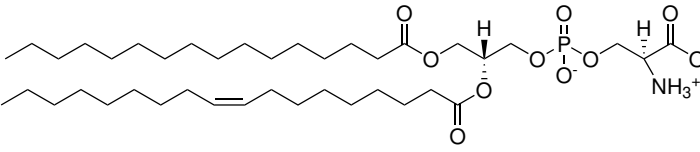


Figure 3.1: Chemical structure of PtdIns[4,5]P₂.

3.1.1.2 Matrix Lipids

Matrix lipids are the major components within artificial bilayers. In contrast to receptor lipids they do not interact with the target proteins. Dependent on the utilized system and technique four different matrix lipids were used in this work.

Table 3.1: Chemical structure and molar mass of matrix lipids used for membrane preparation.

Lipids	
	$M = 760.08 \text{ g mol}^{-1}$ $\text{C}_{44}\text{H}_{84}\text{NO}_8\text{P}$
POPC	
	$M = 846.25 \text{ g mol}^{-1}$ $\text{C}_{48}\text{H}_{96}\text{NO}_8\text{P}$
DPhPC	
	$M = 784.00 \text{ g mol}^{-1}$ $\text{C}_{40}\text{H}_{75}\text{NO}_{10}\text{P}$
POPS	

For measurements on solid supported lipid bilayers (SLBs) 1-palmitoyl-2-oleoyl-*sn*-glycero-3-phosphocholine (POPC, table 3.1) and 1-palmitoyl-2-oleoyl-*sn*-glycero-3-phospho-L-serine (POPS, table 3.1) were used. Both are phospholipids with a glycerol backbone carrying palmitic acid (16:0) at position 1 and oleic acid (18:1, Δ^9) at position 2. At position 3 POPC has a zwitterionic choline head group, whereas POPS bearing a negatively charged phosphoserine head group.

For experiments on pore spanning membranes (PSMs) 1,2-diphytanoyl-*sn*-glycero-3-phosphocholine (DPhPC, table 3.1) was used. DPhPC possesses a glycerol backbone,

a choline head group and two phytanoyl fatty acids at position 1 and 2 forming the hydrophobic tail. All matrix lipids were purchased from *Avanti® polar lipids* (Alabaster, AL, USA).

3.1.2 Fluorophores

In this work fluorescence microscopy was utilized to investigate a variety of experiments, like vesicle spreading and membrane formation or self-organization of minimal actin cortices. Therefore, different kinds of fluorescent probes were used.

3.1.2.1 Lipid coupled fluorophores

Lipid coupled fluorophores were embedded in artificial lipid bilayers and used for membrane detection as well as determination of homogeneity and lateral lipid diffusion.

ATTO 390

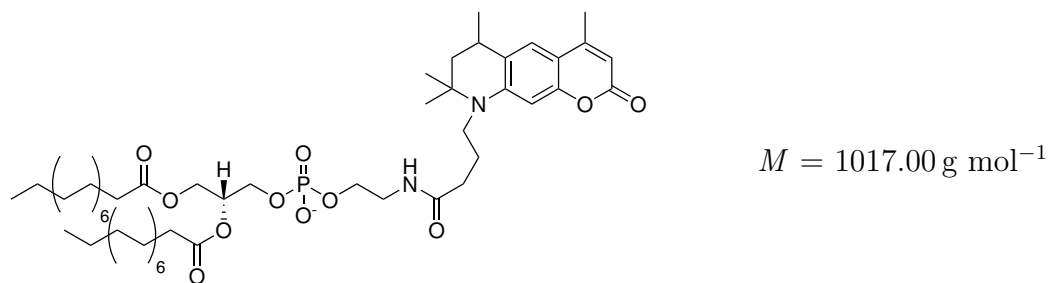
ATTO 390 is a coumarin based fluorophore and was purchased coupled to 1,2-dipalmitoyl-*sn*-glycero-3-phosphoethanolamine (ATTO 390-DPPE, $C_{57}H_{97}N_2O_{11}P$, cf. table 3.2) developed by *Atto-Tec GmbH* (Siegen, Germany). The excitation wavelength was $\lambda_{ex} = 405$ nm and the fluorescence was detected in the range of λ_{em} 450 - 550 nm.

ATTO 488

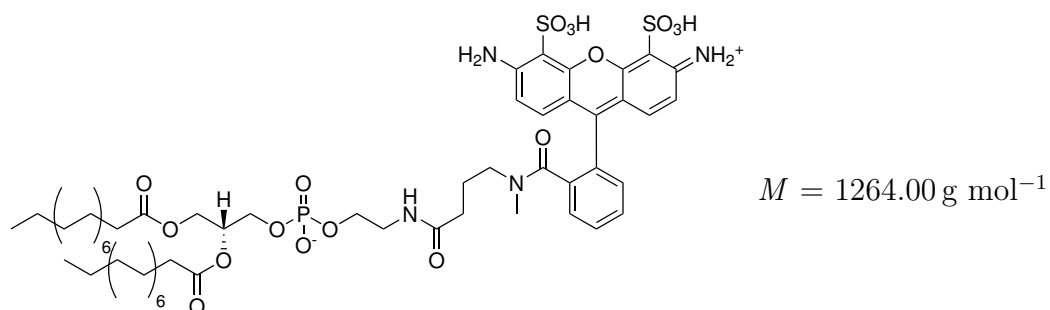
ATTO 488 belongs to the large family of xanthene dyes and was purchased coupled to 1,2-dipalmitoyl-*sn*-glycero-3-phosphoethanolamine (ATTO 488-DPPE, $C_{62}H_{96}N_4O_{17}PS_2$, cf. table 3.2) developed by *Atto-Tec GmbH* (Siegen, Germany). The excitation wavelength was $\lambda_{ex} = 488$ nm and the fluorescence was detected in the range of λ_{em} 520 - 570 nm.

Table 3.2: Chemical structure of lipid coupled fluorescent probes used for membrane preparation.

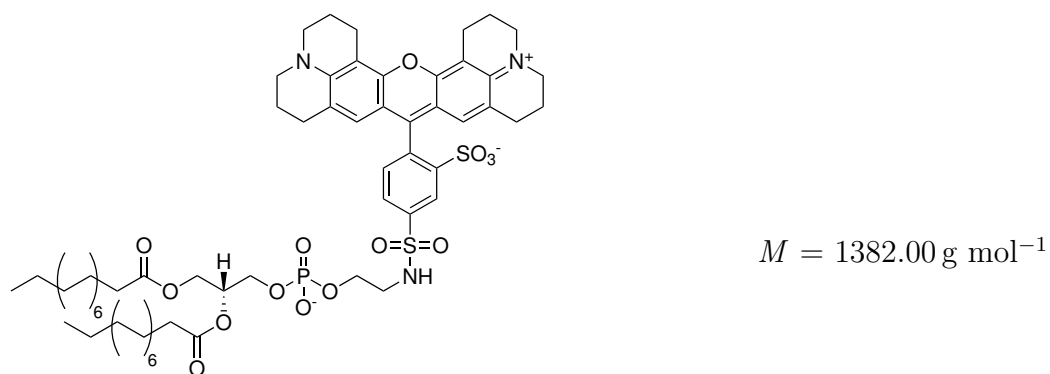
Lipid coupled fluorophores



ATTO 390-DPPE



ATTO 488-DPPE



TxR-DHPE

Texas Red[®]

Texas Red[®] (TxR) is a rhodamine based dye and was purchased coupled to 1,2-dihexadecanoyl-*sn*-glycero-3-phosphoethanolamine (TxR-DHPE, C₇₄H₁₁₇N₄O₁₄PS₂, cf. table 3.2) from *Thermo Fisher Scientific* (Waltham, MA, USA). The excitation wavelength was $\lambda_{ex} = 561$ nm and the fluorescence was detected in the range of λ_{em} 590 - 635 nm.

3.1.2.2 Protein staining fluorophores

Protein staining with fluorescent probes was performed for the investigation of protein localization, self-organization and tracking within the experiments. Depending on the target protein different fluorescent dyes were used.

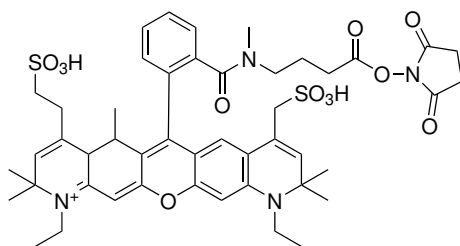
Actin

Actin staining was performed for different actin variants. The monomeric **G-actin** was labeled with a **ATTO 594-N**-hydroxysuccinimide(NHS)-ester (ATTO 594-NHS-ester, cf. table 3.3) developed by *Atto-Tec GmbH* (Siegen, Germany). ATTO 594 is a rhodamine based dye with a excitation wavelength of $\lambda_{ex} = 561$ nm, the fluorescence was detected in the range of λ_{em} 600 - 700 nm.

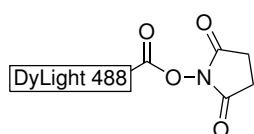
Filamentous **F-actin** was stained with the phalloidin conjugated dyes **Alexa Fluor[™] 488** ($M = 1320.00$ g mol⁻¹) or **Alexa Fluor[™] 633** ($M = 1900.00$ g mol⁻¹) (cf. table 3.3) from *Thermo Fisher Scientific* (Waltham, MA, USA). Alexa Fluor[™] 488 belongs, like ATTO 488, with a excitation wavelength of $\lambda_{ex} = 488$ nm and a detection range of λ_{em} 520 - 570 nm structural to the family of xanthane fluorophores. The Alexa Fluor[™] 633 was excited with wavelength of $\lambda_{ex} = 633$ nm and the fluorescence was detected in the range of λ_{em} 650 - 750 nm.

Myosin II

The monomeric muscle myosin II was fluorescently labeled with the NHS-ester conjugate **DyLight[®] 488** (DyLight[®] 488-NHS-ester, cf. table 3.3) from *Thermo Fisher Scientific* (Waltham, MA, USA). The excitation wavelength was $\lambda_{ex} = 488$ nm and the fluorescence was detected in the range of λ_{em} 520 - 570 nm.

Table 3.3: NHS and phalloidin coupled fluorophores for protein staining.**NHS-ester coupled fluorophores**

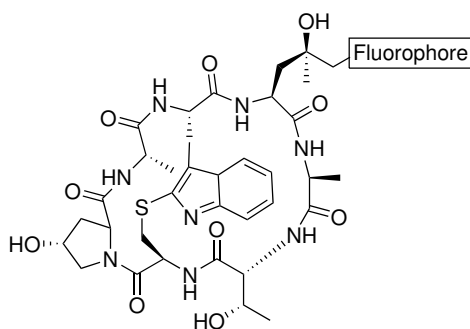
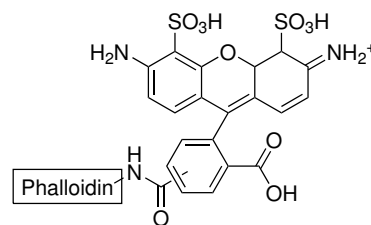
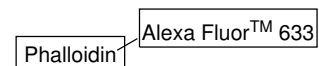
$$M = 1389.00 \text{ g mol}^{-1}$$

ATTO 594-NHS-ester

$$M = 1011.00 \text{ g mol}^{-1}$$

DyLight[®] 488-NHS-ester*

*structure of DyLight[®] 488-NHS-ester is not published.

Phalloidin coupled fluorophores**Phalloidin-****-Alexa Fluor[™] 488****-Alexa Fluor[™] 633****

**structure of Alexa Fluor[™] 633 is not published.

3.2 Proteins and biochemical methods

3.2.1 Ezrin T567D isolation

The recombinant expression of the encoding ezrin T567D sequence, with *N*-terminal hexahistidine-tag (His₆-tag), was performed according to the former work of HERRIG et al.^[76] Molecular cloning and recombinant plasmid preparation of a pET28a+ vector, carrying the encoding ezrin T567D sequence, were conducted and provided by the previous co-worker *Markus Schön*.

For the recombinant protein production of ezrin T567D the T7-expression system of *Escherichia coli* (*E. coli*) was used. The T7-expression system divides into two amplification levels. The first part consists of the *lac* operon (*lacO*) controlling the T7-RNA polymerase expression and is located in the genome of the *E. coli* host cells. The *lacO* is regulated by the *lac* inhibitor (*lacI*) encoding for the *lac* repressor, which is binding and preventing the T7-RNA polymerase expression. *lacI* forms together with the T7-promoter and T7-terminator, controlling the target gene, the second amplification level within the pET28a+ vector.^[77,78]

3.2.1.1 Plasmid transformation

The encoding pET28a+ vector was transformed via heatshock into the competent *E. coli* strain BL21(DE3)pLysS purchased from *Invitrogen* (Carlsbad, CA, USA). Owing to a treatment with calcium chloride and a still not fully resolved mechanism competent *E. coli* cells are permeable for foreign DNA.^[77]

Competent BL21(DE3)pLysS *E. coli* cells (50 μL /aliquot) were thawed on ice. Afterwards 1 μL plasmid (pET28a+, $c = 166 \text{ ng } \mu\text{L}^{-1}$), solved in ultrapure water, was added and incubated for 30 min on ice. The heatshock was subsequently carried out at 42 °C for 30 s in a water bath. Cells were placed on ice for 5 min, afterwards mixed with 450 μL SOC medium (super optimal broth with catabolite repression) and incubated for 1 h in a shaker (37 °C, 180 rpm). For selection, each 250 μL cell solution was plated on a LB (lysogeny broth) agar plate (60 $\mu\text{g}/\text{mL}$ kanamycin, 34 $\mu\text{g}/\text{mL}$ chloramphenicol) and incubated overnight (37 °C).

LB-agar	1.5 % (<i>w/v</i>) agar	SOC-	2 % (<i>w/v</i>) tryptone
	1 % (<i>w/v</i>) tryptone	medium	0.5 % (<i>w/v</i>) yeast extract
	1 % (<i>w/v</i>) NaCl		20 mM glucose
	0.5 % (<i>w/v</i>) yeast extract		10 mM NaCl
	pH = 7.4		10 mM MgCl ₂
			10 mM MgSO ₄
			2.5 mM KCl
			pH = 7.0

3.2.1.2 Heterologous protein expression

Heterologous expression of the protein ezrin T567D was established following a successful transformation and selection of single cell *E. coli* colonies carrying the encoding pET28a+ (cf. chapter 3.2.1.1). A pre-culture was prepared by picking a single colony and incubating overnight in 10 mL LB medium (60 µg/mL kanamycin, 34 µg/mL chloramphenicol). The main-culture (LB, 60 µg/mL kanamycin) was started by the addition of 2 % (*v/v*) grown pre-culture and incubated in a shaker (180 rpm) at 37 °C. The main-culture growing process was monitored until an optical density (OD_{600} , $\lambda = 600$ nm) of 0.6 was reached, subsequently the ezrin T567D gen expression was induced by adding 1 mM isopropyl β -D-thiogalactopyranoside (IPTG) and incubated for 4 h (37 °C, 180 rpm). Afterwards the cell suspension was placed 10 min on ice and centrifuged (2700 g, 20 min, 4 °C, *Allegra X-22R*, *Beckman Coulter*, Brea, USA). The obtained cell pellets were combined and the purification proceeded or cell pellets were stored at -20 °C until purification.

LB medium	1 % (<i>w/v</i>) tryptone
	1 % (<i>w/v</i>) NaCl
	0.5 % (<i>w/v</i>) yeast extract
	pH = 7.4

3.2.1.3 Cell lysis and protein purification

Cell lysis was performed mechanically by means of tip sonification (*Sonopuls, Bandelin electronic GmbH & Co. KG, Berlin, Germany*). For this purpose the cell pellet was solved in lysis buffer and tip sonification was executed on ice (60 % power, 5 x 30). The lysed cell suspension was clarified via ultracentrifugation (*Beckman L70 Ultra Centrifuge, Beckman Coulter, Krefeld, Germany, 100000 g, 4 °C, 1 h*) and the protein containing supernatant stored on ice until purification.

Protein purification was executed via immobilized metal ion affinity chromatography (IMAC). IMAC is based on the transient complex forming properties of metal ions like Ni^{2+} or Co^{2+} with histidine or cysteine residues.^[79] The recombinant ezrin T567D was therefore expressed with a *N*-terminal His₆-tag and purified by means a of nickel-nitrilotriacetic acid (Ni-NTA) agarose (*Quiagen, Hilden, Germany*) column. Within the Ni-NTA complex four of the six binding sites at the octahedral Ni^{2+} center are chelated by NTA. The remaining two ligand sites can be occupied by two histidines (n/n_{+2}) of the His₆-tag.^[79,80] Controlled protein elution can be achieved by means of imidazole, which expresses a high affinity to the Ni^{2+} and displaces the bound His₆-tag.

Ni-NTA columns were filled with a bed volume of 2.5 mL Ni-NTA agarose, washed with ultra pure water and equilibrated with equilibration buffer (EQ, each three column volumes). The supernatant was loaded once on to the Ni-NTA column and incubated during running through by gravity flow. After incubation, excess and unspecific bound proteins were washed of by applying washing buffer I & II (WI & WII, each one column volume). Ezrin T567D was eluted with one column volume of elution buffer and aliquoted in fractions of 1.5 mL. Each step was performed at 4 °C and fractions were collected during lysate incubation and WI- & WII-washing steps.

lysis	300 mM NaCl	EQ buffer	300 mM NaCl
buffer	40 mM HEPES		40 mM HEPES
	20 mM imidazole		20 mM imidazole
	1 mM ETDA		pH = 7.4
	10 mM β -mercaptoethanol*		
	Roche [®] cOmplete [™] *		
	pH = 7.4		

WI buffer	300 mM NaCl 40 mM HEPES 30 mM imidazole 1 mM MgCl ₂ 10 mM β -mercaptoethanol* pH = 7.4	WII buffer	150 mM NaCl 40 mM HEPES 40 mM imidazole 1 mM MgCl ₂ 10 mM β -mercaptoethanol* pH = 7.4
elution buffer	50 mM KCl 20 mM Tris 250 mM imidazole pH = 7.4		

*added prior to usage

3.2.1.4 Sodium dodecyl sulfate polyacrylamide gel electrophoresis (SDS-PAGE)

The successful ezrin T567D isolation was validated by means of sodium dodecyl sulfate polyacrylamide gel electrophoresis (SDS-PAGE). Basis of the SDS-PAGE is the movement of charged particles like proteins within an electric field, which allows a separation by molecular mass.^[81,82] The detergent SDS accumulates via its charged head group and hydrophobic residue at the proteins, induces a protein linearization, covers their intrinsic charge and applies a constant mass-to-charge ratio.^[81] Additionally the SDS-Page is performed under reducing conditions by means of dithiothreitol (DTT) or β -mercaptoethanol, reducing intramolecular disulfide bridges within the proteins. Beside the constant mass-to-charge ratio the porous polyacrylamide gel is a key factor in the separation of proteins by their molecular mass. Using a discontinuous gel electrophoresis with a stacking gel (here 5.2 % acrylamide, pH 8.8) and resolving gel (here 12.5 % acrylamide, pH 8.8) allows a protein stacking and focusing prior to separation.

The polyacrylamide gel preparation was performed with the gel electrophoresis kit Mini-PROTEAN[®] Tetra Cell (*Bio-Rad Laboratories Inc.*, Hercules, USA). Prior to use, the glasses were cleaned in sequence with ultrapure water and isopropanol p.a. and deployed inside the gel electrophoresis kit. Initially the resolving gel (12.5 % acrylamide, pH 8.8) was filled in the gel chamber, covered with isopropanol

p.a. and polymerized for at least 20 min. The polymerization of acrylamide and bisacrylamide was initialized with ammonium peroxydisulfate (APS) and catalyzed by *N,N,N',N'*-tetramethyl ethylenediamine (TEMED). Afterwards, the isopropanol p.a. was removed from the polymerized resolving gel and the stacking gel (5.2 % acrylamide, pH 8.8) was layered above. Sample pockets were formed by placing a comb inside the stacking gel and polymerization was carried out analogously to the resolving gel. Afterwards the polyacrylamide gel was placed inside the electrophoresis chamber and the comb was removed. The chambers in- and outside were filled with electrophoresis buffer and the protein samples loaded into the sample pockets.

The protein samples were prepared during gel polymerization. The collected fractions (cf. chapter 3.2.1.3) were mixed 1:1 with sample buffer and incubated for 10 min at 95 °C. Per sample 10 µL solution were loaded into a sample pocket and per gel one pocket was filled with a molecular marker (*PageRuler™ Plus*, 10 - 250 kDa, 5 µL). Subsequently the chamber was connected to a power source applying an electric tension of 200 V over 50 min. Afterwards the gel was stained with a water-Coomassie brilliant blue solution (0.08 % (*w/v*) Coomassie brilliant blue G-250, 25 mM HCl) in a microwave (800 W, 30-45 s). Decolorizing was performed with two rounds of boiling ultrapure water (each 5 min) and a variable short incubated in destaining solution. After destaining the gels were imaged (*Azure c300*, *Azure Biosystems*, Inc., Dublin, USA).

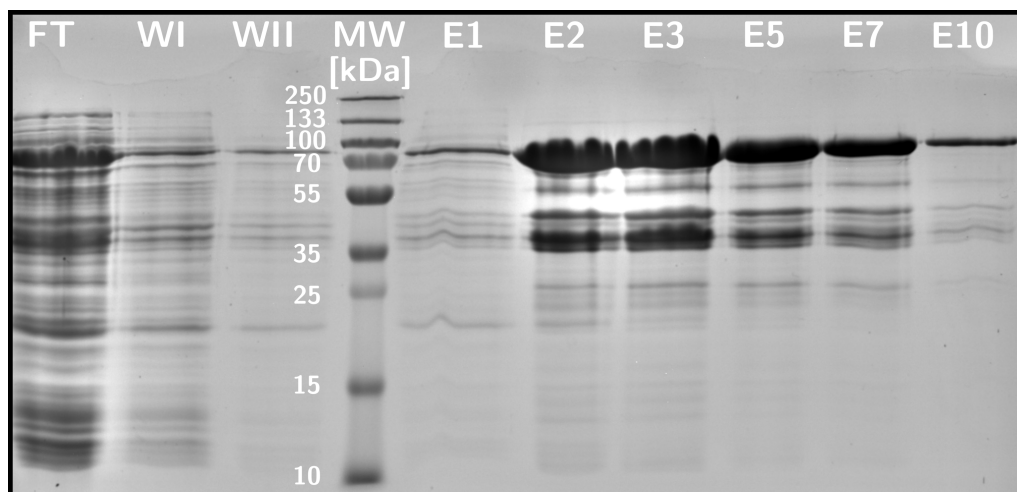


Figure 3.2: Exemplary SDS-PAGE of *N*-terminal His₆-tagged ezrin T567D ($M = 73.25$ kDa) with the flow through (FT), washing steps I & II (WI & II), several elution fractions (E1-10) and a molecular weight marker (MW, *PageRuler™ Plus*, 10 - 250 kDa).

Ezrin T567D ($M = 73.25$ kDa) containing fractions (cf. figure 3.2) were selected, combined and dialysed (4 °C, 24 h) with a 100-fold volume of ezrin buffer (E1). E1 buffer was replaced after 4 and 16 h and ezrin T567D was stored at 4 °C for a maximum of 3 months after concentration determination (cf. chapter 3.2.3).

resolving gel (12.5 %)	2.1 mL 30 % AAmix* 1.6 mL H ₂ O 1.3 mL 1,5 mM Tris 40 µL 10 % (<i>w/v</i>) SDS 40 µL 10 % (<i>w/v</i>) APS 2 µL TEMED pH = 8.8	stacking gel (5.2 %)	0.33 mL 30 % AAmix* 1.4 mL H ₂ O 0.25 mL 1,5 mM Tris 20 µL 10 % (<i>w/v</i>) SDS 20 µL 10 % (<i>w/v</i>) APS 2 µL TEMED pH = 6.8
electroph. buffer	25 mM Tris 192 mM glycine 0.1 % (<i>w/v</i>) SDS pH = 8.3	sample buffer	175 mM Tris 0.3 mM DDT 15 % (<i>w/v</i>) glycerol 5 % (<i>w/v</i>) SDS 0.02 % (<i>w/v</i>) bromophenol blue pH = 6.8
E1 buffer	50 mM KCl 20 mM Tris 0.1 mM NaN ₃ 0.1 mM EDTA pH = 7.4		

*AAmix (acrylamide:bisacrylamide, 37.5:1)

3.2.2 Skeletal rabbit muscle myosin II isolation

Isolation of skeletal rabbit muscle myosin II was performed together with Lucia Baldauf in the laboratories of Prof. Dr. Gijsje Koenderink at the AMOLF institute in Amsterdam.

The skeletal rabbit muscle myosin II was isolated from the leg muscles of a female rabbit, purchased from *Harlan Laboratories* (Belton, Leicestershire, UK), according to the work of MARGOSSIAN and LOWEY.^[83] All isolation steps were performed at 4 °C or with all reagents stored on ice.

Day 1

The isolation was started with 800 g rabbit muscular meat, which was cleaned in the first step. Tendons and remaining fat were cut off and the muscles chopped into small pieces. Subsequently, a meat grinder was rinsed with EDTA solution (20 mM, pH 7.0) and dissected muscles (500 g remaining) were carefully shredded. The muscle mince was extracted under slow constant stirring by hand for 15 min with 1 L of buffer A. Actin isolation was minimized by not extending the extraction over 15-20 min.^[83] Extraction was stopped by diluting the solution with a 4-fold of cold ultra pure water to a total volume of 4 L (cf. figure 3.3 A). Muscle residues were separated by filtrating through three layers of cheesecloth. The extract was precipitated by dilution with a 1.5-fold of cold water to a total volume of 10 L reaching a final ionic strength of ~ 0.04 (10-fold diluted buffer A). Myosin was settled down overnight, forming a white cloud at the bottom portion (cf. figure 3.3 B).

Day 2

The clear supernatant was carefully siphoned off and discarded until a small layer remained over the settled myosin. The remaining precipitated protein was centrifuged (*Avanti J-E, Beckman Coulter, Krefeld, Germany*) for 15 min (8000 g, 4 °C) and the obtained pellet resuspended in 150 mL buffer B for a maximum volume of 400 mL. Afterwards, the protein suspension was dialyzed for 5 h against 4.5 L of buffer C. After dialysis the volume of the protein solution was measured and the solution was slowly diluted with an equal amount of cold ultrapure water. During this dilution the

actomyosin precipitated, where the ionic strength should not be lowered under 0.3, since the myosin may also precipitate (cf. figure 3.3 C).^[83] The diluted suspension was stirred for 30 min and subsequently centrifuged for 15 min (16000 g, 4 °C) to pelletize actomyosin. The pellet was discarded and the supernatant centrifuged for further 1.5 h (38000 g, 4 °C). The pellet was discarded again, the volume of the supernatant was measured and afterwards diluted with 8-fold cold ultrapure water giving a final ionic strength of 0.04 precipitating myosin overnight (cf. figure 3.3 D).

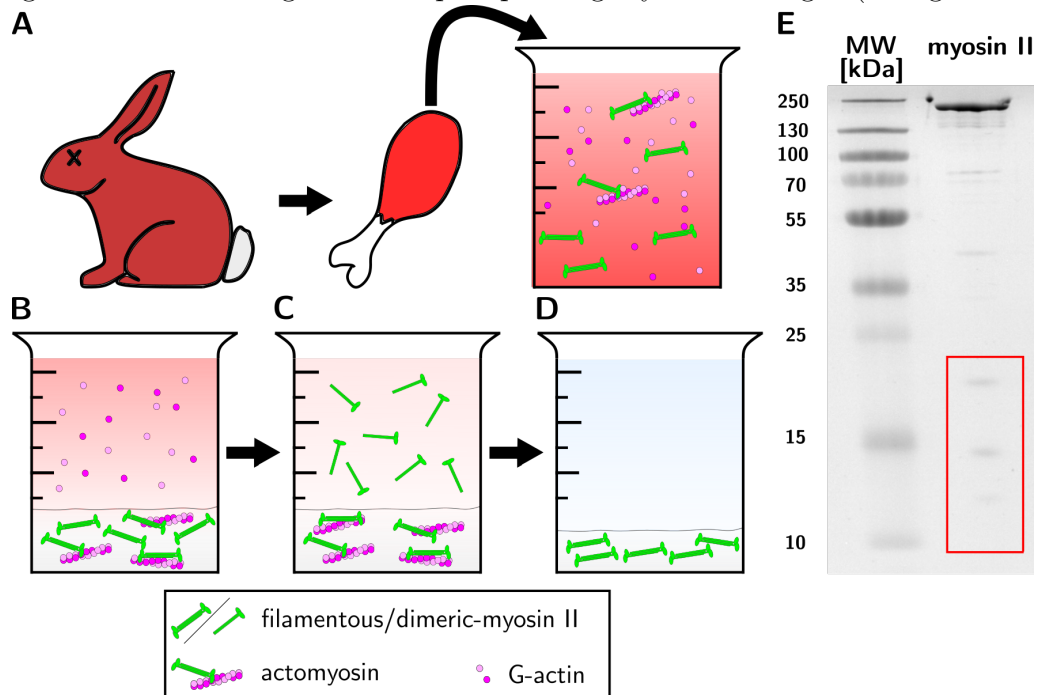


Figure 3.3: Schematic illustration of critical steps within skeletal rabbit muscle myosin II isolation. **A:** Rabbit muscular meat cleaning, grinding and myosin extraction. **B:** First myosin precipitation for separation of soluble proteins. **C:** Separation of actomyosin via precipitation from myosin solution. **D:** Final precipitation of myosin. **E:** Exemplary SDS-PAGE of skeletal rabbit muscle myosin II with a molecular weight marker (MW, *PageRuler™ Plus*, 10 - 250 kDa) and region expected for MLC's highlighted in red.

Day 3

Analogously to day 2, the supernatant was carefully siphoned off and discarded until a small layer remained over the precipitated myosin. The settled protein was centrifuged for 25 min (8200 g, 4 °C). The arisen supernatant was discarded and the pellet was solved in a minimum volume of buffer D. Afterwards the resuspended myosin was dialyzed overnight against 2 L of buffer E.

Day 4

After dialysis, the myosin was centrifuged for 3 h (38000 g, 4 °C) separating the soluble myosin from remaining lipids and insoluble proteins. The myosin containing supernatant was carefully siphoned off without any lipid material floating on top of the protein solution. Afterwards, the myosin concentration was determined (cf. chapter 3.2.3) and subsequently mixed in a 1:1 ratio with precooled glycerol. The myosin/glycerol solution was stored at -20 °C.

The myosin purity was validated by means of SDS-PAGE (cf. figure 3.3 E). Gel preparation as well as all subsequent steps were performed according to chapter 3.2.1.4. The full length dimeric myosin II isolated from rabbit muscles is reported with a molecular weight of 470 kDa.^[83] Each myosin dimer consist of two myosin heavy chains (MHC's, ~220 kDa) with each two additional myosin light chains (MLC's, ~10-25 kDa). Reducing conditions during SDS-PAGE leading to dissociation of the dimeric myosin into two MHC's and four MLC's.^[84,85]

buffer A	300 mM KCl 150 mM KH ₂ PO ₄ ** 20 mM EDTA 5 mM MgCl ₂ 1 mM ATP* pH = 6.5	buffer B	1 M KCl 600 mM KH ₂ PO ₄ ** 25 mM EDTA pH = 6.5
buffer C	600 mM KCl 25 mM KH ₂ PO ₄ ** 10 mM EDTA 1 mM DTT* pH = 6.5	buffer D	3 M KCl 50 mM KH ₂ PO ₄ ** 1 mM DTT* pH = 6.5
buffer E	600 mM KCl 50 mM KH ₂ PO ₄ ** 1 mM DTT* pH = 6.5		

*added prior to usage

**phosphate buffer stock of KH₂PO₄ and K₂HPO₄ at pH = 6.5

3.2.3 Determination of Protein Concentration

The determination of protein concentration is a critical step, since the result forms the basis for subsequent experiments and calculations. Within this work protein concentration was determined by means of UV/Vis spectroscopy. This technique is based on the absorption of light at a wavelength of 280 nm by the aromatic amino acids tryptophan, tyrosine and phenylalanine.^[86] According the LAMBERT-BEER law (cf. equation 3.1), the absorbance (A_{280} , $\lambda = 280$ nm) is a linear function of the protein concentration (c) with the molar attenuation coefficient (ε_{280} , $\lambda = 280$ nm) and the optical light path (d).^[87]

$$A_{280} = \log \frac{I_0}{I} = \varepsilon_{280} \cdot c \cdot d \quad (3.1)$$

For calculation, the initial light intensity (I_0) as well as the intensity after passing the protein solution (I) were needed. UV/Vis spectroscopy measurements were performed with the NanoDrop™ 2000c (*Thermo Fisher Scientific*, Waltham, MA, USA). The molar absorption coefficient of myosin II was taken from ALVARADO and KOENDERINK ($\varepsilon_{280 \text{ myosin}} = 249000 \text{ M}^{-1}\text{cm}^{-1}$) and for ezrin T567D and non-muscle G-actin (*Cytoskeleton*, Denver, CO, USA; human platelet, 85 % β -actin, 15 % γ -actin) theoretically calculated with the online tool ProtParam ($\varepsilon_{280 \text{ ezrin}} = 66935 \text{ M}^{-1}\text{cm}^{-1}$, $\varepsilon_{280 \text{ actin}} = 44350 \text{ M}^{-1}\text{cm}^{-1}$).^[7]

For labeled proteins, the adsorption of the particular fluorophore at a wavelength of 280 nm must be included. Therefore the correction factor (CF_{280}), provided by manufacturer, as well as the maximum fluorophore absorbance (A_{max}) at the absorption wavelength maximum (λ_{max}) must be taken into account. Following this, the protein concentration (c) can be determined according to equation 3.2.

$$c = \frac{A_{280} - (A_{max} \cdot CF_{280})}{\varepsilon_{280}} \quad (3.2)$$

The degree of labeling (DOL) displays the moles of dye per mole protein and can be calculated according to equation 3.3, needing the molar absorption coefficient of the particular fluorophore (ε_{max}) at λ_{max} .

$$DOL = \frac{A_{max}}{\epsilon_{max} \cdot C_{protein}} \quad (3.3)$$

Table 3.4: Overview of the fluorophore-specific parameters used for concentration and *DOL* determination.

	CF_{280}	λ_{max}	ϵ_{max}
ATTO 594	0.500	603 nm	120000 M ⁻¹ cm ⁻¹
DyLight® 488	0.147	493 nm	70000 M ⁻¹ cm ⁻¹

3.2.4 Protein labeling

Fluorescence labeling of proteins is a common method for the visualization of protein localization and interactions within experiments. *N*-hydroxysuccinimide(NHS)-ester modified fluorescent conjugates are commonly used probes for modification of primary amino groups in proteins and were introduced first by ANDERSON et al. [88,89] NHS-esters are characterized by a high selectivity for aliphatic amines, low reaction rates for aromatic amines or primary hydroxyl groups and a physiological reaction pH of 7.0 - 9.0 in aqueous solutions. [90]

Within this work two different *N*-hydroxysuccinimide(NHS)-ester conjugates (cf. chapter 3.1.2.2) were used for the specific fluorescence labeling of actin and myosin II, targeting different lysine residues. The reaction follows a nucleophilic acyl substitution mechanism illustrated in figure 3.4.

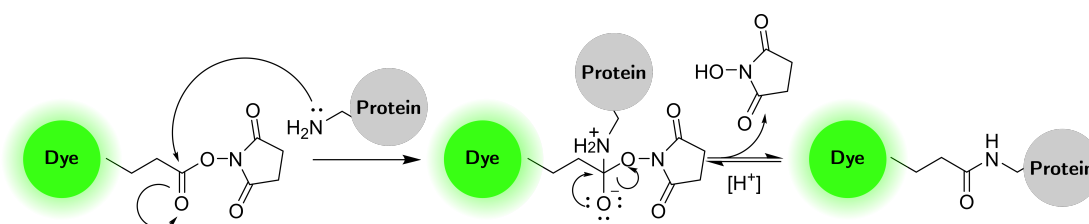


Figure 3.4: Reaction mechanism of an (NHS)-ester conjugated fluorescent probe with primary amino group. The *N*-hydroxysuccinimide ring activates the carbonyl-C-atom for the primary amine nucleophilic attack, following a nucleophilic acyl substitution mechanism.

3.2.4.1 G-actin labeling with ATTO 594-NHS-ester

Non-muscle G-actin (nm actin, 2 mg, human platelet, 85 % β -actin, 15 % γ -actin) purchased from *Cytoskeleton* (Denver, CO, USA) was solved in DTT free G-buffer to a final concentration of 6.67 mg mL⁻¹ and dialyzed (*Slide-A-Lyzer MINI*, 20kDa MWCO, *Thermo Fisher Scientific*, Waltham, MA, USA) overnight against 0.5 L DTT free and N₂-flushed G-buffer at 4 °C. Subsequently, the actin volume was measured and the solution filled up to 1 mL with a final actin concentration of 2 mg mL⁻¹. The solution was transferred in a 1.5 mL eppendorf cup and polymerized with 100 μ L F1-solution for 40 min at 20 °C. ATTO 594-NHS-ester (cf. chapter 3.1.2.2) was solved in water free dimethyl sulfoxide (DMSO) to a final concentration of 21 mM. Labeling was initialized by adding ATTO 594-NHS-ester (14.5 μ L, 21 mM) to the polymerized actin for a final concentration of 0.3 μ M resulting in a 6.5 molar excess. The solution was carefully and slowly mixed with a cut off 1 mL eppendorf pipette, immediately transferred in a 1 mL ultra centrifugation tube and incubated for 1 h at 20 °C. The reaction was stopped by adding 10 mM Tris solution (0.5 M, pH 7.8) and labeled F-actin was centrifuged (100000 g, 12 °C) for 1 h. The obtained supernatant was discarded, the actin pellet resuspended in 500 μ L cold G-buffer and depolymerized on ice for 1 h. G-actin labeled with ATTO 594 was recycled by repolymerizing with the addition of 50 μ L F1-solution (1/10 actin volume) and subsequent incubation (40 min, 20 °C) in freshly prepared ultra centrifugation tubes. The polymerized F-actin was centrifuged (100000 g, 4 °C) for 1 h, the resulting pellet resuspended in 1 mL cold G-buffer and dialyzed (14KDa MWCO, *ZelluTrans*[®], *Carl Roth GmbH+Co. KG*, Karlsruhe, Germany) overnight against 1.5 L G-buffer at 4 °C. During dialysis F-actin depolymerized into G-actin, which was separated from insoluble actin by means of centrifugation (100000 g, 4 °C, 3.5 h). The G-actin containing supernatant was saved and the concentration of ATTO 594 labeled G-actin determined (cf. chapter 3.2.3). Finally the ATTO 594 labeled G-actin was aliquoted, snap frozen in liquid nitrogen and stored at -80 °C.

G-buffer	5 mM HEPES	F1-solution	500 mM KCl
	0.2 mM CaCl ₂		100 mM HEPES
	0.3 mM ATP*		20 mM MgCl ₂
	0.5 mM DTT*		20 mM ATP
	pH = 8.0 (NaOH)		pH = 7.4

*added prior to usage

3.2.4.2 Myosin II labeling with DyLight® 488-NHS-ester

Skeletal rabbit muscle myosin II (cf. chapter 3.2.2) was fluorescently labeled with DyLight® 488 according to a protocol adapted from DEBIASIO et al. and E SILVA et al.^[51,91] All labeling steps were performed at 4 °C or with all reagents stored on ice.

The myosin II isolated from rabbit muscles was stored at -20 °C in myosin storage buffer (MS buffer) containing 50 % (*v/v*) glycerol. For the fluorescent labeling the protein was dialyzed (14KDa MWCO, ZelluTrans®) overnight against 1 L glycerol free myosin buffer (M buffer) and subsequently for 2 h against 500 mL labeling buffer I. Afterwards, the myosin II volume was measured and the concentration determined (cf. chapter 3.2.3). DyLight® 488-NHS-ester (cf. chapter 3.1.2.2) was solved in water free DMSO to a final concentration of 10 mg mL⁻¹ and myosin labeling was initialized by adding a 20-fold molar excess DyLight® 488-NHS-ester to the protein solution. The mixture was incubated for 1 h on ice and the reaction stopped by adding 20 mM D-lysine, with an incubation time of 5 min. The labeled myosin II was separated from unbound dye by dialyzing (14KDa MWCO, ZelluTrans®) against 500 mL labeling buffer II overnight with a complete buffer replacement after 3 h. The dialyzed myosin solution was collected, 10 mM MgCl₂ were added and the polymerized myosin II filaments centrifuged for 10 min (8000 g, 4 °C). The obtained myosin pellet was resuspended in a minimal amount of labeling buffer III and subsequently dialyzed overnight against 1 L of buffer III. After dialysis the finally labeled myosin II was collected and the concentration, as well as the labeling ratio, was determined (cf. chapter 3.2.3). For storage, the labeled myosin was mixed in a 1:1 ratio with pre-cooled glycerol and stored at -20 °C.

MS buffer	300 mM KCl	M buffer	300 mM KCl
	25 mM KH ₂ PO ₄ **		4 mM MgCl ₂
	0.5 mM DTT		20 mM imidazole
	50 % (<i>v/v</i>) glycerol		1 mM DTT*
	pH = 6.5		pH = 7.4

buffer I	10 mM HEPES 50 mM KCl 0.2 mM EGTA 2 mM MgCl ₂ 2 mM ATP** pH = 7.0	buffer II	10 mM HEPES 50 mM KCl 0.2 mM EGTA pH = 7.0
buffer III	600 mM KCl 50 mM KH ₂ PO ₄ 1 mM DTT* pH = 6.5		

*added prior to usage

**phosphate buffer stock of KH₂PO₄ and K₂HPO₄ at pH = 6.5

3.3 Preparative methods

3.3.1 Vesicle preparation

3.3.1.1 Small unilamellar vesicles

Small unilamellar vesicles (SUVs, $\varnothing \sim 100$ nm) were formed from rehydrated lipid films by means of sonification. All SUVs were manufactured on the basis of POPC as matrix lipid. For each additional component added, such as receptor lipids or fluorescent probes, the amount of POPC was reduced by x-mol%.

Based on stock solutions of the required lipids, with concentrations ranging from 1.0 mg mL⁻¹ to 20 mg mL⁻¹, lipid films with a final mass of 0.4 mg were prepared. The desired lipids were mixed in a chloroform containing test tube and subsequently, dried in a water bath above their phase transition temperature under a constant nitrogen stream. For PtdIns[4,5]P₂ containing lipid the lipids films were solved in a methanol:chloroform (1:10 *v/v*) mixture. After solvent evaporation the lipid films were dried in a vacuum chamber (Vacuum drying oven *VD23*, *Binder GmbH*, Tuttlingen, Germany) for at least 2 h and then stored at 4 °C until usage.

SUV preparation was initialized by rehydrating the desired lipid film in 500 μ L sodium citrat buffer (Na-citrat buffer, $c = 0.8$ mg mL⁻¹) for 30 min. Afterwards the

aqueous lipid solution was vortexed three times for 30 s with dwell intervals of 5 min. Subsequently, the obtained multilamellar vesicles (MLVs) were sonicated for 30 min (*Sonopuls*, cycle x 4, 60 %, *Bandelin Electronic GmbH & Co. KG*, Berlin, Germany). The resulting SUV suspension was immediately used for the formation of artificial lipid bilayers.

Na-citrat	50 mM KCl
buffer	20 mM Na-citrat
	0.1 mM EDTA
	0.1 mM NaN ₃
	pH = 4.8

3.3.1.2 Giant unilamellar vesicles

Giant unilamellar vesicles (GUVs) are cell-size liposomes with a diameter ranging from 1 to 200 μm .^[92] Today, a wide range of different manufacturing methods like lipid film hydration, inverted emulsion transfer or microfluidics are known.^[93–95] Within this work a modification of the lipid film hydration method was used, called electroformation. These method was first introduced by ANGELOVA et al. and relies on the lipid film hydration under a external applied electric field.^[96] The applied alternating electric field promotes the lipid film hydration after lipid deposited on a conductive surface.^[92]

Based on lipid stock solutions of the required lipids with concentrations ranging from 1.0 mg mL⁻¹ to 20 mg mL⁻¹ lipid films with a final lipid mass of 0.2 mg were prepared. The desired lipids were mixed in a chloroform containing test tube and equal amounts deposited on two indium tin oxide slides (ITOs). The lipid layers were dried in a vacuum chamber (Vacuum drying oven *VD23*, *Binder GmbH*, Tuttlingen, Germany) for at least 2 h and subsequently assembled to an electroformation chamber, as depicted in figure 3.5. The chamber was filled with sucrose solution (iso-osmolar to the respective spreading buffer) and connected to the voltage source. The electroformation was performed for 2 h at a frequency of 5 Hz and 3 V (peak-to-peak). Afterwards, the GUV solution was collected and immediately used for the formation of artificial lipid bilayers. The used ITOs were cleaned alternating with ethanol p.a. and ultrapure water. Cleaned ITOs were stored for the next preparation.

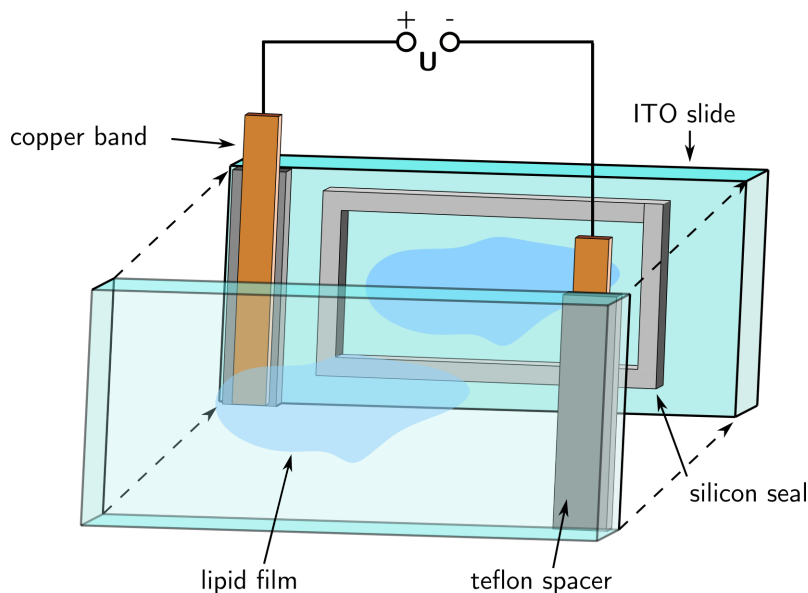


Figure 3.5: Schematic depiction of a GUV chamber. Two ITO slides with dry lipid films (blue) are assembled with a silicon ring, forming the electroformation chamber, and are connected via copper bands to a power source.

3.3.2 Artificial membrane preparation

3.3.2.1 Solid supported lipid bilayers

Solid supported lipid bilayers (SLBs) were prepared on glass substrates and silicon wafers. High precision coverglass (no. 1.5, $170\ \mu\text{m} \pm 5\ \mu\text{m}$) were purchased from *Marienfeld GmbH & Co. KG* (Lauda-Königshofen, Germany). Silicon wafers were coated either with 100 nm (used for fluorescence microscopy) or 5000 nm (used for RfS experiments) SiO_2 and were purchased from *Silicon Materials Inc.* (Glenshaw, PA, USA).

Independent of the material all substrates were hydrophilic functionalized as described in the following. The glass substrates (0.7 cm x 2.4 cm) and silicon wafers (0.8 cm x 1.9 cm) were cut to the required sizes. Subsequently, both were cleaned three times alternating with ultrapure water and ethanol p.a., the glass substrates were additionally cleaned with argon plasma (*PDC 32 G-2, Harrick Plasma*, Ithaca, NY, USA). The cleaned substrates were hydrophilized for 20 min in a aqueous ammonia hydrogen peroxide solution ($\text{H}_2\text{O}:\text{H}_2\text{O}_2$ (30 %): NH_3 (25 %) 5:1:1 (v/v/v))

at 70 °C and rinsed with ultrapure water. The hydrophilized substrates were immediately activated with oxygen plasma, installed in the measuring chambers and chambers filled with spreading buffer. SLBs were formed by the addition of SUVs ($c = 0.8 \text{ mg mL}^{-1}$) and a following incubation (cf. chapter 3.3.4.1).

argon	0.2 mbar process pressure	oxygen	0.2 mbar process pressure
plasma	5.5 min gas supply	plasma	2 min gas supply
	30 process duration		30 process duration
	60 % power		60 % power

3.3.2.2 Pore-spanning membranes

Pore-spanning membranes (PSMs) were prepared by spreading GUVs (cf. chapter 3.3.1.2) on top open porous substrates with pore diameter of 5 μm (*Aquamarijn B. V.*, Zutphen, Netherlands). The 5 \times 5 mm substrates with a porosity of $\sim 37\%$ were composed of a Si-support (0.9 mm) and a 0.5 mm tick topside coating with Si_3N_4 . For the functionalization, the substrates were cleaned three times alternating with ultrapure water/ethanol p.a. and subsequently dried in a nitrogen stream. Afterwards, the substrates were orthogonally evaporated with silicon monoxide (SiO_x , 30-40 nm) at a process pressure of $2\text{-}6 \times 10^{-6}$ mbar and a rate of $0.3\text{-}0.4 \text{ nm s}^{-1}$. After silicon monoxide coating, the substrates were incubated for ~ 16 h in ultrapure water at 55 °C to generate a hydrophilic surface.^[97]

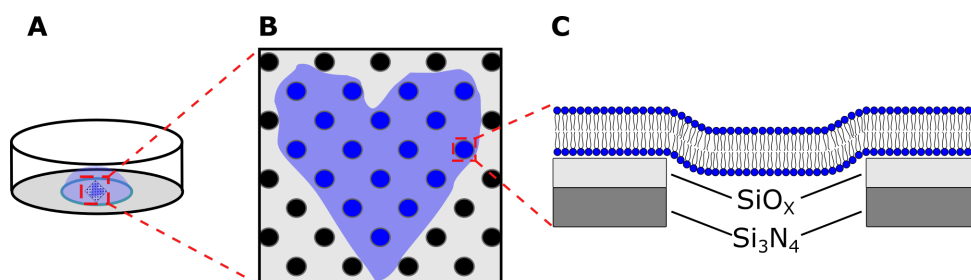


Figure 3.6: Depiction of pore-spanning membranes on SiO_x functionalized substrates. **A:** Small volume chamber within a petri dish. Illustration of the top view (**B**, blue) and side view off pore-spanning membranes on SiO_x functionalized Aquamarijn substrates.

After the incubation the substrates were first rinsed for 20 s with isopropanol p.a. and subsequently twice with Na-citrat buffer for the same duration. Petri dishes were prepared by forming a two layered circle of glue (*picodent twinsil*[®], $\varnothing = 0.8 \text{ mm}$) on the

dish bottom, to enable a small sample volume (cf. figure 3.6 A). The wet substrates were glued into the generated circle, which was then filled with 400 μL Na-citrat buffer. Immediately after substrate fixation, 10 μL GUV suspension were added and incubated for 1 h at 20 $^{\circ}\text{C}$ to generate PSMs (cf. figure 3.6 B-C). Excess lipid material was washed of through multiple exchanges of spreading buffer (10 \times 300 μL).

3.3.3 Filamentous actin polymerization

Filamentous actin (F-actin) networks were pre-polymerized from lyophilized non-muscle G-actin monomers (*Cytoskeleton*, Denver, CO, USA; human platelet, 85 % β -actin, 15 % γ -actin). The purchased G-actin was solved in cold ultrapure water and aliquots (10 μL , $c = 10 \text{ mg mL}^{-1}$) were stored at -80 $^{\circ}\text{C}$. Pre-polymerization was carried out by solving aliquots in cooled G-buffer to a final actin concentration of 0.4 mg mL^{-1} . For F-actin labeling via ATTO 594 labeled G-actin, labeled monomers were mixed with unlabeled G-actin (1:10 (n/n)) and solved in cold G-buffer to a final concentration of 0.44 mg mL^{-1} . Actin multimers were dissolved by adding ATP (0.3 mM) and DTT (0.5 mM) followed by an incubation for 1 h on ice. Remaining oligomers were separated via centrifugation (17000 g, 20 min, 4 $^{\circ}\text{C}$) and the supernatant was polymerized with 10 % v/v polymerization solution (F1 solution). After a polymerization of 20 min at 20 $^{\circ}\text{C}$ the F-actin was mixed with phalloidin in a 1.5 % (n/n) ratio, stabilizing the formed filaments. Unlabeled filaments were mixed with Alexa FluorTM 488- or 633-phalloidin (cf. chapter 3.1.2.2) and ATTO 594 labeled F-actin with untagged phalloidin (from *Amanita phalloides*, purity $\geq 90\%$, in MeOH p.a.). The solution was incubated for further 20 min at 20 $^{\circ}\text{C}$ and subsequently stored for a maximum of 12 h at 4 $^{\circ}\text{C}$.

G-buffer	5 mM Tris	F1-	500 mM KCl
	0.2 mM CaCl_2	solution	100 mM Tris
	0.1 mM NaN_3		20 mM ATP
	pH = 8.0		20 mM MgCl_2
			50 mM guanidine carbonate
			pH = 7.4

Successful actin polymerization was validated in glass chambers composed of a strip double coated adhesive tape (*Tesa SE*, Norderstedt, Germany) between a microscopy slide (Thermo Fisher Scientific, Waltham, MA, USA) and a coverglass (22 \times 22 mm,

cover glass, *VWR International*, Darmstadt, Germany). Before assembling the chamber, a window (0.5 cm x 0.8 cm) was cut into the adhesive tape and filled with 5 μL polymerized F-actin. Subsequently, the chamber was assembled and stored for a maximum of 12 h at 4 °C. Polymerization was controlled by means of confocal laser scanning microscopy.

3.3.4 Preparation of minimal actin cortices

In this thesis minimal actin cortices were prepared either on solid supported membranes or pore spanning membranes. The preparation was performed as described in the following chapters.

3.3.4.1 Solid supported minimal actin cortice preparation

For the preparation of solid supported minimal actin cortices either glass substrates or silicon wafer were functionalized as described in chapter 3.3.2.1. Functionalized silicon dioxid wafers were clamped in Teflon chambers whereas the glass substrates were glued (*picodent twinsil*[®]) to the bottom of conical low volume chambers. The chambers were filled with Na-citrat buffer and subsequently incubated for 1 h at 20 °C with SUVs ($m = 0.2 \text{ mg}$, $c_{\text{glass}} = 0.53 \text{ mg mL}^{-1}$, $c_{\text{wafer}} = 0.08 \text{ mg mL}^{-1}$), prepared according to chapter 3.3.2.1. Excess lipid material was washed of through multiple exchanges of spreading buffer and a subsequent transfer into protein buffer (E1 buffer). The rinsed bilayers (cf. figure 3.7 AI) were incubated overnight with ezrin T567D ($c_{\text{chamber}} = 1 \mu\text{M}$) at 4 °C.

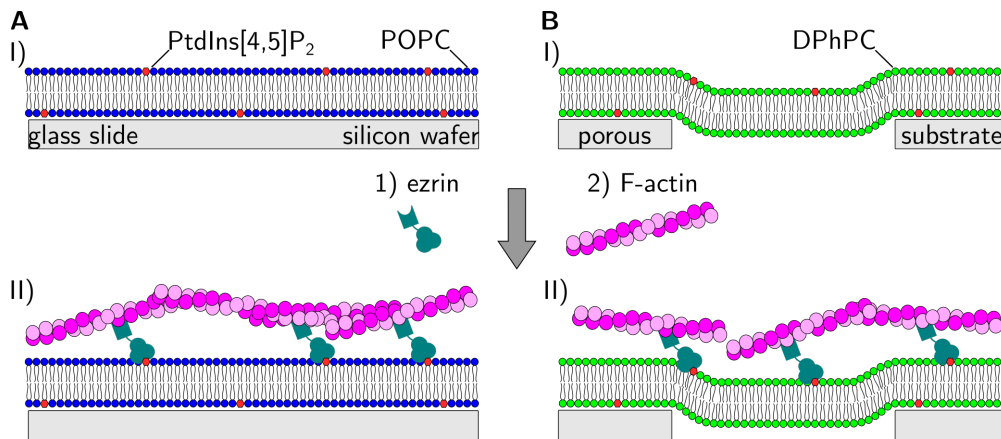


Figure 3.7: Schematic illustration of MAC preparation on solid supported and pore-spanning membranes. A: Solid supported membrane. B: Pore-spanning membrane.

The ezrin decorated membranes were equilibrated to 20 °C for 1 h and subsequently rinsed multiple times with E1 buffer to remove unbound protein. For the binding of pre-polymerized F-actin (cf. chapter 3.3.3) the buffer system was changed to F-buffer. Afterwards the pre-polymerized F-actin was carefully added ($c_{\text{glass}} = 4.65 \mu\text{M}$, $c_{\text{wafer}} = 1.05 \mu\text{M}$) and minimal actin cortices (3.7 AII) formed over an incubation time of 4.5 h. In the final step, unbound F-actin was removed by rinsing with F-buffer.

F-buffer 20 mM Tris
 50 mM KCl
 2 mM MgCl₂
 0.1 mM NaN₃
 pH = 7.4

3.3.4.2 Pore spanning minimal actin cortice preparation

For the preparation of minimal actin cortices on pore-spanning membranes (PSMs), PSMs were generated by spreading GUVs on top of the functionalized substrates (cf. chapter 3.3.2.2 and figure 3.7 BI). After rinsing the samples with spreading buffer to remove excess lipid material, the samples were transferred into protein buffer (E1 buffer, $10 \times 300 \mu\text{L}$). Subsequently, the PSMs were incubated for 1 h at 20 °C with $1 \mu\text{M}$ ezrin T567D. Afterwards, the samples were rinsed with E1 buffer and F-buffer (each $10 \times 300 \mu\text{L}$) and then allowed to stand for 30 min to decay possible flows through the pores. Next, pre-polymerized F-actin (cf. chapter 3.3.3) was added

to $c = 2.7 \mu\text{M}$ and incubated over night at $4 \text{ }^\circ\text{C}$. At the following day, the samples were equilibrated to $20 \text{ }^\circ\text{C}$ for 1 h and subsequently rinsed with F buffer ($10 \times 300 \mu\text{L}$) to remove unbound protein.

3.3.5 Reorganization of minimal actin cortices by myosin II

The dynamic reorganization of minimal actin cortices by the motor protein myosin II was imaged by means of total internal reflection fluorescence microscopy (TIRF, cf. chapter 3.5.1.4). For this purpose minimal actin cortices were prepared, according to chapter 3.3.4.1, on glass substrates with 10 % (1:10, n/n) ATTO 594 labeled pre-polymerized F-actin (cf. chapter 3.2.4.1, 3.3.3) and were transferred into actomyosin buffer (AM-buffer). Unlabeled myosin II (cf. chapter 3.2.2) was mixed in a 1:10 (n/n) ratio with DyLight[®] 488 labeled myosin II (cf. chapter 3.2.4.2) and dialyzed ($4 \text{ }^\circ\text{C}$, *Slide-A-Lyzer MINI*, 20kDa MWCO, *Thermo Fisher Scientific*, Waltham, MA, USA) over night from the glycerol containing storage buffer into M buffer. Subsequently, insoluble myosin II was removed by centrifugation ($4 \text{ }^\circ\text{C}$, 120000 g, 20 min) and the concentration of the remaining myosin was determined according to chapter 3.2.3. The high concentration of monovalent cations (300 mM KCl) within the M buffer were used to prevent an uncontrolled self-assembling into biopolar myosin II filaments. Controlled polymerization was induced by diluting the prepared myosin II with polymerization buffer (P1-buffer, 0 mM KCl) to a final concentration of 50 mM KCl. The solution was incubated for 10 min at $20 \text{ }^\circ\text{C}$ and subsequently directly used for reorganization experiments.

Reorganization of minimal actin cortices was performed in AM-buffer and the final concentrations of reagents were chosen according to ALVARADO and KOENDERINK (cf. table 3.5).^[7]

Table 3.5: Final concentration of all reagents for the reorganization of membrane-bound minimal actin cortices by myosin II.

0.4 μM	myosin II
0.1 mM	ATP
10 mM	creatine phosphate
0.1 mg mL^{-1}	creatine kinase

During reorganization ATP is consumed via the myosin ATPase activity, providing a dynamic myosin II motion. To maintain a constant ATP concentration of around

0.1 mM an ATP-regeneration system composed of creatine kinase (CK) and creatine phosphate (CP) was used. CK catalyzes the transfer of a phosphat group from CP to ADP, and restore with this the accessible ATP pool.^[7] For reorganization experiments CK and CP were kept separated as long as possible and were added immediately prior to myosin II addition. The AM buffer composition with DTT was chosen to prevent actin-actin cross-linking via disulfid bonds, which can form under oxidative conditions.^[98] Trolox were added for the prevention of photobleaching during long time measurements.^[99]

P1-	0 mM KCl	AM-	50 mM KCl
buffer	20 mM imidazole	buffer	20 mM imidazole
	1.6 mM MgCl ₂		2 mM MgCl ₂
	1 mM DTT*		1 mM DTT*
	1.2 mM Trolox*		1 mM Trolox*
	pH = 7.4		pH = 7.4

*added prior to usage

3.4 Biosensing techniques

3.4.1 Reflectometric interference spectroscopy

Reflectometric interference spectroscopy (RIfS) is a non-invasive technique allowing the observation of biomolecular interactions with a high sensitivity. RIfS is based on the refraction, reflection and transmission of white light at transparent thin layers and the resulting interference pattern.^[100] The interference pattern is a product of the superposition of the partial beams and can be converted in a change of optical thickness, which is given by the physical layer thickness, the angle of incidence and the different refraction indices.^[100–102]

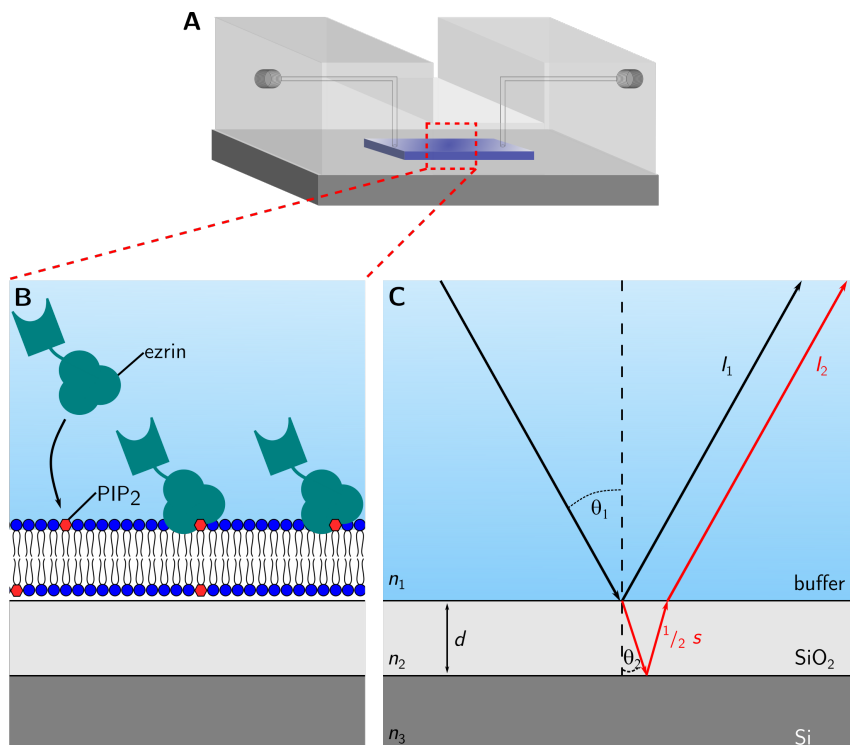


Figure 3.8: RIfS setup and the light pathway during experiments. **A:** Depiction of the flow-through chamber used for RIfS experiments assembled of an alumina base, an acrylic glass top and a silicon wafer clamped in-between. **B:** Exemplary scheme of ezrin binding to PtdIns[4,5]P₂ on a solid supported membrane in the flow-through chamber. **C:** Scheme of the light pathway in RIfS, with the incident light being reflected (I_1 , black) at the buffer/SiO₂ interface and partly transmitted (I_2 , red). The transmitted light beam is hitting the SiO₂-Si interface where it is reflected and subsequently refracted by passing the buffer/SiO₂ interface a second time.

In this work, RIfS experiments were performed in a flow-chamber (cf. figure 3.8 A)

for the investigation of ezrin T567D binding to solid supported bilayers (cf. figure 3.8 B). The system was composed of three different optical phases separated in the aqueous protein buffer with $n_1 = 1.333$ ($\lambda = 589$ nm, 20 °C), a hydrophilic functionalized silicon dioxid layer for membrane formation with $n_2 = 1.458$ ($\lambda = 589$ nm, 20 °C) and an opaque silicon layer.^[103,104]

When light enters the interface of two media with different refraction indices (n) under a given angle of incidence (θ_1), the refraction angle (θ_2) can be described by Snell's law (equation 3.23). According to this law, light gets refracted towards the normal of the interface if n_2 is higher than n_1 , causing $\theta_1 > \theta_2$. As depicted in figure 3.8 C for the RIfS experiments, the irradiated light is split into a reflected (I_0) and partly transmitted (I_1) beam, when traveling through an aqueous buffer and hitting the buffer/SiO₂ interface. The refracted beam crosses the SiO₂ layer and is fully reflected at the opaque silicon layer. By passing the buffer/SiO₂ interface a second time the transmitted beam (I_1) is refracted by the initial angle of incidence (θ_1) and traveling parallel to the reflected beam (I_0). The longer distance s of I_1 , crossing the SiO₂ layer, can be defined by equation 3.4.

$$s = \frac{2 d}{\cos(\theta_2)} \quad (3.4)$$

The distance s can further be converted in a difference in optical path (Δs , cf. equation 3.5), by transferring the thickness d in an optical thickness ($OT = n \times d$). Therefore, extending Δs with e.g. a solid supported membrane or a membrane-bound protein layer with a refractive index ($n = \sim 1.44$) similar to n_2 (SiO₂) index enable the detection of biomolecular adsorption.^[105]

$$\Delta s = \frac{2 d n_2}{\cos(\theta_2)} \quad (3.5)$$

In the used RIfS setup the light was emitted vertical to the substrate surface, resulting in $\theta_1 = \theta_2 = 0^\circ$ and allowing a simplification of equation 3.5:

$$\Delta s = 2 d n_2 \quad (3.6)$$

The different path lengths between I_0 and I_1 causing a path shift ($\Delta\varphi$) between

both beams. By using an interference layer (n_2 , SiO_2) thickness of $5 \mu\text{m}$, within the coherence length of white light, the superposition of both beams results in a distinct interference pattern. The superposition of both waves can lead to a constructive (cf. equation 3.7) or destructive interference (cf. equation 3.8), when Δs is a multiple (m) of the emitted wavelength (λ) or a half of the wavelength.

$$m \lambda_{\max} = \Delta s ; m \in \mathbb{N} \quad (3.7)$$

$$(m + \frac{1}{2}) \lambda_{\min} = \Delta s ; m \in \mathbb{N} \quad (3.8)$$

For an angle of incidence $\theta_1 = 0^\circ$ the phase shift $\Delta\varphi$ of the partial light is defined by:

$$\Delta\varphi(\lambda) = \frac{2 \pi}{\lambda} n_2 d = \frac{2 \pi}{\lambda} OT \quad (3.9)$$

Following equation 3.9 enables the calculation of the optical thickness (OT), according the measured phase shift.

Data evaluation

The change in optical thickness (ΔOT) was tracked over time, using a MATLAB script written by *Dr. I. P. Mey* from the University of Göttingen. For this purpose, reference spectra of a full reflective surface (reflectivity $\geq 98.5 \%$, *Chroma Technology GmbH*, Olching, Germany) were recorded with the light source switch on (I_r , bright spectrum) and off (I_d , dark spectrum). For each experiment the reflectivity spectrum (R , cf. equation 3.10) of the substrates was recorded (Spectra Suite, *Ocean Insight*, Duiven, Netherlands) taking the specific substrate spectrum (I_m) and reference spectra (I_r/I_d) into account.

$$R = \frac{I_m - I_d}{I_r - I_d} \quad (3.10)$$

The reflectivity of non-absorbing layers are defined by the reflective FRESNEL coefficient (r_{123}):

$$R(\varphi) \equiv |r_{123}|^2 = \frac{r_{12}^2 + r_{23}^2 + 2 r_{12} r_{23} \cos(2 \Delta\varphi)}{1 + r_{12}^2 r_{23}^2 + 2 r_{12} r_{23} \cos(2 \Delta\varphi)} \quad (3.11)$$

with the individual FRESNEL coefficients (r_{xy}) defined as:

$$r_{xy} = \frac{n_x - n_y}{n_x + n_y} \quad (3.12)$$

Combining the phase shift (equation 3.9) with the reflectivity (equation 3.11), allows the determination of ΔOT within the RIfS measurements and results in:

$$R(\lambda, OT) = \frac{r_{12}^2 + r_{23}^2 + 2 r_{12} r_{23} \cos(\frac{4}{\lambda} \pi OT)}{1 + r_{12}^2 r_{23}^2 + 2 r_{12} r_{23} \cos(\frac{4}{\lambda} \pi OT)} \quad (3.13)$$

The aforementioned MATLAB script fitted equation 3.13 to the measured reflectivity spectra and enabled the detection of adsorption processes e.g. spreading of solid supported bilayers.

RIfS measurement setup and implementation

RIfS experiments were performed in flow-through chambers (cf. figure 3.8 A) composed of an alumina base and an acrylic glass top. Hydrophilic functionalized silicon substrates (cf. chapter 3.3.2.1) were clamped with a silicone seal in-between and in/out-flow via a tubing system were attached to the acrylic glass top. A constant flow of 0.7 mL min^{-1} was adjusted by means of a peristaltic pump (*IDEX Health & Science*, Wertheim, Germany). An optical fiber was placed on top of the flow-through chamber, perpendicular to the silicon surface, ensuring an angle of incidence $\theta_1 = 0^\circ$. Light, generated by a light source ($\lambda = 360 - 950 \text{ nm}$, HL-2000-LL, *Ocean Optics GmbH*, Ostfildern, Germany), was emitted through the outer emitting fibers and collected by the inner detection fiber connected to a FLAME-S spectrometer (*Ocean Optics GmbH*, Duiven, Netherlands).

Data acquisition and baseline recording was started after flushing the system with spreading buffer. Each rinsing step (duration $\sim 5 - 10 \text{ min}$) was performed in an open system, whereas the addition of lipids and proteins were performed in a closed system. Membrane spreading was initiated by the addition of a SUV solution ($m = 0.2 \text{ mg}$, $c = 0.8 \text{ mg mL}^{-1}$, cf. chapter 3.3.1.1) and recorded over 5-10 min until a bilayer

baseline was formed. Excess lipid material was washed off by rinsing with spreading buffer followed by a transfer into the protein buffer (E1). For the binding of ezrin T567D to POPS containing membranes, the system was passivated with BSA in E1 buffer ($c_{\text{BSA}} = 1 \text{ mg mL}^{-1}$, 5 min) and rinsed with E1 buffer prior to protein addition. Afterwards, ezrin T567D was added ($c_{\text{ezrin}} = 0.8 \text{ }\mu\text{M}$) and the binding to the solid supported bilayer was recorded for 10 min. Reversibly bound protein was washed off by rinsing in a final step with E1 buffer and the amount of irreversible bound protein was determined. The data acquisition was stopped, the flow-through system washed with ultrapure water and the acrylic glass top cleaned, together with the silicon seal, three times by ultrasonication (15 min each, 1 x Muca-sol[®] solution (0.5 %), 2 x ultrapure water).

3.5 Biophysical methods

3.5.1 Fluorescence microscopy

Fluorescence microscopy includes a variety of different light microscopy techniques, which all rely on the use of small molecules, called fluorophores. These fluorophores are characterized by the ability to absorb light at a specific wavelength and emit it at a different one, which is called fluorescence. Fluorescence occurs within nanoseconds after the absorption of light and is an intrinsic property of some natural organic compounds or proteins e.g. the green fluorescent protein. However, the majority of fluorophores are selectively synthesized and are characterized by conjugated double bonds within their structure. The outer orbital electrons within these π -bonds have a small energy difference between their ground state S_0 and excited state S_1 orbitals, allowing a transition from S_0 to S_1 already by the absorption of low-energy light. The wavelength difference between the absorbed and emitted light, known as Stokes-shift, relies on the vibronic transition of an excited electron from a higher vibrational state into the lowest energy state of S_1 , caused by vibrational energy transfer to the surrounding molecules. The emission of a photon occurs, as the excited electron transmits from the lowest energy state of S_1 to S_0 . The emitted photon usually has a lower energy than the excitation light, which is the origin of the Stokes-shift, and enables a simultaneous excitation and detection with a high contrast.^[106]

Starting from standard fluorescence microscopic methods such as wide-field microscopy, a significant improvement in resolution has been achieved through the development of new methods like confocal laser scanning microscopy and total internal reflection microscopy, which was utilized in this thesis.^[107,108]

3.5.1.1 Confocal laser scanning microscopy

Confocal laser scanning microscopy (CLSM) is an improved version of conventional light microscopy and based on the exclusion of out-of-focus light, first presented in the 1950s by MINSKY.^[109] In modern CLSMs, this is achieved with a combination of a tightly focused laser beam, providing a point like illumination of the sample, and a pinhole in front of the detectors, blocking out-of-focus light. As the excitation light is focused point like in the optical plane, the focused spot is

scanned in x-y-direction over the specimen, allowing a precise 2D mapping of the sample. By changing the focal plane, the specimen can be scanned over several levels enabling a 3D imaging of the sample. The key components of a CLSM are schematically shown in figure 3.9, together with the illumination and emission light path.

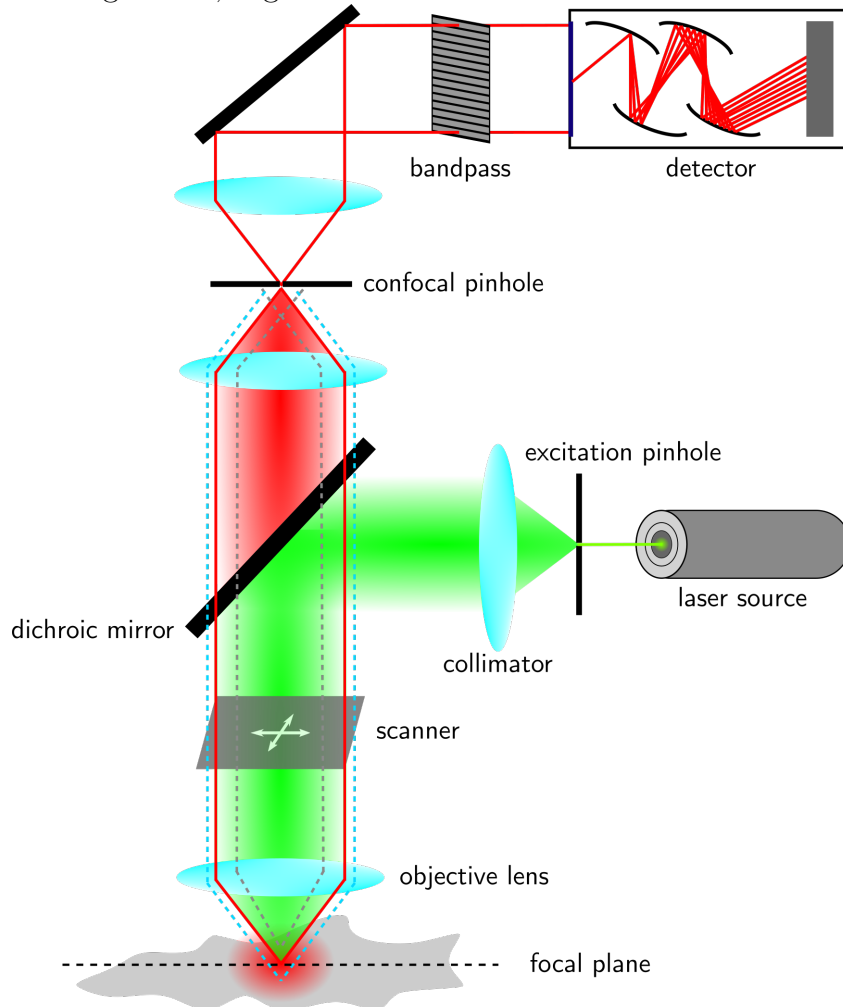


Figure 3.9: Schematic illustration of a principle confocal laser scanning microscopy setup. The excitation light (green), produced by a laser source, is focused over the reflection at a dichroic mirror and the objective lens into the focal plane. The illumination beam passes thereby the excitation pinhole, collimator and scanner unit. The emitted fluorescence (red, solid line) is focused through the confocal pinhole, which blocks the out-of-focus light (dotted lines), and is amplified after bandpass selection.

Coherent light (green), generated by a laser source at a defined wavelength, passes the excitation pinhole and is converted in a parallelized beam via a collimator. The beam is reflected at a dichroic mirror over the scanning unit and focused by the objective lens into the specimen. The excited fluorophores within the focal plane emit light at a lower wavelength (red, solid line), which is collected through the objective lens and

focused on the confocal pinhole. The pinhole blocks out-of-focus light (dotted lines) from non focal planes, and enables a selective fluorescence amplification by means of e.g. photomultiplier tubes (PMTs).

Both, the excitation light as well as the emitted light of a point like emitter are diffracted by apertures within the CLSM setup, e.g. at the end of the objective, resulting in a 3D diffraction pattern generally referred to as a point spread function (PSF).^[110] As light can not be focused by an objective in a infinite small spot, interference occurs leading to the typical lateral (cf. figure 3.10 A) and axial (cf. figure 3.10 B) diffraction pattern of an PSF. The lateral PSF pattern is referred to as an airy disc, with the diameter of the central maximum being defined as an airy unit (AU, cf. figure 3.10 A). As schematically depicted in figure 3.10 C, the axial (blue) intensity distribution of an PSF is in general larger than the lateral (orange) one.

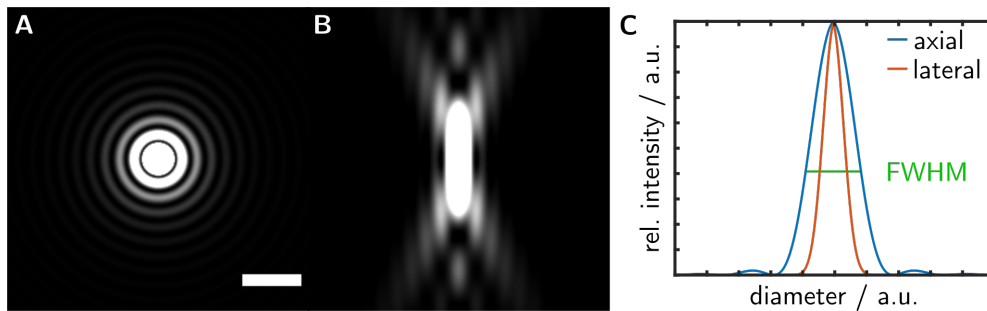


Figure 3.10: Exemplary representation of the point spread function. (A) Lateral and (B) axial geometric pattern of the PSF with their relative intensity distribution (C). PSFs were calculated using the ImageJ plugin *PSF Generator* with $\lambda = 488 \text{ nm}$, $NA = 1.0$ and $n=1.33$.^[111,112] Scale bar: $1 \mu\text{m}$. Modified from *M. Gleisner*.^[113]

The resolution in fluorescence microscopy is the minimal distance (d) between two emitting objects, which is needed to distinguish them from each other. According to the RAYLEIGH criterion, this distance is reached, if the PSF intensity maximum of one emitter is overlapping exactly with the first PSF minimum of a second emitter. This leads to the Rayleigh resolution (d_{Rayleigh}) given by:

$$d_{\text{Rayleigh}} = 0.61 \frac{\lambda}{NA} \quad (3.14)$$

at a specific wavelength (λ) and depending on the objective numerical aperture (NA).^[114] Since d_{Rayleigh} is difficult to determine in practice, the full width at the half maximum intensity (FWHM) (cf. figure 3.10 C) is used more frequently to define

the resolution in a microscope (d_{FWHM}). In a confocal microscope the total PSF ($\text{PSF}_{\text{total}}$), measured behind the confocal pinhole, is a product of the illumination PSF ($\text{PSF}_{\text{ill.}}$) and detection PSF ($\text{PSF}_{\text{det.}}$). While the $\text{PSF}_{\text{ill.}}$ is mainly defined by the wavelength, the numerical aperture of the objective and the optical aberrations within the system, the $\text{PSF}_{\text{det.}}$ can be additionally modified by the confocal pinhole diameter.^[115] While a small pinhole diameter (< 0.25 AU) would decrease the $\text{PSF}_{\text{det.}}$ into the range of the $\text{PSF}_{\text{ill.}}$, which would increase the resolution, this is accompanied by a simultaneous decrease in the signal to noise ratio (SNR). In theory, the resolution could be increased by a factor of 1.4, compared to conventional light microscopy, leading to a lateral and axial resolution of:^[116,117]

$$d_{\text{FWHM,xy}} = 0.37 \frac{\bar{\lambda}}{NA} \quad (3.15)$$

$$d_{\text{FWHM,z}} = 0.67 \frac{\bar{\lambda}}{n - \sqrt{n^2 - NA^2}} \quad (3.16)$$

with $\bar{\lambda} \approx \sqrt{\lambda_{\text{ex}} \cdot \lambda_{\text{em}}}$, n being the refractive index of the immersion media and the excitation/emission wavelength $\lambda_{\text{ex}}/\lambda_{\text{em}}$. As a result of the significantly decreased SNR, the pinhole diameter is traditionally set to 1 AU, offering a compromise between resolution and SNR.^[118] Consequently, the lateral and axial resolution of a confocal microscope, with a pinhole diameter of ≥ 1 AU, is defined by:^[110]

$$d_{\text{FWHM, xy}} = 0.51 \frac{\lambda_{\text{ex}}}{NA} \quad (3.17)$$

$$d_{\text{FWHM, z}} = 0.88 \frac{\lambda_{\text{ex}}}{n - \sqrt{n^2 - NA^2}} \quad (3.18)$$

Therefore, the resolution of conventional confocal laser scanning microscopes is laterally limited to 200 - 250 nm and axial to 500 - 700 nm.^[119]

3.5.1.2 Airyscan technique

The Airyscan technique, developed by *Zeiss Microscopy GmbH* (Oberkochen, Germany), uses a new detector design, based on a 32-channel GaAsP-PMT, where each of the 32 detector elements functions as a small individual pinhole, enabling an increased resolution paired with a high intensity collection of a large pinhole.^[118] This is achieved by projecting 1.25 AU of the detected light onto the detector surface using

focus lenses. As schematically shown in figure 3.11 A, the Airyscan detector diameter is formed by six detector elements, where each element represents a sub-pinhole diameter of 0.2 AU.

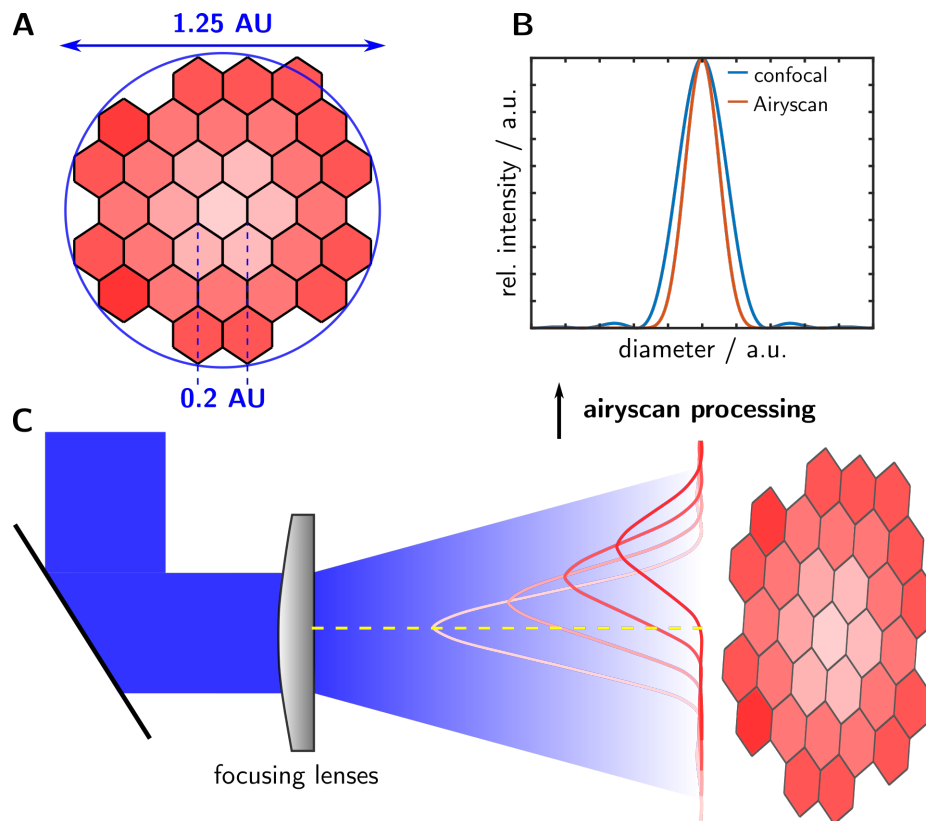


Figure 3.11: Schematic illustration of the Airyscan detector and its principle. (A): Scheme of the 32 GaAsP-PMT detector elements arrangement in the Airyscan detector. (B): Schematic comparison between the PSF of a confocal (blue) and the narrowed PSF of an Airyscan detector (orange) after processing. (C): Schematic representation of the beam path widened by the focus lenses with the different detected PSFs over the Airyscan detector cross chapter. Figure inspired by KOROBCEVSKAYA et al. and WEISSHART.^[120,121]

While only the central detector element is adjusted to lie directly in the optical axis, the other elements are displaced from the optical axis by a defined distance. Therefore, the recorded PSFs of these elements, as shown in figure 3.11 C, are displaced as well. Since each detector element records a separated PSF and with this an individual image, the underlying position information stored in the detector design, can be used for a linear deconvolution step. Thereby, the individual images are applied separately to a deconvolution, followed by a re-shifting and summing of all intensities according to their detector positions. This increases the spatial-frequency contrast and with this the Airyscan detector can record images with a significantly improved SNR and higher resolution (cf. figure 3.12).^[118]

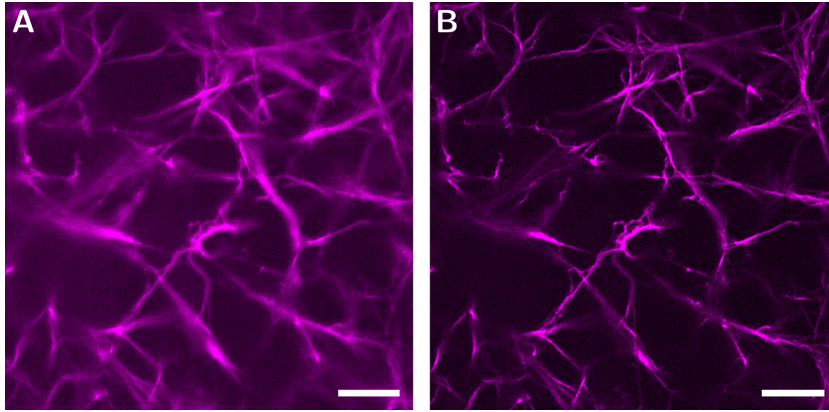


Figure 3.12: Exemplary resolution comparison between an confocal and Airyscan image of a 3D F-actin network. The F-actin was recorded with a Zeiss *LSM 880*, using equal system settings. (A): Standard GaAsP-PMT detector, pinhole diameter = 1 AU; (B): Airyscan detector, pinhole diameter = 1.25 AU. Actin was labeled 1:10 with ATTO 594 G-actin. Scale bars: 10 μm .

The Airyscan detector can increase the resolution by approximately 1.7, compared to traditional CLSMs with a pinhole diameter of 1 AU, in all three spatial dimensions. For a wavelength of 480 nm a lateral resolution of 140 nm and an axial resolution of 400 nm can be achieved.^[118,121]

Within this work the *LSM 880* (Zeiss Microscopy GmbH, Oberkochen, Germany) equipped with an Airyscan detector and a 40x objective (W Plan-Apochromat M27, NA = 1.0, Carl Zeiss Microscopy GmbH, Oberkochen, Germany) has been used for sample imaging.

3.5.1.3 Fluorescence recovery after photobleaching (FRAP)

Fluorescence recovery after photobleaching (FRAP) is a frequently used technique for the investigation of the diffusive behavior of fluorescently labeled molecules in lipid membranes.^[122,123] In this thesis, FRAP was used for the quantitative determination of 2D-diffusion coefficients in solid supported membranes. For this purpose, the intensity of lipid coupled fluorescent probes (blue circles, figure 3.13 A-C) was recorded during the FRAP experiments in a region of interest (ROI, dashed circle, figure 3.13 A-C). The principal procedure of a FRAP experiment is shown in figure 3.13. After recording the initial fluorescence intensity within the ROI (I_s , cf. figure 3.13 A), the fluorescently labeled lipids were irreversibly bleached by means of a high-energy laser radiation (t_0 , cf. figure 3.13 B). As a consequence, the measured

fluorescence intensity drops to a respective minimum intensity (I_0 , cf. figure 3.13 D). The simultaneous diffusion of unbleached fluorophore molecules from the ROI environment into and bleached fluorophore molecules out of the ROI subsequently leads to a fluorescence recovery (cf. figure 3.13 C-D). The finally reached intensity allows a determination of the diffusion coefficient and the immobility fraction.^[124]

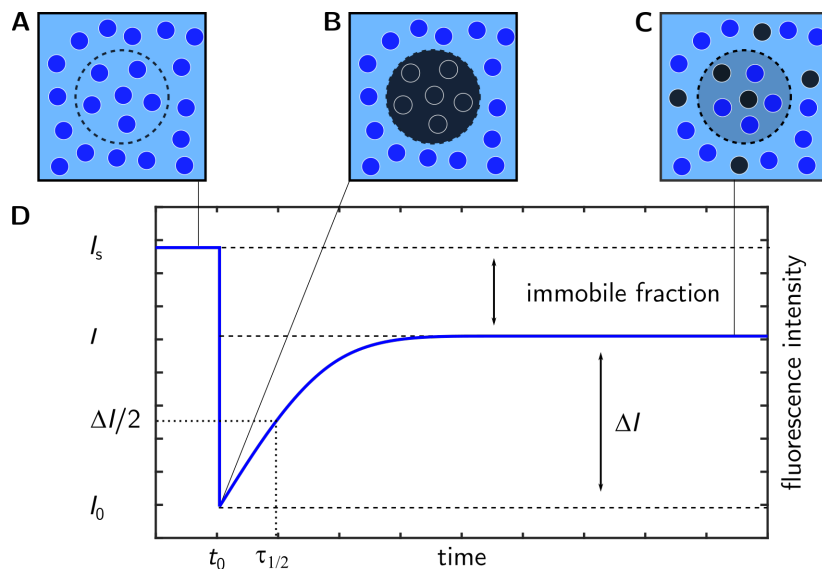


Figure 3.13: Schematic illustration of a typical FRAP measurement. Scheme of lipid coupled fluorescent probes (blue circles) prior (**A**), immediately after photobleaching (**B**) and after fluorescence recovery (**C**) in the region of interest (ROI, dashed circle). (**D**): Illustration of a typical FRAP intensity profile corresponding to the schemes A-C, with the initial fluorescence intensity (I_s) prior and immediately after photobleaching (I_0). Simultaneous diffusion of bleached fluorophores out of the ROI and unbleached fluorophores into the ROI leads to fluorescence recovery (I).

The FRAP recovery curve of planar and isotropic systems can be described with Fick's 2nd law (equation 3.19)

$$\frac{\delta c_i(r, t)}{\delta t} = D_i \nabla^2 c_i(r, t) \quad (3.19)$$

with $c_i(r, t)$ being the relative concentration of unbleached fluorophore, r the radial distance from the bleach center, the time t and D_i the diffusion coefficient of the i^{th} order. The amount of mobile lipids F_m can be calculated via the intensity ratios during the FRAP experiment as shown in equation 3.20.^[124]

$$F_m = \frac{I - I_0}{I_s - I_0} \quad (3.20)$$

In this work FRAP data were quantitatively analyzed according to JÖNSSSEN et al. with their provided MATLAB script.^[125] The analysis is based on a Hankel transformation of equation 3.19 in polar form, assuming a bleaching region with circular symmetry, with the solution:^[124]

$$f_i(k, t) = f_i(k, 0) \exp(-4\pi^2 D_i k^2 t) \quad (3.21)$$

where $f_i(k, t)$ is given for the spatial frequency k as:

$$f_i(k, t) = \int_0^\infty (1 - c_i(r, t)) J_0(2\pi k r) r \, dx \quad (3.22)$$

with J_0 being the 0th order Bessel function. For a single diffusing component, the diffusion coefficient D_i can therefore be obtained from equation 3.21.^[125]

Experimental procedure

Solid supported membranes were prepared on glass substrates as described in chapter 3.3.2.1 and in the case of membrane-bound minimal actin cortices as in chapter 3.3.3. FRAP experiments were conducted with the settings listed in table 3.6 using a FluoView 1200 CLSM (*Olympus*, Tokyo, Japan).

Table 3.6: Parameter settings for FRAP experiments on SLBs.

laser power 488	100 % (20 mW)
frame time	65 ms
N (frames)	200
resolution	256 × 256 pixels
t (bleach pulse)	65 ms
bleach pulse power	100 %
r (bleach radius)	1.25 μm

3.5.1.4 Total internal reflection fluorescence microscopy

Total internal reflection fluorescence (TIRF) microscopy is a near-field fluorescence imaging technique providing a high lateral and axial resolution based on sample

illumination via a thin electromagnetic standing wave called evanescent field.^[107] The physical principle of TIRF microscopy can be described by SNELL's law (cf. equation 3.23) and the reflection, refraction and transmission of light at the interface of two media with different refractive indices (n).^[108]

$$n_1 \cdot \sin(\theta_1) = n_2 \cdot \sin(\theta_2) \quad (3.23)$$

Since TIRF microscopy is typically based on inverted microscope designs, in which the samples must be prepared on cover slips, the refractive indices of the immersion oil ($n = 1.51$), the cover glass ($n_1, n = 1.52$) and the aqueous sample ($n_2, n = 1.33$) must be taken into account.^[126] As the refractive indices of the immersion oil and the cover glass are matching, they can be considered together. According to SNELL's law, light will be refracted away from the normal, when it passes from a medium with a higher refractive index (n_1) into a medium with a lower one (n_2 , cf. figure 3.14 A).

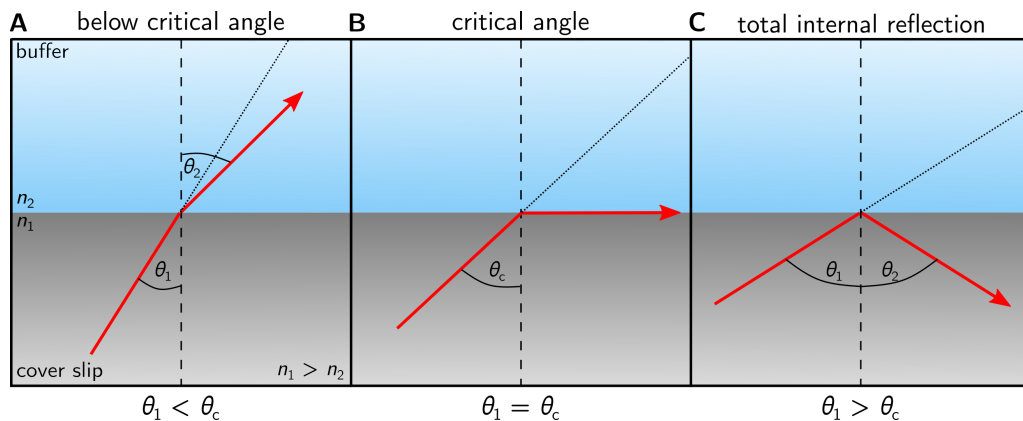


Figure 3.14: Schematic illustration of SNELL's law in terms of TIRF microscopy. (A) When incident light with the angle θ_1 passes from a medium with a higher refractive index (n_1 , cover slip) into a medium with a lower refractive index (n_2 , aqueous sample), the light will get refracted with the angle θ_2 being larger than θ_1 . (B) If θ_1 is chosen so that θ_2 is equal to 90° the critical angle θ_c is reached. (C) In case of $\theta_1 > \theta_c$ the entire light is reflected at the media interface leading to total internal reflection.

At a specific angle of incidence (θ_1), called critical angle (θ_c), the angle of refraction (θ_2) corresponds to 90° (cf. figure 3.14 B, $\theta_1 = \theta_c$), which enables a simplification of SNELL's law as shown in equation 3.24.

$$n_1 \cdot \sin(\theta_c) = n_2 \quad (3.24)$$

The critical angle θ_c can therefore be expressed as described in equation 3.25.

$$\theta_c = \sin^{-1} \left(\frac{n_2}{n_1} \right) \quad (3.25)$$

If the angle of incidence is increased beyond the critical angle ($\theta_1 > \theta_c$) the light undergoes total internal reflection, preventing the transmission of light into the second medium (cf. figure 3.14 C).^[127]

The reflection of light at the coverglass-sample interface generates a thin electromagnetic field within the sample, which is called the evanescent field, having the same frequency as the incident light. In TIRF microscopy this evanescent field is used for the excitation of sample fluorophores as schematically depicted in figure 3.15 A. Since the intensity (I) of the evanescent field decreases exponentially with increasing distance (z) from the coverglass-sample interface, only interface near fluorophores get excited. This reduces photodamage and at the same time increases the signal-to-noise ratio in TIRF microscopy, since background fluorescence is reduced to a minimum.^[108,126]

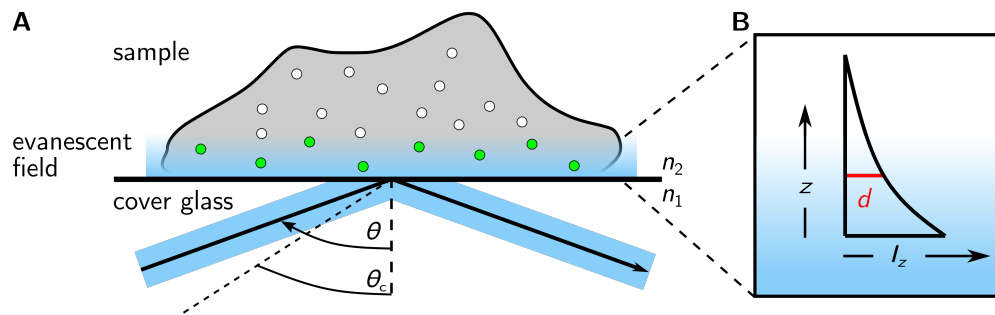


Figure 3.15: Schematic illustration of the evanescent field in TIRF microscopy. (A) Increasing the incident illumination beam angle θ within TIRF microscopy beyond the critical angle θ_c , leads to total internal reflection at the cover glass-sample interface and generates an evanescent field within the sample. Depending on the distance to the media interface, fluorophores can be excited (green dots) by the evanescent field. (B) The intensity in z -direction I_z of the evanescent field decays exponentially with increasing distance (z) from the interface. Figure inspired by MATTHEYSES et al. and FISH.^[108,126]

The decreasing evanescent field intensity can be expressed as shown in equation 3.26, with the initial intensity (I_0) at the media interface ($z = 0$) and d being the distance away from the interface at which I decreases to e^{-1} respectively 37 % of I_0 (cf. figure 3.15 B).

$$I_z = I_0^{-z/d} \quad (3.26)$$

The penetration depth d of the evanescent field can be described by:

$$d = \left(\frac{\lambda_0}{4\pi} \right) (n_1^2 \sin^2(\theta) - n_2^2)^{-\frac{1}{2}} \quad (3.27)$$

with the incident wavelength λ_0 , the angle of incidence θ and the refractive indices of the cover slip/immersion oil (n_1) and the aqueous sample (n_2).^[108,126]

Due to the low penetration depth of the evanescent field, TIRF microscopy is characterized by a high axial resolution of 100 nm and a lateral resolution of 200-300 nm.^[119]

TIRF microscopes can be based on two different approaches to generate total internal reflection, the *prism-based* and, the in this work used, *through-the-objective* TIRF. For the objective based approach high *NA* objectives are utilized combined with a specific off-axis focusing of the excitation beam at the back focal plane (BFP) of the objectives. Since the off-axis focusing at the objective BFP directly correlates to the angle of incidence at the cover glass-sample interface, fiber motors can be used to control the off-axis adjustment and thereby apply a defined angle of incidence.^[107,108,126]

Figure 3.16 illustrates the major modules as well as the beam path of the *through-the-objective* TIRF setup (*IXpolre TIRF*, *cellTIRF-4Line*, *Olympus Deutschland GmbH*, Hamburg, Germany) used in this work. In this system, the coherent excitation beam (cf. figure 3.16 green), generated by a laser source, was coupled into the system via a variable fiber motor, adjusting the off-axis position at the objective BFP. Beside the off-axis TIRF mode the centered fiber position additionally enabled the specimen investigation in a quasi-wide-field mode. By using a movable focus lens, the excitation beam was focused over a field stop and the dichroic mirror through the objective into the sample. The under total internal reflection emerging evanescent field excites the sample fluorophores in a defined distance from the cover glass surface. The emitted fluorescence (cf. figure 3.16 red) was collected back through the objective, over the dichroic mirror, and detected via a sCMOS camera (*Zyla 4.2 sCMOS*, *Andor Technology Ltd.*, Belfast, UK).

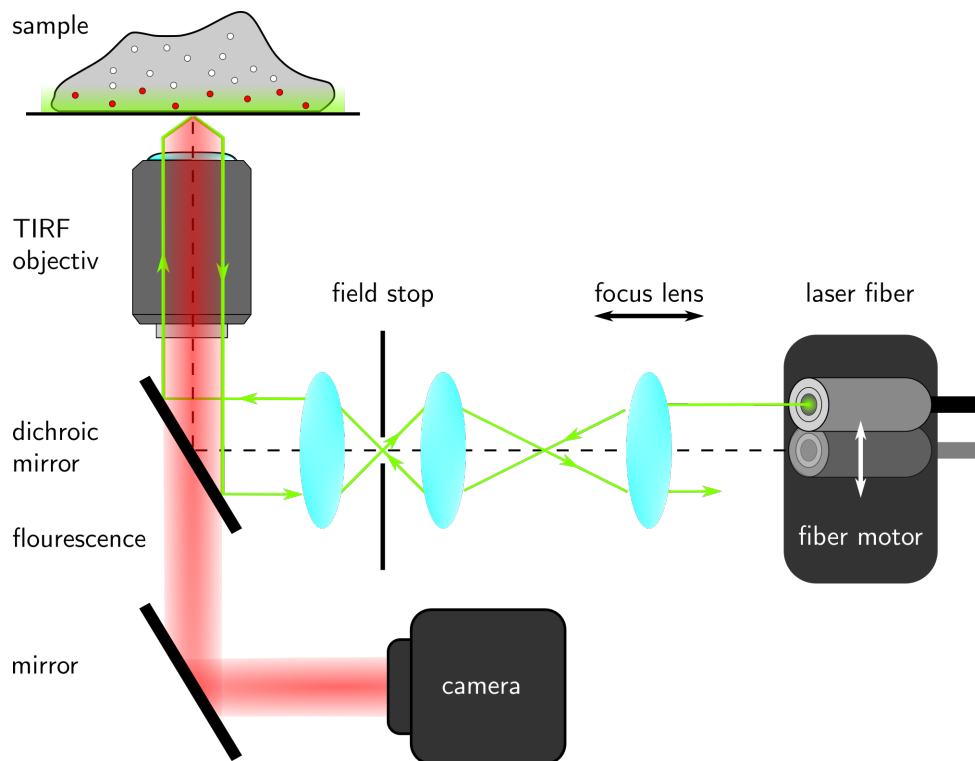


Figure 3.16: Schematic illustration of a principle total internal reflection fluorescence microscopy setup. Coherent excitation light, produced by a laser source, is coupled in the setup via a variable fiber motor, controlling the off-axis/centered position of the laser at the objective BFP. A focus lens focuses the excitation beam through the objective, by passing a field stop and dichroic mirror, into the specimen. The emitted fluorescence is collected by the objective, filtered through the dichroic mirror and detected via a camera.

3.5.2 Atomic force microscopy

The principle of atomic force microscopy (AFM) is the detection of forces arising between a specimen surface and the AFM-cantilever tip, which is used to probe the sample, in a range of p-nN.^[128] For biological samples such as lipid membranes or proteins, the AFM resolution limit is lateral around 1.0 nm and axial about 0.1 nm.^[129] In this work AFM has been utilized for the detection of sample topography and to capture mechanical properties such as elasticity and surface tension of freestanding pore-spanning membranes.

3.5.2.1 Principal of atomic force microscopy

The general setup of the JPK *Nanowizard 4* (JPK Instruments, Berlin, Germany) AFM used in this work is schematically illustrated in figure 3.17. In this system, the cantilever position was controlled by x -, y - and z -piezo elements, which allowed a three dimensional scanning of the specimens. The attractive and repulsive interactions occurring during the scanning process between the sample and the probe tip results in a deflection of the cantilever.

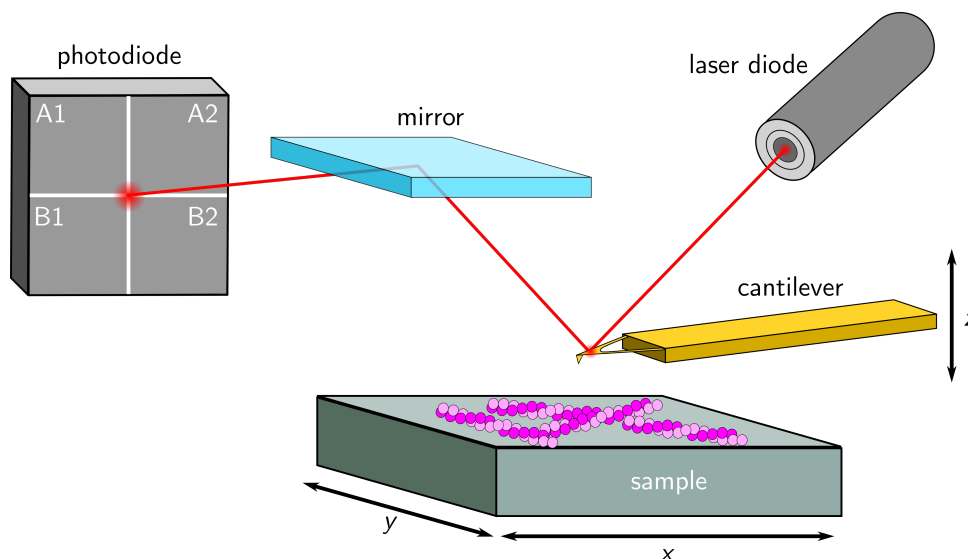


Figure 3.17: Schematic illustration of the central modules of an atomic force microscope. The sample topography is scanned via a piezo controlled cantilever in the x , y and z dimension. Cantilever deflection is detected via the reflection of laser beam from the backside of a cantilever, which focused on a position-sensitive photodiode (PSD).

This lateral and vertical deflections were detected via a laser aligned with the cantilever tip and reflected towards a position-sensitive photodiode (PSD). From the PSD the deflection can be read out as described in equation 3.28, via the ratio of the laser intensity difference (ΔI) between the diod segments and the total laser intensity (I) on the PSM.^[130,131]

$$\frac{\Delta I}{I} = \frac{I(A1 - A2) - I(B1 - B2)}{I(A1 + A2) + I(B1 + B2)} \quad (3.28)$$

Since the interaction forces between the cantilever tip and the specimen are short-range and both attractive and repulsive, the interaction potential can be described approximately by the LENNARD-JONES potential ($U_{LJ}(r)$, cf. equation 3.29).^[132]

$$U_{LJ}(r) = 4U_0 \left[\left(\frac{\sigma}{r} \right)^{12} - \left(\frac{\sigma}{r} \right)^6 \right] \quad (3.29)$$

With U_0 being the potential well depth, the sample-tip distance r and σ the distance at which $U_{LJ}(r)$ is zero. Accordingly, for a larger sample-tip distance the interactions are dominated by attractive forces (van-der-Waals interactions, $-\frac{1}{r^6}$ term), whereas closing the distance leads to repulsive interactions ($-\frac{1}{r^{12}}$ term), as the electron orbitals of sample and tip starts to overlap.^[132,133]

The general force needed to deflect the cantilever can be described by HOOK's law:

$$F = k_c z_c \quad (3.30)$$

with the applied force F , the cantilever spring constant k_c and the cantilever deflection z_c .^[133]

3.5.2.2 Force distance curves

Force distance curves (FDCs) are conducted by approaching the cantilever towards the sample surface and recording the cantilever deflection, which is proportional to the applied force. While the FDCs can be used to determine parameters such as the specimen elasticity and adhesion forces^[132], the cantilever deflection (z_c) can be described by equation 3.31:^[131]

$$z_c = \frac{F}{k_c} = \frac{4FL_c^3}{Ew_c t_c^3} \quad (3.31)$$

With the applied force F , the Young's modulus E and the cantilever specific parameters k_c (spring constant), w_c (width), L_c (length) and t_c (thickness).

A schematic illustration of a typical FDC is displayed in figure 3.18, showing the detected force as function of the z -piezo movement. Approaching the cantilever towards the sample (blue, I) leads in the first stage to no detectable force, as sample and cantilever are not in contact. At a sufficiently small distance between the cantilever and the specimen, van-der-Waals interactions lead to a *snap on*, which is indicated by a small dip (II). Upon reaching the contact point (dashed line), the recorded force increases linearly with z -piezo motion until a predefined force (setpoint, III). Retracting the cantilever (red) leads to a similar force response as during approaching (III).

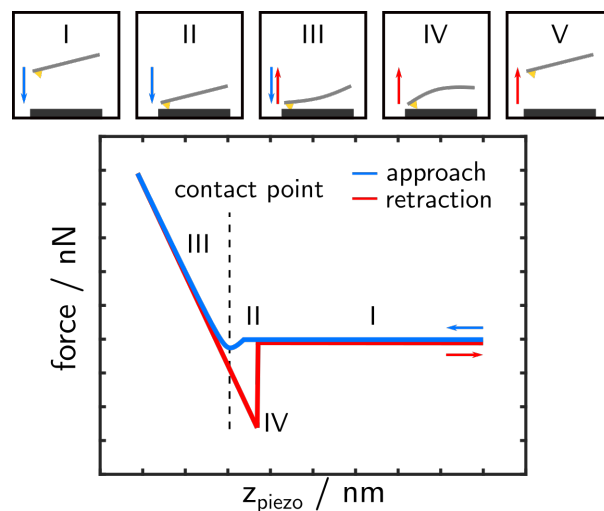


Figure 3.18: Depiction of an exemplary force distance curve.

Adhesion forces between cantilever tip and sample can lead to a *snap off* (IV), while further retraction leads to the initial force situation and no detectable cantilever deflection (V).

In order to represent the z -piezo motion as a function of the detected force, as displayed in figure 3.18, the cantilever spring constant was determined by recording a thermal noise spectrum according to equation 3.32.

$$\frac{1}{2} k_c \langle \Delta z_{\text{th}}^2 \rangle = \frac{1}{2} k_B T \quad (3.32)$$

With the mean square of the thermal noise amplitude $\langle \Delta z_{\text{th}}^2 \rangle$, the cantilever spring constant k_c and the thermal energy $k_B T$.^[134] Further, FDCs were recorded and the sensitivity S (nm V⁻¹) was determined from the FDC slope (cf. figure 3.18 III).

3.5.2.3 Lateral membrane tension determination

In order to determine the mechanical properties of freestanding pore-spanning membranes (f-PSMs), FDCs were recorded in the f-PSMs centers. By fitting the recorded force response (F) of the FDCs to equation 3.33, the lateral membrane tension (σ) of the f-PSMs was extracted.

$$F = 2\pi R \sigma_z \frac{u(R)'}{\sqrt{1 + u(R)^2}} \quad (3.33)$$

With R being the pore radius and $u(R)$ the indentation depth (z) dependent membrane geometry.^[135,136] The indentation tension σ_z is defined by equation 3.34:

$$\sigma_z = \sigma + K_A \frac{A_z - A_0}{A_0}, \quad (3.34)$$

with the lateral membrane tension σ , as result of the energy difference between s- and f-PSM^[137,138], the area compressibility modulus K_A and the initial ($A_0 = \pi R^2$) area and increasing f-PSM area A_z during indentation. The indenter geometry has been taken into account as described by HUBRICH *et al.*^[135]

For the viscoelasticity of f-PSMs with membrane-bound minimal actin cortices the time dependent (t) compressibility modulus $K_A(t)$ was described by:

$$K_A(t) = K_A^0 \left(\frac{t}{t_0} \right)^{-\beta}, \quad (3.35)$$

with $t_0 = 1$ s and the fluidity parameter β ($0 \leq \beta \leq 1$). Thus data have been fitted according to JANSHOFF.^[139]

3.5.2.4 Experimental procedure

AFM experiments on porous substrates were performed by preparing pore-spanning membranes as described in chapter 3.3.2.2 for pure PSMs and 3.3.4.2 for minimal actin cortices attached to PSMs. The samples were carried by a portable BIOMAT™ station (*JK Instruments*, Berlin, Germany) enabling a correlation of the CLSM field of view (*LSM 880, Zeiss Microscopy GmbH*, Oberkochen, Germany) and the AFM (*Nanowizard 4, JPK Instruments*, Berlin, Germany) scanning region as illustrated in figure 3.19. Atomic force micrographs were recorded via the quantitative imaging (QI™)-mode. This mode was chosen since the underlying recording of single FDCs is performed at constant x/y -positions and thus no lateral forces are applied to the specimen, which should be avoided in particular for membrane-bound minimal actin cortices.^[140,141]

AFM measurements were performed with a MLCT cantilever ("D" cantilever, *Bruker AFM Probes*, Camarillo, USA). Prior to all experiments the cantilever was calibrated as described in chapter 3.5.2.2. The calibration FDC was recorded at a constant velocity of $1 \mu\text{m s}^{-1}$ and a setpoint of 0.3-0.4 V. In order to correlate the observation regions of the AFM and CLSM, a correlation-cross was first centered under the CLSM and subsequently aligned with the AFM-scanning region (cf. figure 3.19, top) After the alignment QI™ micrographs of the pore-spanning membranes were recorded at a setpoint of 0.1-0.3 nN and a z -length of 0.3-2.0 μm (cf. figure 3.19, bottom).

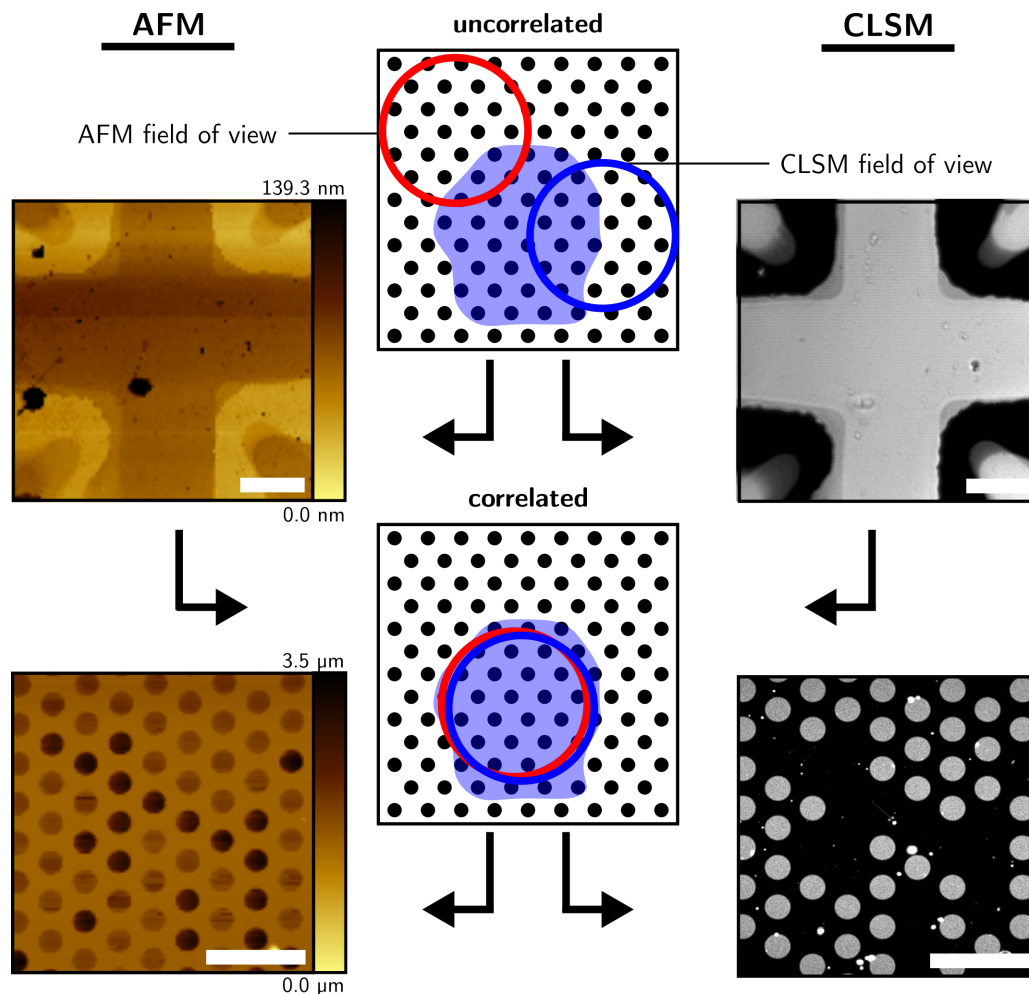


Figure 3.19: Schematic illustration of AFM-CLSM correlation. **Top:** Exemplary atomic force (left) and confocal micrographs (right) of the correlation-cross. Scale bars: 5 μm . **Bottom:** Exemplary atomic force and confocal micrographs of pore-spanning membranes after correlation. Scale bars: 20 μm .

After AFM micrograph acquisition, indentation experiments were performed by recording FDCs in the f-PSM centers at a constant velocity of $1 \mu\text{m s}^{-1}$ and varied setpoints of 0.15-0.3 nN. FDCs were evaluated according to chapter 3.5.2.3, using a MATLAB script written by *Prof. Dr. A. Janshoff* from the University of Göttingen.

3.6 Data evaluation

3.6.0.1 Tube filter analysis and network skeletonization

Tube filter analysis was developed by apl. Prof. Dr. Burkhard Geil from the University of Göttingen.

Fluorescence micrographs of membrane-bound F-actin networks were subjected to the python™ based *tube filter* analysis in order to enhance the signal-to-noise ratio of the images and enable a determination of filamentous and background pixels.

For this purpose, a two-step exposure correction of the F-actin network micrographs (cf. figure 3.20 A) was performed initially. First, a contrast limited adaptive histogram equalization (CLAHE) was used to equilibrate the global image intensity and improve the local image-contrast by varying the applied image-*tiles* and *contrast-limit* depending on the respective image. Second, high-frequency noise was reduced by applying a two dimensional Gaussian-filter, which is given by equation 3.36

$$G_{\sigma}(x, y) = \frac{1}{2\pi\sigma^2} e^{-\frac{x^2+y^2}{2\sigma^2}}, \quad (3.36)$$

with the varied standard deviation σ and the respective x/y -positions.^[142] The exposure-corrected image (cf. figure 3.20 B1) was subsequently subjected to the *tube-filter*. The *tube-filter* analysis is based on the calculation of the Hessian image matrix ($H_I(x, y)$), given by equation 3.37:

$$G_{\sigma}(x, y) H_I(x, y) = G_{\sigma}(x, y) \begin{bmatrix} \frac{\delta^2 I}{\delta x^2}(x, y) & \frac{\delta^2 I}{\delta y \delta x}(x, y) \\ \frac{\delta^2 I}{\delta x \delta y}(x, y) & \frac{\delta^2 I}{\delta y^2}(x, y) \end{bmatrix}, \quad (3.37)$$

where $\frac{\delta^2 I}{\delta x^2}(x, y)$, $\frac{\delta^2 I}{\delta y \delta x}(x, y)$, $\frac{\delta^2 I}{\delta x \delta y}(x, y)$, $\frac{\delta^2 I}{\delta y^2}(x, y)$ are the second partial derivatives of the input image ($I(x, y)$). The Hessian matrix describes the intensity dependent three dimensional surface curvature of the two dimensional input image (cf. figure 3.20 B2). In order to determine the maximal curvature for each image pixel, which is given by the maximum eigenvalue, the eigenvalues $\lambda_1(x, y)$ and $\lambda_2(x, y)$ of $H_I(x, y)$ were calculated. The signal-to-noise enhanced tube-filtered images were generated

via the second eigenvalue ($\lambda_2(x, y)$) containing the minimal surface curvature at each image pixel of $I(x, y)$ (cf. figure 3.20 C).^[143]

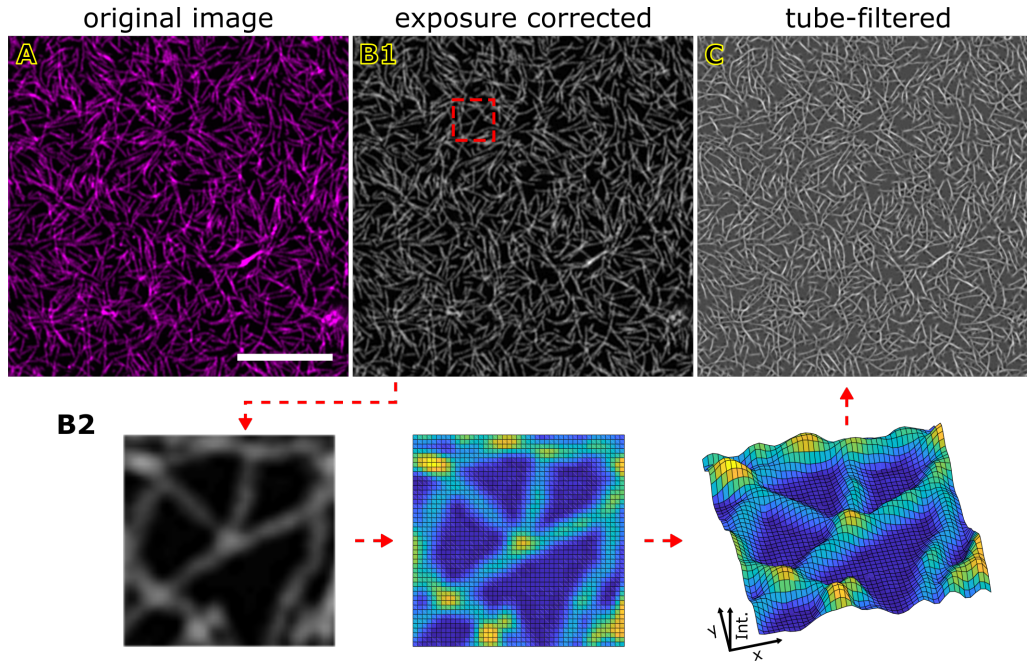


Figure 3.20: Exemplary illustration of the individual processing steps performed by the *tube-filter* analysis. **A:** Initial fluorescence micrograph of a membrane-bound minimal actin cortex (magenta), labeled with ATTO 594 G-actin. **B1:** Exposure-corrected image of the fluorescence micrograph shown in A. **B2:** Illustration of the three dimensional surface curvature of the two dimensional exposure-corrected image, given by the F-actin intensity (Int.). **C:** Tube-filtered image, calculated via the Hessian matrix and the magnitude of the maximum eigenvalue of each pixel. Scale bar: 10 μm .

The tube-filtered images were subsequently thresholded by applying a global adaptive threshold according to OTSU (cf. figure 3.21 A).^[144] These images were binarized by utilizing the skeletonization algorithm according to LEE et al. (cf. figure 3.21 B1)^[145] From the skeletonized-images filament intersections were detected, which are referred to as nodes in the following. A node was defined as a filament-pixel (white) with more than two directly neighboring filamentous pixels (cf. figure 3.21 B 2/3). Detected nodes of the skeletonized image 3.21 B1 are exemplary displayed in figure 3.21 C as red crosses. The node density of an image was calculated by dividing the detected node number of the respective image by the image size (in μm^2).

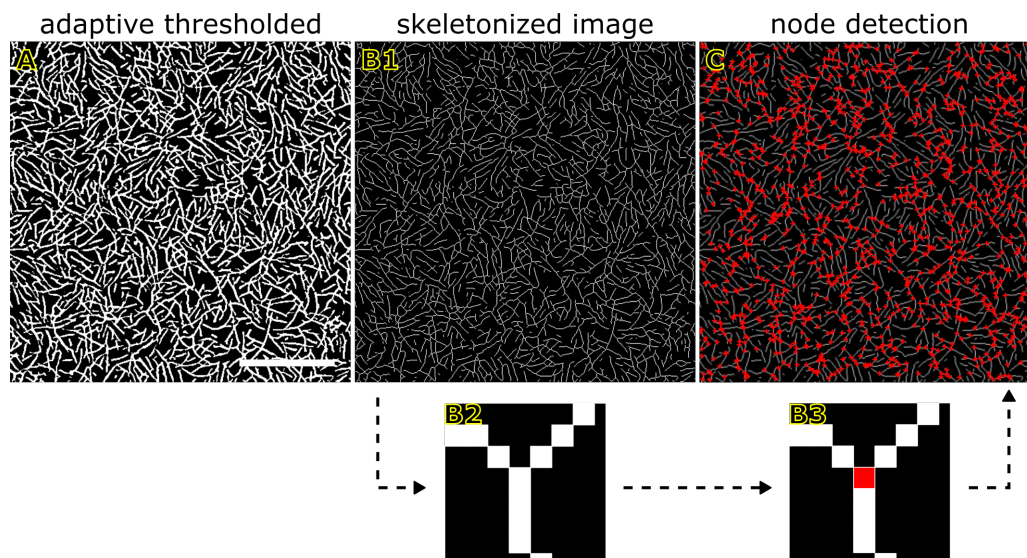


Figure 3.21: Exemplary skeletonization and node detection of a tube-filtered image. **A:** Adaptive thresholded image of the tube-filtered micrograph in figure 3.20 C. **B1:** Skeletonized image with detected filamentous pixels (white) and background pixels (black). **B 2/3:** Illustration of a filament intersection (B2) and the detected node (red, B3). **C:** Overlay of the skeletonized image B1 and all detected nodes (red crosses). Scale bar: 10 μm .

The skeleton network density was calculated via the ratio of filamentous (white pixels) to all image pixels of a skeletonized image (cf. figure 3.21 B1).

3.6.0.2 Nematic order parameter

The nematic order parameter (q) was calculated according to SEARA et al. in order to obtain quantitative excess to the organization of membrane-bound minimal actin cortices (cf. figure 3.22 A 1/2).^[146] For this purpose, a director field (cf. figure 3.22 B 1/2) was initially generated based on small pre-defined windows, which overlap by 50 % (cf. chapter A.3).^[147] This director field represents the local F-actin orientation within the pre-defined windows (cf. figure 3.22 B 1/2). From the determined director field, the nematic order parameter (q) was calculated according to equation 3.38 for each local F-actin direction.

$$q = 2 \left\langle \cos^2 \theta - \frac{1}{2} \right\rangle \quad (3.38)$$

The angle θ was defined as the difference of the central F-actin direction in 3×3 kernel compared to the surrounding orientations (cf. figure 3.22 B 3). For a perfect alignment of the F-actin orientations in the 3×3 kernel ($\theta = 0^\circ$) q is maximized and equals to 1. In contrast, for a minimal alignment ($\theta \sim 45^\circ$) q is equals to 0.^[146] By applying the 3×3 kernel to each local F-actin orientation, the local nematic order parameter was determined (cf. figure 3.22 C). The averaged nematic order parameter (q_{mean}) of an entire image was calculated via the absolute values of local nematic order parameters.

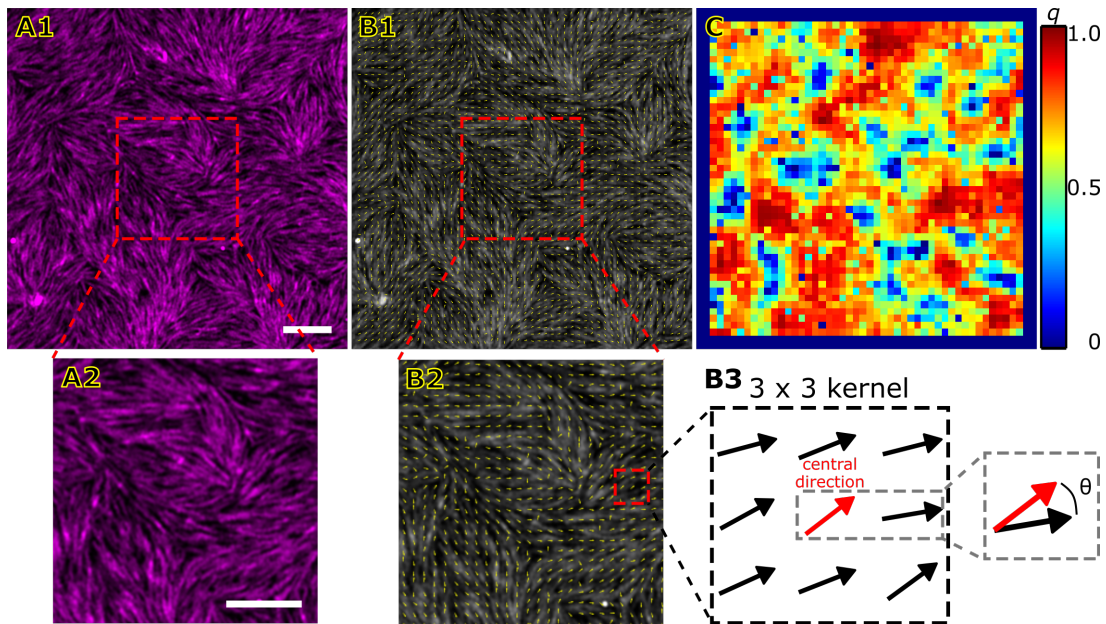


Figure 3.22: Exemplary illustration of a director and nematic order field. **A1/2:** Fluorescence micrograph of an membrane-bound F-actin network (magenta). **B1/2:** Director field (yellow), displaying the F-actin (gray) orientation. **B3:** Schematic depiction of the 3×3 kernel, comparing the orientation of a central direction (red) with the surrounding F-actin orientation (black) **C:** Heatmap of the nematic order parameter q . Scale bars: $5 \mu\text{m}$.

4 Results

4.1 Minimal actin cortex self-organization on lipid bilayers

The cellular cortex is a thin actin network, which is directly coupled to the inner plasma membrane of cells in a variety of eukaryotic organisms, controlling cell shape, migration and further essential cellular functions.^[8,10,33] In order to unravel the impact of specific cortex components, membrane-bound minimal actin cortices (MACs), based on solid supported bilayers, have been developed in the past decade.^[60] Recently, NÖDING et al., established a biomimetic minimal actin cortex by attaching pre-polymerized F-actin via the receptor lipid PtdIns[4,5]P₂ and the T567D mutant of the ERM protein ezrin to solid supported membranes.^[60,72]

In the present work, this model system was initially transferred to and characterized on supporting cover-glass substrates, enabling the investigation of myosin II induced MAC-contraction by means of TIRF microscopy. Further, aiming for an improved understanding of the cellular interactions controlling membrane-bound cortical actin, the MAC complexity has been increased by mimicking *in vivo* conditions, such as the plasma membrane lipid composition, cytoplasm density and a branched cortical actin network.

4.1.1 The minimal actin cortex

Since the formation of solid-supported membranes depends on several parameters such as the surface of the substrate and, in case of PtdIns[4,5]P₂ containing systems in particular on the pH value, as a first step the formation of a minimal actin cortex (MAC) was investigated on glass substrates.^[148,149]

Following the detailed instructions in chapter 3.3.4.1, MACs were formed by first preparing solid-supported bilayers (SLBs) on hydrophilized glass slides and subsequently attaching pre-polymerized F-actin (ATTO 594-labeled) via the ezrin mutant T567D. Ezrin is capable of binding the receptor lipid PtdIns[4,5]P₂ via the N-terminal domain, while the C-terminal part is able to bind F-actin. Confocal laser scanning microscopy (CLSM) images were taken to analyze the critical preparation steps of membrane spreading and specific actin binding.

Membrane-bound minimal actin cortices were obtained by binding pre-polymerized F-actin to ezrin decorated membranes containing PtdIns[4,5]P₂. The fluorescence micrographs in figure 4.1 show an exemplary F-actin network attachment for a membrane containing 3 mol% PtdIns[4,5]P₂. While figure 4.1 A displays the ATTO 390-DPPE membrane fluorescence (gray), figure 4.1 B show the ATTO 594-G-actin labeled actin network (magenta) at the same position.

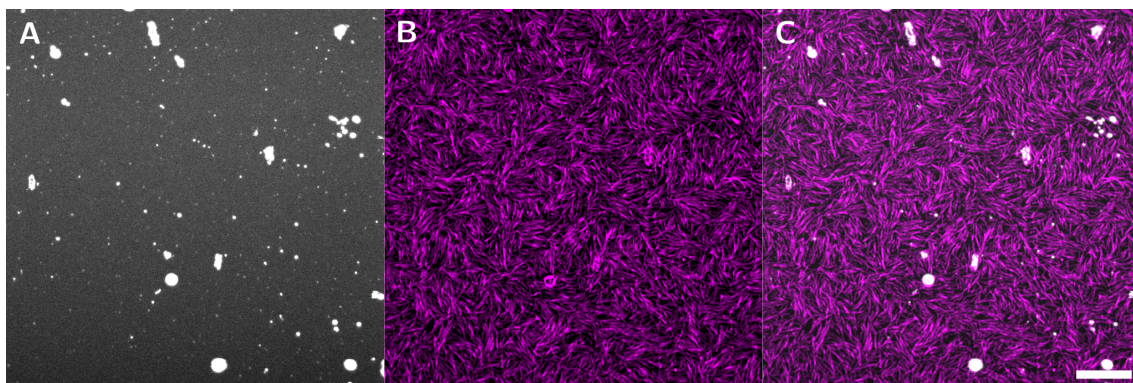


Figure 4.1: Fluorescence micrographs showing the specific binding of a minimal actin cortex to an ezrin T567D decorated membrane. A: POPC/PtdIns[4,5]P₂/ATTO 390-DPPE (96.6:3:0.4) SLB (gray), with brighter signals originating from aggregated lipid material. **B:** Membrane-bound F-actin (magenta), labeled with ATTO 594 G-actin, forming the minimal actin cortex. **C:** Membrane (A) and F-actin (B) overlay. Scale bar: A-C 5 μ m.

As shown in figure 4.1 A, homogeneous defect-free SLBs were generated on hydrophilized glass surfaces by spreading small unilamellar vesicles (SUVs), which was qualitatively verified via fluorescence recovery after photobleaching experiments (data not shown). Homogeneous SLBs were characterized by a uniform fluorescence (cf. figure 4.1 A, gray), whereas membrane defects were recognizable as dark patches (not shown). Aggregated lipid material, which is visible as bright signals, was observed in certain cases, depending on the recorded substrate position. As illustrated by the overlay in figure 4.1 C, a dense actin network was formed on the homogeneous SLB, whereas no or reduced binding to lipid aggregates was observed in general.

To exclude a non-specific interaction of the matrix lipid or the membrane label with the pre-polymerized F-actin, SLBs lacking the receptor lipid PtdIns[4,5]P₂ were prepared and incubated with ezrin T567D and F-actin. As shown in figure 4.2 A, F-actin showed a non-relevant amount of binding to those membranes. Further, a non-specific attachment of F-actin to PtdIns[4,5]P₂ containing membranes without the membrane-linker ezrin T567D could be ruled out as shown in figure 4.2 B.

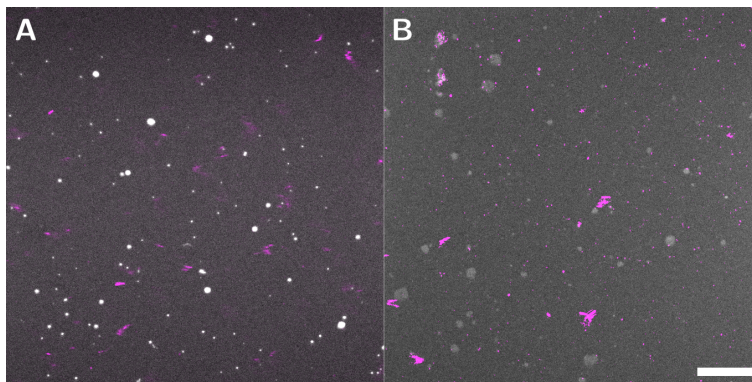


Figure 4.2: Fluorescence micrographs of the F-actin binding to lipid membranes lacking the receptor lipid or ezrin linkage. Each image shows an overlay of a solid supported lipid membrane (gray) and the non-specific attached F-actin network (magenta), labeled with ATTO 594 G-actin. **A:** POPC/ATTO 390-DPPE (99.6:0.4) membrane after incubation with ezrin T567D and F-actin. **B:** POPC/PtdIns[4,5]P₂/ATTO 390-DPPE (91.6:8:0.4) membrane after incubation with only F-actin. Scale bar: A-B 5 μ m.

Fluorescence recovery after photobleaching (FRAP, cf. chapter 3.5.1.3) experiments were conducted to analyze the membrane fluidity of SLBs and to investigate the influence of a MAC attachment. To ensure quantitative comparability, all experiments were performed on SLBs doped with 0.4 mol% ATTO 488-DPPE and 3 mol% PtdIns[4,5]P₂. All time series were recorded in the same manner on defect- and aggregate-free SLBs over 200 frames ($t_{\text{frame}} = 65$ ms). The exemplary fluorescence mi-

crographs in figure 4.3 A1-4 display the membrane pre-bleaching (A1, $t = -0.32$ s), immediately after-bleaching (A2, $t = 0.00$ s) and the fluorescence recovery (A3-4, $t = +0.45$ s and $+12.6$ s) during a FRAP experiment in the region of interest (ROI, red circle).

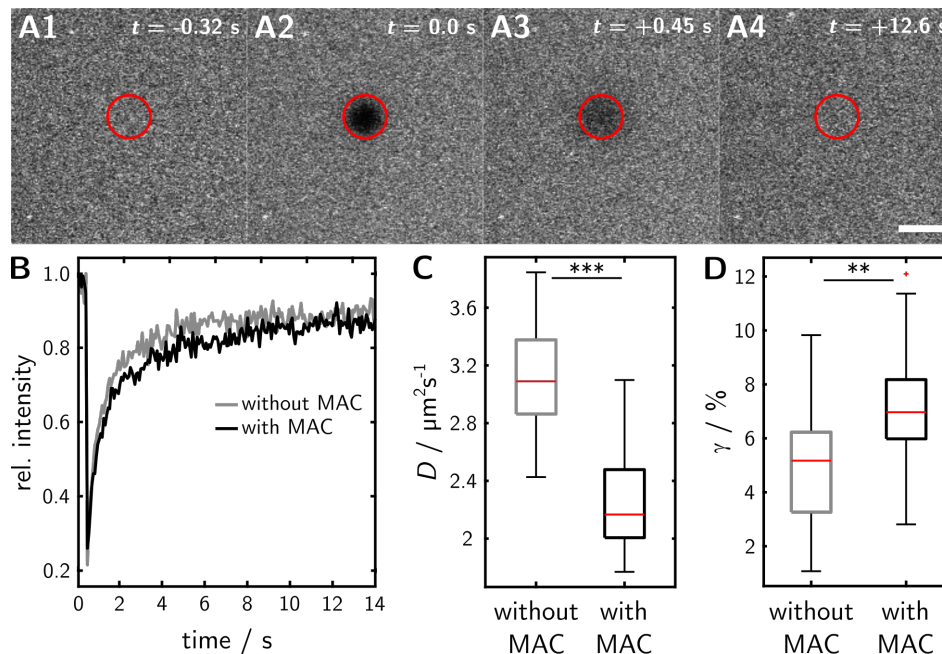


Figure 4.3: Comparison of lipid diffusion in solid-supported bilayers with and without attached MAC. A1-4: Exemplary time series with four frames ($t = -0.32$ s, 0 s, 0.45 s, 12.6 s) showing characteristic bleaching and recovering during a FRAP experiment on a pure SLB (POPC/PtdIns[4,5]P₂/ATTO 488-DPPE (96.6:3:0.4)) within the region of interest (ROI, red circle). Scale bar 5 μm . B: Exemplary intensity profiles from FRAP experiments with (black) and without (gray) membrane-bound MAC. Box plot diagrams displaying the extracted diffusion coefficients (D , C) as well as the immobile fractions (γ , D) for lipid bilayers without ($3.1 \pm 0.4 \mu\text{m}^2\text{s}^{-1}$, 5.0 ± 2.3 %, $n = 34$) and with attached MAC ($2.2 \pm 0.3 \mu\text{m}^2\text{s}^{-1}$, 7.1 ± 2.2 %, $n = 34$). Boxes ranging from 25th to 75th percentiles of the sample, while whiskers represent to the most extreme data points not considered outliers. Medians are shown as red horizontals within the boxes. Statistical t -test: ***: $p \leq 0.001$, **: $p \leq 0.01$.

The recorded intensity profiles for SLBs with (black) and without (gray) a membrane-bound MAC, representatively shown in figure 4.3 B, were quantitatively analyzed according to JÖNSSSEN et al. (cf. chapter 3.5.1.3).^[125] The determined diffusion coefficients (D , cf. figure 4.3 C) revealed a significant reduced lipid diffusion for SLBs with a membrane-bound MAC ($2.2 \pm 0.3 \mu\text{m}^2\text{s}^{-1}$, $n = 34$), compared to pure SLBs ($3.1 \pm 0.4 \mu\text{m}^2\text{s}^{-1}$, $n = 34$). Simultaneously, a significant increased immobile fraction (γ , cf. figure 4.3 D) was found for membranes with attached MAC (7.1 ± 2.2 %,

$n = 34$) in comparison to pure SLBs (5.0 ± 2.3 %, $n = 34$).

4.1.2 Characterization of F-actin binding to solid supported lipid bilayers as a function of the PtdIns[4,5]P₂ content

Parts of the CLSM experiments presented in this chapter were performed by Loan Vuong as part of her master thesis.

The organization and network density of membrane-bound minimal actin cortices, linked via ezrin T567D, have been shown to be a function of the receptor lipid (PtdIns[4,5]P₂) concentration.^[72] As the surface of the membrane supporting substrates is known to alter the distribution of receptor lipids, increasing PtdIns[4,5]P₂ concentrations of 1 - 8 mol% were investigated in terms of the minimal actin cortex morphology on the in this work introduce glass substrates.^[150,151] The obtained results were used as reference data in following chapters, to reveal the effects of the aforementioned *in vivo* mimicking conditions such as the influence of the actin binding protein Arp2/3.

MACs were formed according to the detailed description in chapter 3.3.4.1 by spreading ATTO 390-DPPE (0.4 mol%) doped and PtdIns[4,5]P₂ (1 - 8 mol%) containing SUVs on hydrophilized glass slides. Pre-polymerized F-actin, labeled with ATTO 594-G-actin, was specifically attached via the ezrin T567D mutant. After rinsing, CLSM images of the bilayer fluorescence were taken to validate the formation of continuous lipid bilayers (data not shown), to ensure that the F-actin network morphology was only analyzed for homogeneous and defect-free SLBs.

Exemplary fluorescence micrographs of F-actin networks bound to SLBs, containing 1, 2, 3, 5 and 8 mol% PtdIns[4,5]P₂, are shown in figure 4.4. The visual inspection clearly demonstrates, that the MAC density increases from single filaments at 1 - 2 mol% PtdIns[4,5]P₂ to dense networks, already present at 3 mol% PtdIns[4,5]P₂. This findings are generally in line with the observations of NÖDING et al., obtained on silicon wafers, showing an increased network density with increased PtdIns[4,5]P₂ content.^[72]

To quantitatively analyze the network density, the F-actin micrographs were subjected to a "tube filter" analysis.(cf. chapter 3.6.0.1) This filter allows a skeletonization of the membrane-bound networks and subsequently the determination of the skeleton

network density, as well as the node density. While the skeleton network density is the ratio of filamentous pixels to all image pixels, filament intersections are represented by the node density (cf. chapter 3.6.0.1).^[72]

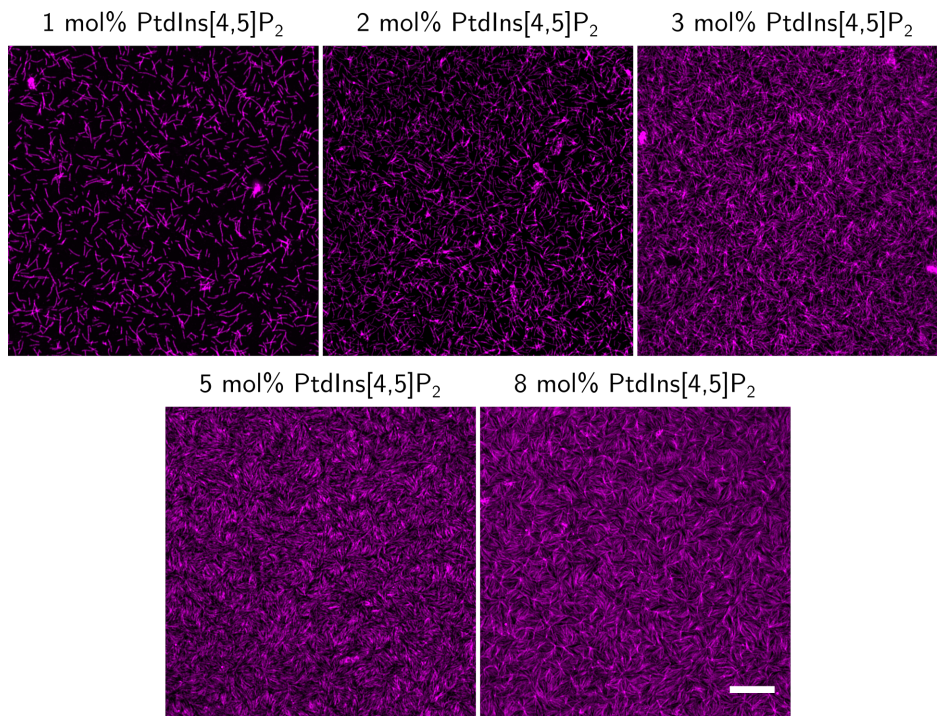


Figure 4.4: Exemplary fluorescence micrographs showing the F-actin binding to SLBs containing 1 - 8 mol% PtdIns[4,5]P₂. Fluorescence micrographs showing the actin network (magenta), labeled with ATTO 594-G-actin, binding to SLBs doped with 1 - 8 mol% PtdIns[4,5]P₂. Scale bar: 10 μm .

The visually observed increased network density, for 1-3 mol% PtdIns[4,5]P₂ (cf. figure 4.4; 1-3 mol%), is reflected in both parameters. While the node density increases from $0.08 \pm 0.06 \mu\text{m}^{-2}$ ($n = 30$, $N = 4$) to $1.43 \pm 0.39 \mu\text{m}^{-2}$ ($n = 34$, $N = 4$) between 1-3 mol% PtdIns[4,5]P₂, the mean skeleton network density raises in the same range by a factor of ~ 5.5 (cf. figure 4.5 A-B). However, for 5-8 mol% receptor lipid the mean skeleton network density decreases by a factor of up to 0.9, as well as reduced node densities of $1.29 \pm 0.19 \mu\text{m}^{-2}$ ($n = 20$, $N = 2$) and $0.939 \pm 0.10 \mu\text{m}^{-2}$ ($n = 31$, $N = 3$) were detected (cf. figure 4.5 A-B). In contrast, a visual inspection of actin cortices attached to membranes with these particular PtdIns[4,5]P₂ concentrations (cf. figure 4.4; 5-8 mol%) did not reveal a decreased network density. However, these MACs showed an enhanced parallel organization of the membrane-bound F-actin into local domains (cf. also figure 4.6 A). Since node density, due to the definition of a node as the intersection of two actin filaments,

depends in particular on the network organization, the mean coarse-grained nematic order parameter (q_{mean}) was calculated as described in chapter 3.6.0.2 according to SEARA et al., giving quantitative access to the network organization.^[146] q_{mean} is a quantitative measure of the uniform orientation of the membrane-bound filaments, ranging from 0 to 1, where 0 corresponds to a maximum disorder and 1 to a maximum uniform or parallel organization.

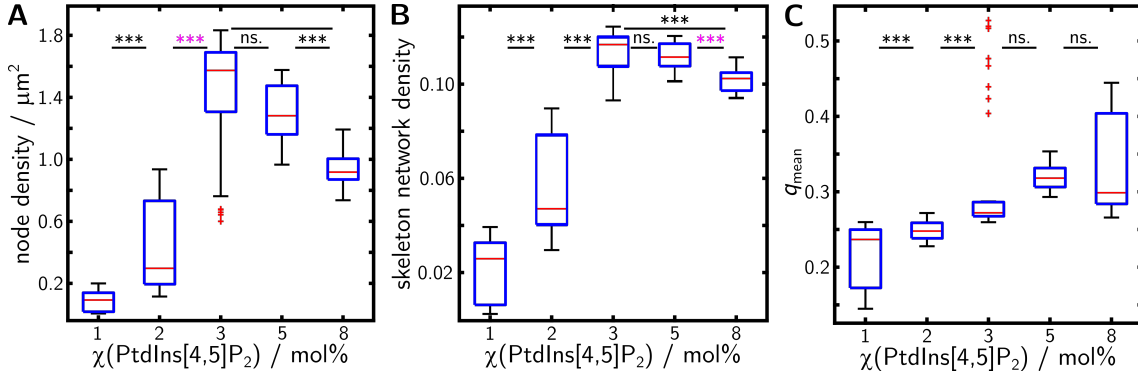


Figure 4.5: Box plots showing the actin network node density, skeleton network ratio and q_{mean} of membrane-bound MACs depending on PtdIns[4,5]P₂ content. Comparison of actin network node density (A), skeleton network ratio (B) and q_{mean} (C) for 1-8 mol% PtdIns[4,5]P₂. The analyses were performed with n images from N preparations. 1 mol% ($n = 30$, $n_{q,\text{mean}} = 30$, $N = 4$), 2 mol% ($n = 23$, $n_{q,\text{mean}} = 24$, $N = 3$), 3 mol% ($n = 34$, $n_{q,\text{mean}} = 39$, $N = 4$), 5 mol% ($n = 20$, $n_{q,\text{mean}} = 20$, $N = 2$) and 8 mol% ($n = 31$, $n_{q,\text{mean}} = 31$, $N = 3$). Boxes ranging from 25th to 75th percentiles of the sample, while whiskers represent to the most extreme data points not considered outliers (red crosses). Medians are shown as red horizontals within the boxes. Statistical t -test: ***: $p \leq 0.001$, ns.: $p > 0.05$; Welch-test: ***: $p \leq 0.001$.

The obtained q_{mean} values are displayed in figure 4.5 C, as a function of the PtdIns[4,5]P₂ concentration ($\chi(\text{PtdIns}[4,5]\text{P}_2)$). While only the low receptor lipid concentrations ($\chi(\text{PtdIns}[4,5]\text{P}_2) = 1-3$ mol%) show a significant q_{mean} increase, the global shift (1-8 mol% PtdIns[4,5]P₂) towards higher nematic orders implies a change in network organization from isotropic to anisotropic organized filaments with increasing PtdIns[4,5]P₂ content (cf. figure 4.5 C; 1-8 mol%).

Beside the overall network organization, the single filament structure of membrane-bound actin filaments was investigated by means of a skeleton-based intensity analysis. The exemplary fluorescence micrographs, displayed in figure 4.6 A, of membrane-bound MACs for 3 and 8 mol% PtdIns[4,5]P₂, suggest a modified single filament structure for increasing PtdIns[4,5]P₂ concentrations. While membrane-bound actin filaments at low PtdIns[4,5]P₂ concentrations appeared to be mainly bound as single filaments (cf. figure 4.6 A; 3 mol% PtdIns[4,5]P₂), binding to membranes

containing a high receptor lipid content seemed to bundle filaments, indicated by a broader diameter and higher actin fluorescence intensity (cf. figure 4.6 A; 8 mol% PtdIns[4,5]P₂).

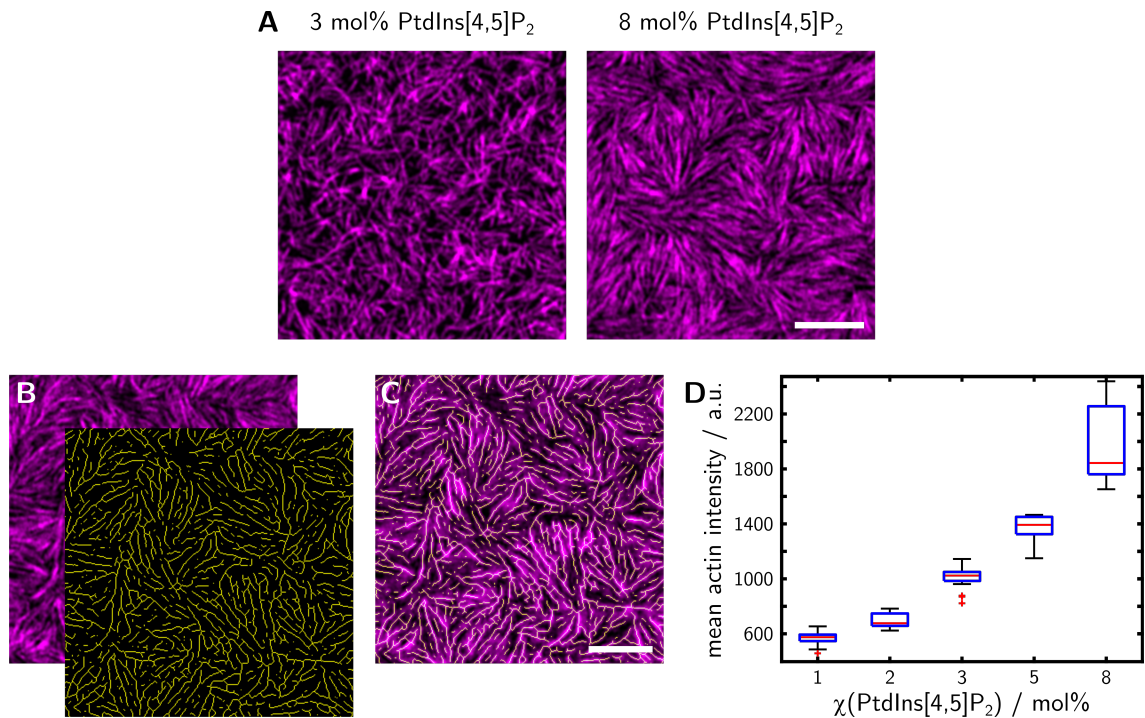


Figure 4.6: Skeleton based actin intensity determination. **A:** Exemplary fluorescence micrographs of membrane-bound minimal actin cortices at 3 and 8 mol% PtdIns[4,5]P₂ displaying an altered single filament structure. **B:** The fluorescence intensity of membrane-bound F-actin was determined, masking actin fluorescence images (magenta) by means of the corresponding actin skeletons (yellow). **C:** Actin fluorescence was read out at the overlapping positions. **D:** Comparison of the mean actin intensity as a function of the PtdIns[4,5]P₂ content. The analysis was performed with n images from N preparations. 1 mol% ($n = 30$, $N = 4$), 2 mol% ($n = 23$, $N = 3$), 3 mol% ($n = 34$, $N = 4$), 5 mol% ($n = 20$, $N = 2$) and 8 mol% ($n = 31$, $N = 3$). Boxes ranging from 25th to 75th percentiles of the sample, while whiskers represent to the most extreme data points not considered outliers (red crosses). Medians are shown as red horizontals within the boxes. Scale bar: 5 μm .

To get quantitative access to the single filament structure, fluorescence micrographs of membrane-bound MACs were analyzed using the aforementioned skeleton-based intensity analysis. Since a respective increase in fluorescence intensity can be expected for bundled filaments in proportion to the number of individual filaments, the actin intensity was extracted by masking the fluorescence images with the corresponding skeletonized networks (cf. figure 4.6 B). As depicted in figure 4.6 C, the actin intensity (magenta) was only quantified at the positions of tracked filaments within

the skeletonized networks (yellow). The so determined averaged actin intensity per image, shown in figure 4.6 D, confirm the visual observation of bundled actin filaments for increasing receptor lipid concentrations, as the mean actin intensity along a detected filament raises from 1 to 8 mol% PtdIns[4,5]P₂ by a factor of ~ 3.4 .

4.1.3 Minimal actin cortices under cellular mimicking conditions.

4.1.3.1 Characterization of actin binding to solid supported bilayers with the crowding agent methyl cellulose as a function of PtdIns[4,5]P₂ content

Experiments in this chapter have been carried out by Iris Langebrake as part of her bachelor thesis.

The cytoplasm of eukaryotic cells is a dense fluid containing a broad range of diverse macromolecules, such as proteins, nucleic acids, polysaccharides and cytoskeletal compounds. The fraction occupied by this biomolecules ranges between 20-40 % of the total cytoplasmatic volume.^[152,153] Since no single highly concentrated macromolecule, but the entirety of all of them, is responsible for this particular characteristic, such solutions are referred to as crowded media.^[152] *In vivo* crowded solutions are known to effect biochemical reactions and equilibria.^[154,155] To mimic this cellular condition *in vitro*, inert crowding agents like methyl cellulose (MC) can be used.

In order to reveal the effect of a crowded media on actin network organization, minimal actin cortices were treated with MC. MACs were prepared, as described in detail in chapter 3.3.4.1, on hydrophilized silicon wafers by spreading TxR-DHPE (0.3 mol%) doped SUVs, containing various PtdIns[4,5]P₂ concentrations (1-5 mol%). Pre-polymerized F-actin, labeled with Alexa FluorTM488 phalloidin, was linked by means of the ezrin mutant T567D to the preformed SLBs. During the membrane binding process, MACs were treated with MC using different concentrations. CLSM experiments were conducted after rinsing the samples with F-actin buffer.

Since MC concentrations above 0.2-0.3 *w/v* % are known to bundle F-actin filaments, the impact of increasing MC concentrations was tested first in terms of the MAC morphology.^[156,157] To estimate the MC induced effect, actin cortices were prepared on SLBs with 2 mol% PtdIns[4,5]P₂ and exposed to MC concentrations of 0.06-0.44 *w/v* % during the actin-binding process. The visual inspection of these networks

revealed no change in actin filament or network organization at low MC concentrations of 0.06 *w/v* % in comparison to untreated (data not shown) networks (cf. figure 4.7). However, for the highest tested concentration of 0.44 *w/v* % MC, a strong bundling of actin filaments and the formation of dense membrane-bound networks, showing nematic aligned bundles, was observed (cf. figure 4.7). The visual comparison of MC treated and non-treated MACs revealed, a optimal MC concentration of 0.18 *w/v* %, showing an increased F-actin-membrane binding, while no change in single filament structure was observable (cf. figure 4.7).

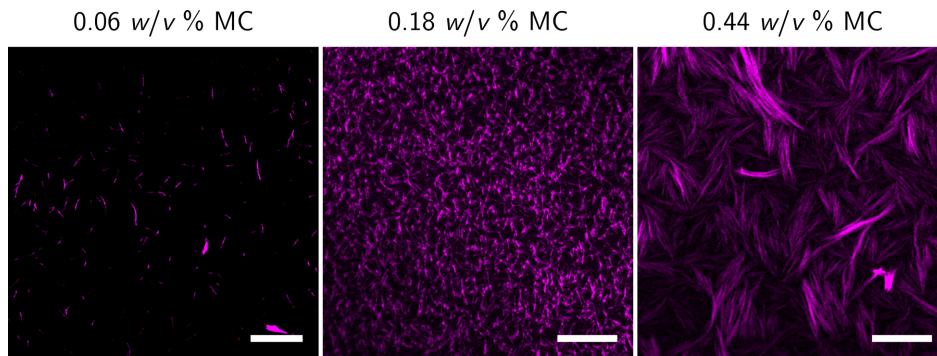


Figure 4.7: Exemplary fluorescence micrographs showing the F-actin binding to SLBs containing 2 mol% PtdIns[4,5]P₂ depending on methyl cellulose (MC) concentration. Actin (magenta), labeled with Alexa Fluor® 488-phalloidin, binding to SLBs (POPC/PtdIns[4,5]P₂/TxR (97.7:2:0.3)) for 0.06-0.44 *w/v* % MC. Scale bars: 10 μ m.

To exclude an unspecific F-actin-membrane interaction induced by 0.18 *w/v* % MC, the attachment of pre-polymerized F-actin was investigated for membranes lacking PtdIns[4,5]P₂ and PtdIns[4,5]P₂ containing membranes without the linker ezrin T567D. In both cases (data not shown) no significant F-actin binding to continuous SLBs could be detected after rinsing the samples with MC-free F-actin buffer.

Since a treatment with MC seems to effect the membrane attachment of minimal actin cortices, the condensing properties of 0.18 *w/v* % MC were investigated for varied receptor lipid concentrations of 1-5 mol% PtdIns[4,5]P₂, shown in figure 4.8 (bottom row). As reference for non-treated MACs the experiments with MC of this work were compared with the data of NÖDING et al., who used the same preparation of SLBs, membrane-linkage and actin staining (cf. figure 4.8; top row).^[72] The visual comparison of both data sets showed, that the addition of MC increases the network density for low PtdIns[4,5]P₂ concentrations of 1-3 mol%, whereas no significant modification was observable at 5 mol% PtdIns[4,5]P₂. For a quantitative comparison the data were applied, as described in sectin 3.6.0.1, to a "tube filter" analysis, enabling

the determination of the node and skeleton network density (cf. figure 4.9).

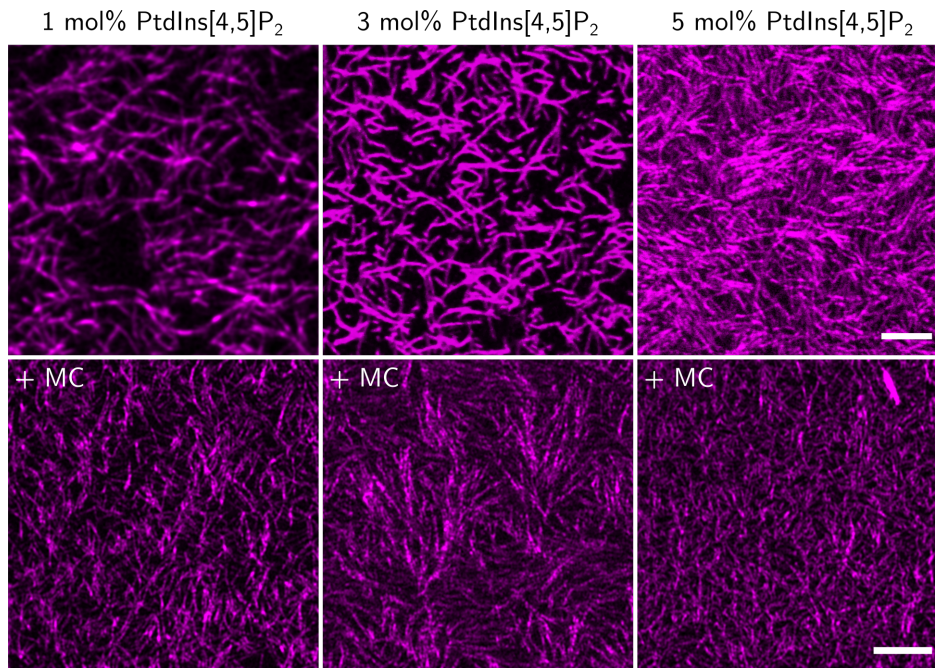


Figure 4.8: Exemplary fluorescence micrographs displaying the F-actin binding to SLBs containing 1 - 5 mol% PtdIns[4,5]P₂ with and without 0.18 *w/v* % MC. The upper row displays the F-actin (magenta), labeled with Alexa Fluor® 488-phalloidin, binding to SLBs doped with 1-5 mol% PtdIns[4,5]P₂ without MC and the lower row with 0.18 *w/v* % MC. Scale bars: 5 μm . For comparison MC-free data were taken from NÖDING et al.^[72]

As the optical inspection indicated, both parameters confirm that MC treated MACs show a significantly increased network density. As displayed in figure 4.9, this effect seems to be especially pronounced at low PtdIns[4,5]P₂ concentrations of 1 mol%, showing an increase in node density from $0.04 \pm 0.09 \mu\text{m}^{-2}$ (green, -MC) to $1.56 \pm 0.64 \mu\text{m}^{-2}$ (blue, +MC) and a ~ 6 -fold increase in skeleton network density. While this trend is still clearly present at the highest tested PtdIns[4,5]P₂ concentration of 5 mol%, the increase in node density from $1.57 \pm 1.15 \mu\text{m}^{-2}$ (green, -MC) to $3.48 \pm 1.05 \mu\text{m}^{-2}$ (blue, +MC) and skeleton density (~ 1.4 -fold) is less noticeable pronounced.

Although, shift in network organization towards nematically aligned filaments could be partially observed for MC treated samples (cf. figure 4.8; 3 mol%), no network analysis could be performed according to SEARA et al., since the fluorescence micrographs seemed to be not suited.^[146] This might be attributable to the low staining ratio of 1.5 % (*n/n*, G-actin : Alexa Fluor® 488-phalloidin) and the accompanying poor signal-to-noise ratio. Also, the described skeleton based actin intensity determination

(cf. chapter 4.1.2) could not be executed, since the fluorescence micrographs were recorded with different CLSM settings.

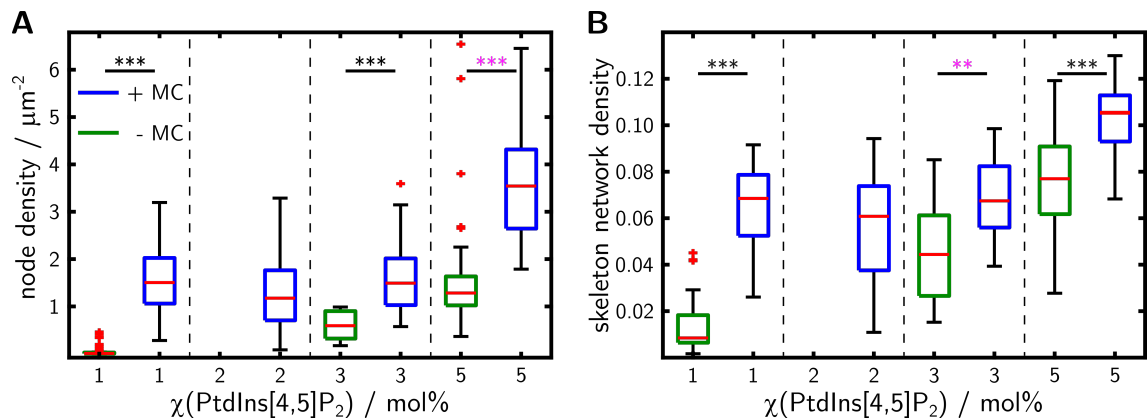


Figure 4.9: Box plots showing the actin network node- and skeleton network density of membrane-bound MACs depending on PtdIns[4,5]P₂ content and MC treatment. Comparison of the node density (**A**) and skeleton network density (**B**) of MC treated (blue) and untreated (green) membrane-bound minimal actin cortices for 1-5 mol% PtdIns[4,5]P₂. For the analysis, n images of N preparations were evaluated. 1 mol% ($n = 59$, $N = 2$; $n = 68$, $N = 2$), 2 mol% ($n = 73$, $N = 3$), 3 mol% ($n = 57$, $N = 2$; $n = 12$, $N = 2$) and 5 mol% ($n = 83$, $N = 3$; $n = 48$, $N = 4$). Boxes ranging from 25th to 75th percentiles of the sample, while whiskers represent to the most extreme data points not considered outliers (red crosses). Medians are shown as red horizontals within the boxes. Statistical t -test: ***: $p \leq 0.001$; Welch-test: ***: $p \leq 0.001$, **: $p \leq 0.01$. Data without MC have been re-evaluated from NÖDING et al. by means of "tube filter" analysis (cf. chapter 3.6.0.1).^[72]

4.1.3.2 Branched MAC's with the Arp2/3-VCA complex

Experiments in this chapter have been carried out by Loan Vuong as part of her master thesis.

In cellular systems the dynamic and organization of cortical actin filaments is controlled by over a hundred of different actin binding proteins (ABPs).^[10] Since the impact of a particular ABPs is therefore rather difficult to determine, biomimetic systems like minimal actin cortices are appropriate *in vitro* model systems, to reveal the individual functions of ABPs. The Arp2/3 protein complex is one of the most abundant ABPs within cellular actin networks, branching actin networks by polymerizing new daughter-filaments from pre-existing F-actin.^[158,159] As the Arp2/3 complex plays a critical role in lamellipodium organization and cellular motion, the self-organization of membrane-bound Arp2/3 branched actin networks was investigated in terms of the MAC morphology.^[160,161]

Since Arp2/3 stimulates the polymerization of filament branches at pre-formed actin filaments, it was added during F-actin polymerization.^[158] As the addition can influence both, the principal actin filament structure and the morphology of membrane attached networks, two approaches were used to study the impact of Arp2/3. In a first approach, the impact of Arp2/3 was investigated with regard to the principle F-actin structure in solution. Therefore, branched actin networks were polymerized from a mixture of G-actin/VCA/Arp2/3 (80:20:1), as described in chapter 3.3.3. The VCA-domain of N-WASP, acting as nucleation promoting factor (NPF) protein, was added since the Arp2/3 complex requires an activation via the association with a NPF protein. The structures of these F-actin-Arp2/3 gels were investigated in solution by means of CLSM fluorescence micrographs and compared to pure F-actin networks. In a second approach, the attachment of Arp2/3 branched F-actin networks, prepared as aforementioned described, to ezrin T567D decorated membranes was investigated as function of the receptor lipid PtdIns[4,5]P₂ concentration, forming branched MACs on glass supported SLBs as described in chapter 3.3.4.1.

Comparing the 3D organization of pure F-actin networks and Arp2/3-actin gels by means of CLSM z-stacks, revealed a significant structural change within the branched networks. As displayed in figure 4.10 A1/2, untreated actin networks were characterized by loosely entangled actin filaments, forming a wide-meshed F-actin

network over several microns in height. Furthermore, the visual inspection of figure 4.10 A2 indicates, that the network consisted of both, long individual filaments and filament bundles with a size of several tens of microns. In contrast, for Arp2/3 branched actin filaments the formation of gel-like networks could be monitored (cf. figure 4.10 B1/2).

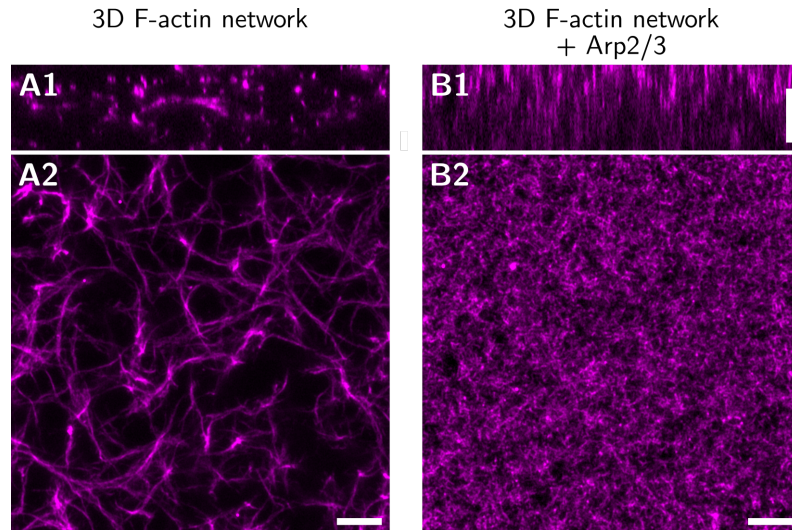


Figure 4.10: Fluorescence micrographs of 3-D F-actin gels polymerized in the absence or presence of Arp2/3. A/B1: Exemplary xz-projection of the three dimensional organization of a pure F-actin network (left, magenta) and an Arp2/3 branched actin gel (right), labeled with ATTO 594 G-actin and obtained from CLSM z-stacks in solution. A/B2: Z-projection (xy-cross chapter) of the networks shown in (A/B1), summed over several fluorescence micrograph layers with a total height of 10 μm . Scale bars: 10 μm .

These networks were featured by an increased actin density in all three dimensions, which becomes particularly evident by the visual inspection of figure 4.10 B1, showing the xz-projection of a CLSM z-stack. Further, the z-projection of the Arp2/3 branched network, displayed in figure 4.10 B2, demonstrates not only a reduced actin filament length, but also a high interconnection within the branched actin network.

To gather information about the organization of branched actin filaments in membrane-bound cortices, Arp2/3-MACs were attached to ezrin decorated membranes for varied receptor lipid concentrations of 2-8 mol% PtdIns[4,5]P₂. Exemplary fluorescence micrographs of Arp2/3-MACs are displayed in figure 4.11 and compared to MACs without Arp2/3 branching. As illustrated, minimal actin cortices prepared from Arp2/3 branched actin filaments exhibit a decreased network density for low PtdIns[4,5]P₂ concentrations of 2-3 mol%, whereas a similar MAC density was observed with

increasing the PtdIns[4,5]P₂ content to 8 mol% (cf. figure 4.11). However, the low binding of Arp2/3 branched filaments, especially at $\chi(\text{PtdIns}[4,5]\text{P}_2) = 2 \text{ mol}\%$, enabled the imaging of individual filaments and their branches (cf. figure 4.11, left column, yellow box). While the increased network density of Arp2/3 branched MACs at $\chi(\text{PtdIns}[4,5]\text{P}_2) = 8 \text{ mol}\%$ impaired the observation of single filaments, the general actin network exhibited an altered morphology, showing a highly entangled network with no nematically aligned F-actin (cf. figure 4.11, right column, top and bottom).

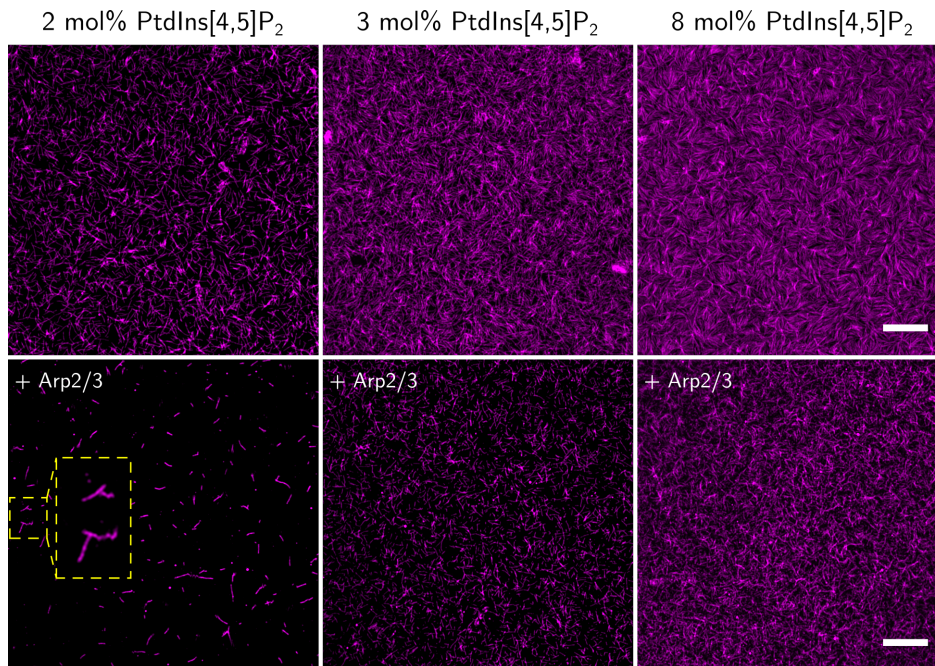


Figure 4.11: Exemplary fluorescence micrographs showing the binding of Arp2/3 branched and unbranched F-actin networks to SLBs containing 1-8 mol% PtdIns[4,5]P₂. The upper row displays the membrane binding of unbranched actin filaments (magenta), labeled with ATTO 594 G-actin, and the lower row represents the attachment of Arp2/3 branched actin networks to SLBs doped with 1-8 mol% PtdIns[4,5]P₂. Scale bars: 10 μm . For comparison unbranched actin networks were replotted from chapter 4.1.2.

To quantify the network density, fluorescence micrographs of membrane-bound Arp2/3 networks were tube-filtered, according to chapter 3.6.0.1, and skeletonized images were used for node- and sekeleton network density determination. Both parameters are displayed in figure 4.12 and compared to the data of unbranched networks, presented in chapter 4.1.2. The data confirm a significantly decreased network density of Arp2/3 branched MACs in the range of $\chi(\text{PtdIns}[4,5]\text{P}_2) = 2 - 5 \text{ mol}\%$, compared to pure F-actin networks. Simultaneously, the data indicate an in-

creased network density within the branched networks for increasing PtdIns[4,5]P₂ concentrations from 2-5 mol%. Furthermore, the equal skeleton network density of approximately 0.1 for both, Arp2/3 branched and unbranched MACs at $\chi(\text{PtdIns}[4,5]\text{P}_2) = 8 \text{ mol}\%$, suggest a comparable network density displayed in figure 4.11 (right panel, $\chi(\text{PtdIns}[4,5]\text{P}_2) = 8 \text{ mol}\%$). By contrast, the significantly larger node density of $1.26 \pm 0.36 \mu\text{m}^{-2}$ of the Arp2/3 networks ($\chi(\text{PtdIns}[4,5]\text{P}_2) = 8 \text{ mol}\%$) indicates an increased entanglement of the membrane-bound actin filaments, and with this an altered network morphology (cf. figure 4.12 A).

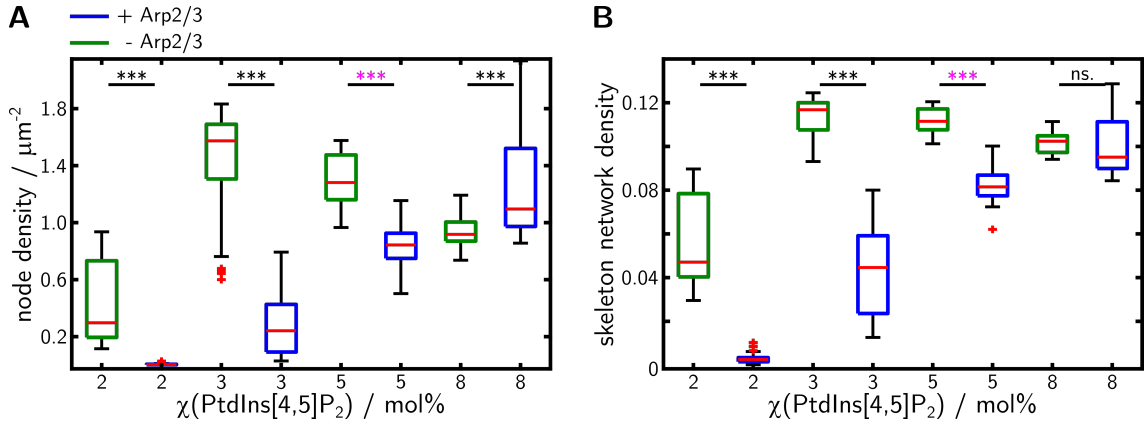


Figure 4.12: Box plots showing the actin network node and skeleton network density of branched and unbranched membrane-bound MACs as a function of the PtdIns[4,5]P₂ content. Comparison of the node density (A) and skeleton network density (B) of Arp2/3 branched (blue) and unbranched (green) membrane-bound MACs for 2-8 mol% PtdIns[4,5]P₂. For the analysis, n images of N preparations were evaluated. 2 mol% ($n = 60$, $N = 7$; $n = 23$, $N = 3$), 3 mol% ($n = 48$, $N = 5$; $n = 34$, $N = 4$), 5 mol% ($n = 40$, $N = 4$; $n = 20$, $N = 2$) and 8 mol% ($n = 20$, $N = 2$; $n = 31$, $N = 3$). Boxes ranging from 25th to 75th percentiles of the sample, while whiskers represent to the most extreme data points not considered outliers (red crosses). Medians are shown as red horizontals within the boxes. Statistical t -test: ***: $p \leq 0.001$, ns.: $p > 0.05$; Welch-test: ***: $p \leq 0.001$. For comparison unbranched actin data were replotted from chapter 4.1.2.

In order to confirm a modified organization of Arp2/3 branched networks, the mean nematic order parameter (q_{mean}) was determined for the membrane-bound MACs (cf. chapter 3.6.0.2). While the low q_{mean} of the Arp2/3 branched MACs at $\chi(\text{PtdIns}[4,5]\text{P}_2) = 2 \text{ mol}\%$ is originated by the non-existent actin networks, as only single filaments were attached to those membranes, the by a factor of ~ 0.7 decreased q_{mean} at $\chi(\text{PtdIns}[4,5]\text{P}_2) = 5-8 \text{ mol}\%$ indicated no significantly nematic alignment (cf. figure 4.13 A).

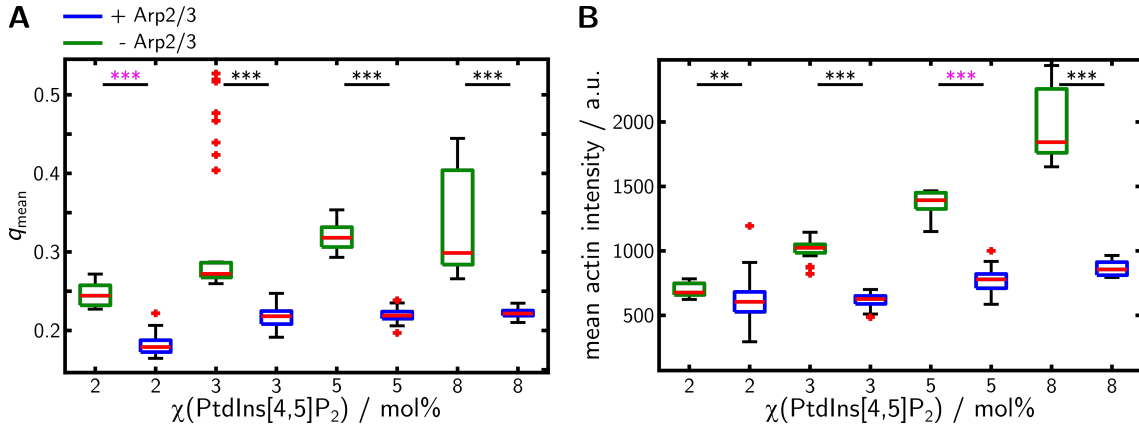


Figure 4.13: Box plot showing the mean nematic order parameter (q_{mean}) and the mean actin intensity of branched and unbranched membrane-bound MACs as a function of the PtdIns[4,5]P₂ content. Comparison of q_{mean} (A) and the mean actin intensity (B) of Arp2/3 branched (blue) and unbranched (green) membrane-bound MACs for 2-8 mol% PtdIns[4,5]P₂. For the analysis, n images of N preparations were evaluated. 2 mol% ($n_{q,\text{mean}} = 59$, $n = 60$, $N = 7$; $n_{q,\text{mean}} = 24$, $n = 23$, $N = 3$), 3 mol% ($n_{q,\text{mean}} = 51$, $n = 48$, $N = 5$; $n_{q,\text{mean}} = 39$, $n = 34$, $N = 4$), 5 mol% ($n_{q,\text{mean}} = 40$, $n = 40$, $N = 4$; $n_{q,\text{mean}} = 20$, $n = 20$, $N = 2$) and 8 mol% ($n_{q,\text{mean}} = 21$, $n = 20$, $N = 2$; $n_{q,\text{mean}} = 31$, $n = 31$, $N = 3$). Boxes ranging from 25th to 75th percentiles of the sample, while whiskers represent to the most extreme data points not considered outliers (red crosses). Medians are shown as red horizontals within the boxes. Statistical t -test: ***: $p \leq 0.001$, **: $p \leq 0.01$; Welch-test: ***: $p \leq 0.001$. For comparison unbranched actin data were replotted from chapter 4.1.2.

To gather further information about the single filament organization within the Arp2/3 networks, fluorescence micrographs of membrane-bound Arp2/3-MACs were analyzed by means of the skeleton-based actin intensity analysis, introduced in chapter 4.1.2. The determined averaged actin intensities, along the skeletonized actin filaments are displayed in figure 4.13 B, as a function of the receptor lipid content ($\chi(\text{PtdIns}[4,5]\text{P}_2)$). While the raising actin intensities without Arp2/3 branching (green), presented in chapter 4.1.2, suggest a growing bundling of membrane-bound actin filaments with raising PtdIns[4,5]P₂ content, the comparatively significantly reduced actin intensity for Arp2/3 branched networks (blue) indicate no bundle formation. In summary, the data demonstrate that for a PtdIns[4,5]P₂ content of 8 mol% Arp2/3 branched and unbranched MACs have similar skeleton network densities, yet exhibit different network organizations.

4.1.3.3 Influence of POPS on the minimal actin cortex architecture

Biological membranes, as the plasma membrane of mammalian cells, are known to have an asymmetric lipid distribution across their leaflets. While the extra cellular leaflet of eukaryotic cells mainly consists of phosphatidylcholine (PC) and sphingomyelin (SM), the cytoplasmic leaflet is rich in e.g. phosphatidylserine (PS) and phosphatidylinositols.^[162] Although, the interaction between the membrane-bound actin cortex and the plasma membrane is in general known to control the cell morphology, the direct interplay between the inner leaflet lipid composition and actin cortex organization is still poorly understood.^[8,10]

In order to investigate the effect of a lipid composition, mimicking the cytoplasmic leaflet on the minimal actin cortex architecture, SLBs were doped with 17 mol% POPS, resembling the amount of PS in the inner human plasma membrane (15-20 mol% PS).^[162] Reflectometric interference spectroscopy (RIfS) was used (cf. chapter 3.4.1) to study the binding of ezrin T567D to solid supported membranes. MACs were formed on hydrophilized glass substrates (cf. chapter 3.3.4.1) and CLSM experiments were conducted to examine the actin cortex organization after rinsing.

Since it is known from the literature, that the amount of membrane-bound ezrin T567D directly influences the minimal actin cortex organization, RIfS experiments were conducted to quantify the ezrin binding to POPC/POPS/PtdIns[4,5]P₂ SLBs.^[72] Figure 4.14 shows an exemplary RIfS experiment with the time profile of the measured ΔOT . The reference baseline, recorded during rinsing with spreading buffer (Na-citrate buffer, I), allows the verification of lipid bilayer formation ($\Delta(\Delta OT_{\text{SUV}}) \approx 6$ nm) after spreading SUVs (POPC/POPS/PtdIns[4,5]P₂, (78:17:5), II) and rinsing the system with spreading buffer (III), to remove excess lipid material. By rinsing subsequently with E1 buffer (IV), passivating membrane defects with BSA ($c_{\text{BSA}} = 1$ mg mL⁻¹, in E1 buffer, V) and removing excess passivation by washing with E1 buffer (VI) the system was prepared for the incubation with ezrin T567D. While the small increase in ΔOT during BSA incubation (V) indicates the unspecific adsorption of BSA to the SLBs, the followed decrease during rinsing with E1 buffer (VI) verifies no unspecific irreversible BSA binding to POPS containing membranes. After adding ezrin T567D (0.8 μ M, VII) the ΔOT increased, displaying the protein adsorption to the membrane. Rinsing with E1 buffer (VIII) leads to a decrease in ΔOT , as reversibly bound ezrin was washed off. The fraction of irreversible bound ezrin T567D ($\Delta(\Delta OT_{\text{ezrin}})$) was determined after reaching an equilibrium (VIII).

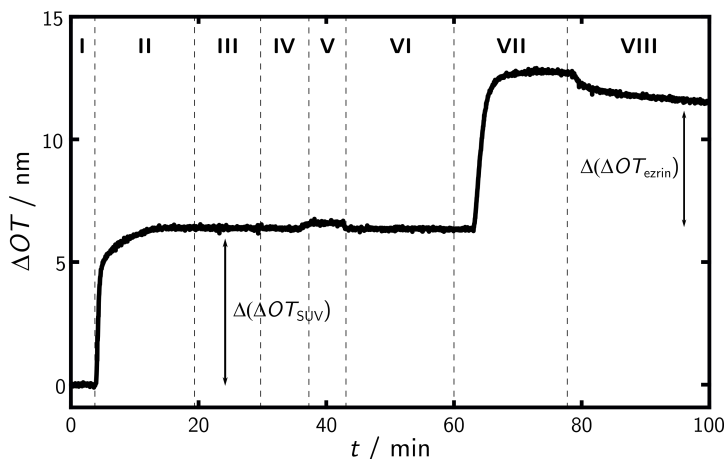


Figure 4.14: Exemplary RIfS measurement displaying the specific binding of ezrin T567D to a PtdIns[4,5]P₂ doped SLB. Recorded change in optical thickness (ΔOT) during a typical RIfS measurement started with establishing a baseline by rinsing the system with spreading buffer (**I**) followed by spreading SUVs (POPC/POPS/PtdIns[4,5]P₂, (78:17:5)) to a OT of ~ 6 nm (**II**). By flushing afterwards with spreading buffer (**III**) and E1 buffer (**IV**) excess lipid material was removed. Membrane defects were passivated by adding BSA ($c_{BSA} = 1$ mg mL⁻¹, **V**). Excess BSA was removed by rinsing with E1 buffer (**VI**), preparing the system for the incubation with ezrin T567D (0.8 μ M, **VII**). Reversibly bound protein was washed off by rinsing with E1 buffer (**VIII**), allowing the determination of irreversibly bound ezrin T567D ($\Delta(\Delta OT_{ezrin})$).

To exclude an unspecific interaction of ezrin T567D with the matrix lipid POPS, RIfS experiments with POPC/POPS SLBs (83:17) were conducted. The low mean $\Delta(\Delta OT_{ezrin})$ of 0.04 ± 0.06 nm ($n = 4$) determined for those membranes, lacking the receptor lipid PtdIns[4,5]P₂, indicated no unspecific binding of ezrin T567D to the matrix lipid POPS (cf. chapter A.4).

Subsequently the impact of the matrix lipid POPS on the amount of membrane-bound ezrin T567D was investigated for molar ratios of PtdIns[4,5]P₂ ranging from 1 - 8 mol%. The estimated $\Delta(\Delta OT_{ezrin})$ are summarized in figure 4.15 and compared to the results of NÖDING et al., for different PtdIns[4,5]P₂ concentrations in the absence of POPS (cf. figure 4.15, green).^[72] While the data of NÖDING et al., lacking POPS, shows a sigmoidal ezrin binding behavior with a slow increase from 0.08 ± 0.13 nm to 0.6 ± 0.08 nm between 1 - 3 mol% PtdIns[4,5]P₂ and a saturation at ~ 4.5 nm above 6 mol% PtdIns[4,5]P₂, the addition of 17 mol% POPS results in a generally increased amount of membrane-bound ezrin T567D.

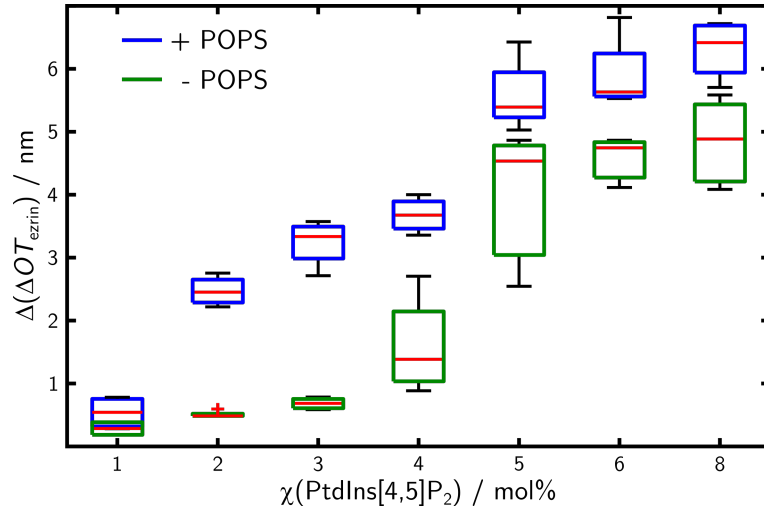


Figure 4.15: Box plot showing the change in optical thickness for ezrin T567D adsorption on SLBs depending on PtdIns[4,5]P₂ and POPS content. Change in optical thickness caused by irreversibly bound ezrin T567D ($\Delta(\Delta OT_{\text{ezrin}})$) on SLBs doped with (blue) or without (green) 17 mol% POPS as a function of the PtdIns[4,5]P₂ content ($\chi(\text{PtdIns}[4,5]\text{P}_2)$). Data from n individual experiments were analyzed. 1 mol% ($n=4$, $n=2$), 2 mol% ($n=4$, $n=5$), 3 mol% ($n=4$, $n=5$), 4 mol% ($n=4$, $n=4$), 5 mol% ($n=6$, $n=3$), 6 mol% ($n=4$, $n=3$) and 8 mol% ($n=4$, $n=7$). Boxes ranging from 25th to 75th percentiles of the sample, while whiskers represent to the most extreme data points not considered outliers (red crosses). Medians are shown as red horizontals within the boxes. For comparison data without POPS were taken from Nöding et al.^[72]

As displayed in figure 4.15, the observed increase in optical thickness is most prominent at low receptor lipid concentrations of 1-3 mol% PtdIns[4,5]P₂ with estimated $\Delta(\Delta OT_{\text{ezrin}})$ from 0.45 ± 0.25 nm to 3.15 ± 0.37 nm and an up to 5-fold increased ezrin T567D adsorption, compared to the POPS free system. In contrast to the data of NÖDING et al. the amount of ezrin bound to POPS doped membranes depends linearly on PtdIns[4,5]P₂ content (up to 5.48 ± 0.52 nm at 5 mol% PtdIns[4,5]P₂). Above $\chi(\text{PtdIns}[4,5]\text{P}_2) = 5$ mol%, the amount of bound ezrin appears to saturate, which is however not reached at the highest tested PtdIns[4,5]P₂ concentration of 8 mol%.

As the RIFs measurements showed for low PtdIns[4,5]P₂ concentrations from 1-3 mol% the most pronounced effect of POPS upon the amount of membrane-bound ezrin, this lipid compositions were further employed to address the question how pre-polymerized F-actin organize on the membranes. In figure 4.16 exemplary fluorescence micrographs of membrane-bound minimal actin cortices on POPS doped membranes with 1-3 mol% PtdIns[4,5]P₂ (bottom row) are compared to actin networks attached to membranes with the same PtdIns[4,5]P₂ content, but lacking POPS (top row,

replotted from chapter 4.1.2). As the visual inspection clearly demonstrates, the overall filament density is strongly increased for POPS containing membranes. While in absence of POPS the amount of membrane-bound F-actin increases from single filaments at 1 mol% to an entangled network at 3 mol% PtdIns[4,5]P₂, in the presence of POPS an entangled network is already evident at 1 mol% which further densifies up to 3 mol% PtdIns[4,5]P₂. A significant unspecific interaction of F-actin and POPS could be excluded by control experiments, which showed only a minimal non-reproducible F-actin adsorption to POPS-membranes lacking PtdIns[4,5]P₂ (data not shown).

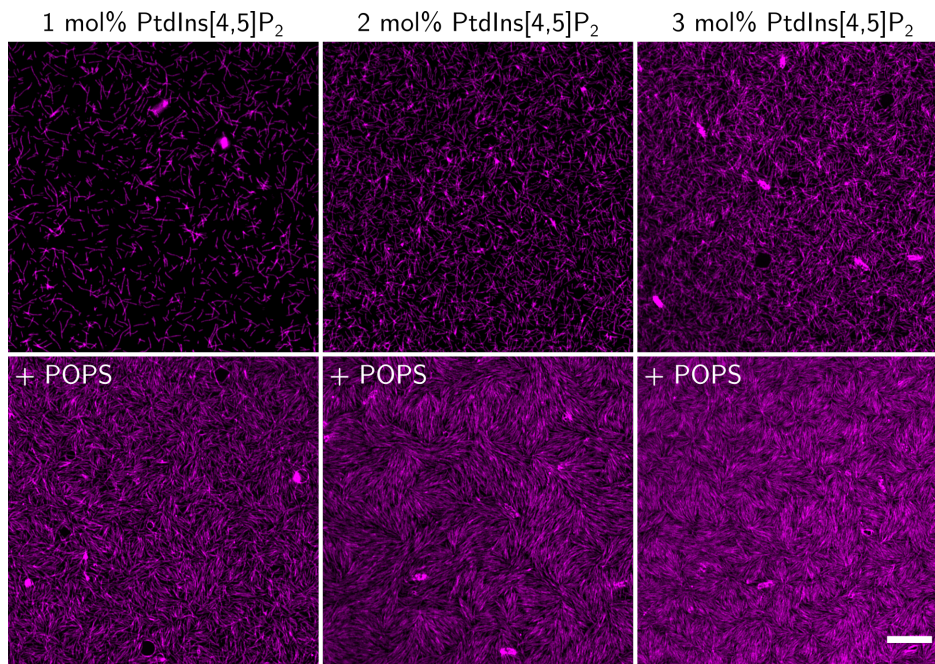


Figure 4.16: Exemplary fluorescence micrographs showing the F-actin binding to SLBs containing 1 - 3 mol% PtdIns[4,5]P₂ depending on POPS content. The upper row representatively shows F-actin (magenta), labeled with ATTO 594-G-actin, bound to POPS free and the lower row to POPS containing SLBs doped with 1-3 mol% PtdIns[4,5]P₂. Scale bar: 10 μ m. For comparison data without POPS were replotted from chapter 4.1.2.

Beside the enhanced network density, the fluorescence micrographs in figure 4.16 also show a modified organization of the membrane-bound MACs dependent on the POPS content. While F-actin bound to POPS free membranes forms entangled networks for a PtdIns[4,5]P₂ content of 1 - 3 mol%, the actin on POPS containing membranes, with the same PtdIns[4,5]P₂ content, tend to align into local nematic domains. This observation was quantified by calculating q_{mean} , according to SEARA et al. (cf. chapter 3.6.0.2), as shown in figure 4.17 A. The determined averaged nematic order

parameters clearly indicate that in the absence of POPS (cf. figure 4.17 A, green) no significant nematic order increase can be observed. By contrast, the direct comparison reveals for each tested PtdIns[4,5]P₂ concentration an increased nematic order on POPS containing membranes and shows overall an increased q_{mean} from 0.26 ± 0.04 at 1 mol% to 0.38 ± 0.08 at 3 mol% PtdIns[4,5]P₂ (cf. figure 4.17 A, blue).

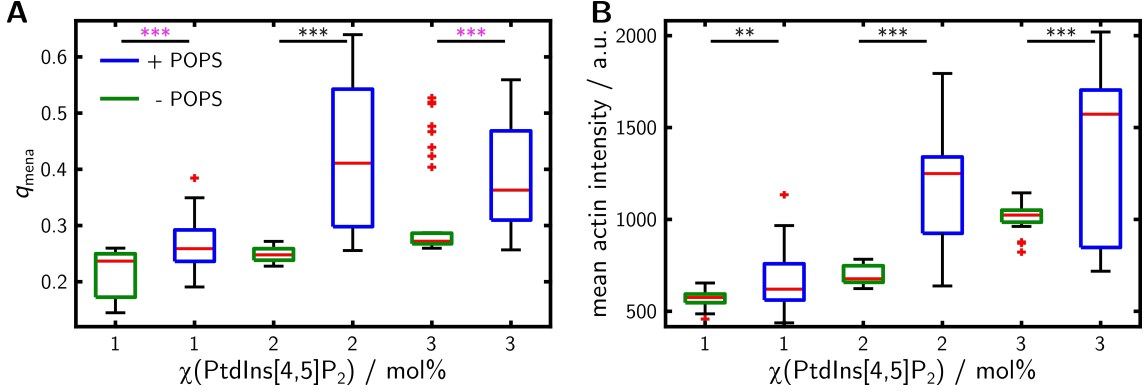


Figure 4.17: Box plot showing the mean nematic order parameter (q_{mean}) and the mean actin intensity of membrane-bound MACs depending on PtdIns[4,5]P₂ and POPS content. Comparison of q_{mean} (A) and the skeleton based mean actin intensity (B) between SLBs doped with (blue) and without POPS (green) for 1-3 mol% PtdIns[4,5]P₂. For the analysis, n images of N preparations were evaluated. 1 mol% ($n_{\text{q,mean}} = 37$, $n = 34$, $N = 4$; $n_{\text{q,mean}} = 30$, $n = 30$, $N = 4$), 2 mol% ($n_{\text{q,mean}} = 52$, $n = 60$, $N = 6$; $n_{\text{q,mean}} = 24$, $n = 23$, $N = 3$), 3 mol% ($n_{\text{q,mean}} = 56$, $n = 40$, $N = 6$; $n_{\text{q,mean}} = 39$, $n = 34$, $N = 4$). Boxes ranging from 25th to 75th percentiles of the sample, while whiskers represent to the most extreme data points not considered outliers (red crosses). Medians are shown as red horizontals within the boxes. Statistical t -test: ***: $p \leq 0.001$, **: $p \leq 0.01$; *Welch*-test: ***: $p \leq 0.001$. For comparison data without POPS were replotted from chapter 4.1.2.

To relate the calculated q_{mean} to the network density and single filament structure, the fluorescence micrographs were applied to the "tube filter" analysis (cf. chapter 3.6.0.1).

According to chapter 4.1.2 (cf. figure 4.6), the skeletonized images were first used to estimate the membrane-bound actin filament structure by means of the skeleton based actin intensity determination. The calculated mean F-actin intensities of the respective lipid compositions are displayed in figure 4.17 B. Both systems, with and without POPS, generally show an increased mean F-actin intensity for raising PtdIns[4,5]P₂ concentrations, indicating the formation of filament bundles. While the mean F-actin intensity on POPS free membranes increases gradually from 568 ± 44 a.u. at 1 mol% to 1014 ± 71 a.u. at 3 mol% PtdIns[4,5]P₂, the enhancement for POPS containing membranes from 655 ± 159 a.u. at 1 mol% to 1332 ± 443 a.u. at 3 mol% PtdIns[4,5]P₂ is significantly pronounced. These findings suggest, that the formation

of membrane-bound F-actin bundles is a function of the PtdIns[4,5]P₂ concentration. In addition, the formation of filament bundles appears to be a characteristic of nematicallly organized MACs, as both rise analogously.

The network density of membrane-bound MACs was quantified by calculating the node- and sekeleton network density from the tube-filtered fluorescence micrographs (cf. chapter 3.6.0.1). As show in figure 4.18 A-B, both parameters reflect the observed increased network density with increasing PtdIns[4,5]P₂ in the presence or absence of POPS (cf. figure 4.16).

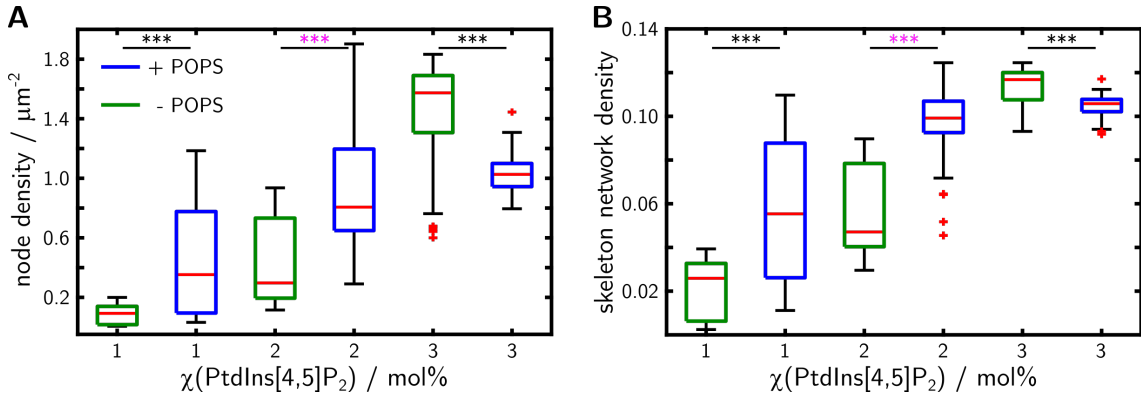


Figure 4.18: Box plots showing the actin network node and skeleton network density of membrane-bound MACs depending on PtdIns[4,5]P₂ and POPS content. Comparison of actin network node density (A) and skeleton network density (B) between SLBs doped with (blue) and without POPS (green) for 1-3 mol% PtdIns[4,5]P₂. For the analysis, n images of N preparations were evaluated. 1 mol% ($n = 34$, $N = 4$; $n = 30$, $N = 4$), 2 mol% ($n = 60$, $N = 6$; $n = 23$, $N = 3$), 3 mol% ($n = 40$, $N = 6$; $n = 34$, $N = 4$). Boxes ranging from 25th to 75th percentiles of the sample, while whiskers represent to the most extreme data points not considered outliers (red crosses). Medians are shown as red horizontals within the boxes. Statistical t -test: ***: $p \leq 0.001$; Welch-test: ***: $p \leq 0.001$. For comparison data without POPS were replotted from chapter 4.1.2.

In absence of POPS, the calculated node density (cf. figure 4.18 A, green) reflects the increasing network density of entangled actin filaments, as projected in figure 4.16 (top row), raising from $0.08 \pm 0.06 \mu\text{m}^{-2}$ ($\chi(\text{PtdIns}[4,5]\text{P}_2) = 1 \text{ mol}\%$) to $1.43 \pm 0.39 \mu\text{m}^{-2}$ ($\chi(\text{PtdIns}[4,5]\text{P}_2) = 3 \text{ mol}\%$). As a result of the formation of nematic domains and the parallel F-actin organization, the node density shows a different behavior in the presence of POPS. While a five fold increase in node density is found at 1 mol% PtdIns[4,5]P₂ ($0.44 \pm 0.38 \mu\text{m}^{-2}$), only a tow fold increase was detected for 2 mol% ($0.90 \pm 0.59 \mu\text{m}^{-2}$) and a 0.7 fold decrease at 3 mol% ($1.04 \pm 0.13 \mu\text{m}^{-2}$, cf figure 4.18 A, blue).

Since the skeleton network density is calculated via the ratio of filamentous to

background pixels, the analysis is independent of the formation of nematic domains. However, the skeleton network density reflects the increasing network density in the same manner as the node density, showing a 2.8 fold increase at 1 mol%, a 1.7 fold one at 2 mol% and a 0.9 fold decrease at 3 mol% PtdIns[4,5]P₂. Nevertheless, this behavior must be considered in relation to the increased bundling of membrane-bound F-actin, as indicated in figure 4.17 B for POPS containing membranes.

4.2 Dynamics of membrane-bound minimal actomyosin cortices

The cellular actin cortex is strongly associated with the motor protein myosin II, forming an actomyosin cortex.^[10,70] Several myosin II hexamers can align tail-to-tail via electrostatic interactions in a parallel and anti-parallel manner, forming bipolar myofilaments with several motor domains on each filament end.^[50–52] *In vivo*, this actomyosin cortex is capable of generating contractile stress, enabling cortex reorganization and controlling cell migration.^[163–165]

In the recent past, membrane-bound minimal actin cortices have been successfully used to study the fundamental actin-myosin interactions *in vitro*. These works contributed to an improved understanding on the single actomyosin filament level, revealed the reciprocal influence of cortex and membrane or demonstrated the direct impact of myosin II on the actin cortex contractility.^[69–71] Further, it was shown that a membrane attachment modulates the actomyosin contractility.^[166]

The present work addresses for the first time how a biomimetic membrane-attachment via ezrin T567D impacts the minimal actin cortex reorganization by myosin II.

4.2.1 Single filament motion in actomyosin networks

The contraction of the cellular actomyosin cortex is an active process, fueled by the hydrolysis of ATP through the ATPase activity of the myosin II motor domains.^[52,167] In order to verify whether the reorganization of membrane-bound actin filaments in the minimal actin cortices is an active motion, induced by myosin II, single actin filament tracking experiments were conducted.

Membrane-bound minimal actin cortices were prepared on hydrophilized glass substrates, following the detailed instructions in chapter 3.3.4.1. Since the motion of individual actin filaments needed to be observed, labeled and unlabeled actin filaments were mixed in a ratio of 1:5 and applied to POPC/PtdIns[4,5]P₂/ATTO390-DPPE (96.6:3:0.4) membranes with a medium PtdIns[4,5]P₂ content of 3 mol%. The reorganization of ATTO 594-labeled actin filaments (cf. chapter 3.3.3) was induced by the addition of pre-assembled bipolar myosin II, as described in chapter 3.3.5. Dual color fluorescence micrographs were recorded by means of TIRF microscopy at

a frame interval of 400 ms, enabling the tracing of moving actin filaments (cf. figure 4.19 A).

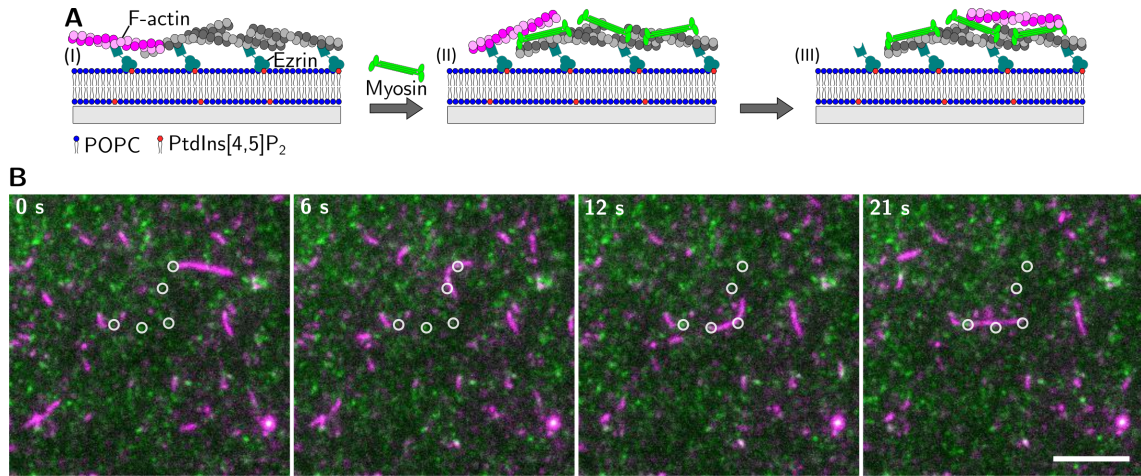


Figure 4.19: Exemplary time series displaying single actin filament motion in dependence of the myosin II clusters. **A:** Schematic illustration of the myosin II induced motion of membrane attached single actin filament (magenta) within an unlabeled actin network (gray). (I) Minimal actin cortex prior to the addition of bipolar myosin II filaments, (II) starting single filament motion (III) and finale filament dwelling. **B:** Exemplary overlay of the actin (magenta) and myosin II (green) channels, showing the time dependent motion (0-21 s) of F-actin along myosin II clusters (white circles) bound within the membrane attached F-actin network. Scale bar: 5 μm .

As displayed by the overlay of the F-actin (magenta) and myosin II (green) channels in figure 4.19 B, single actin filaments were propelled along small myosin II clusters (white circles), which seemed to stuck within the unlabeled MAC. To gather information about the filament motion, individual actin filaments were tracked via the ImageJ plugin *Jfilament* (2D).^[168,169] An exemplary filament tracking is shown in figure 4.20, with the tracked filament highlighted in blue and the recorded filament tip trajectory shown in yellow. Since actin filaments tend to dwell at various positions during their motion, only the active parts in between start and dwelling were used for further calculations, which are referred to as active trajectory sections in the following.

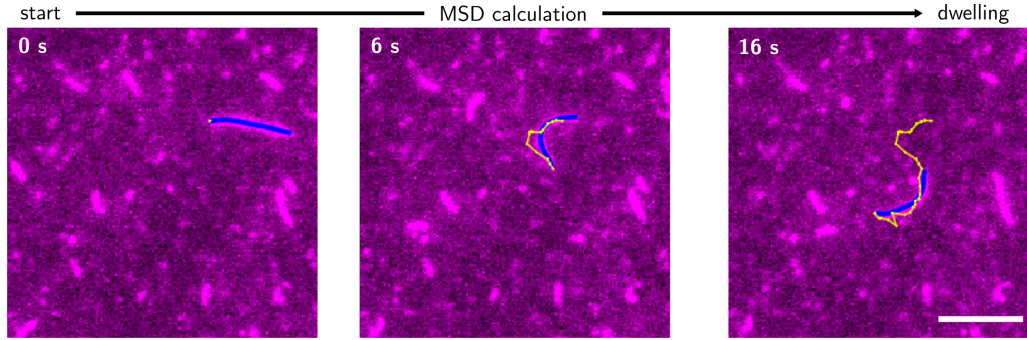


Figure 4.20: Exemplary time series showing single actin filament tracking during myosin II induced motion. Exemplary fluorescence micrographs, mapping the time-dependent active trajectory section (yellow, start-dwelling) of a tracked single actin filament (blue). Scale bar: 5 μm .

In order to quantify the tracked actin reorganization as directed motion, the active trajectory sections of filaments tracked for a minimum duration of 10 frames were used to calculate the mean squared displacement (MSD). MSD calculation was performed according to equation 4.1, using a custom written MATLAB routine,

$$\text{MSD}(\tau) = \left\langle \frac{1}{k} \sum_{i=1}^k |r(t + \tau) - r(t)|^2 \right\rangle \quad (4.1)$$

with $r(t)$ being the filament tip position at a certain time t , the lag time (τ) between two positions and the total amount of positions k over the $\text{MSD}(\tau)$. An exemplary MSD of the filament trajectory shown in figure 4.20 is displayed in the figure 4.21 A (blue dashed line).

$$\text{MSD}(\tau) = a x^\alpha + b \quad (4.2)$$

To determine the motion behavior, the MSD data were fitted with the equation 4.2 (cf. figure 4.21 A, red line), enabling the extraction of the exponent α . Since a directed active movement, also known as superdiffusion, is characterized by $\alpha > 1$, the exponent provides quantitative access to the motion mode.^[170,171]

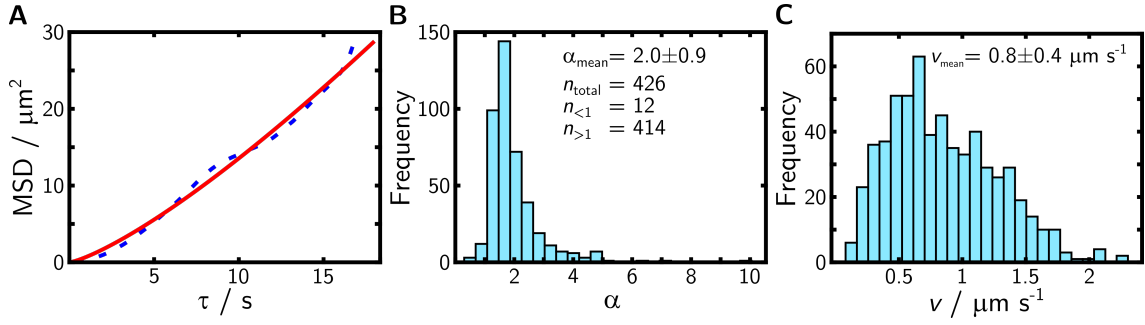


Figure 4.21: Exemplary mean squared displacement and quantitative motion evaluation of membrane-bound single actin filaments. **A:** Exemplary mean squared displacement (MSD) was extracted from the actin filament trajectory shown in figure 4.20 (blue, dashed line) and fitted according to equation 4.2 (red, solid line). **B:** Histogram of the exponent (α), extracted from active trajectory sections of moving filaments tracked longer than 10 frames ($n_{\text{total}} = 426$, $N = 2$). **C:** Histogram of the actin filament velocity (v) extracted from the time-dependent displacement of all active filaments ($n = 607$, $N = 2$).

The distribution of the calculated exponents, is summarized by the histogram shown in figure 4.21 B, with an averaged $\alpha = 2.0 \pm 0.9$ ($n_{\text{MSD}} = 426$ filaments, $N = 2$). Out of all tracked filaments, exhibiting an active trajectory section larger than 10 frames, 414 showed $\alpha > 1$ ($n_{>1}$) and only 12 $\alpha < 1$ ($n_{<1}$), strongly indicating an active motion. The velocity of tracked filaments was calculated by averaging the filament displacement in their active trajectory sections. The velocity distribution of all tracked filaments is displayed in the histogram in figure 4.21 C, showing a mean velocity of $v_{\text{mean}} = 0.8 \pm 0.4 \mu\text{m s}^{-1}$ ($n = 607$, $N = 2$).

4.2.2 Contractility of membrane-bound actomyosin networks

To quantify how myosin II motors reorganize physiological membrane-bound F-actin networks as a function of the lipid composition, minimal actin cortices were formed on POPC/PtdIns[4,5]P₂ and POPC/POPS/PtdIns[4,5]P₂ bilayers doped with 0.4 mol% ATTO390-DPPE. By comparing the MAC contractility between both lipid compositions, the effect of the inner plasma membrane lipid POPS was investigated in terms of the actomyosin dynamics.

The reorganization of membrane-bound MACs, prepared according to chapter 3.3.4.1 on glass substrates, was conducted as described in chapter 3.3.5, by the addition of pre-formed bipolar myofilaments (cf. figure 4.22 A). Dual color fluorescence micrographs were recorded via TIRF microscopy, enabling sample imaging at a high temporal and spatial resolution (cf. chapter 3.5.1.4).

The exemplary time series in figure 4.22 B/C display the generally observed reorganization of minimal actin cortices (magenta) in the absence (B) or presence (C) of 17 mol% POPS, after the addition of ATP and myosin II (green). In both cases, the addition of bipolar myosin II filaments led to a fast myosin binding within several seconds (figure 4.22 B/C +20 s). While the formation of myosin II clusters (figure 4.22 B/C +60-600 s) was observed in both systems, an extensive reorganization of the membrane-bound F-actin networks was mainly observed for MACs on POPS containing membranes (cf. figure 4.22 C). The reorganization led to a fast local clustering of actin filaments with dense myosin II centers, which are designated as actomyosin asters (cf. figure 4.22 C +20-600 s). The aster formation was associated with a loss of actin intensity, around the formed asters, indicating a network collapse. In contrast, in the absence of POPS, membrane-bound MAC showed predominantly no large scale reorganization respectively aster formation, implying no network collapse (cf. figure 4.22 B). Nevertheless, in non-contractual networks single filament motion could be monitored, as described in chapter 4.2.1. However, due to the high amount of membrane-bound F-actin, it was not possible to analyze this motion, as tracking of the individual actin filaments was not possible.

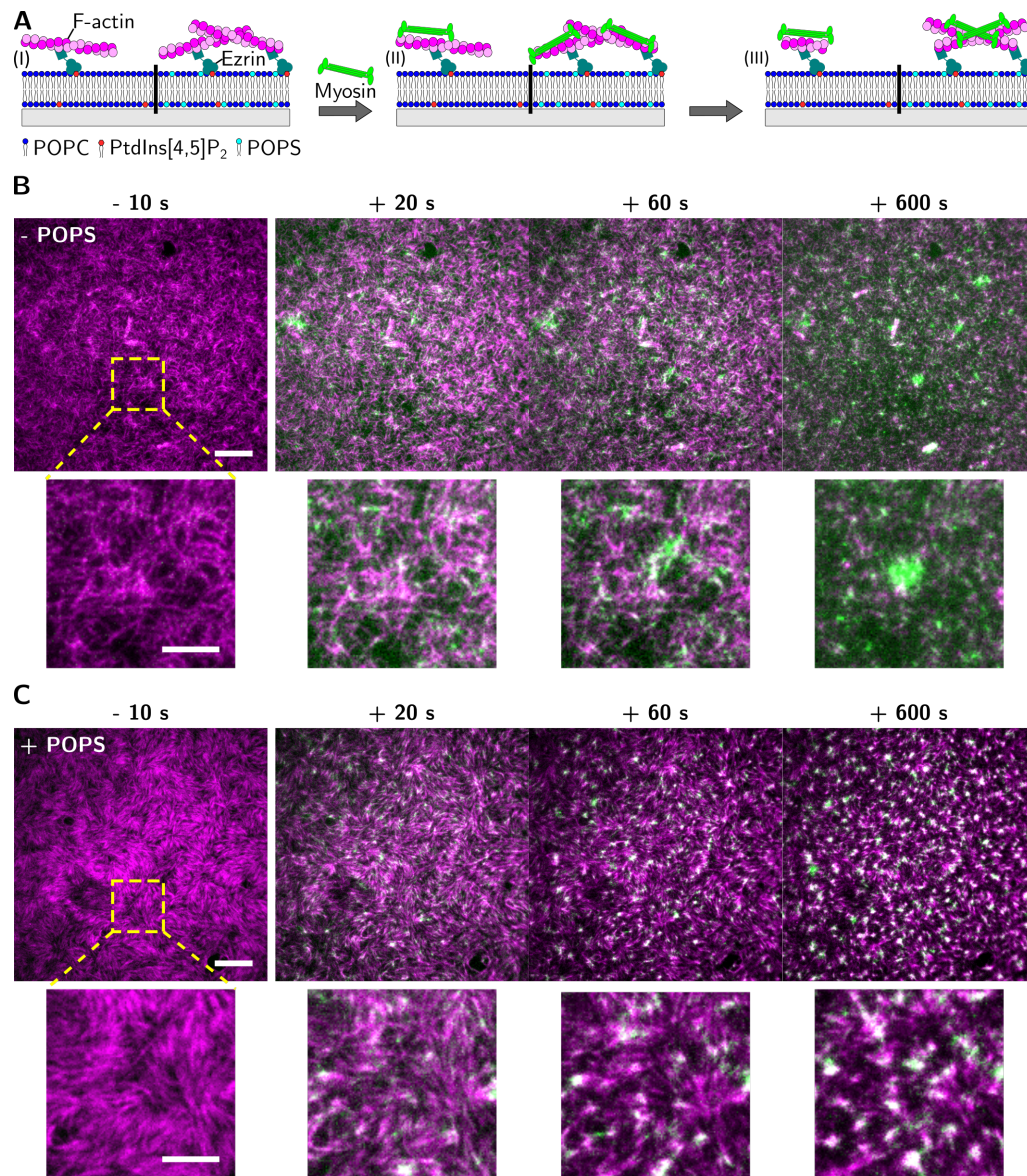


Figure 4.22: Exemplary time series displaying the myosin II induced reorganization of membrane-bound minimal actin cortices as a function of the POPS content. **A:** Schematic illustration of the myosin II induced reorganization of membrane attached MACs in the absence (left) and presence of POPS (right). (I) Minimal actin cortex prior to the addition of bipolar myosin II filaments, (II) during myosin II binding and (III) after reorganization. **B/C:** Exemplary fluorescence micrographs of SLB ($\chi(\text{PtdIns}[4,5]\text{P}_2) = 3 \text{ mol}\%$) attached F-actin networks (magenta) in the absence (B) and presence of POPS (C), prior (-10 s) and after (+20-600 s) the addition of bipolar myosin II filaments (light green). Scale bars: 5 and 10 μm .

To analyze the observed myosin II binding, the time-dependent normalized averaged fluorescence intensity of myosin II was investigated. As displayed in figure 4.23 A (dotted lines), the myosin II intensity showed a similar increase within both systems.

Parallel, the normalized averaged actin intensity (cf. figure 4.23 A, blue and green solid lines) decreases within the same time, independent of the membrane composition. As exemplary displayed by the black solid line in figure 4.23 A, the decrease was partly overlaid by actin bleaching, which becomes more significant at longer time scales (cf. figure 4.22 B, +60-600 s). Combined with the decreasing actin intensity, selected experiments revealed a shortening of the membrane-bound actin filaments. Since the binding of myosin to membrane-bound F-actin have been shown to cause F-actin buckling and breaking, the decreased actin intensity might provide insight into the principal reorganization mechanism.^[69,70]

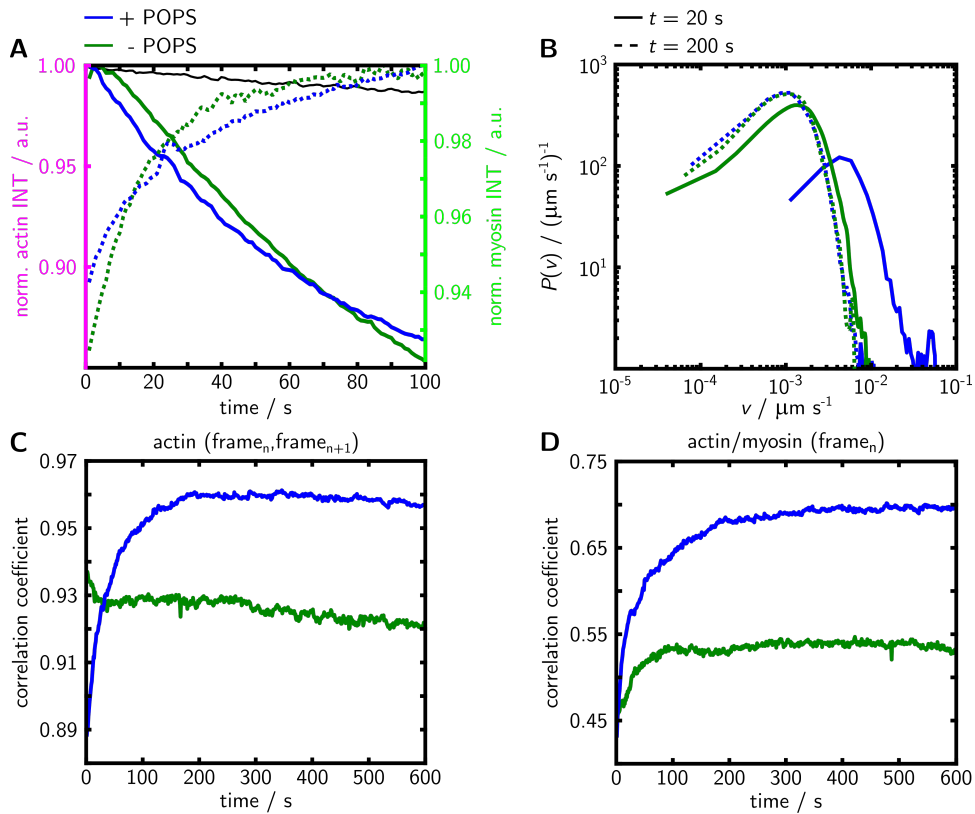


Figure 4.23: Exemplary quantification of the myosin II induced reorganization of the membrane-bound MACs shown in figure 4.22 B. **A:** Time-dependent normalized intensity profiles of the actin (solid line) and myosin II (dotted line) fluorescence within the first 100 s after myosin II binding, compared to the overlaid actin-bleaching (black line). **B:** Velocity magnitude probability distribution of the F-actin network reorganization 20 s (solid line) and 200 s (dotted line) after myosin binding. **C:** Time-dependent evolution of the 2D cross correlation coefficient of the F-actin fluorescence intensity from each frame (frame_n) to the following one (frame_{n+1}) and **(D)** of the F-actin/myosin II fluorescence intensity with the same frame.

In order to study and compare the contractile F-actin activity, the exemplary time series in figure 4.22 B/C were analyzed by means of particle image velocimetry (PIV) using the MATLAB based *PIVlab* from THIELICKE and SONNTAG (cf. chapter A.5).^[172] Comparing the F-actin velocity magnitude probability distribution at $t = 20$ s (solid line) and $t = 200$ s (dashed line) after the binding of myosin II, reveals that contractile networks exhibits higher F-actin velocities during the incipient reorganization (cf. figure 4.23 B, blue line, 20 s) than non-contractile networks (green line, 20 s). Furthermore, the significantly decreased F-actin velocity from 20-200 s, similar to the velocity distribution of non-contractile networks after 20 s respectively 200 s, indicate a completed network reorganization, which is in a good agreement with the visual inspection of the time series in figure 4.22 B/C.

Fundamental differences between collapsing and non-collapsing actomyosin networks were identified by means of image cross-correlation. The actin fluorescence signal of each frame (frame_n) was position wise correlated to the following frame (frame_{n+1}), as shown in figure 4.23 C. For the non-collapsing MAC attached to the POPS-free membrane, shown in the time series in figure 4.22 B, the correlation coefficient drops slightly in the beginning to ~ 0.93 and stabilizes afterwards (cf. figure 4.23 C, green line). This indicates no network reorganization into actin asters, as the F-actin co-localization is not increasing over time. In contrast, the correlation coefficient of the collapsing network, shown in the time series in figure 4.22 C, increases from 0.89 to approximately 0.96, within 200 s (cf. figure 4.23 C, blue line). Combined with the raising correlation coefficient of the actin and myosin fluorescence signal from 0.45 to 0.68 within the same frame (frame_n), shown in figure 4.23 D, the data suggest the formation of actomyosin asters. However, as the correlation coefficient of the actin fluorescence signal ($\text{frame}_n/\text{frame}_{n+1}$) do not increase for the non-collapsing network, the increasing actin/myosin coefficient suggest only the binding of myosin II to actin filaments.

Beside the two extremes of collapsing (cf. figure 4.24, right, cyan) and non-collapsing (cf. figure 4.24, left, green) networks, a third version of contraction was observed, which is referred to as partial collapse (cf. figure 4.24, center). Partial collapsing networks were characterized by a local formation of actomyosin asters (cf. figure 4.24, center, yellow), while other substrate regions showed no contraction (cf. figure 4.24, center, blue).

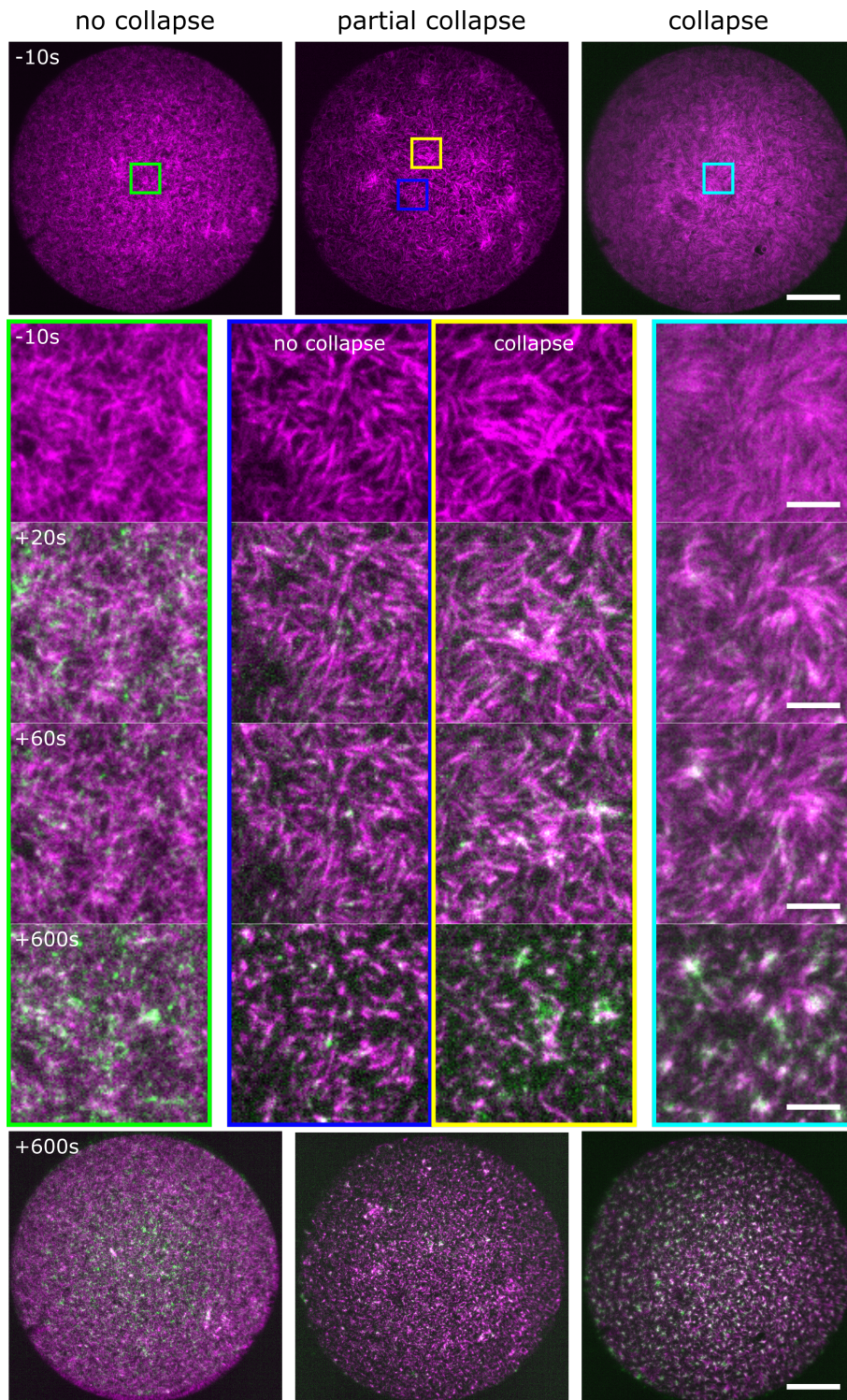


Figure 4.24: Comparison of the three general types of network contraction, observed in membrane-bound MACs. Exemplary time series showing the reorganization of membrane-bound F-actin networks (magenta) by myosin II (light green) for no collapsing (left), partial collapsing (center) and fully collapsing networks (right). Membrane composition: POPC/PtdIns[4,5]P₂/ATTO390-DPPE (96.6:3:0.4, left); POPC/PtdIns[4,5]P₂/POPS/ATTO390-DPPE (79.6:3:17:0.4, center-right). Scale bars: 5 and 20 μm .

This membrane composition independent classification is reflected by the mean probability distribution of the velocity magnitude, shown in figure 4.25. As depicted, the mean velocity magnitude probability distribution 20 s after myosin binding (solid lines) directly correlate with the contraction classification, showing a shift towards lower velocities with decreasing network contractility. Further, as the non collapsing networks (black, solid line) shows a similar distribution of mean velocity magnitude as the collapsing/partial collapsing networks 200 s (dashed line) after myosin II binding, these findings indicate a completed network contraction throughout the networks.

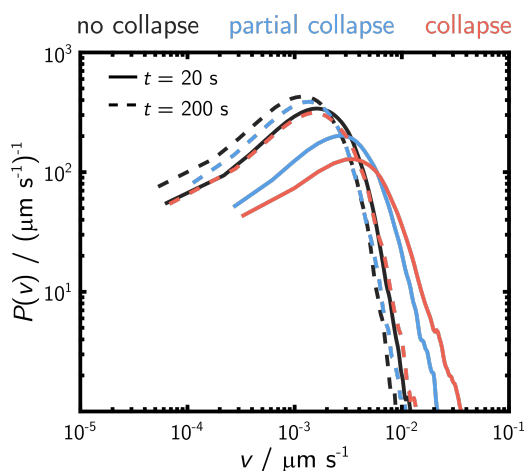


Figure 4.25: Comparison of the contraction type dependent mean F-actin velocity magnitude probability distribution. F-actin network mean velocity magnitude probability distribution 20 s (solid line, active state) and 200 s (dashed line, passive state) after myosin II binding for all non collapsing ($n = 19$), partial collapsing ($n = 8$) and full collapsing ($n = 10$) MACs, independent of the SLB composition. The probability distribution was averaged over n experiments. Time series were analyzed by means of PIV (cf. chapter A.5).

In total the myosin II induced reorganization of membrane attached MACs was investigated in the absence of POPS for a receptor lipid content ranging from 1-8 mol% and in presence of 17 mol% POPS for 1-3 mol% PtdIns[4,5]P₂, mimicking the inner plasma membrane composition (cf. chapter 4.1.3.3). Since MACs attached to membranes without POPS and a receptor lipid content of 1 mol% PtdIns[4,5]P₂, were composed of single isolated actin filaments (cf. figure 4.16), the data were not considered in terms of network contractility. The classification of the individual experiments dependent on the observed reorganization is shown in figure 4.26 A.

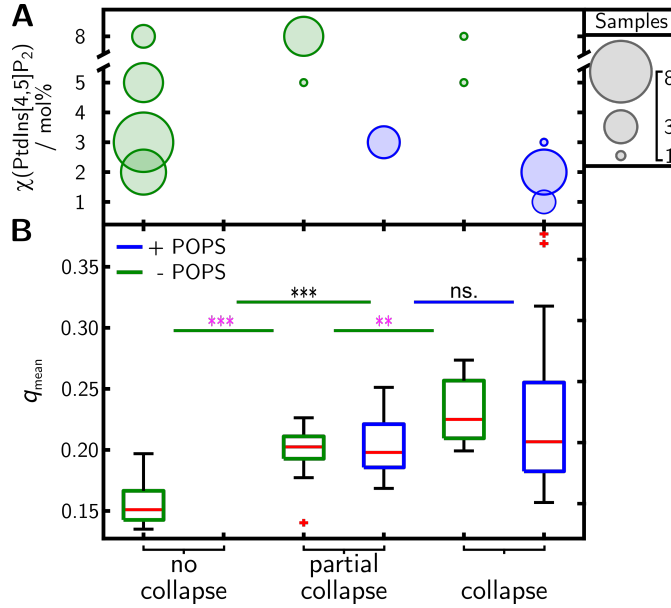


Figure 4.26: Dependence of actomyosin contractility upon the F-actin network architecture and lipid membrane composition. Dependence of the F-actin network architecture and lipid membrane composition on the myosin II induced reorganization. **A:** Specimen distribution dependent on the membrane composition with (blue) or without 17 mol% POPS (green), as function of the PtdIns[4,5]P₂ concentration and the observed actomyosin contraction. **B:** Averaged mean nematic order parameter (q_{mean}) of F-actin networks attached to SLBs doped with (blue) or without 17 mol% POPS (green), prior to myosin II addition, as a function of the observed actomyosin reorganization. For the analysis n images with N preparations were used. No collaps ($n = 55$, $N = 19$), partial collaps ($n = 20$, $N = 5$; $n = 12$, $N = 3$) and full collaps ($n = 9$, $N = 2$; $n = 33$, $N = 8$). Boxes ranging from 25th to 75th percentiles of the sample, while whiskers represent to the most extreme data points not considered outliers (red crosses). Medians are shown as red horizontals within the boxes. Statistical t -test: ***: $p \leq 0.001$, ns.: $p > 0.05$; Welch-test: ***: $p \leq 0.001$, **: $p \leq 0.01$.

As displayed, MACs attached to membranes lacking POPS (green) and doped with a low PtdIns[4,5]P₂ concentration of 2-3 mol% showed in all measurements no network contraction. For an increased PtdIns[4,5]P₂ content of 5-8 mol% a partial and full network collapse could be monitored, however, only in a few cases. In contrast, MACs bound to membranes with 17 mol% POPS and a PtdIns[4,5]P₂ content of 1-2 mol% showed in all experiments a full network collapse and for $\chi(\text{PtdIns}[4,5]\text{P}_2) = 3$ mol% at least a partial collapse. Determining the nematic order parameter q_{mean} of the classified measurements displayed in figure 4.26 A, prior to the addition of myosin II, revealed a dependence of the observed network contraction on the MAC architecture. For the cases, where no contraction could be observed, the F-actin networks exhibit a low q_{mean} of 0.15 ± 0.02 . In case of networks attached to POPS-free membranes,

the q_{mean} significantly increases from partial (0.20 ± 0.02) to full collapsing networks (0.23 ± 0.03). In the presence of POPS, similar q_{mean} values were obtained for partially and fully collapsing networks, showing no significant difference. Since the fluorescence micrographs of the present chapter were obtained via TIRF microscopy, a direct comparison with the q_{mean} values of the previous chapters is impaired, as the utilized Airyscan-CLSM setup provides a higher spatial resolution.

4.3 Mechanical properties of membrane-bound minimal actin cortices

The cellular actin cortex is directly linked to the inner leaflet of the plasma membrane of mammalian cells and is a key player in cell shape controlling.^[10,173] While several *in vivo* and *in vitro* studies investigated the role of the actin cortex in context of the cell mechanics, the direct impact of the membrane-cortex linkage via ERM proteins is still not fully resolved as the complex cellular framework of cross-linkers^[174,175] and motor proteins^[135,176] has been shown to contribute to the cellular mechanical properties.

In order to reveal how the membrane-attachment of a biomimetic minimal actin cortex alters the mechanical properties of the underlying lipid bilayer, pore-spanning membranes (PSMs) with ezrin-PtdIns[4,5]P₂ linked F-actin networks were established and probed via AFM-indentation experiments. For this purpose GUVs (DPhPC/PtdIns[4,5]P₂/ATTO390-DPPE (91.6:8:0.4)) were prepared as described in chapter 3.3.1.2 and spreaded on SiO_x functionalized porous substrates ($\varnothing = 5 \mu\text{m}$) to generate PSMs (cf. chapter 3.3.2.2). Minimal actin cortices were attached via the biomimetic ezrin-PtdIns[4,5]P₂ linkage as specified in chapter 3.3.4.2. AFM-CLSM correlation experiments were conducted to relate the recorded MAC organization to the determined mechanical properties (cf. chapter 3.5.2.4).

In the following, only the data for a successful MAC attachment to the freestanding PSMs (f-PSMs) are presented. An overview of all tested substrates, functionalizations, and lipid mixtures is given in chapter A.6.3.

The fluorescence micrographs in figure 4.27 A1-2, show typical PSMs with the freestanding parts (f-PSMs) identified as bright circles (light gray) and solid-supported areas (s-PSMs) with a reduced fluorescence (dark gray), while uncovered pores can be recognized as black circles. PSMs composed of DPhPC/PtdIns[4,5]P₂/ATTO390-DPPE (91.6:8:0.4) were stable for at least two days, enabling the membrane attachment of minimal actin cortices via the ezrin-PtdIns[4,5]P₂ linkage. The specific MAC attachment to the f- and s-PSMs is displayed in figure 4.27 B/C1-2, showing the membrane-bound F-actin, stained with Alexa FluorTM 633 phalloidin, in magenta. Since no individual actin filaments could be resolved, the specific F-actin attachment was verified via further control experiments (cf. chapter A.6.1)

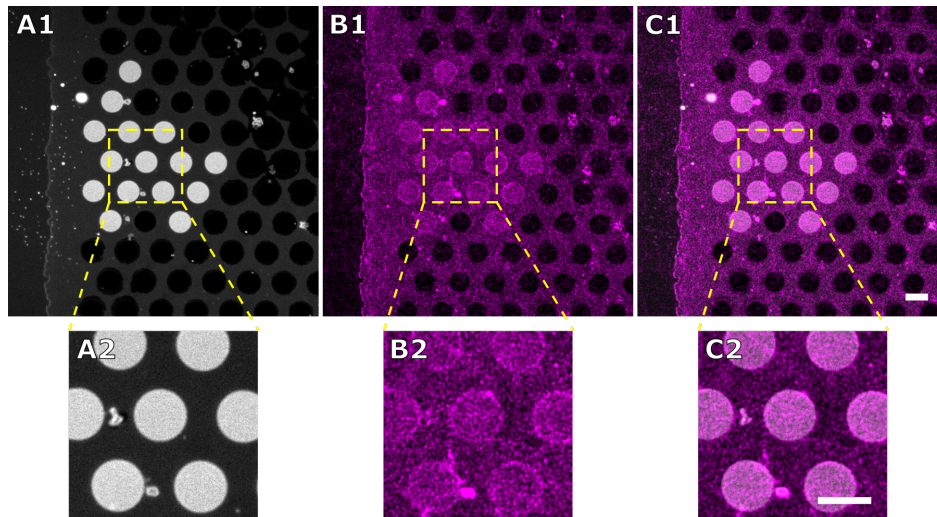


Figure 4.27: Exemplary fluorescence micrographs of MACs attached to PSMs via the biomimetic ezrin-PtdIns[4,5]P₂-likeage A1-2: DPhPC/PtdIns[4,5]P₂/ATTO390-DPPE (91.6:8:0.4) PSMs (gray), with freestanding PSMs identifiable as bright circles and dimmer solid-supported parts. **B1-2:** Corresponding fluorescence micrographs of Alexa Fluor™ 633 phalloidin stained MACs (false colored in magenta) attached to the lipid bilayer. **C1-2:** PSMs (A1-2) and MAC (B1-2) overlay. Scale bars: 5 μ m.

To study the initial mechanical properties of pore-spanning membranes, the pure PSMs were probed via AFM-indentation experiments. Using a Biomat station enabled the alignment of the AFM-scanning region and the CLSM-field of view (cf. chapter 3.5.2.4). Figure 4.28 A/B1 display the fluorescence and the corresponding atomic force micrograph (QI mode, set point: 0.3-0.4 nN) of pure PSMs, respectively. Covered and uncovered pores can be distinguished on the basis of the intensity (cf. figure 4.28 A2) and height profile (cf. figure 4.28 B2), extracted from the blue lines in figure 4.28 A1/B1. The normalized intensity profile of the membrane fluorescence in figure 4.28 A2 reveals that the s-PSM intensity was approximately 20 % of the f-PSM intensity. The extracted exemplary height profile in figure 4.28 B2 shows a low indentation depth corresponding to the averaged depth of 44 ± 9 nm ($n = 31$) for covered and around 1.2μ m for uncovered pores. In order to determine the mechanical properties of these PSMs, force distance curves (FDCs) were recorded in the f-PSM centers. An exemplary FDC for pure PSMs is shown in figure 4.30 B1 (set point: 0.3 nN), representing the principal curve profile for all preparations. The superposition of trace and retrace during the indentation process demonstrates a fully elastic behavior of the f-PSM during indentation. The lateral membrane tension (σ) of the PSMs were determined according to chapter 3.5.2.3 and are summarized

in figure 4.30 A ($\sigma = 6.8 \pm 1.3 \text{ mN m}^{-1}$, $n = 49$, $N = 2$).

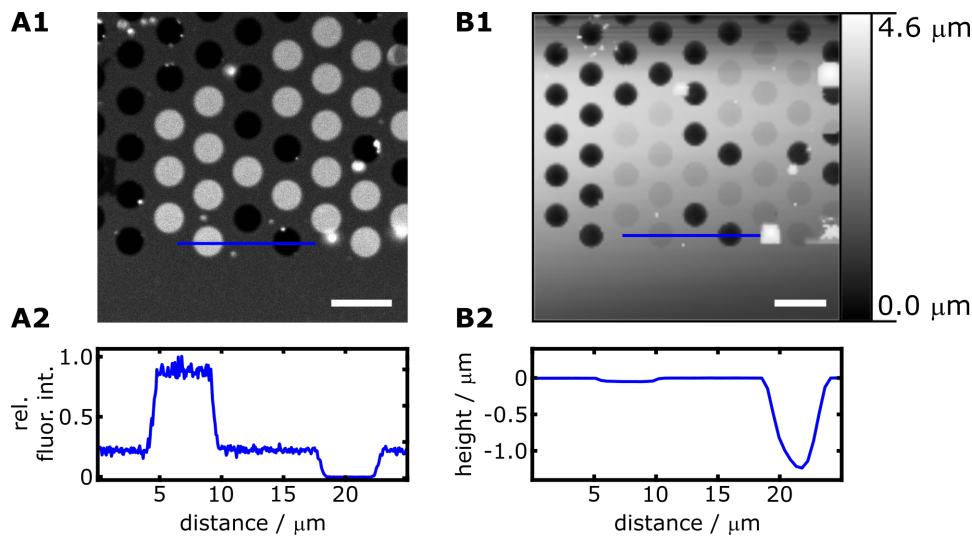


Figure 4.28: Fluorescence and atomic force micrographs of PSMs prior to MAC attachment. Fluorescence micrograph of PSMs (A1) with corresponding intensity profile (A2) along the blue line. Correlated atomic force micrograph (B1) and height profile (B2) along the blue line. Membrane composition: DPhPC/PtdIns[4,5]P₂/ATTO390-DPPE (91.6:8:0.4). Scale bars: 10 μm .

To determine the influence of a MAC attachment on the f-PSM mechanics, AFM-CLSM correlation experiments were conducted analogous to the aforementioned pure PSMs. While the general attachment of a minimal actin cortex to f-PSMs was observed in several preparations (cf. figure 4.27), the in the following presented PSMs were the only evaluable ones. Therefore, this data should be considered in qualitative manner. The fluorescence micrograph in figure 4.29 A1 shows an overlay of PSMs (gray) and the membrane-bound F-actin network (magenta). The intensity profile in figure 4.29 A2 displays the normalized membrane fluorescence intensity (rel. fluor int. membrane, blue) and the actin fluorescence intensity (fluor. int. actin, magenta) along the blue line in figure 4.29 A1. While the membrane intensity shows the same intensity reduction between the s- and f-PSM as the protein free PSMs, the actin profile reveals a slightly increased intensity at the pore rims and an approximately equal intensity between s- and f-PSM. The figures 4.29 B1-2 display the correlated atomic force micrograph (B1, QI mode, set point: 0.3-0.4 nN) and the corresponding height profile (B2). In contrast to the indentation depth of covered pores from pure PSMs ($44 \pm 9 \text{ nm}$, $n = 31$, cf. figure 4.28 B2) the height profile in figure 4.29 B2 indicates an indentation depth of around 900 nm for covered pores with a membrane-bound MAC. To determine the lateral membrane tension,

FCDs (set point: 0.1 nN) were recorded in the center of the f-PSMs and analyzed according to chapter 3.5.2.3. An exemplary FDC for a f-PSM with membrane attached MAC is shown in figure 4.30 B2. The hysteresis between trace and retrace during indentation suggests a viscoelastic behavior of the f-PSM, which has been observed for all recorded FDCs with a membrane-bound MAC. A reduced lateral membrane tension of $\sigma = 0.5 \pm 0.3 \text{ mN m}^{-1}$ ($n = 3$, $N = 1$) was calculated for f-PSMs with a membrane-bound MAC (cf. figure 4.30 A). Further, the fluidity parameter β (power law exponent, cf. chapter 3.5.2.3) was determined to 0.4 ± 0.2 . β describes the fluidity behavior of the membrane, if β is 0, the membrane behaves like an elastic solid, while a maximal β of 1 represents a Newtonian liquid.^[135]

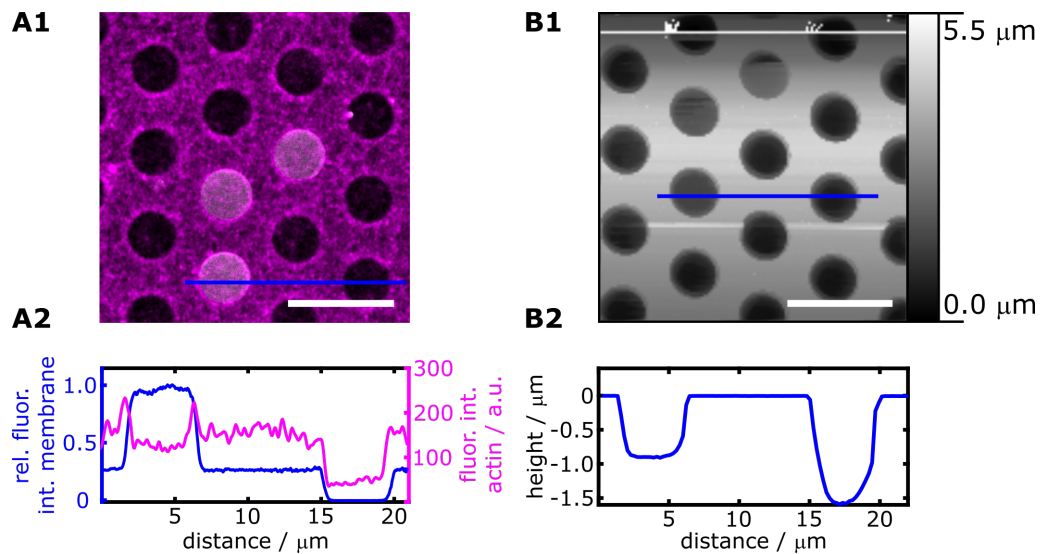


Figure 4.29: Fluorescence and atomic force micrographs of PSMs with membrane-bound MAC. **A1**: Fluorescence micrograph overlay of the PSMs (gray) and membrane attached MAC (false colored in magenta). **A2**: Intensity profiles of the PSM (blue) and Alexa Fluor™ 633 labeled F-actin (magenta) along the blue line in A1. **B1**: Corresponding atomic force micrograph. **B2**: Height profile along the blue line in B1. Membrane composition: DPhPC/PtdIns[4,5]P₂/ATTO390-DPPE (91.6:8:0.4). Scale bars: 10 μm.

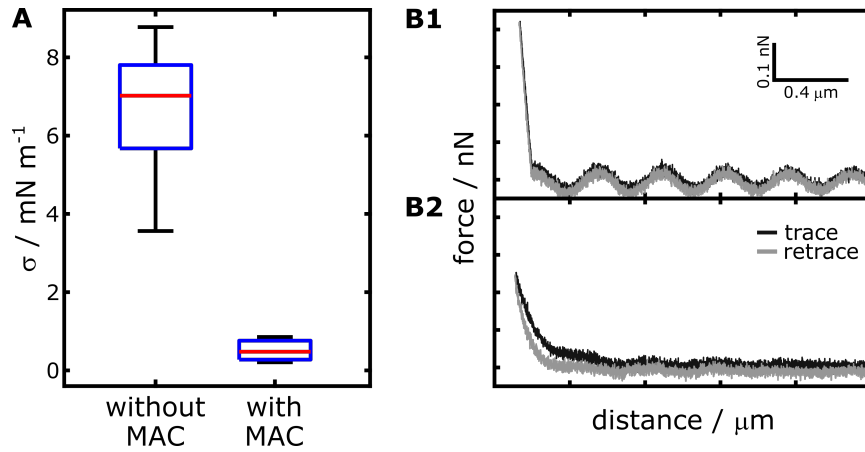


Figure 4.30: Box plot of the lateral membrane tension (σ) with/without membrane-bound MAC and exemplary force distance curves. **A:** Lateral membrane tension of PSMs with ($\sigma = 0.5 \pm 0.3 \text{ mN m}^{-1}$, $n = 3$, $N = 1$) and without ($\sigma = 6.8 \pm 1.3 \text{ mN m}^{-1}$, $n = 49$, $N = 2$) membrane-bound MAC. For the analysis n force distance curves from N preparations were evaluated. Boxes ranging from 25th to 75th percentiles of the sample, while whiskers represent to the most extreme data points not considered outliers (red crosses). Medians are shown as red horizontals within the boxes. **B1-2:** Exemplary force distance curve of PSMs without (B1) and with (B2) membrane attached minimal actin cortex. Membrane composition of all measurements: DPhPC/PtdIns[4,5]P₂/ATTO390-DPPE (91.6:8:0.4).

5 Discussion

To gain a more detailed understanding of the organization and dynamics associated with the cellular actin cortex, biomimetic actin- and actomyosin cortices were studied in this thesis. For this purpose, the organization of membrane-bound minimal actin cortices was investigated by confocal laser scanning microscopy (CLSM), dependent on the ezrin-PtdIns[4,5]P₂ linkage and cellular mimicking conditions. As the cellular actin cortex dynamics are largely governed by myosin II, the reorganization ability of membrane-bound actomyosin cortices was investigated as a function of MAC attachment and membrane composition using total internal reflection (TIRF) microscopy. In order to analyze how the binding of a minimal actin cortex via the biomimetic ezrin-PtdIns[4,5]P₂ linkage alters the membrane tension and viscoelasticity, a MAC model system on pore-spanning membranes was established and tested via a CLSM-AFM correlation. Here the obtained results will be discussed and compared to the known literature.

5.1 Reciprocal interaction of the membrane-actin cortex linkage

5.1.1 Membrane composition dependent F-actin attachment and self-organization

The membrane composition dependent attachment and self-organization of ezrin-PtdIns[4,5]P₂ linked minimal actin cortices (MACs) was investigated by means of confocal laser scanning microscopy (CLSM). By generating solid supported membranes from vesicle spreading, the amount of membrane attached F-actin could be monitored not only as a function of the ezrin specific receptor lipid PtdIns[4,5]P₂, but also for a defined POPS content. POPS is a characteristic lipid of the cytoplasmic leaflet in the eukaryotic plasma membranes and was used to resemble the inner human plasma membrane (15 - 20 mol% PS).^[162]

Characterization of F-actin binding to solid supported lipid bilayers as a function of the PtdIns[4,5]P₂ content

Linking pre-polymerized F-actin via the constitutively active ezrin mutant T567D to solid supported POPC membranes on glass substrates, doped with varied receptor lipid concentrations ($\chi(\text{PtdIns}[4,5]\text{P}_2)$) from 1 - 8 mol% PtdIns[4,5]P₂, revealed an increasing MAC density from single filaments ($\chi(\text{PtdIns}[4,5]\text{P}_2) = 1$ mol%) to dense entangled networks, already present at $\chi(\text{PtdIns}[4,5]\text{P}_2) = 3$ mol% (cf. figure 4.4). This visual observation could be validated by an increasing node density from $0.08 \pm 0.06 \mu\text{m}^{-2}$ to $1.43 \pm 0.39 \mu\text{m}^{-2}$ and a ~ 5.5 -fold increase in skeleton density for 1 - 3 mol% PtdIns[4,5]P₂. These general observations are in line with the findings of NÖDING et al., showing an increased amount membrane attached cortical actin for raising PtdIns[4,5]P₂ concentrations, since the F-actin-membrane linker ezrin binds specifically via its N-terminal domain to the receptor lipid PtdIns[4,5]P₂.^[44,72,76] Furthermore, a non-specific membrane attachment via the matrix lipid POPC could be excluded, since linkage studies without PtdIns[4,5]P₂ demonstrated no significant F-actin binding (cf. figure 4.2). However, the visually evident increase in network density from 3 - 8 mol% PtdIns[4,5]P₂ was not reflected in the node and skeleton density (cf. figure 4.5 A-B). This finding discrepancy can be partly attributed to the simultaneously altered organization of the membrane-bound F-actin, switching from an entangled to a locally nematic aligned network (cf. figure 4.4; $\chi(\text{PtdIns}[4,5]\text{P}_2) = 3 - 8$ mol%). The formation of nematic phases, respectively the spatial parallel alignment of membrane-bound actin filaments, could be confirmed by the determination of the mean nematic order parameter (q_{mean}), which indicates a general increase of the nematic order from 1 to 8 mol% PtdIns[4,5]P₂ (cf. figure 4.5 C). The formation of nematic phases can generally be described by the theoretical work of ONSAGER, for rigid rods, and the extended model of F-actin like rods from KHOKHLOW et al.^[177,178] According to both models, the transition of an isotropic network, present in this work at 1 - 3 mol% PtdIns[4,5]P₂, into a nematic organized system (5 - 8 mol% PtdIns[4,5]P₂) depends on a critical packing density, above which filaments align nematicly.^[177-179] While this critical packing density is, apart from other parameters, a function of the filament length and diameter, the nematic phase formation itself is energetically preferable, as the parallel orientation reduces the filament exclusion volume at high densities.^[180] *In vitro* assays showed, that the required critical F-actin concentration in solution can range from 75 - 100 μM ,

while low concentrations of ~ 2.5 - $5 \mu\text{M}$ are sufficient for nematic phase formation, if crowding agents like methyl cellulose (MC) are applied.^[146,157,181] Since the transition of an isotropically to nematically organized F-actin network was observed in this work for a low F-actin concentration of $\sim 1.7 \mu\text{M}$, without the addition of any crowding agent or applied shear forces, the data implies that the critical packing density can be reached by attaching F-actin in a quasi-2D network on a membrane. Further, as the nematic phase formation depends on the filament density, both the increasing q_{mean} with raising PtdIns[4,5]P₂ content, as well as the altered MAC morphology suggest an increased amount of membrane-bound F-actin for 5-8 mol% PtdIns[4,5]P₂. Whereas the progressively parallel orientation of the membrane-bound actin filaments explains the reduction in node density from 5-8 mol% PtdIns[4,5]P₂, the decrease in skeleton density implies a change in the morphology, not only of the actin network but also of the single filaments, considering the assumption of an increasing amount of membrane-bound actin.

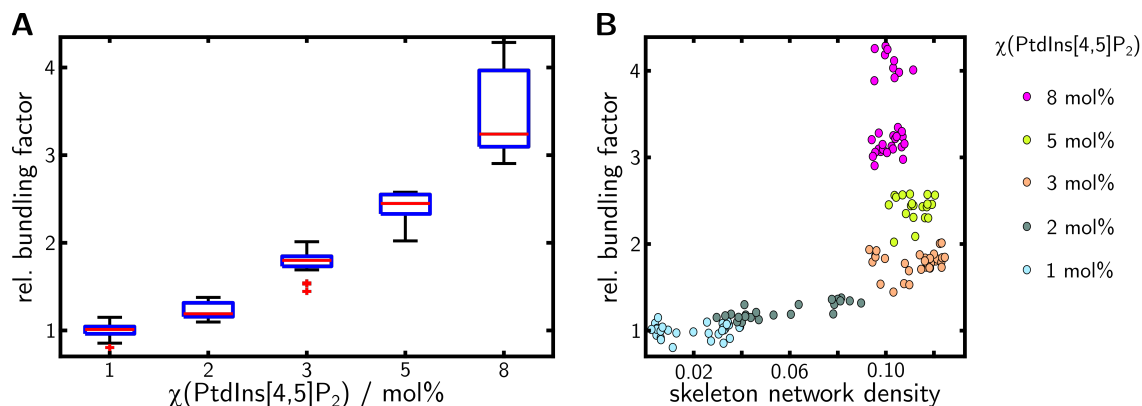


Figure 5.1: Dependence of the F-actin bundling upon the receptor lipid content and skeleton network density. **A:** Relative F-actin bundling factor (δ) as a function of the PtdIns[4,5]P₂ content ($\chi(\text{PtdIns}[4,5]\text{P}_2)$). The mean actin intensity of n images from N preparations was normalized by the averaged mean actin intensity at $\chi(\text{PtdIns}[4,5]\text{P}_2)=1$ mol%. 1 mol% ($n = 30$, $N = 4$), 2 mol% ($n = 23$, $N = 3$), 3 mol% ($n = 34$, $N = 4$), 5 mol% ($n = 20$, $N = 2$) and 8 mol% ($n = 31$, $N = 3$). Boxes ranging from 25th to 75th percentiles of the sample, while whiskers represents to the most extreme data points not considered outliers (red crosses). Medians are shown as red horizontals within the boxes. **B:** Scatterplot of the relative bundling factor against the skeleton network density of the respective MAC attached to membranes with 1-8 mol% PtdIns[4,5]P₂.

Addressing this hypothesis by means of a skeleton based intensity analysis, revealed an increasing mean actin intensity of the skeletonized filaments with growing PtdIns[4,5]P₂ content (cf. figure 4.6). Since all analyzed fluorescence micrographs

were imaged using the same F-actin labeling (10 % (n/n), ATTO 594 G-actin) and CLSM settings, the raising mean actin intensity displays a progressive bundling of membrane-bound F-actin, with increasing receptor lipid content. While cellular F-actin is bundled via cross-linker proteins, such as fascin^[182] or α -actinin^[183], the formation of artificial actin-bundles have been reported for high concentrations of divalent cations^[180] and increased concentrations of crowding agents such as methyl cellulose or polyethylene glycol (PEG)^[156]. The bundling properties of divalent cations arise from electrostatic interactions with the negatively charged F-actin, whereas the bundling effect of the depletion agents MC and PEG are based, similar to the formation of nematic phases, on the reduction of the exclusion volume.^[156,180] This leads to the assumption that the enhanced bundling of membrane-bound actin filaments, is caused by the increased amount of membrane attached F-actin with increasing PtdIns[4,5]P₂ content. Determining a relative F-actin bundling factor (δ), by normalizing the mean actin intensity from 1 - 8 mol% PtdIns[4,5]P₂ (cf. figure 4.6) to the averaged mean actin intensity at $\chi(\text{PtdIns}[4,5]\text{P}_2) = 1 \text{ mol}\%$, reveals an 3 to 4-fold increased F-actin bundling at $\chi(\text{PtdIns}[4,5]\text{P}_2) = 8 \text{ mol}\%$ (cf. figure 5.1 A). Simultaneously, assuming only single actin filaments at $\chi(\text{PtdIns}[4,5]\text{P}_2) = 1 \text{ mol}\%$ the data implies an actin bundle composition of 3-4 filaments at $\chi(\text{PtdIns}[4,5]\text{P}_2) = 8 \text{ mol}\%$. This corresponds to the number of filaments per actin bundle, reported for the cross-linkers α -actinin and fascin (~ 3 -30 filaments).^[184] Combining the information of the 2D network density, given by the skeleton network, with the quasi-3D network information from the relative bundling factor, enables the definition of two organization respectively membrane-attachment regimes for F-actin, with increasing PtdIns[4,5]P₂ content. (cf. figure 5.1 B). While the first regime from 1 - 3 mol% is characterized by a continuously increasing skeleton density and a slightly growing relative bundling factor, indicating the membrane attachment of primarily individual actin filaments, the constant skeleton density and increasing relative bundling factor in the second regime, suggest a progressive F-actin binding and organization in filament bundles. In addition, the graph in figure 5.1 B allows the approximate determination of a threshold value of 0.1 skeleton network density, above which the organization of the attaching F-actin into bundles is energetically more favorable than the binding of single filaments.

In conclusion, the discussed data for the membrane-attachment of minimal actin cortices via the biomimetic ezrin-PtdIns[4,5]P₂-linkage demonstrate, that the amount

of membrane-bound F-actin increases as a function of the receptor lipid content from 1 - 8 mol% PtdIns[4,5]P₂, correlating with the increasing amount of membrane-bound ezrin (cf. figure 4.15, -POPS). Furthermore, it could be highlighted, that growing amounts of membrane attached F-actin lead to a morphology change, not only of the actin networks from entangled (1 - 3 mol% PtdIns[4,5]P₂) into nematically aligned (5 - 8 mol% PtdIns[4,5]P₂), but also of the membrane-bound actin filaments from single filaments (1 - 3 mol% PtdIns[4,5]P₂) into filament bundles (5 - 8 mol% PtdIns[4,5]P₂).

Influence of POPS on the minimal actin cortex architecture

As the cellular actin cortex is attached to the cytoplasmatic plasma membrane leaflet of eukaryotic cells, which is composed of several lipid species, the question arises how a plasma membrane mimicking lipid composition effects the minimal actin cortex attachment. Since phosphatidylserine is one of the most prominent lipids in the plasma membrane of eukaryotic cells, POPC-membranes were doped with 17 mol% POPS and varied concentrations of PtdIns[4,5]P₂ (1 - 8 mol%), resembling the cytoplasmatic lipid composition of the human plasma membranes.^[162,185] In a first step the impact of the altered membrane composition was investigated with regard to the ezrin-PtdIns[4,5]P₂ linkage and the ezrin binding was quantified as a function of the membrane composition by means of RIfS experiments (cf. chapter 4.1.3.3). As presented in chapter 4.1.3.3, the ezrin T567D binding to POPC/POPS/PtdIns[4,5]P₂ membranes was quantified for varied PtdIns[4,5]P₂ concentrations from 1 - 8 mol% and compared to the data of NÖDING et al., for POPC/PtdIns[4,5]P₂ membranes with the same receptor lipid content.^[72] It was found that the amount of membrane-bound ezrin was generally increased for membranes containing POPS (cf. figure 4.15). Thereby, the most prominent effect was observed for low receptor lipid concentrations from 1 - 3 mol% PtdIns[4,5]P₂, showing an up to 5-fold increased protein adsorption. Since membranes containing POPS and lacking PtdIns[4,5]P₂ did not show any substantial ezrin binding an unspecific interaction was excluded (cf. figure A.2). This finding of no ezrin-POPS binding is in contradiction to the data of NIGGLI et al., showing an interaction of ezrin with PS doped LUVs at a similar concentration of 20 mol% PS.^[186] Similar observations were made by BLIN et al., however they were able to show that the ezrin-PS binding is a weak interaction compared to the ezrin-PtdIns[4,5]P₂ interaction.^[187]

A crucial parameter for the binding of proteins to SLBs is the amount of accessible receptor lipid in the solvent-facing leaflet. As demonstrated by SCHÄFER et al., with a comparable RIfS system and the N-terminal FERM domain of ezrin (N-ERMAD), PtdIns[4,5]P₂ shows an asymmetric leaflet distribution in SLBs, suggesting a PtdIns[4,5]P₂ accumulation in the surface-attached leaflet.^[151] Additionally, DRÜCKER et al. showed a time-dependent depletion of accessible PtdIns[4,5]P₂ in the solvent-facing leaflet of formed SLBs.^[150] As suggested in both studies attractive interactions between the hydrophilic substrates and the negatively charged receptor PtdIns[4,5]P₂, via hydrogen bond formation, leads to a depletion of accessible pinning points. Comparing the mobile fraction of fluorescently labeled PtdIns[4,5]P₂ in SLBs and supported lipid monolayers, revealed an increased immobile fraction for SLBs and supports this assumption^[149,151]. However, DRÜCKER et al. were able to show, that the incorporation of an additional negatively charged lipid like POPS prevents the depletion of accessible PtdIns[4,5]P₂.^[150] Thus, the used lipid composition with POPS does not only reflect the inner plasma membrane composition, but at the same time leads to an improved accessibility of the receptor lipid in the solvent-facing leaflet, which declares the in general increased amount of membrane-bound ezrin T567D (cf. figure 4.15) for POPS containing membranes.

In addition, the data suggest an altered organization of the membrane-bound ezrin T567D, when binding to POPS containing membranes. AFM studies of SHABARDINA et al. showed, that the detectable average height for the ezrin wild-type binding to PtdIns[4,5]P₂ doped membranes (3.0 ± 0.4 nm), is dominated by the N-ERMAD height (~ 3.4 nm) and not significantly influenced by the C-terminal actin binding domain (C-ERMAD).^[188] Similar observations were made for the ezrin mutant T567D bound to the receptor lipid DOGS Ni-NTA at a high density, revealing an averaged height of 3.2 ± 0.9 nm. Based on the work of CHAMBERS and BRETSCHNER, as well as JAYASUNDAR et al., SHABARDINA et al. concluded, that the globular structures of the membrane-bound ezrin wild-type and T567D mutant originate from an inter- and intramolecular contact of the N-ERMAD/C-ERMAD domain (cf. figure 5.2 B).^[188–190] Based on the presented $\Delta(\Delta OT_{\text{ezrin}})$ values in figure 4.15, the averaged physical layer thickness (d) can be calculated according to equation 5.1, by assuming a refractive index of $n_{\text{prot}} = 1.455$ for the adsorbing ezrin layers.^[191]

$$\Delta(\Delta OT_{\text{ezrin}}) = n \cdot d \quad (5.1)$$

Since RfS averages the change in optical thickness over an area of $\sim 1 \text{ mm}^2$, a comparison of the physical layer thickness and the AFM measurements of SHABARDINA et al. is only valid for fully ezrin T567D decorated membranes. As the data in figure 4.15 indicate a saturation at $\chi(\text{PtdIns}[4,5]\text{P}_2) \geq 6 \text{ mol}\%$, a physical layer thickness of $3.2 \pm 0.4 \text{ nm}$ for $\chi(\text{PtdIns}[4,5]\text{P}_2) \geq 6 \text{ mol}\%$ and $4.1 \pm 0.4 \text{ nm}$ for $\chi(\text{PtdIns}[4,5]\text{P}_2) \geq 6 \text{ mol}\% + 17 \text{ mol}\% \text{ POPS}$ were calculated.

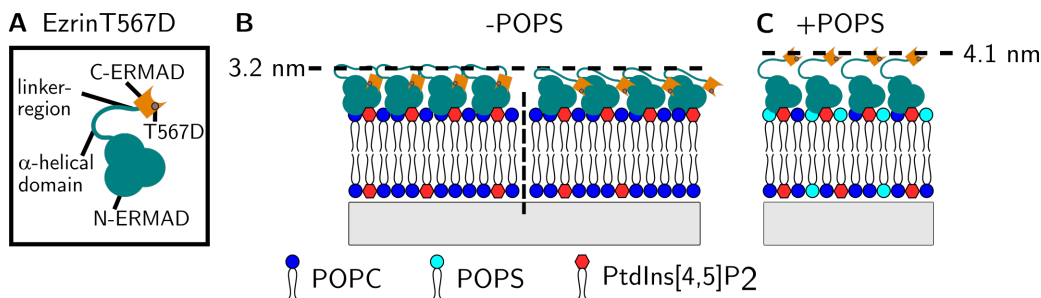


Figure 5.2: Proposed modes of the ezrin T567D organization on solid supported membranes depending on the lipid composition. **A:** Schematic illustration of ezrin T567D. **B:** Based on SHABARDINA et al. expected organization of ezrin T567D on SLBs doped with a high content of PtdIns[4,5]P₂, showing intra- (left) and intermolecular (right) interactions of the N- and C-ERMAD domains. **C:** Proposed elongated organization of ezrin T567D bound to SLBs with a high content of PtdIns[4,5]P₂ and 17 mol% POPS. Figure inspired by SHABARDINA et al. and M. SCHÖN.^[188,192]

While the physical ezrin height bound to membranes lacking POPS corresponds to the data of SHABARDINA et al. (cf. figure 5.2 B), the increased layer height for POPS membranes suggests a structurally different binding behavior of ezrin T567D (cf. figure 5.2 C). Since the α -helical domain, linker region and C-ERMAD domain of ezrin T567D exhibit a negatively net charge under the experimental conditions, repulsive interactions with the highly negatively charged membrane might lead to a more elongated ezrin structure and with this to an increased layer thickness (cf. figure 5.2 A). Charge estimations were performed by using the web-tool Prot pi and the ezrin domain organization according to FEHON et al.^[44,193]

Since the RfS experiments indicated the most pronounced effect of POPS on the amount of membrane-bound ezrin T567D at low receptor lipid concentrations of 1 - 3 mol% PtdIns[4,5]P₂, matching the averaged PtdIns[4,5]P₂ content of eukaryotic cells, this lipid composition was investigated in terms of the MAC attachment.^[194] The attachment of pre-polymerized F-actin via the ezrin T567D-PtdIns[4,5]P₂ linkage to SLBs doped with 1 - 3 mol% PtdIns[4,5]P₂ and 17 mol% POPS revealed a significantly

enhanced actin attachment compared to membranes lacking POPS (cf. figure 4.16). This principal observation reflects not only the aforementioned increased amount of membrane-bound ezrin T567D, but was also validated by the raising node and skeleton densities from CLSM micrographs (cf. figure 4.18 A-B). Beside the enlarged surface coverage of F-actin, the visual inspection of the fluorescence micrographs, further revealed the formation of nematically organized actin filaments in the presence of POPS, which were already identifiable at 1 mol% PtdIns[4,5]P₂. As discussed above for the POPC/PtdIns[4,5]P₂ membranes, the formation of nematic phases is a function of the amount of membrane-bound F-actin. The actin binding, in turn, is conditioned by the ezrin T567D attachment, which is a function of the receptor lipid PtdIns[4,5]P₂ and could be quantified by means of RIfS experiments. The fact that an increased q_{mean} (0.42 ± 0.12) was determined in the presence of POPS and 2 mol% PtdIns[4,5]P₂ compared to 8 mol% PtdIns[4,5]P₂ (0.33 ± 0.06) in the absence of POPS, whereas the RIfS measurements for 8 mol% without POPS showed an increased ezrin T567D binding (cf. figure 4.15), indicates a possible influence of POPS on the amount of membrane-bound F-actin, which might be caused e.g. by the proposed elongated ezrin organization in presence of POPS. As displayed in figure 5.3 A, F-actin bundling generally increases with POPS, both within a certain PtdIns[4,5]P₂ concentration and with increasing PtdIns[4,5]P₂ content. Although, the relative bundling factor shows the same dependence on skeleton network density for MACs on POPS doped membranes as for POPC/PtdIns[4,5]P₂ SLBs and increases significantly above a threshold of 0.1 (cf. figure 5.3 B), q_{mean} and filament bundling do not show the same correlation as without POPS. As discussed above, the formation of nematic phases and filament bundles are principally based on the same factor, the reduction of the exclusion volume with increasing F-actin density, and showed a clear correlation in their increase for membranes without POPS. However, the finding of a higher nematic order ($q_{\text{mean},2\text{ mol}\%} = 0.42 \pm 0.12$, $q_{\text{mean},3\text{ mol}\%} = 0.38 \pm 0.08$) and reduced bundling ($\delta_{2\text{ mol}\%} = 2.07 \pm 0.57$, $\delta_{3\text{ mol}\%} = 2.34 \pm 0.77$) at 2-3 mol% PtdIns[4,5]P₂ with POPS than at 8 mol% without POPS ($q_{\text{mean}} = 0.33 \pm 0.06$, $\delta = 3.44 \pm 0.46$) suggests an influence of POPS on F-actin organization and/or bundling.

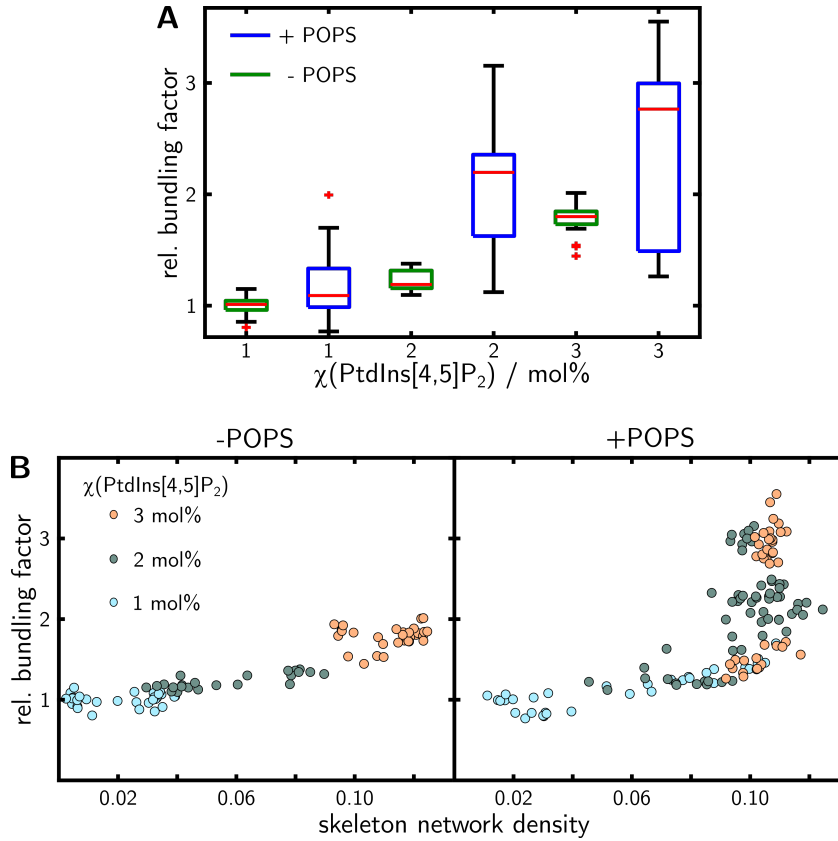


Figure 5.3: Dependence of the F-actin bundling on POPS doped SLBs upon the receptor lipid content and skeleton network density. **A:** Relative F-actin bundling factor (δ) as a function of the PtdIns[4,5]P₂ content ($\chi(\text{PtdIns}[4,5]\text{P}_2)$) and the presence (blue) or absence (green) of POPS. The mean actin intensity of n images from N preparations was normalized by the averaged mean actin intensity at $\chi(\text{PtdIns}[4,5]\text{P}_2)=1$ mol% (-POPS). 1 mol% ($n=34$, $N=4$; $n=30$, $N=4$), 2 mol% ($n=60$, $N=6$; $n=23$, $N=3$), 3 mol% ($n=40$, $N=6$; $n=34$, $N=4$). Boxes ranging from 25th to 75th percentiles of the sample, while whiskers represents to the most extreme data points not considered outliers (red crosses). Medians are shown as red horizontals within the boxes. **B:** Scatterplot of the relative bundling factor against the skeleton network density of the respective MAC attached to membranes with 1-3 mol% PtdIns[4,5]P₂ in the presence (right) or absence (left) of POPS.

A possible explanation could be an improved actin binding via the proposed elongated ezrin structure, which might facilitate the formation of nematic phases, and a simultaneous competition between the strongly negatively charged membrane and the F-actin for divalent cations (buffer: 2 mM Mg²⁺), which would prevent a charge-induced bundling and at the same time increase the amount of membrane-bound F-actin.^[180,184] Both combined would explain the increased q_{mean} with a simultaneously decreased actin bundling. Nevertheless, it is noteworthy to mention that previous studies demonstrated charge mediated membrane adsorption for F-actin and PS

lipids only at divalent cation concentrations larger than 6 mM.^[195,196] One of the rare indications of an interaction of cortical actin and PS *in vivo* are given by KAY et al., who monitored an effect of the actin cortex in HeLA cells on the mobility of PS lipids in the plasma membrane. However, the authors attributed this observation to the interaction of the cortical actin with PS associated proteins.^[197] Furthermore, THOMPSON et al. observed an increased externalization of PS in Chinese hamster ovary cells after actin depolymerization, but again the high complexity of the cellular system does not allow a direct conclusion of the dependency between PS and actin cortex.^[198]

To conclude, the presented data for the binding of MACs to SLBs with a plasma membrane mimicking lipid composition revealed an increased attachment of the membrane-linker ezrin T567D in the presence of POPS, which was reflected by a significantly increased F-actin density combined with a nematic network organization at low receptor lipid concentrations. Simultaneously, there were indications for an altered ezrin organization on POPS doped membranes, which may have a direct influence on the general MAC and single actin filament organization.

5.1.2 Influence of actin cortex binding on lipid membrane dynamics

To answer the question how the membrane attachment of a minimal actin cortex, via the ezrin-PtdIns[4,5]P₂ linkage, alters the lipid diffusion within the supporting bilayers, fluorescence recovery after photobleaching (FRAP) experiments were conducted on pure SLBs and SLBs with an attached MAC. To exclude an effect of the membrane composition, all membranes were composed of POPC/PtdIns[4,5]P₂/ATTO 488-DPPE (96.6:3:0.4). Evaluating the FRAP-data according to JÖNSSSEN et al. (cf. chapter 3.5.1.3), revealed a significant decreased diffusion coefficient (D) for SLBs with an attached minimal actin cortex ($D = 2.2 \pm 0.3 \mu\text{m}^2\text{s}^{-1}$) compared to pure SLBs ($D = 3.1 \pm 0.4 \mu\text{m}^2\text{s}^{-1}$).^[125] Additionally, the former exhibited an increased immobile fraction (γ) by a factor of 1.4 ($\gamma = 7.1 \pm 2.2 \%$, cf. chapter 4.1.1). The determined value for the pure SLBs is in good agreement with the diffusion coefficients reported by BRAUGNER et al. (POPC/PtdIns[4,5]P₂/Bodipy TMR-PtdIns[4,5]P₂/perylene; 96:2.5:0.5:1) and SCHÄFER et al. (POPC/PtdIns[4,5]P₂/Bodipy TMR-PtdIns[4,5]P₂;

90:9:1) on hydrophilized silicon wafers with each $D = 2.9 \pm 0.2 \mu\text{m}^2\text{s}^{-1}$.^[149,151] However, NÖDING et al., using the same ezrin-PtdIns[4,5]P₂ linkage for the binding of minimal actin cortices, defined a diffusion coefficient of $D = 1.7 \mu\text{m}^2\text{s}^{-1}$ for both, pure SLBs as well as SLBs with an attached MAC.^[72] This decreased diffusion coefficient of the pure SLBs could be attributed to the final functionalization step performed in this work and the previous mentioned publications. While the substrate functionalization was conducted in the same manner in all studies, the final activation of the substrates with oxygen plasma is missing in the work of NÖDING et al. Since oxygen plasma treatment has been shown to increase the surface hydrophilicity, this might be a possible explanation for the reduced lipid diffusion.^[192,199] Furthermore, this could explain why NÖDING et al. could not observe any influence of MAC attachment, as their system was generally dominated by slow lipid diffusion due to the lack of oxygen plasma treatment. The general observation of a reduced diffusion coefficient and an increased immobile fraction for membranes with attached MAC in this work can be described by the „picket-fence“ model.^[200] This model hypothesizes that the direct linkage of proteins or lipids (pickets) to cortical actin network (fences) creates diffusion barriers restricting the lateral diffusion of other membrane components.^[201] As illustrated in figure 5.4 A, these barriers define compartments in which molecules can diffuse freely, while the transition between two compartments requires a „hop“, which is referred to as hop-diffusion (cf. figure 5.4 B).^[57]

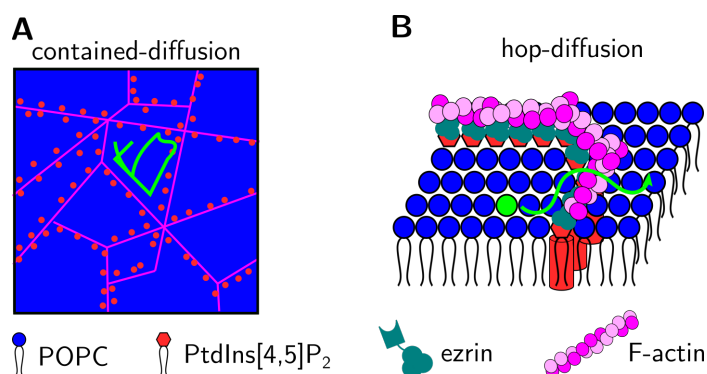


Figure 5.4: Schematic illustration of the potential diffusion modes resulting from cortical actin. **A:** Contained diffusion path (green) of a lipid molecule in a compartment defined by the F-actin network (magenta) and associated linkers (red). **B:** Transition of a lipid molecule (green) between two compartments by hop-diffusion. Figure inspired by ANDRADE et al. and SCHNEIDER et al.^[201,202]

Since ANDRADE et al. were able to show via *in silico* STED-FCS experiments, that the diffusion coefficient is dependent on the compartment size (actin network mesh size), the observation area and the hopping probability of the respective

molecule, a direct comparison between diffusion coefficients of different systems is not reasonable.^[201] However, the finding of a reduced lateral lipid diffusion induced by the attachment of a minimal actin cortex in this work, is in line with the observations of actin cortex hindered diffusion of membrane proteins^[203-205], such as glycoproteins, and phospholipids as DOPE^[202,206]. Thus, it can be generally concluded that the biomimetic ezrin-PtdIns[4,5]P₂ linkage is sufficient to mimic the basic interaction of actin cortex with other membrane components. Further, HEINEMANN et al. showed in an *in vitro* assay with a minimal actin cortex on pore-spanning membranes, attached via neutravidin/biotin interaction, that the reduction of both, lipid and membrane protein diffusion directly correlate with the amount of membrane-bound F-actin.^[207] This also suggests that lipid diffusion for the MAC system presented in this work can be regulated by the receptor lipid concentration, as this defines the amount of membrane-bound F-actin (cf. chapter 5.1.1).

In summary, the data of this work are in agreement with the literature and indicate that the membrane binding of an F-actin network hinders the lateral mobility of lipids within the underlying bilayer. Moreover, this shows that the ezrin-PtdIns[4,5]P₂ linkage is sufficient to reflect the essential aspect of cellular actin cortices.

5.2 Impact of cellular mimicking conditions on the actin cortex self-organization

5.2.1 Influence of the crowding agent methyl cellulose

As the cytoplasm of eukaryotic cells is a dense fluid enriched with various macromolecules, occupying 20-40% of the total volume, the crowding agent methyl cellulose (MC) was used to mimic these conditions and was tested in terms of the membrane attachment of minimal actin cortices.^[152,153] Since crowding agents as MC are known to induce F-actin bundling, increasing MC-concentrations were trialed with respect to the F-actin morphology.^[184] By preparing minimal actin cortices on SLBs doped with 2 mol% PtdIns[4,5]P₂ and treated with various MC concentrations of 0.06-0.44 *w/v* %, a visual inspection of the membrane-bound MACs revealed an optimal MC concentration of 0.18 *w/v* % (cf. chapter 4.1.3.1). At this particular concentration no structural transformation of the membrane-bound F-actin could be observed, whereas the network density appeared to be increased. This findings are in a good agreement with the data of KÖHLER et al., who were able to determine a critical MC concentration of 0.2 *w/v* % for F-actin and MC in solution, above which bundling of actin filaments occurs.^[156] Similar observations were made by POPP et al. for F-actin and 0.2 *w/v* % MC via scanning electron microscopy measurements.^[157] Furthermore, as the viscosity of 0.2 *w/v* % MC was determined to 4.9 cP^[208] by PEYER et al., the 0.18 *w/v* % MC seems to reflect the cytoplasm of mammalian cells (1.1-6 cP)^[209,210] in a good manner. Membrane binding of minimal actin cortices via the ezrin-PtdIns[4,5]P₂ linkage was then investigated for the determined optimal MC concentration as a function of PtdIns[4,5]P₂ content (1-5 mol%). In this context, an increased F-actin network density was quantified for the implementation of 0.18 *w/v* % MC (cf. figures 4.8 and 4.9). This observation could be attributed to the principal crowding effect of MC, as utilized in several studies for the preparation of dense cytoskeletal networks on inert surfaces.^[211-213] However, since the samples were rinsed prior to the network analysis and no significant binding was monitored without the ezrin-PtdIns[4,5]P₂ linkage, a simple crowding effect can be excluded. Yet, the MC crowding could promote the specific membrane attachment via the ezrin-PtdIns[4,5]P₂ linkage. Without MC, the F-actin-membrane attachment is driven by the diffusion of actin filaments onto the membrane. Since HERRIG et al.

showed the formation of ezrin clusters^[76], it is conceivable that already bound actin filaments shield these clusters from the binding of further filaments both sterically and by the high negative charge of F-actin ($0.15 e/\text{nm}^2$)^[214]. As crowding agent induced depletion forces are known to overcome the repulsive interactions between F-actin^[184], this and the enhanced density of the crowded F-actin might explain the increased amount of membrane-bound F-actin.

In addition to the increased network density, a shift in MAC organization towards nematically aligned F-actin was partially observed for MC treated samples (cf. figure 4.8; 3 mol% PtdIns[4,5]P₂). Although this, as well as the potential bundling of actin filaments could not be quantitatively determined, the fundamental observation of nematically arranged actin filaments suggests filament bundling, as both arise through a reduction of the exclusion volume, as discussed in chapter 5.1.1. Besides, a bundling effect of MC cannot be fully ruled out, since INOUE et al. observed at 0.1 w/v % MC microtubule bundling, even below the critical MC concentration of 0.2 w/v % determined by KÖHLER et al.^[156,215]

To conclude, MC has been shown to be a useful extension of minimal actin cortices to increase the amount of membrane-bound F-actin. However, crowding agents such as MC need to be used with caution, as they can induce major structural changes in cytoskeletal filaments, even at low concentrations.

5.2.2 Influence of the actin binding protein Arp2/3

Since the actin binding protein (ABP) complex Arp2/3 is one of the most abundant ABPs within cellular actin networks, Arp2/3 branching was investigated in terms of the minimal actin cortex architecture (cf. chapter 4.1.3.2).^[10] As Arp2/3 was added during F-actin polymerization the 3D F-actin network organization was first investigated in solution. By means of CLSM z-stacks it could be shown, that the addition of Arp2/3, combined with the nucleation promoting VCA-domain from N-WASP, leads to an increased network density in all three dimensions (cf. figure 4.10 A-B). The Arp2/3 complex itself is composed of two actin-related proteins Arp2 and Arp3 and five supporting subunits ArpC1-5.^[35,216] By binding to pre-existing F-actin (mother filament), the Arp2/3 complex stimulates the polymerization of new branches (daughter filaments) at a characteristic angle of $\sim 70^\circ$.^[217] While the *in*

in vitro experiments of HIGGS and POLLARD revealed a low nucleation ability of the pure Arp2/3 complex, nucleation promoting factors (NPFs) as the N-WASP (type I NPF) or cortactin (type II NPF) have been proven to activate the Arp2/3 complex significantly.^[159,218] Further, it was shown that *in vitro* three factors collectively trigger the nucleation activity of Arp2/3: The aforementioned NPFs, actin monomers (G-actin) and mother filaments.^[35,219] As in this work F-actin networks with Arp2/3 were polymerized from a mixture of G-actin/VCA/Arp2/3 (80:20:1), containing all stimulating factors, the enhanced network density can be directly linked to the filament branch formation. SMITH et al. showed for a comparable *in vitro* experiment, that only $\sim 1\%$ of filament-bound Arp2/3 complex lead to branch formation, as the complex dissociated fast with a time constant of up to 2 s from the F-actin.^[220] However, the fact that an increase in network density was observed clearly above $\sim 1\%$ branching, the observation can be attributed to phalloidin, which was added in a 1:70 ratio (phalloidin:G-actin) to stabilize the polymerized actin filaments. As shown by MAHAFFY and POLLARD (1:1, phalloidin:G-actin), phalloidin does not only prevent the dissociation of Arp2/3 branches, but also stimulates the branch formation of Arp2/3-VCA-actin by more than 10-fold.^[221] As the binding affinity of phalloidin is only 2-4 times higher for F-actin than for Arp2/3, it is likely that a significant proportion of the filament-bound Arp2/3 complexes were stabilized by phalloidin.^[221,222]

The observed reduced F-actin length of Arp2/3 treated networks can further be attributed to the filament branching. To estimate approximately the decrease in F-actin length, the CLSM z-stacks presented in figure 4.10 were analyzed with the software SOAX. SOAX was developed by XU et al and is originated for the analysis of 3D biopolymer networks.^[223] By applying the same set of parameters (cf. chapter A.7) an averaged filament length of $8.2 \pm 4.8 \mu\text{m}$ ($n = 22$) for pure F-actin networks and $1.5 \pm 1.3 \mu\text{m}$ ($n = 7562$) for Arp2/3 branched networks was determined. This 5-fold decrease in filament length corresponds exactly to the simulated data of LIMAN et al., who determined the same decrease.^[224]

Attaching pre-polymerized Arp2/3 networks via the ezrin-PtdIns[4,5]P₂ linkage to solid supported membranes, revealed for low and medium PtdIns[4,5]P₂ concentrations (2-5 mol%) a significantly decreased network density, in comparison to unbranched F-actin networks (cf. figure 4.11). However, it could be quantitatively shown that the network density of Arp2/3 branched MACs gradually increased from 2-8 mol% PtdIns[4,5]P₂ and at 8 mol% corresponds to that of an unbranched network

(cf. figure 4.12). This shows that the principle membrane-attachment respectively network density of Arp2/3 branched MACs is a function of the ezrin-PtdIns[4,5]P₂ linkage. The mismatch between the dense Arp2/3 networks in solution and the significantly decreased network density for low and medium PtdIns[4,5]P₂ concentration of the Arp2/3-MACs might result from two factors. As the Arp2/3 branched networks were characterized by a high density of strongly entangled F-actin, only the bottom layer of these dense actin networks might bind to the membrane, whereas the major portion remains above the membrane as a network in solution and was ripped off during buffer exchange. Another explanation would be that only single filaments, which are not integrated in the dense Arp2/3 networks, were bound to the membrane. Both options would explain an increasing network density of membrane-bound MACs with rising receptor lipid content, as either more individual filaments or a larger portion of the lower layer would bind to the membrane. However, since fluorescence micrographs of the Arp2/3 branched MACs taken before and after rinsing did not show any significant change in network density, the binding of single filaments seems to be more likely. However, this does not explain the reduced network density at 2-5 mol% PtdIns[4,5]P₂ compared to unbranched networks, as in both cases single actin filaments are bound via the ezrin-PtdIns[4,5]P₂ linkage. Here, it could be hypothesized that the binding of vertebrate filaments is sterically hindered or that the F-actin binding of the C-ERMAD domain is disrupted by Arp2/3. However, both cannot be proven neither on the basis of the data gathered in the context of this thesis nor with the known literature.

Besides the reduced network density, membrane-bound Arp2/3 MACs showed no significant nematic domain formation, which could be quantified via the averaged nematic order parameter (q_{mean} , cf. figure 4.13 A). This non existing parallel organization of the membrane-bound F-actin explains the increased node density at 8 mol% PtdIns[4,5]P₂ of Arp2/3 branched MACs ($1.3 \pm 0.4 \mu\text{m}^{-2}$) compared to the unbranched ($0.9 \pm 0.1 \mu\text{m}^{-2}$) actin networks. Simultaneously, the determination of the average actin intensity along the skeletonized networks, revealed a minimal increase of 1.4-fold from 2-8 mol% PtdIns[4,5]P₂ for Arp2/3 MACs, while the pure F-actin networks exhibited a ~ 3 -fold increase in the same range (cf. figure 4.13 B). Transferring this, according to chapter 5.1.1, into a relative bundling factor (cf. figure 5.5 A) unveils low filament bundling of 1.5 ± 0.1 for Arp2/3 branched compared to a strong bundling of 3.5 ± 0.5 for pure F-actin at 8 mol% PtdIns[4,5]P₂. As displayed in figure 5.5 B, by plotting the relative bundling factor against the skeleton network

density, Arp2/3 branched MACs at 8 mol% (right, magenta) are directly comparable to unbranched MACs at 3 mol% PtdIns[4,5]P₂ (left, orange), as both exhibit similar filament bundling at the same skeleton density.

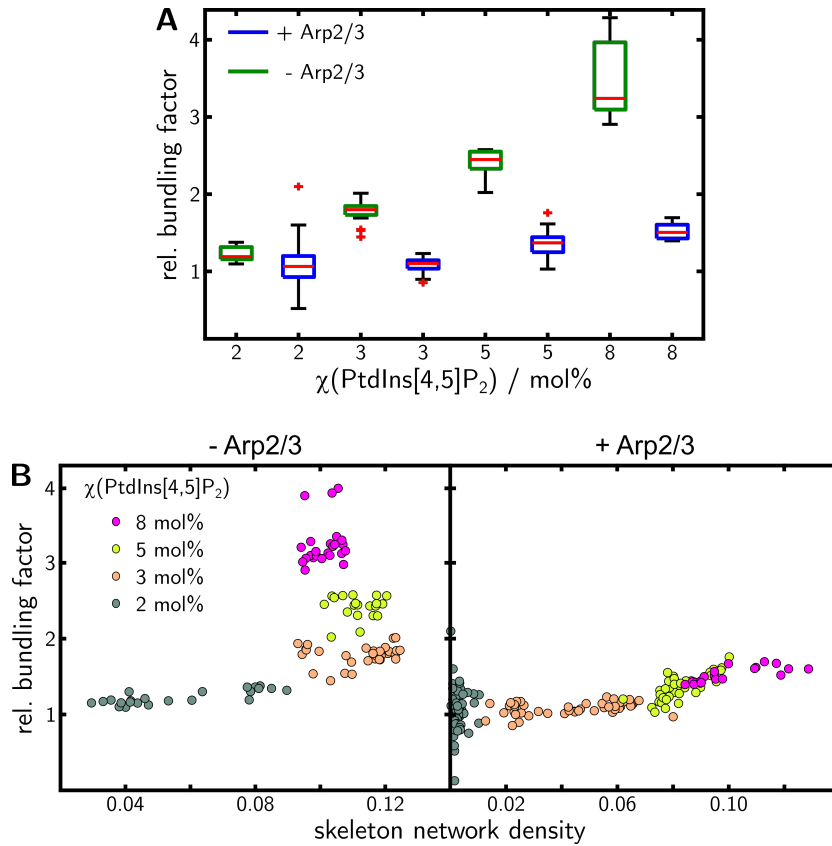


Figure 5.5: Dependence of the F-actin bundling upon the receptor lipid content and Arp2/3 branching. **A:** Relative F-actin bundling factor (δ) as a function of the PtdIns[4,5]P₂ content ($\chi(\text{PtdIns}[4,5]\text{P}_2)$) and Arp2/3 branched (blue) or unbranched (green) F-actin networks. The mean actin intensity of n images from N preparations was normalized by the averaged mean actin intensity at $\chi(\text{PtdIns}[4,5]\text{P}_2) = 1 \text{ mol}\%$ (-Arp2/3). 2 mol% ($n = 60$, $N = 7$; $n = 23$, $N = 3$), 3 mol% ($n = 48$, $N = 5$; $n = 39$, $N = 4$), 5 mol% ($n = 40$, $N = 4$; $n = 20$, $N = 2$) and 8 mol% ($n = 20$, $N = 2$; $n = 31$, $N = 3$). Boxes ranging from 25th to 75th percentiles of the sample, while whiskers represents to the most extreme data points not considered outliers (red crosses). Medians are shown as red horizontals within the boxes. **B:** Scatterplot of the relative bundling factor against the skeleton network density of the respective MAC attached to membranes with 2-8 mol% PtdIns[4,5]P₂ for Arp2/3 branched (right) or unbranched (left) F-actin networks.

Since a significant increase in filament bundling for pure F-actin networks was observed only above 3 mol% PtdIns[4,5]P₂, the weak bundling of Arp2/3 at 8 mol% PtdIns[4,5]P₂ could be caused by two factors. First, the reduced membrane-binding of Arp2/3 branched filaments may not be sufficient to exceed the critical filament

density (cf. chapter 5.1.1) above which nematic phases and filament bundles are formed. Second, the principal formation of filament branches could sterically prevent the parallel alignment of actin filaments. A combination of both would also be conceivable.

In conclusion, it was shown that Arp2/3 mediated actin branching increases the 3D network density in solution, while it simultaneously decreases the F-actin length. Further, membrane-bound Arp2/3 branched networks could be generated showing a reduced network density and no nematic phase formation.

5.3 Membrane-bound actomyosin contractility

Since the cellular actin cortex contractility is largely controlled by the motor protein myosin II, membrane-bound minimal actomyosin cortices were used to study the reorganization ability as a function of the biomimetic ezrin-PtdIns[4,5]P₂ linkage and the membrane composition.

The principal contractility of actin networks is based on the F-actin polarity and the directional motion of myosin II along this polarity. Briefly, G-actin polymerizes to F-actin by a head-to-tail assembly, leading to a structural polarity with two defined filament ends, which are designated as barbed- (plus-end) and pointed-ends (minus-end, cf. chapters 1.2 and 1.3). If bipolar myosin II filaments are bound to F-actin, the myosin head domain specifically moves towards the plus-end, leading e.g. in the case of two antiparallel actin filaments, to an opposite movement of the filaments.^[56] The motion of individual actin filaments by stationary bound myosin has been investigated since a long time by means of *in vitro* motility assays.^[225] These assays differ from the system used in this work, as myosin is immobilized on surfaces such as glass slides and F-actin movement is examined on these densely myosin decorated surfaces without any membrane attachment or F-actin network formation. However, by tracking fluorescently labeled actin filaments within membrane-bound MACs a similar F-actin motion was monitored. By determining the MSDs (cf. chapter 4.2.1) from the recorded single filament trajectories, it was determined, that the actin reorganization is an active motion, driven by myosin II. As displayed in figure 4.19 B the single filament motion seemed to originate from stationary myosin II filaments respectively small myosin clusters, which were stuck within the unlabeled MACs. Since distinct

myosins exhibit specific F-actin translocation properties, and parameters such as the ionic strength can influence the F-actin velocity, a direct comparison of the determined single filament velocity of this work ($v_{\text{mean}} = 0.8 \pm 0.4 \mu\text{m s}^{-1}$) with motility assays is rather difficult and will only serve as a classification.^[226] However, the similar conditions including rabbit myosin II basically allow a rough comparison with BUTT et al., who determined a F-actin velocity of $v_{\text{mean}} = 1.9 \pm 0.01 \mu\text{m s}^{-1}$ by means of single filament tracking.^[227] The only by 2-fold decreased filament velocity in this work, despite the ezrin-PtdIns[4,5]P₂ linkage and relatively high network density of MACs at 3 mol% (cf. figure 4.4), demonstrates the eminent dynamics of the established membrane-bound minimal actomyosin cortices.

The contractility of entire actin networks is known to be a function of the network connectivity and organization. Several publications highlighted, that cross-linkers can be used to control the F-actin network contraction and allow the switch between contractile and non-contractile networks by increasing the network connectivity.^[228–230] Furthermore, *in vitro* studies revealed that cross-linkers^[166] and capping proteins^[71] determine the length scale of actomyosin network contraction. Beside the network connectivity, the network architecture respectively organization have been found to be a key parameter of actomyosin contractility.^[231,232] Since the membrane attachment of cortical actin *in vivo* have been shown to play an essential role in cortical processes^[233,234], *in vitro* approaches have been established to investigate the actomyosin contraction on membranes. Similar to the minimal actomyosin cortices established in this work, contraction and network collapse into actomyosin asters was observed for crowded F-actin networks on membranes^[166,212,235] or membrane-bound actin networks via the artificial streptavidin-biotin linkage^[69] or His-tagged linker-proteins and Ni-NTA-DGS receptor lipids^[70,71,236]. Independent of the membrane attachment a common observation in those actomyosin networks was the fragmentation of F-actin upon the addition of myosin II. Similar observations were made in this work for the ezrin/PtdIns[4,5]P₂ membrane linked minimal cortices not only for collapsing networks, but also for non-collapsing ones (cf. figure 4.23 A). Actin filaments are semi-flexible biopolymers ($l_p = \sim 10 \mu\text{m}$) and resistant to tension, however, they easily buckle under compression force, which can be generated by single myosin motors ($\sim 2 \text{ pN}$).^[56,69,166] As shown by VOGEL et al. for membrane-bound actin networks via the quasi-covalently streptavidin-biotin linkage, bipolar myofilaments induce F-actin buckling and subsequently filament breaking (cf. figure 5.6 A).^[69] They hypothesized that filament buckling and breaking contribute to the

fundamental contraction mechanism of actomyosin cortices. While the buckling of actin filaments could not be monitored within this work, the observed shortening of membrane-bound F-actin (cf. chapter 4.2.2), as well as the selectively observed breaking of individual actin filaments (cf. figure 5.6 C) suggest a similar interaction mechanism for biomimetic membrane-bound actomyosin cortices. Nevertheless, the collapse of actomyosin networks in polar-asters, characterized by a central myosin cluster with surrounding actin filaments (cf. figure 5.6 B), suggests simultaneously a fundamentally polaritate-induced reorganization (cf. chapter 4.2.2) as shown by WOLLRAB et al. via *in vitro* and *in silico* studies.^[213] *In vivo* experimental evidence of buckling-induced contraction of cellular actin cortices is lacking. However, MEDEIROS et al. observed the myosin II induced severing of cellular F-actin bundles, which might be in indication of a similar process in cellular actin cortices.^[56,237]

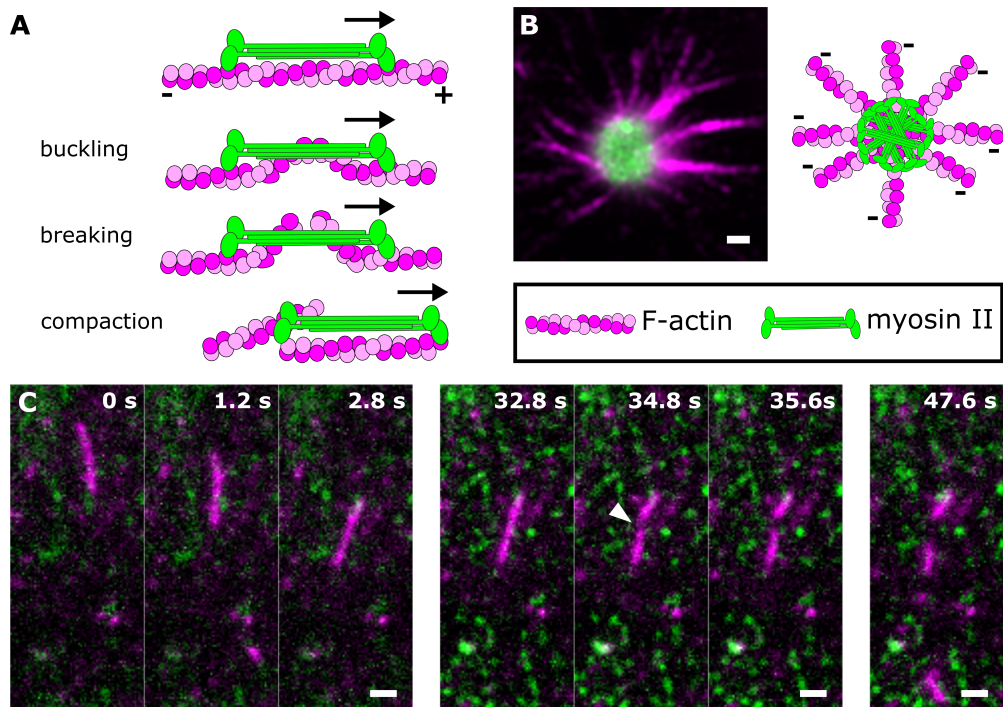


Figure 5.6: Illustration of the myosin II induced F-actin fragmentation and polar actomyosin aster structure. Schematic illustration of the myosin II induced F-actin fragmentation via filament buckling and breaking (A) and polar-aster structure formed in collapsing networks (B). Exemplary fluorescence micrographs (C), displaying the myosin II induced F-actin motion (0 - 2.8 s), filament dwelling (2.8 - 32.8 s), filament fragmentation (32.8 - 35.6 s, white arrow) and final filament resting (47.6 s). Subfigure A adapted from VOGEL et al.^[69] Scale bars: 1 μm .

While the mechanism of reorganization seemed to be independent of the membrane composition, as F-actin degradation was observed in collapsing and non-collapsing net-

works for different lipid compositions, the general network contractility of membrane-bound actomyosin cortices appears to be determined by the membrane composition. In general three different contraction modes were observed for the reorganization of the ezrin-PtdIns[4,5]P₂ attached actomyosin cortices. While the cortices attached to POPC/PtdIns[4,5]P₂ membranes showed mostly no collapse (I), (II) partially collapsing or (III) fully collapsing networks could be monitored for a membrane composition of POPC/POPS/PtdIns[4,5]P₂ in all conducted experiments (cf. figure 4.24 and figure 4.26).

However, for POPC/PtdIns[4,5]P₂ membranes, lacking POPS, the nematic order of the membrane-bound actin turned out to be a crucial parameter for the collapsing ability of actomyosin cortices (cf. figure 4.26, green). While actin networks with a low nematic order ($q_{\text{mean}} = \sim 0.15$, $N = 19$ of 26) showed no collapse into polar asters, partially and fully collapsing networks were observed at 5-8 mol% PtdIns[4,5]P₂ respectively at high nematic orders ($q_{\text{mean}} = \sim 0.2 - 0.25$, $N = 7$ of 26). As 5-8 mol% PtdIns[4,5]P₂ corresponds to an increased ezrin-PtdIns[4,5]P₂-linkage of the membrane-bound actomyosin cortices, these findings are contrary to the observations of MURREL and GARDEL, reporting a decreased network contractility with rising membrane attachment.^[166] However, this difference can be attributed to the utilized biomimetic ezrin-PtdIns[4,5]P₂ linkage and the nematic organization of the membrane-bound F-actin. As recently revealed by KORKMAZHAN and DUNN, investigating the ezrin-F-actin binding via optical trap assays, ezrin is capable of sliding along actin filaments and relaxes force when F-actin is moved in a parallel manner.^[238] Further, the authors showed that for an orthogonal force respectively movement of the actin filaments, the ezrin-F-actin interaction can be described as a slip bond, as the binding lifetime decreases with applied force. This suggests that for the used ezrin-PtdIns[4,5]P₂ linkage a minor influence of membrane attachment on the actomyosin cortex contractility is expected. However, the nematic order seems to have a greater influence, as the contractility showed a direct dependence on the nematic order (cf. figure 4.26). The formation of nematic phases generally increases the filament-filament connectivity as the membrane-bound F-actin aligns. While such increased connectivity may already have a promoting effect on network contractility^[228-230], the formation of nematic phases simultaneously also leads to bundling of membrane-bound filaments, as discussed in chapter 5.1.1. As shown by SCHÖN et al., bundling of membrane-bound F-actin via the cross-linker fascin leads to an increased filament/bundle length.^[60] As the length scale of contraction

risers with growing filament/bundle length^[71,213], nematic phase-induced bundling is likely to promote network contraction in a similar manner. Furthermore, the organization of F-actin is a major parameter controlling the network contractility. As shown by REYMANN et al. via micro patterning assays, anti-parallel organized actin bundles promote the network contraction.^[232] Assuming a random orientation of the membrane-bound F-actin, a filament bundle composition of equal amounts of parallel and anti-parallel aligned filaments (related to the filament polarity) is plausible. Since the bundle alignment can be anticipated to be random as well, a high ratio of anti-parallel aligned filaments respectively bundles would further clarify the contraction-enhancing effect of nematic phases. The distance between aligned actin filaments/bundles in nematic phases were determined to ~ 12 nm by IKAWA via AFM experiments.^[239] This gap corresponds to the the spacing within actin bundles formed by the cross-linkers α -actinin (~ 35 nm)^[240], fascin ($\sim 6 - 12$ nm)^[240,241] and fimbrin ($\sim 8 - 13$ nm)^[240,242]. WEIRICH et al. analyzed the motion of myofilaments along actin bundles formed by those three cross-linkers and revealed myosin II trapping for anti-parallel bundled actin filaments.^[243] By means of *in silico* experiments the authors were able to show that the force, generated by bipolar myosin II filaments, is directly related to the trap duration and maximized not only for an equal mixture of parallel and anti-parallel filaments within actin bundles but also for a reduced filament spacing/cross-linking distance. Since an equal distribution of parallel and anti-parallel arranged filaments/bundles is expected for nematic phases and a small distance between aligned filaments/bundles (~ 12 nm) can be assumed, the findings of WEIRICH et al. can be attributed to the observed dependence of network contraction and the degree of nematic order.

Thus, as an intermediate conclusion, the observed dependence of the network contractility on the nematic filament alignment can be attributed to an increased network connectivity and most likely also to the filament organization within the nematic phases. Furthermore, it can be stated that the formation of nematic phases seems to compensate for a strong membrane linkage of the minimal actomyosin cortices.

As mentioned above, partial or full collapse of membrane-bound actomyosin cortices was observed for all experiments on POPC/POPS/PtdIns[4,5]P₂ membranes with a low PtdIns[4,5]P₂ content of 1 - 3 mol%. In addition, in the presence of POPS the contraction of minimal actomyosin cortices showed no clear dependency between contractility and nematic order. This findings are in contrast to the POPC/PtdIns[4,5]P₂ system, where network contraction was only monitored for an increased PtdIns[4,5]P₂

content of 5-8 mol% and highly nematic order F-actin networks. However, since F-actin networks on POPS containing membranes form nematic domains already at a low PtdIns[4,5]P₂ content (cf. chapter 4.1.3.3 and 5.1.1), this discrepancy can be attributed to the general formation of nematic phases and their aforementioned discussed contraction-directing effect. In addition, as the RfS experiments presented in chapter 4.1.3.3 revealed a decreased amount of membrane-bound ezrin T567D for 1-3 mol% PtdIns[4,5]P₂ in the presence of POPS, then for 5-8 mol% PtdIns[4,5]P₂ in the absence of POPS, the reduced membrane linkage might further explain the increased contractility on POPS containing membranes. This assumption is in line with findings of NÖDING et al., who reported a decreasing network stiffness of membrane-bound MACs with a reduced ezrin-PtdIns[4,5]P₂ linkage.^[72] The hypothesis is further supported by the observation, that actomyosin networks attached to POPS containing membranes showed a full network collapse already at a q_{mean} of ~ 0.15 , while a q_{mean} of ~ 0.20 was found for POPC/PtdIns[4,5]P₂ membranes. Moreover, the network contractility on POPS containing membranes could be facilitated via repulsive interactions between the negatively charged membrane and F-actin^[214,244], as well as by the in chapter 5.1.1 suggested altered binding mode of ezrin T567D.

While for POPC/PtdIns[4,5]P₂ membranes the formation of nematic phases with increasing PtdIns[4,5]P₂ content counteracts a potential reduced network contractility for an increasing F-actin-membrane-linkage, this effect could be resolved for the POPS-system. Actomyosin cortices attached to POPS containing membranes and a PtdIns[4,5]P₂ content of 1-2 mol% PtdIns[4,5]P₂ showed in all cases a full network contraction. In contrast, only one of four cortices collapsed fully when bound to POPS membranes doped with 3 mol% PtdIns[4,5]P₂, while partial and full collapsing networks showed no significant difference in nematic order (blue, cf. figure 4.26). This suggests, that an increasing F-actin-membrane linkage reduces also for the biomimetic ezrin-PtdIns[4,5]P₂ system the contractility of membrane-bound networks.

With respect to the cell, these data show that the lipid composition is an essential factor in the regulation of actin cortex contractility and that the cellular plasma membrane composition of the inner leaflet with ~ 1 mol% PtdIns[4,5]P₂^[194] and 15-20 mol% PS^[162] promotes the actin cortex contractility. These findings reveal that lipids which are not involved in direct binding of cytoskeletal structures have an impact on those and require consideration in the design of prospective studies.

5.4 Membrane attachment of biomimetic MACs alters the mechanical properties of pore-spanning membranes

Since the cellular actin cortex is key player of the cell shape regulation and a major structural component of cellular mechanics^[10,139,173], a MAC model system on pore-spanning membranes (PSMs) was established via the biomimetic ezrin-PtdIns[4,5]P₂ linkage, to analyze by means of CLSM-AFM correlation how the binding of a MAC alters the membrane tension (σ) and viscoelasticity.

PSMs were generated by spreading DPhPC/PtdIns[4,5]P₂/ATTO390-DPPE GUVs (91.6:8:0.4) on SiO_x functionalized porous substrates ($\varnothing = 5 \mu\text{m}$). The successful preparation of PSMs could be verified by means of confocal laser scanning microscopy (cf. figure 4.28). While the freestanding PSMs (f-PSMs) could be identified as bright circles, line profiles revealed for the solid supported PSMs (s-PSMs) a reduced fluorescence intensity ($\sim 20\%$ of f-PSM intensity). These observations are in line with the findings of TESKE et al. who showed for the same surface functionalization a s-PSM fluorescence intensity of $46 \pm 20\%$ of that of the f-PSM.^[97] The authors attributed this observation to the fluorescence quenching effect of the SiO_x ($1 < x < 2$) layer.^[245] To determine the initial mechanical properties of the pure PSM, the membranes were imaged via atomic force microscopy and force distance curves (FDCs) were recorded in the f-PSM centers. The height profiles extracted from the atomic force micrographs revealed an averaged height difference of $44 \pm 9 \text{ nm}$ between the pore rim and the f-PSMs (cf. figure 4.28 B2). Since the substrates were functionalized with a SiO_x layer of 30-40 nm corresponding to the determined height difference, it might be assumed that the lipid membrane follows the SiO_x layer at the pore edge as reported for gold functionalized substrates.^[138,246] The recorded FDCs showed a fully elastic indentation for the protein-free f-PSMs, indicated by the superposition of trace and retrace (cf. figure 4.30 B1), which is in line with the indentation of f-PSMs in previous studies.^[138] From the recorded FDCs the lateral membrane tension was determined to $\sigma = 6.8 \pm 1.3 \text{ mN m}^{-1}$ ($n = 49$, $N = 2$), which is one order of magnitude higher than the reported membrane tension of DPhPC f-PSMs on SiO₂ substrates ($0.15 \pm 0.05 \text{ mN m}^{-1}$)^[138] and 6-mercapto-1-hexanol (6MH) functionalized gold substrates (1.4 mN m^{-1})^[137]. However, it corresponds approximately to the lateral tension of DOPC f-PSMs ($10.5 \pm 4.3 \text{ mN m}^{-1}$)^[247] on

SiO_x coated porous substrates. As the lateral membrane tension of f-PSMs results from the energy difference between the freestanding and solid supported part, these differences can be attributed to the different substrate functionalization and the adhesion strength of the s-PSM to the solid support.^[137,138]

While the attachment of minimal actin cortices to f-PSMs was observed in several preparations, only three f-PSMs could be analyzed via force indentation experiments. Therefore, the obtained results for the f-PSMs mechanics with a membrane-bound MAC will be discussed in a qualitative manner and only with respect to the monitored trends.

The successful f-PSM attachment of minimal actin cortices via the ezrin-PtdIns[4,5]P₂ linkage was basically shown via fluorescence micrographs (cf. figure 4.27 and 4.29). While a comparable F-actin fluorescence intensity could be detected on both, s- and f-PSMs, the exemplary actin intensity profile in figure 4.29 A2, indicates a F-actin accumulation at the pore rim of a covered pore. Since TSAI et al. reported an enhanced attachment of ezrin T567D to positively curved membranes, the F-actin accumulation might be attributed to an enrichment of ezrin-PtdIns[4,5]P₂ linkage at the s-/f-PSM junction.^[248] The finding that individual actin filaments could not be resolved on the f-PSMs might be explainable by a length-dependent respectively geometry dependent F-actin attachment to the freestanding PSMs. F-actin exhibits a persistence length of 10 - 18 μm^[8,9], which corresponds to at least twice of the utilized pore radius of $\varnothing = 5 \mu\text{m}$. Since the atomic force micrographs revealed a height difference between s- and f-PSMs of $44 \pm 9 \text{ nm}$ for the pure DPhPC membranes and an even pronounced difference for the MAC attached PSMs, the f-PSM geometry and persistence length of F-actin are likely to prevent a binding of large actin filaments to the freestanding membranes. This hypothesis is supported by the finding that for ATT0-594 labeled actin filaments, under the same conditions, long filaments were observed on the s-PSMs but not on f-PSMs (cf. chapter A.6.2). The AFM indentation experiments revealed a decreased lateral membrane tension from $\sigma = 6.8 \pm 1.3 \text{ mN m}^{-1}$ for pure DPhPC f-PSMs to $\sigma = 0.5 \pm 0.3 \text{ mN m}^{-1}$ for f-PSMs with an attached minimal actin cortex. While the underlying origin of this effect remains unclear as control experiments are missing, the general trend is in line with the findings of SCHÖN using pore spanning membranes and an electrostatic F-actin-membrane-attachment.^[192] Furthermore, the determined lateral membrane tension of $\sigma = 0.5 \pm 0.3 \text{ mN m}^{-1}$ resembles the reported tensions of apical cell membranes ($0.24 \pm 0.22 \text{ mN m}^{-1}$) and membranes with electrostatic attached

MACs ($0.49 \pm 0.32 \text{ mN m}^{-1}$) on porous substrates reported by HUBRICH et al.^[135] Since the viscoelastic behavior of cells upon external deformation have been attributed in several studies to the cortical actin network^[10,249,250], the detected viscoelastic response of f-PSMs with an membrane-bound MAC suggest that the established minimal MAC model system is capable of resembling this fundamental mechanical property (cf. figure 4.30 B2).

To conclude, the presented results are despite the small sample size in harmony with the known literature and suggest that the established model system is capable of mimicking essential mechanical properties of the cellular actin cortex. Thus, the novel minimal actin cortex on pore-spanning membranes attached via the physiological relevant ezrin-PtdIns[4,5]P₂ linkage seems to be a promising *in vitro* approach to disentangle the complex interrelationships of cellular mechanics.

6 Conclusion

The actin cortex of mammalian cells, being a thin plasma membrane linked actin layer, regulates fundamental aspect of cellular processes such as exocytosis, membrane trafficking and cell morphogenesis. Essential for these characteristics are the organization and contractility of the cortical actin network, which are controlled by a manifold of actin-binding proteins (ABPs). To identify fundamental components and their functionalities membrane-bound minimal actin cortices (MACs) have been studied over the past decades.

In this thesis biomimetic membrane-bound MACs were generated by attaching pre-polymerized filamentous actin (F-actin) via the ERM protein ezrin to L- α -phosphatidylinositol-4,5-bisphosphate (PtdIns[4,5]P₂) doped solid-supported lipid bilayers (SLBs). The MAC organization was studied with regard to membrane composition by means of confocal laser scanning microscopy (CLSM) and reflectometric interference spectroscopy (RIfS). It could be demonstrated that the amount of membrane-bound F-actin increases as a function of the ezrin-PtdIns[4,5]P₂ linkage from 1 - 8 mol% PtdIns[4,5]P₂. Moreover, it was shown, that growing amounts of membrane attached F-actin lead to a morphology change, from entangled (1 - 3 mol% PtdIns[4,5]P₂) into nematically aligned (5 - 8 mol% PtdIns[4,5]P₂) networks and also from single filaments (1 - 3 mol% PtdIns[4,5]P₂) into filament bundles (5 - 8 mol% PtdIns[4,5]P₂). In addition, it was found that a membrane-bound MAC alters the diffusive properties of the underlying membrane. To analyze the ezrin-linkage and F-actin membrane attachment for a membrane composition resembling the inner human plasma membrane, SLBs were doped with POPS. RIfS experiments revealed a generally increased amount of membrane-bound ezrin in the presence of POPS compared to membranes lacking POPS. The increased amount of membrane-bound ezrin was reflected by a significantly increased F-actin density and nematically network organization at low receptor lipid concentrations (1 - 3 mol% PtdIns[4,5]P₂). The effect of a branched F-actin network and a crowded media, mimicking the cytoplasm, on MAC organization was investigated with the actin-related-protein 2/3 complex (Arp2/3), polymerizing actin branches at pre-formed filaments, and the crowding agent methyl cellulose (MC). While Arp2/3 branched actin networks were proven to form dense 3D networks in solution, membrane attachment studies via the ezrin-PtdIns[4,5]P₂ linkage revealed a decreased network density in comparison to unbranched networks. Simultaneously, it was shown that membrane-bound and

Arp2/3 branched networks failed to form nematic phases or filament bundles despite a high PtdIns[4,5]P₂ content (8 mol%). For MC crowded and ezrin-PtdIns[4,5]P₂ membrane-bound MACs, an optimal concentration of 0.18 *w/v* % MC, showing no crowding agent induced filament bundling, was determined to increase the amount of membrane-bound F-actin in comparison to uncrowded conditions. As no unspecific membrane attachment could be monitored for crowded networks in the absence of the ezrin-PtdIns[4,5]P₂-linkage, the results might indicate that the crowded cellular cytoplasm affects the cortical actin organization.

As the actin cortex is a key regulator of the cell membrane tension, a MAC model system on pore-spanning membranes (PSMs) was established via the biomimetic ezrin-PtdIns[4,5]P₂ linkage, in order to probe the lateral membrane tension of freestanding-PSMs (f-PSMs) by means of AFM indentation experiments. Although, a quantitative interpretation of the data could not be performed due to the small sample size, the qualitative changes of a reduced lateral membrane tension and viscoelastic force response of f-PSMs with membrane-bound MACs show that the established model system is a promising approach to explore the complex interrelationships of cellular mechanics.

In order to reveal how myosin II motors reorganize membrane-bound MACs as a function of the ezrin-PtdIns[4,5]P₂ linkage and membrane composition, MACs were prepared on SLBs with a different PtdIns[4,5]P₂ content and in the absence or presence of POPS. The MAC contractility were generally found to be a function of the network organization and membrane attachment, which are both dictated by the membrane composition. In particular, the results indicated, that an increasing membrane-actin linkage via ezrin-PtdIns[4,5]P₂ leads to a reduced network contractility. In contrast, a dense network organization into nematically aligned phases has been shown to promote contraction and also appears to have a greater influence than the membrane linkage, as the formation of nematic phases seems to compensate for an increased membrane linkage. A membrane composition of 1-2 mol% PtdIns[4,5]P₂ and 17 mol% POPS, resembling the inner plasma membrane composition of human cells, has been shown to combine both, a low level of ezrin-PtdIns[4,5]P₂ linkage and high nematic phase formation, promoting the actomyosin contractility. With respect to the *in vivo* situation, this data shows that the lipid composition is an essential factor in the regulation of actin cortex contractility. Moreover, these findings highlight that lipids which are not associated with the direct binding of cytoskeletal structures require consideration in the design of prospective studies.

7 Bibliography

- [1] T. Hohmann, F. Dehghani, The cytoskeleton—a complex interacting meshwork, *Cells* **2019**, *8*(4), 362.
- [2] H. Y. G. Lim, N. Plachta, Cytoskeletal control of early mammalian development, *Nature Reviews Molecular Cell Biology* **2021**, *22*(8), 548–562.
- [3] F. Huber, A. Boire, M. P. López, G. H. Koenderink, Cytoskeletal crosstalk: when three different personalities team up, *Current Opinion in Cell Biology* **2015**, *32*, 39–47.
- [4] D. A. Fletcher, R. D. Mullins, Cell mechanics and the cytoskeleton, *Nature* **2010**, *463*(7280), 485–492.
- [5] D. Sept, Microtubule polymerization: one step at a time, *Current Biology* **2007**, *17*(17), 764–766.
- [6] J. Käs, H. Strey, J. Tang, D. Finger, R. Ezzell, E. Sackmann, P. Janmey, F-actin, a model polymer for semiflexible chains in dilute, semidilute, and liquid crystalline solutions, *Biophysical Journal* **1996**, *70*(2), 609–625.
- [7] J. Alvarado, G. H. Koenderink, Reconstituting cytoskeletal contraction events with biomimetic actin–myosin active gels, *Methods in cell biology* **2015**, *128*, 83–103.
- [8] L. Blanchoin, R. Boujemaa-Paterski, C. Sykes, J. Plastino, Actin dynamics, architecture, and mechanics in cell motility, *Physiological Reviews* **2014**, *94*(1), 235–263.
- [9] F. Gittes, B. Mickey, J. Nettleton, J. Howard, Flexural rigidity of microtubules and actin filaments measured from thermal fluctuations in shape., *The Journal of Cell Biology* **1993**, *120*(4), 923–934.
- [10] P. Chugh, E. K. Paluch, The actin cortex at a glance, *Journal of Cell Science* **2018**, *131*(14), jcs186254.
- [11] D. S. Kudryashov, E. Reisler, ATP and ADP actin states, *Biopolymers* **2013**, *99*(4), 245–256.

- [12] I. M. Herman, Actin isoforms, *Current Opinion in Cell Biology* **1993**, 5(1), 48–55.
- [13] R. Dominguez, K. C. Holmes, Actin structure and function, *Annual Review of Biophysics* **2011**, 40, 169–186.
- [14] W. Kabsch, H. G. Mannherz, D. Suck, E. F. Pai, K. C. Holmes, Atomic structure of the actin: DNase I complex, *Nature* **1990**, 347(6288), 37–44.
- [15] R. Dominguez, Actin-binding proteins—a unifying hypothesis, *Trends in Biochemical Sciences* **2004**, 29(11), 572–578.
- [16] L. R. Otterbein, P. Graceffa, R. Dominguez, The crystal structure of uncomplexed actin in the ADP state, *Science* **2001**, 293(5530), 708–711.
- [17] T. D. Pollard, G. G. Borisy, Cellular motility driven by assembly and disassembly of actin filaments, *Cell* **2003**, 112(4), 453–465.
- [18] E. D. Korn, M.-F. Carrier, D. Pantaloni, Actin polymerization and ATP hydrolysis, *Science* **1987**, 238(4827), 638–644.
- [19] A. Wegner, Head to tail polymerization of actin, *Journal of Molecular Biology* **1976**, 108(1), 139–150.
- [20] S. Kühn, H. G. Mannherz, *Actin: structure, function, dynamics, and interactions with bacterial toxins*, Springer, **2016**, 1–34.
- [21] T. Oda, Y. Maéda, Multiple conformations of F-actin, *Structure* **2010**, 18(7), 761–767.
- [22] L. Blanchoin, T. D. Pollard, Hydrolysis of ATP by polymerized actin depends on the bound divalent cation but not profilin, *Biochemistry* **2002**, 41(2), 597–602.
- [23] D. I. Levitsky, A. V. Pivovarova, V. V. Mikhailova, O. P. Nikolaeva, Thermal unfolding and aggregation of actin: Stabilization and destabilization of actin filaments, *The FEBS Journal* **2008**, 275(17), 4280–4295.
- [24] J.-M. Neuhaus, M. Wanger, T. Keiser, A. Wegner, Treadmilling of actin, *Journal of Muscle Research & Cell Motility* **1983**, 4(5), 507–527.

-
- [25] K. Murakami, T. Yasunaga, T. Q. Noguchi, Y. Gomibuchi, K. X. Ngo, T. Q. Uyeda, T. Wakabayashi, Structural basis for actin assembly, activation of ATP hydrolysis, and delayed phosphate release, *Cell* **2010**, *143*(2), 275–287.
- [26] J. Hanson, J. Lowy, The structure of F-actin and of actin filaments isolated from muscle, *Journal of Molecular Biology* **1963**, *6*(1), 46–IN5.
- [27] E. Grazi, What is the diameter of the actin filament?, *FEBS Letters* **1997**, *405*(3), 249–252.
- [28] T. Fujii, A. H. Iwane, T. Yanagida, K. Namba, Direct visualization of secondary structures of F-actin by electron cryomicroscopy, *Nature* **2010**, *467*(7316), 724–728.
- [29] T. D. Pollard, Actin and actin-binding proteins, *Cold Spring Harbor Perspectives in Biology* **2016**, *8*(8), a018226.
- [30] T. D. Pollard, L. Blanchoin, R. D. Mullins, Molecular mechanisms controlling actin filament dynamics in nonmuscle cells, *Annual Review of Biophysics and Biomolecular Structure* **2000**, *29*(1), 545–576.
- [31] M. Edwards, A. Zwolak, D. A. Schafer, D. Sept, R. Dominguez, J. A. Cooper, Capping protein regulators fine-tune actin assembly dynamics, *Nature Reviews Molecular cell biology* **2014**, *15*(10), 677–689.
- [32] T. P. Stossel, J. Condeelis, L. Cooley, J. H. Hartwig, A. Noegel, M. Schleicher, S. S. Shapiro, Filamins as integrators of cell mechanics and signalling, *Nature Reviews Molecular cell biology* **2001**, *2*(2), 138–145.
- [33] T. M. Svitkina, Actin cell cortex: structure and molecular organization, *Trends in Cell Biology* **2020**, *30*(7), 556–565.
- [34] S. Tojkander, G. Gateva, P. Lappalainen, Actin stress fibers—assembly, dynamics and biological roles, *Journal of Cell Science* **2012**, *125*(8), 1855–1864.
- [35] S. Espinoza-Sanchez, L. A. Metskas, S. Z. Chou, E. Rhoades, T. D. Pollard, Conformational changes in Arp2/3 complex induced by ATP, WASp-VCA, and actin filaments, *Proceedings of the National Academy of Sciences* **2018**, *115*(37), E8642–E8651.

- [36] M. Biro, Y. Romeo, S. Kroschwald, M. Bovellan, A. Boden, J. Tcherkezian, P. P. Roux, G. Charras, E. K. Paluch, Cell cortex composition and homeostasis resolved by integrating proteomics and quantitative imaging, *Cytoskeleton* **2013**, *70*(11), 741–754.
- [37] M. Roh-Johnson, G. Shemer, C. D. Higgins, J. H. McClellan, A. D. Werts, U. S. Tulu, L. Gao, E. Betzig, D. P. Kiehart, B. Goldstein, Triggering a cell shape change by exploiting preexisting actomyosin contractions, *Science* **2012**, *335*(6073), 1232–1235.
- [38] S. Hannemann, R. Madrid, J. Stastna, T. Kitzing, J. Gasteier, A. Schönichen, J. Bouchet, A. Jimenez, M. Geyer, R. Grosse, et al., The Diaphanous-related Formin FHOD1 associates with ROCK1 and promotes Src-dependent plasma membrane blebbing, *Journal of Biological Chemistry* **2008**, *283*(41), 27891–27903.
- [39] K. M. Eisenmann, E. S. Harris, S. M. Kitchen, H. A. Holman, H. N. Higgs, A. S. Alberts, Dia-interacting protein modulates formin-mediated actin assembly at the cell cortex, *Current Biology* **2007**, *17*(7), 579–591.
- [40] N. Morone, T. Fujiwara, K. Murase, R. S. Kasai, H. Ike, S. Yuasa, J. Usukura, A. Kusumi, Three-dimensional reconstruction of the membrane skeleton at the plasma membrane interface by electron tomography, *The Journal of Cell Biology* **2006**, *174*(6), 851–862.
- [41] A. G. Clark, K. Dierkes, E. K. Paluch, Monitoring actin cortex thickness in live cells, *Biophysical Journal* **2013**, *105*(3), 570–580.
- [42] A. Bretscher, K. Edwards, R. G. Fehon, ERM proteins and merlin: integrators at the cell cortex, *Nature Reviews Molecular Cell Biology* **2002**, *3*(8), 586–599.
- [43] Y. Senju, F.-C. Tsai, A biophysical perspective of the regulatory mechanisms of ezrin/radixin/moesin proteins, *Biophysical Reviews* **2022**, 1–10.
- [44] R. G. Fehon, A. I. McClatchey, A. Bretscher, Organizing the cell cortex: the role of ERM proteins, *Nature Reviews Molecular Cell Biology* **2010**, *11*(4), 276–287.

-
- [45] S. Yonemura, T. Matsui, S. Tsukita, S. Tsukita, Rho-dependent and-independent activation mechanisms of ezrin/radixin/moesin proteins: an essential role for polyphosphoinositides in vivo, *Journal of Cell Science* **2002**, *115*(12), 2569–2580.
- [46] B. T. Fievet, A. Gautreau, C. Roy, L. Del Maestro, P. Mangeat, D. Louvard, M. Arpin, Phosphoinositide binding and phosphorylation act sequentially in the activation mechanism of ezrin, *The Journal of Cell Biology* **2004**, *164*(5), 653–659.
- [47] M. Katan, S. Cockcroft, Phosphatidylinositol (4, 5) bisphosphate: diverse functions at the plasma membrane, *Essays in Biochemistry* **2020**, *64*(3), 513–531.
- [48] W. J. Smith, N. Nassar, A. Bretscher, R. A. Cerione, P. A. Karplus, Structure of the active N-terminal domain of ezrin: conformational and mobility changes identify keystone interactions, *Journal of Biological Chemistry* **2003**, *278*(7), 4949–4956.
- [49] K. Dasbiswas, S. Hu, F. Schnorrer, S. A. Safran, A. D. Bershadsky, Ordering of myosin II filaments driven by mechanical forces: experiments and theory, *Philosophical Transactions of the Royal Society B: Biological Sciences* **2018**, *373*(1747), 20170114.
- [50] A. B. Verkhovskiy, G. G. Borisy, Non-sarcomeric mode of myosin II organization in the fibroblast lamellum., *The Journal of Cell Biology* **1993**, *123*(3), 637–652.
- [51] M. S. e Silva, M. Depken, B. Stuhmann, M. Korsten, F. C. MacKintosh, G. H. Koenderink, Active multistage coarsening of actin networks driven by myosin motors, *Proceedings of the National Academy of Sciences* **2011**, *108*(23), 9408–9413.
- [52] N. Bhagavan, C.-E. Ha, in *Essentials of Medical Biochemistry (Second Edition)*, Academic Press, San Diego, second edition edition, **2015**, 339–361.
- [53] M. Vicente-Manzanares, X. Ma, R. S. Adelstein, A. R. Horwitz, Non-muscle myosin II takes centre stage in cell adhesion and migration, *Nature Reviews Molecular Cell Biology* **2009**, *10*(11), 778–790.

- [54] E. Behrmann, M. Müller, P. A. Penczek, H. G. Mannherz, D. J. Manstein, S. Raunser, Structure of the rigor actin-tropomyosin-myosin complex, *Cell* **2012**, *150*(2), 327–338.
- [55] T. Svitkina, The actin cytoskeleton and actin-based motility, *Cold Spring Harbor Perspectives in Biology* **2018**, *10*(1), a018267.
- [56] G. H. Koenderink, E. K. Paluch, Architecture shapes contractility in actomyosin networks, *Current Opinion in Cell Biology* **2018**, *50*, 79–85.
- [57] D. V. Köster, S. Mayor, Cortical actin and the plasma membrane: inextricably intertwined, *Current Opinion in Cell Biology* **2016**, *38*, 81–89.
- [58] E. Sitarska, A. Diz-Muñoz, Pay attention to membrane tension: Mechanobiology of the cell surface, *Current Opinion in Cell Biology* **2020**, *66*, 11–18.
- [59] N. C. Gauthier, M. A. Fardin, P. Roca-Cusachs, M. P. Sheetz, Temporary increase in plasma membrane tension coordinates the activation of exocytosis and contraction during cell spreading, *Proceedings of the National Academy of Sciences* **2011**, *108*(35), 14467–14472.
- [60] M. Schön, I. Mey, C. Steinem, Influence of cross-linkers on ezrin-bound minimal actin cortices, *Progress in Biophysics and Molecular Biology* **2019**, *144*, 91–101.
- [61] J. D. Cortese, B. Schwab, C. Frieden, E. L. Elson, Actin polymerization induces a shape change in actin-containing vesicles, *Proceedings of the National Academy of Sciences* **1989**, *86*(15), 5773–5777.
- [62] W. Häckl, M. Bärmann, E. Sackmann, Shape changes of self-assembled actin bilayer composite membranes, *Physical Review Letters* **1998**, *80*(8), 1786.
- [63] E. Schäfer, M. Vache, T.-T. Kliesch, A. Janshoff, Mechanical response of adherent giant liposomes to indentation with a conical AFM-tip, *Soft Matter* **2015**, *11*(22), 4487–4495.
- [64] E. Schäfer, T.-T. Kliesch, A. Janshoff, Mechanical properties of giant liposomes compressed between two parallel plates: impact of artificial actin shells, *Langmuir* **2013**, *29*(33), 10463–10474.

-
- [65] Y. Zhang, C.-m. Cheng, B. Cusick, P. R. LeDuc, Chemically encapsulated structural elements for probing the mechanical responses of biologically inspired systems, *Langmuir* **2007**, *23*(15), 8129–8134.
- [66] K. Guevorkian, J. Manzi, L.-L. Pontani, F. Brochard-Wyart, C. Sykes, Mechanics of biomimetic liposomes encapsulating an actin shell, *Biophysical Journal* **2015**, *109*(12), 2471–2479.
- [67] E. Helfer, S. Harlepp, L. Bourdieu, J. Robert, F. MacKintosh, D. Chatenay, Microrheology of biopolymer-membrane complexes, *Physical Review Letters* **2000**, *85*(2), 457–460.
- [68] L. Limozin, E. Sackmann, Polymorphism of cross-linked actin networks in giant vesicles, *Physical Review Letters* **2002**, *89*(16), 168103.
- [69] S. K. Vogel, Z. Petrasek, F. Heinemann, P. Schwille, Myosin motors fragment and compact membrane-bound actin filaments, *Elife* **2013**, *2*, e00116.
- [70] K. A. Ganzinger, S. K. Vogel, J. Mücksch, P. Blumhardt, P. Schwille, Myosin-II activity generates a dynamic steady state with continuous actin turnover in a minimal actin cortex, *Journal of Cell Science* **2019**, *132*(4), jcs219899.
- [71] D. V. Köster, K. Husain, E. Iljazi, A. Bhat, P. Bieling, R. D. Mullins, M. Rao, S. Mayor, Actomyosin dynamics drive local membrane component organization in an in vitro active composite layer, *Proceedings of the National Academy of Sciences* **2016**, *113*(12), E1645–E1654.
- [72] H. Nöding, M. Schön, C. Reinermann, N. Dörrer, A. Kürschner, B. Geil, I. Mey, C. Heussinger, A. Janshoff, C. Steinem, Rheology of membrane-attached minimal actin cortices, *The Journal of Physical Chemistry B* **2018**, *122*(16), 4537–4545.
- [73] S. Bosk, J. A. Braunger, V. Gerke, C. Steinem, Activation of F-actin binding capacity of ezrin: synergism of PIP2 interaction and phosphorylation, *Biophysical Journal* **2011**, *100*(7), 1708–1717.
- [74] M. A. Lemmon, Phosphoinositide recognition domains, *Traffic* **2003**, *4*(4), 201–213.

- [75] D. Lupyan, M. Mezei, D. E. Logothetis, R. Osman, A molecular dynamics investigation of lipid bilayer perturbation by PIP₂, *Biophysical Journal* **2010**, *98*(2), 240–247.
- [76] A. Herrig, M. Janke, J. Austermann, V. Gerke, A. Janshoff, C. Steinem, Cooperative adsorption of ezrin on PIP₂-containing membranes, *Biochemistry* **2006**, *45*(43), 13025–13034.
- [77] C. Langlais, B. Korn, *Recombinant Protein Expression in Bacteria*, Springer Berlin Heidelberg, Berlin, Heidelberg, **2006**, 1609–1616.
- [78] J. W. Dubendorf, F. W. Studier, Controlling basal expression in an inducible T7 expression system by blocking the target T7 promoter with lac repressor, *Journal of Molecular Biology* **1991**, *219*(1), 45–59.
- [79] H. Block, B. Maertens, A. Spriestersbach, N. Brinker, J. Kubicek, R. Fabis, J. Labahn, F. Schäfer, Immobilized-metal affinity chromatography (IMAC): a review, *Methods in Enzymology* **2009**, *463*, 439–473.
- [80] E. Hochuli, H. Döbeli, A. Schacher, New metal chelate adsorbent selective for proteins and peptides containing neighbouring histidine residues, *Journal of Chromatography A* **1987**, *411*, 177–184.
- [81] U. K. Laemmli, Cleavage of structural proteins during the assembly of the head of bacteriophage T4, *Nature* **1970**, *227*(5259), 680–685.
- [82] H. Schägger, Tricine–sds-page, *Nature Protocols* **2006**, *1*(1), 16–22.
- [83] S. S. Margossian, S. Lowey, Preparation of myosin and its subfragments from rabbit skeletal muscle, *Methods in Enzymology* **1982**, *85*, 55–71.
- [84] H. N. Aguilar, B. Mitchell, Physiological pathways and molecular mechanisms regulating uterine contractility, *Human reproduction update* **2010**, *16*(6), 725–744.
- [85] G. J. Lutz, R. L. Lieber, Skeletal muscle myosin II structure and function., *Exercise and Sport Sciences Reviews* **1999**, *27*, 63–77.
- [86] B. J. Olson, Assays for determination of protein concentration, *Current Protocols in Pharmacology* **2016**, *73*(1), A–3A.

-
- [87] G. R. Grimsley, C. N. Pace, Spectrophotometric Determination of Protein Concentration, *Current Protocols in Protein Science* **2003**, *33*(1), 3.1.1–3.1.9.
- [88] C. P. Toseland, Fluorescent labeling and modification of proteins, *Journal of Chemical Biology* **2013**, *6*(3), 85–95.
- [89] G. W. Anderson, J. E. Zimmerman, F. M. Callahan, The use of esters of N-hydroxysuccinimide in peptide synthesis, *Journal of the American Chemical Society* **1964**, *86*(9), 1839–1842.
- [90] M. Brinkley, A brief survey of methods for preparing protein conjugates with dyes, haptens and crosslinking reagents, *Bioconjugate Chemistry* **1992**, *3*(1), 2–13.
- [91] R. L. DeBiasio, L.-L. Wang, G. W. Fisher, D. L. Taylor, The dynamic distribution of fluorescent analogues of actin and myosin in protrusions at the leading edge of migrating Swiss 3T3 fibroblasts., *The Journal of Cell Biology* **1988**, *107*(6), 2631–2645.
- [92] T. Litschel, P. Schwille, Protein reconstitution inside giant unilamellar vesicles, *Annual Review of Biophysics* **2021**, *50*, 525–548.
- [93] J. P. Reeves, R. M. Dowben, Formation and properties of thin-walled phospholipid vesicles, *Journal of Cellular Physiology* **1969**, *73*(1), 49–60.
- [94] S. Pautot, B. J. Frisken, D. Weitz, Production of unilamellar vesicles using an inverted emulsion, *Langmuir* **2003**, *19*(7), 2870–2879.
- [95] B. Haller, K. Göpfrich, M. Schröter, J.-W. Janiesch, I. Platzman, J. P. Spatz, Charge-controlled microfluidic formation of lipid-based single- and multicompartments, *Lab on a Chip* **2018**, *18*(17), 2665–2674.
- [96] M. I. Angelova, D. S. Dimitrov, Liposome electroformation, *Faraday Discussions of the Chemical Society* **1986**, *81*, 303–311.
- [97] N. Teske, J. Sibold, J. Schumacher, N. K. Teiwes, M. Gleisner, I. Mey, C. Steinem, Continuous Pore-Spanning Lipid Bilayers on Silicon Oxide-Coated Porous Substrates, *Langmuir* **2017**, *33*(49), 14175–14183.

- [98] J. X. Tang, P. A. Janmey, T. P. Stossel, T. Ito, Thiol oxidation of actin produces dimers that enhance the elasticity of the F-actin network, *Biophysical Journal* **1999**, *76*(4), 2208–2215.
- [99] T. Cordes, J. Vogelsang, P. Tinnefeld, On the mechanism of Trolox as antiblinking and antibleaching reagent, *Journal of The American Chemical Society* **2009**, *131*(14), 5018–5019.
- [100] G. Proll, G. Markovic, L. Steinle, G. Gauglitz, in *Biosensors and Biodetection*, Springer, **2009**, 167–178.
- [101] A. Brecht, G. Gauglitz, W. Nahm, Interferometric measurements used in chemical and biochemical sensors, *Analisis* **1992**, *20*(3), 135–140.
- [102] G. Gauglitz, A. Brecht, G. Kraus, W. Mahm, Chemical and biochemical sensors based on interferometry at thin (multi-) layers, *Sensors and Actuators B: Chemical* **1993**, *11*(1-3), 21–27.
- [103] I. Thormählen, J. Straub, U. Grigull, Refractive index of water and its dependence on wavelength, temperature, and density, *Journal of Physical and Chemical Reference Data* **1985**, *14*(4), 933–945.
- [104] I. H. Malitson, Interspecimen comparison of the refractive index of fused silica, *Josa* **1965**, *55*(10), 1205–1209.
- [105] N. Granqvist, M. Yliperttula, S. Vaaelimaeki, P. Pulkkinen, H. Tenhu, T. Viitala, Control of the morphology of lipid layers by substrate surface chemistry, *Langmuir* **2014**, *30*(10), 2799–2809.
- [106] J. W. Lichtman, J.-A. Conchello, Fluorescence microscopy, *Nature Methods* **2005**, *2*(12), 910–919.
- [107] M. J. Sanderson, I. Smith, I. Parker, M. D. Bootman, Fluorescence microscopy, *Cold Spring Harbor Protocols* **2014**, *2014*(10), pdb.top071795.
- [108] A. L. Mattheyses, S. M. Simon, J. Z. Rappoport, Imaging with total internal reflection fluorescence microscopy for the cell biologist, *Journal of Cell Science* **2010**, *123*(21), 3621–3628.
- [109] M. Minsky, Memoir on inventing the confocal scanning microscope, *Scanning* **1988**, *10*(4), 128–138.

-
- [110] R. W. Cole, T. Jinadasa, C. M. Brown, Measuring and interpreting point spread functions to determine confocal microscope resolution and ensure quality control, *Nature Protocols* **2011**, 6(12), 1929–1941.
- [111] H. Kirshner, D. Sage, M. Unser, in *Proceedings of the Twelfth International Conference on Methods and Applications of Fluorescence Spectroscopy, Imaging and Probes (MAF'11)*, 154.
- [112] H. Kirshner, F. Aguet, D. Sage, M. Unser, 3-D PSF fitting for fluorescence microscopy: implementation and localization application, *Journal of Microscopy* **2013**, 249(1), 13–25.
- [113] M. Gleisner, PhD thesis, Niedersächsische Staats-und Universitätsbibliothek Göttingen, **2016**.
- [114] L. Rayleigh, XV. On the theory of optical images, with special reference to the microscope, *The London, Edinburgh, and Dublin Philosophical Magazine and Journal of Science* **1896**, 42(255), 167–195.
- [115] S. Hell, G. Reiner, C. Cremer, E. H. Stelzer, Aberrations in confocal fluorescence microscopy induced by mismatches in refractive index, *Journal of Microscopy* **1993**, 169(3), 391–405.
- [116] J.-A. Conchello, J. W. Lichtman, Optical sectioning microscopy, *Nature Methods* **2005**, 2(12), 920–931.
- [117] S. Wilhelm, B. Gröbler, M. Gluch, H. Heinz, Die konfokale laser scanning mikroskopie, *Mikroskopie von Carl Zeiss* **2003**.
- [118] J. Huff, The Airyscan detector from ZEISS: confocal imaging with improved signal-to-noise ratio and super-resolution, *Nature Methods* **2015**, 12(12), i–ii.
- [119] L. Schermelleh, R. Heintzmann, H. Leonhardt, A guide to super-resolution fluorescence microscopy, *Journal of Cell Biology* **2010**, 190(2), 165–175.
- [120] K. Korobchevskaya, B. C. Lagerholm, H. Colin-York, M. Fritzsche, in *Photonics*, Vol. 4, Multidisciplinary Digital Publishing Institute, Vol. 4, 41.
- [121] K. Weisshart, The basic principle of airyscanning, *Zeiss Technology Note* **2014**, 22.

- [122] F. Pincet, V. Adrien, R. Yang, J. Delacotte, J. E. Rothman, W. Urbach, D. Tareste, FRAP to characterize molecular diffusion and interaction in various membrane environments, *PLoS One* **2016**, *11*(7), e0158457.
- [123] T. K. Meyvis, S. C. De Smedt, P. Van Oostveldt, J. Demeester, Fluorescence recovery after photobleaching: a versatile tool for mobility and interaction measurements in pharmaceutical research, *Pharmaceutical Research* **1999**, *16*(8), 1153–1162.
- [124] N. Lorén, J. Hagman, J. K. Jonasson, H. Deschout, D. Bernin, F. Cella-Zanacchi, A. Diaspro, J. G. McNally, M. Ameloot, N. Smisdom, et al., Fluorescence recovery after photobleaching in material and life sciences: putting theory into practice, *Quarterly Reviews of Biophysics* **2015**, *48*(3), 323–387.
- [125] P. Jönsson, M. P. Jonsson, J. O. Tegenfeldt, F. Höök, A method improving the accuracy of fluorescence recovery after photobleaching analysis, *Biophysical Journal* **2008**, *95*(11), 5334–5348.
- [126] K. N. Fish, Total internal reflection fluorescence (TIRF) microscopy, *Current Protocols in Cytometry* **2009**, *50*(1), 12–18.
- [127] T. J. F. Stephen T. Ross, Stanley Schwartz, M. W. Davidson, Total Internal Reflection Fluorescence (TIRF) Microscopy, <https://www.microscopyu.com/techniques/fluorescence/total-internal-reflection-fluorescence-tirf-microscopy>, **Dec. 2021**.
- [128] D. J. Müller, A. C. Dumitru, C. Lo Giudice, H. E. Gaub, P. Hinterdorfer, G. Hummer, J. J. De Yoreo, Y. F. Dufrêne, D. Alsteens, Atomic force microscopy-based force spectroscopy and multiparametric imaging of biomolecular and cellular systems, *Chemical Reviews* **2020**, *121*(19), 11701–11725.
- [129] T. Ando, T. Uchihashi, S. Scheuring, Filming biomolecular processes by high-speed atomic force microscopy, *Chemical Reviews* **2014**, *114*(6), 3120–3188.
- [130] E. Meyer, Atomic force microscopy, *Progress in Surface Science* **1992**, *41*(1), 3–49.

-
- [131] H.-J. Butt, B. Cappella, M. Kappl, Force measurements with the atomic force microscope: Technique, interpretation and applications, *Surface Science Reports* **2005**, *59*(1-6), 1–152.
- [132] B. Voigtländer, *Atomic Force Microscopy*, Springer, **2019**.
- [133] S. Maghsoudy-Louyeh, M. Kropf, B. Tittmann, Review of progress in atomic force microscopy, *The Open Neuroimaging Journal* **2018**, *12*(1).
- [134] J. L. Hutter, J. Bechhoefer, Calibration of atomic-force microscope tips, *Review of Scientific Instruments* **1993**, *64*(7), 1868–1873.
- [135] H. Hubrich, I. P. Mey, B. R. Brückner, P. Mühlenbrock, S. Nehls, L. Grabenhorst, T. Oswald, C. Steinem, A. Janshoff, Viscoelasticity of native and artificial actin cortices assessed by nanoindentation experiments, *Nano Letters* **2020**, *20*(9), 6329–6335.
- [136] S. Nehls, A. Janshoff, Elastic properties of pore-spanning apical cell membranes derived from MDCK II cells, *Biophysical Journal* **2017**, *113*(8), 1822–1830.
- [137] J. W. Kuhlmann, I. P. Mey, C. Steinem, Modulating the lateral tension of solvent-free pore-spanning membranes, *Langmuir* **2014**, *30*(27), 8186–8192.
- [138] I. Mey, M. Stephan, E. K. Schmitt, M. M. Müller, M. Ben Amar, C. Steinem, A. Janshoff, Local membrane mechanics of pore-spanning bilayers, *Journal of the American Chemical Society* **2009**, *131*(20), 7031–7039.
- [139] A. Janshoff, Viscoelasticity of basal plasma membranes and cortices derived from MDCK II cells, *Biophysical Reports* **2021**, *1*(2), 100024.
- [140] L. Chopinet, C. Formosa, M. Rols, R. Duval, E. Dague, Imaging living cells surface and quantifying its properties at high resolution using AFM in QI™ mode, *Micron* **2013**, *48*, 26–33.
- [141] JPK-instruments, QI mode - Quantitative Imaging with the NanoWizard 3 AFM, <https://www.jpk.com/app-technotes-img/AFM/pdf/jpk-tech-quantitative-imaging.14-1.pdf>, accessed: **Dec. 2021**.
- [142] F. Cabello, J. León, Y. Iano, R. Arthur, in *2015 Signal Processing: Algorithms, Architectures, Arrangements, and Applications (SPA)*, IEEE, 28–33.

- [143] Z. Zhang, X. Su, L. Ding, Y. Wang, et al., Multi-scale image segmentation of coal piles on a belt based on the Hessian matrix, *Particuology* **2013**, *11*(5), 549–555.
- [144] N. Otsu, A threshold selection method from gray-level histograms, *IEEE Transactions on Systems, Man, and Cybernetics* **1979**, *9*(1), 62–66.
- [145] T.-C. Lee, R. L. Kashyap, C.-N. Chu, Building skeleton models via 3-D medial surface axis thinning algorithms, *CVGIP: Graphical Models and Image Processing* **1994**, *56*(6), 462–478.
- [146] D. S. Seara, V. Yadav, I. Linsmeier, A. P. Tabatabai, P. W. Oakes, S. A. Tabei, S. Banerjee, M. P. Murrell, Entropy production rate is maximized in non-contractile actomyosin, *Nature Communications* **2018**, *9*(1), 1–10.
- [147] M. Cetera, R.-S. Juan, R. Guillermina, P. W. Oakes, L. Lewellyn, M. J. Fairchild, G. Tanentzapf, M. L. Gardel, S. Horne-Badovinac, Epithelial rotation promotes the global alignment of contractile actin bundles during *Drosophila* egg chamber elongation, *Nature Communications* **2014**, *5*(1), 1–12.
- [148] K. H. Biswas, J. A. Jackman, J. H. Park, J. T. Groves, N.-J. Cho, Interfacial forces dictate the pathway of phospholipid vesicle adsorption onto silicon dioxide surfaces, *Langmuir* **2018**, *34*(4), 1775–1782.
- [149] J. A. Braunger, C. Kramer, D. Morick, C. Steinem, Solid supported membranes doped with PIP2: influence of ionic strength and pH on bilayer formation and membrane organization, *Langmuir* **2013**, *29*(46), 14204–14213.
- [150] P. Drücker, D. Grill, V. Gerke, H.-J. Galla, Formation and characterization of supported lipid bilayers containing phosphatidylinositol-4, 5-bisphosphate and cholesterol as functional surfaces, *Langmuir* **2014**, *30*(49), 14877–14886.
- [151] J. Schäfer, J. Nehls, M. Schön, I. Mey, C. Steinem, Leaflet-dependent distribution of PtdIns [4, 5] P2 in supported model membranes, *Langmuir* **2020**, *36*(5), 1320–1328.
- [152] R. J. Ellis, Macromolecular crowding: obvious but underappreciated, *Trends in Biochemical Sciences* **2001**, *26*(10), 597–604.

-
- [153] D. Miyoshi, N. Sugimoto, Molecular crowding effects on structure and stability of DNA, *Biochimie* **2008**, *90*(7), 1040–1051.
- [154] A. P. Minton, [7] Molecular crowding: analysis of effects of high concentrations of inert cosolutes on biochemical equilibria and rates in terms of volume exclusion, *Methods in Enzymology* **1998**, *295*, 127–149.
- [155] S. B. Zimmerman, A. P. Minton, Macromolecular crowding: biochemical, biophysical, and physiological consequences, *Annual Review of Biophysics and Biomolecular Structure* **1993**, *22*(1), 27–65.
- [156] S. Köhler, O. Lieleg, A. R. Bausch, Rheological characterization of the bundling transition in F-actin solutions induced by methylcellulose, *PloS One* **2008**, *3*(7), e2736.
- [157] D. Popp, A. Yamamoto, M. Iwasa, Y. Maéda, Direct visualization of actin nematic network formation and dynamics, *Biochemical and Biophysical Research Communications* **2006**, *351*(2), 348–353.
- [158] L. A. Helgeson, B. J. Nolen, Mechanism of synergistic activation of Arp2/3 complex by cortactin and N-WASP, *Elife* **2013**, *2*, e00884.
- [159] J. D. Rotty, C. Wu, J. E. Bear, New insights into the regulation and cellular functions of the ARP2/3 complex, *Nature Reviews Molecular Cell Biology* **2013**, *14*(1), 7–12.
- [160] T. M. Svitkina, G. G. Borisy, Arp2/3 complex and actin depolymerizing factor/cofilin in dendritic organization and treadmilling of actin filament array in lamellipodia, *The Journal of Cell Biology* **1999**, *145*(5), 1009–1026.
- [161] K. G. Campellone, M. D. Welch, A nucleator arms race: cellular control of actin assembly, *Nature Reviews Molecular cell biology* **2010**, *11*(4), 237–251.
- [162] V. Kiessling, C. Wan, L. K. Tamm, Domain coupling in asymmetric lipid bilayers, *Biochimica et Biophysica Acta - Biomembranes* **2009**, *1788*(1), 64–71.
- [163] C. A. Wilson, M. A. Tsuchida, G. M. Allen, E. L. Barnhart, K. T. Applegate, P. T. Yam, L. Ji, K. Keren, G. Danuser, J. A. Theriot, Myosin II contributes

- to cell-scale actin network treadmilling through network disassembly, *Nature* **2010**, *465*(7296), 373–377.
- [164] J. H. Henson, C. E. Ditzler, A. Germain, P. M. Irwin, E. T. Vogt, S. Yang, X. Wu, C. B. Shuster, The ultrastructural organization of actin and myosin II filaments in the contractile ring: new support for an old model of cytokinesis, *Molecular Biology of the Cell* **2017**, *28*(5), 613–623.
- [165] A. Diz-Muñoz, M. Krieg, M. Bergert, I. Ibarlucea-Benitez, D. J. Muller, E. Paluch, C.-P. Heisenberg, Control of directed cell migration in vivo by membrane-to-cortex attachment, *PLoS biology* **2010**, *8*(11), e1000544.
- [166] M. P. Murrell, M. L. Gardel, F-actin buckling coordinates contractility and severing in a biomimetic actomyosin cortex, *Proceedings of the National Academy of Sciences* **2012**, *109*(51), 20820–20825.
- [167] A. P. Baldo, J. C. Tardiff, S. D. Schwartz, Mechanochemical function of myosin II: Investigation into the recovery stroke and ATP hydrolysis, *The Journal of Physical Chemistry B* **2020**, *124*(45), 10014–10023.
- [168] T. C. Smith, Z. Fang, E. J. Luna, Novel interactors and a role for supervillin in early cytokinesis, *Cytoskeleton* **2010**, *67*(6), 346–364.
- [169] H. Li, T. Shen, M. B. Smith, I. Fujiwara, D. Vavylonis, X. Huang, in *2009 IEEE International Symposium on Biomedical Imaging: From Nano to Macro*, IEEE, 1302–1305.
- [170] R. Metzler, J. Klafter, The restaurant at the end of the random walk: recent developments in the description of anomalous transport by fractional dynamics, *Journal of Physics A: Mathematical and General* **2004**, *37*(31), R161.
- [171] F. C. MacKintosh, Active diffusion: the erratic dance of chromosomal loci, *Proceedings of the National Academy of Sciences* **2012**, *109*(19), 7138–7139.
- [172] W. Thielicke, R. Sonntag, Particle Image Velocimetry for MATLAB: Accuracy and enhanced algorithms in PIVlab, *Journal of Open Research Software* **2021**, *9*(1).
- [173] G. Salbreux, G. Charras, E. Paluch, Actin cortex mechanics and cellular morphogenesis, *Trends in Cell Biology* **2012**, *22*(10), 536–545.

-
- [174] B. R. Brückner, A. Pietuch, S. Nehls, J. Rother, A. Janshoff, Ezrin is a major regulator of membrane tension in epithelial cells, *Scientific Reports* **2015**, 5(1), 1–16.
- [175] E. M. Reichl, Y. Ren, M. K. Morphew, M. Delannoy, J. C. Effler, K. D. Girard, S. Divi, P. A. Iglesias, S. C. Kuo, D. N. Robinson, Interactions between myosin and actin crosslinkers control cytokinesis contractility dynamics and mechanics, *Current Biology* **2008**, 18(7), 471–480.
- [176] E. Fischer-Friedrich, A. A. Hyman, F. Jülicher, D. J. Müller, J. Helenius, Quantification of surface tension and internal pressure generated by single mitotic cells, *Scientific Reports* **2014**, 4(1), 1–8.
- [177] L. Onsager, The effects of shape on the interaction of colloidal particles, *Annals of the New York Academy of Sciences* **1949**, 51(4), 627–659.
- [178] A. Khokhlov, A. Semenov, Liquid-crystalline ordering in the solution of long persistent chains, *Physica A: Statistical Mechanics and its Applications* **1981**, 108(2-3), 546–556.
- [179] D. Popp, R. C. Robinson, Supramolecular cellular filament systems: How and why do they form?, *Cytoskeleton* **2012**, 69(2), 71–87.
- [180] J. Alvarado, B. M. Mulder, G. H. Koenderink, Alignment of nematic and bundled semiflexible polymers in cell-sized confinement, *Soft Matter* **2014**, 10(14), 2354–2364.
- [181] E. Helfer, P. Panine, M.-F. Carlier, P. Davidson, The interplay between viscoelastic and thermodynamic properties determines the birefringence of F-actin gels, *Biophysical Journal* **2005**, 89(1), 543–553.
- [182] Y. S. Aratyn, T. E. Schaus, E. W. Taylor, G. G. Borisy, Intrinsic dynamic behavior of fascin in filopodia, *Molecular Biology of the Cell* **2007**, 18(10), 3928–3940.
- [183] D. S. Courson, R. S. Rock, Actin cross-link assembly and disassembly mechanics for α -actinin and fascin, *Journal of Biological Chemistry* **2010**, 285(34), 26350–26357.

- [184] N. Castaneda, J. Park, E. H. Kang, Regulation of Actin Bundle Mechanics and Structure by Intracellular Environmental Factors, *Frontiers in Physics* **2021**, *9*.
- [185] T. Kobayashi, A. K. Menon, Transbilayer lipid asymmetry, *Current Biology* **2018**, *28*(8), R386–R391.
- [186] V. Niggli, C. Andréoli, C. Roy, P. Mangeat, Identification of a phosphatidylinositol-4, 5-bisphosphate-binding domain in the N-terminal region of ezrin, *FEBS Letters* **1995**, *376*(3), 172–176.
- [187] G. Blin, E. Margeat, K. Carvalho, C. A. Royer, C. Roy, C. Picart, Quantitative analysis of the binding of ezrin to large unilamellar vesicles containing phosphatidylinositol 4, 5 bisphosphate, *Biophysical Journal* **2008**, *94*(3), 1021–1033.
- [188] V. Shabardina, C. Kramer, B. Gerdes, J. Braunger, A. Cordes, J. Schäfer, I. Mey, D. Grill, V. Gerke, C. Steinem, Mode of ezrin-membrane interaction as a function of PIP2 binding and pseudophosphorylation, *Biophysical Journal* **2016**, *110*(12), 2710–2719.
- [189] D. N. Chambers, A. Bretscher, Ezrin mutants affecting dimerization and activation, *Biochemistry* **2005**, *44*(10), 3926–3932.
- [190] J. J. Jayasundar, J. H. Ju, L. He, D. Liu, F. Meilleur, J. Zhao, D. J. Callaway, Z. Bu, Open conformation of ezrin bound to phosphatidylinositol 4, 5-bisphosphate and to F-actin revealed by neutron scattering, *Journal of Biological Chemistry* **2012**, *287*(44), 37119–37133.
- [191] J. Vörös, The density and refractive index of adsorbing protein layers, *Biophysical Journal* **2004**, *87*(1), 553–561.
- [192] M. Schön, PhD thesis, Niedersächsische Staats-und Universitätsbibliothek Göttingen, **2018**.
- [193] R. Josuran, Prot pi, <https://www.protpi.ch/>, accessed: **Jan. 2022**.
- [194] T. F. Martin, in *Phosphoinositides II: The Diverse Biological Functions*, Springer, **2012**, 111–130.

-
- [195] M. Hase, K. Yoshikawa, Structural transition of actin filament in a cell-sized water droplet with a phospholipid membrane, *The Journal of Chemical Physics* **2006**, *124*(10), 104903.
- [196] C. F. Schroer, L. Baldauf, L. van Buren, T. A. Wassenaar, M. N. Melo, G. H. Koenderink, S. J. Marrink, Charge-dependent interactions of monomeric and filamentous actin with lipid bilayers, *Proceedings of the National Academy of Sciences* **2020**, *117*(11), 5861–5872.
- [197] J. G. Kay, M. Koivusalo, X. Ma, T. Wohland, S. Grinstein, Phosphatidylserine dynamics in cellular membranes, *Molecular Biology of the Cell* **2012**, *23*(11), 2198–2212.
- [198] G. L. Thompson, C. Roth, G. Tolstykh, M. Kuipers, B. L. Ibey, Disruption of the actin cortex contributes to susceptibility of mammalian cells to nanosecond pulsed electric fields, *Bioelectromagnetics* **2014**, *35*(4), 262–272.
- [199] A. Alam, M. Howlader, M. Deen, The effects of oxygen plasma and humidity on surface roughness, water contact angle and hardness of silicon, silicon dioxide and glass, *Journal of Micromechanics and Microengineering* **2014**, *24*(3), 035010.
- [200] A. Kusumi, C. Nakada, K. Ritchie, K. Murase, K. Suzuki, H. Murakoshi, R. S. Kasai, J. Kondo, T. Fujiwara, Paradigm shift of the plasma membrane concept from the two-dimensional continuum fluid to the partitioned fluid: high-speed single-molecule tracking of membrane molecules, *Annual Review of Biophysics and Biomolecular Structure* **2005**, *34*, 351–378.
- [201] D. M. Andrade, M. P. Clausen, J. Keller, V. Mueller, C. Wu, J. E. Bear, S. W. Hell, B. C. Lagerholm, C. Eggeling, Cortical actin networks induce spatio-temporal confinement of phospholipids in the plasma membrane—a minimally invasive investigation by STED-FCS, *Scientific Reports* **2015**, *5*(1), 1–12.
- [202] F. Schneider, D. Waithe, M. P. Clausen, S. Galiani, T. Koller, G. Ozhan, C. Eggeling, E. Sezgin, Diffusion of lipids and GPI-anchored proteins in actin-free plasma membrane vesicles measured by STED-FCS, *Molecular Biology of the Cell* **2017**, *28*(11), 1507–1518.

- [203] S. Saha, I.-H. Lee, A. Polley, J. T. Groves, M. Rao, S. Mayor, Diffusion of GPI-anchored proteins is influenced by the activity of dynamic cortical actin, *Molecular Biology of the Cell* **2015**, *26*(22), 4033–4045.
- [204] M. Edidin, S. C. Kuo, M. P. Sheetz, Lateral movements of membrane glycoproteins restricted by dynamic cytoplasmic barriers, *Science* **1991**, *254*(5036), 1379–1382.
- [205] K. Gowrishankar, S. Ghosh, S. Saha, C. Rumamol, S. Mayor, M. Rao, Active remodeling of cortical actin regulates spatiotemporal organization of cell surface molecules, *Cell* **2012**, *149*(6), 1353–1367.
- [206] M. P. Clausen, B. C. Lagerholm, Visualization of plasma membrane compartmentalization by high-speed quantum dot tracking, *Nano Letters* **2013**, *13*(6), 2332–2337.
- [207] F. Heinemann, S. K. Vogel, P. Schwille, Lateral membrane diffusion modulated by a minimal actin cortex, *Biophysical Journal* **2013**, *104*(7), 1465–1475.
- [208] K. E. Peyer, F. Qiu, L. Zhang, B. J. Nelson, in *2012 IEEE/RSJ International Conference on Intelligent Robots and Systems*, IEEE, 2553–2558.
- [209] E. Puchkov, Intracellular viscosity: Methods of measurement and role in metabolism, *Biochemistry (Moscow) Supplement Series A: Membrane and Cell Biology* **2013**, *7*(4), 270–279.
- [210] A. M. Mastro, M. A. Babich, W. D. Taylor, A. D. Keith, Diffusion of a small molecule in the cytoplasm of mammalian cells, *Proceedings of the National Academy of Sciences* **1984**, *81*(11), 3414–3418.
- [211] A. Szuba, F. Bano, G. Castro-Linares, F. Iv, M. Mavrakis, R. P. Richter, A. Bertin, G. H. Koenderink, Membrane binding controls ordered self-assembly of animal septins, *Elife* **2021**, *10*, e63349.
- [212] M. Murrell, M. L. Gardel, Actomyosin sliding is attenuated in contractile biomimetic cortices, *Molecular Biology of the Cell* **2014**, *25*(12), 1845–1853.
- [213] V. Wollrab, J. M. Belmonte, L. Baldauf, M. Leptin, F. Nédélec, G. H. Koenderink, Polarity sorting drives remodeling of actin-myosin networks, *Journal of Cell Science* **2019**, *132*(4), jcs219717.

-
- [214] M. Hosek, J. Tang, Polymer-induced bundling of F actin and the depletion force, *Physical Review E* **2004**, *69*(5), 051907.
- [215] D. Inoue, B. Mahmot, A. M. R. Kabir, T. I. Farhana, K. Tokuraku, K. Sada, A. Konagaya, A. Kakugo, Depletion force induced collective motion of microtubules driven by kinesin, *Nanoscale* **2015**, *7*(43), 18054–18061.
- [216] L. M. Machesky, S. J. Atkinson, C. Ampe, J. Vandekerckhove, T. D. Pollard, Purification of a cortical complex containing two unconventional actins from *Acanthamoeba* by affinity chromatography on profilin-agarose., *Journal of Cell Biology* **1994**, *127*(1), 107–115.
- [217] R. D. Mullins, J. A. Heuser, T. D. Pollard, The interaction of Arp2/3 complex with actin: nucleation, high affinity pointed end capping, and formation of branching networks of filaments, *Proceedings of the National Academy of Sciences* **1998**, *95*(11), 6181–6186.
- [218] H. N. Higgs, T. D. Pollard, Regulation of actin polymerization by Arp2/3 complex and WASp/Scar proteins, *Journal of Biological Chemistry* **1999**, *274*(46), 32531–32534.
- [219] M. J. Dayel, R. D. Mullins, M. W. Kirschner, Activation of Arp2/3 complex: addition of the first subunit of the new filament by a WASP protein triggers rapid ATP hydrolysis on Arp2, *PLoS biology* **2004**, *2*(4), e91.
- [220] B. A. Smith, K. Daugherty-Clarke, B. L. Goode, J. Gelles, Pathway of actin filament branch formation by Arp2/3 complex revealed by single-molecule imaging, *Proceedings of the National Academy of Sciences* **2013**, *110*(4), 1285–1290.
- [221] R. E. Mahaffy, T. D. Pollard, Influence of phalloidin on the formation of actin filament branches by Arp2/3 complex, *Biochemistry* **2008**, *47*(24), 6460–6467.
- [222] E. M. De La Cruz, T. D. Pollard, Transient kinetic analysis of rhodamine phalloidin binding to actin filaments, *Biochemistry* **1994**, *33*(48), 14387–14392.
- [223] T. Xu, D. Vavylonis, F.-C. Tsai, G. H. Koenderink, W. Nie, E. Yusuf, I.-J. Lee, J.-Q. Wu, X. Huang, SOAX: a software for quantification of 3D biopolymer networks, *Scientific Reports* **2015**, *5*(1), 1–10.

- [224] J. Liman, C. Bueno, Y. Eliaz, N. P. Schafer, M. N. Waxham, P. G. Wolynes, H. Levine, M. S. Cheung, The role of the Arp2/3 complex in shaping the dynamics and structures of branched actomyosin networks, *Proceedings of the National Academy of Sciences* **2020**, *117*(20), 10825–10831.
- [225] T. Yanagida, M. Nakase, K. Nishiyama, F. Oosawa, Direct observation of motion of single F-actin filaments in the presence of myosin, *Nature* **1984**, *307*(5946), 58–60.
- [226] J. R. Sellers, in *Cell Biology (Third Edition)*, Academic Press, **2006**, 387–392.
- [227] T. Butt, T. Mufti, A. Humayun, P. B. Rosenthal, S. Khan, S. Khan, J. E. Molloy, Myosin Motors Drive Long Range Alignment of Actin Filaments 2, *Journal of Biological Chemistry* **2010**, *285*(7), 4964–4974.
- [228] P. M. Bendix, G. H. Koenderink, D. Cuvelier, Z. Dogic, B. N. Koeleman, W. M. Brieher, C. M. Field, L. Mahadevan, D. A. Weitz, A quantitative analysis of contractility in active cytoskeletal protein networks, *Biophysical Journal* **2008**, *94*(8), 3126–3136.
- [229] J. Alvarado, M. Sheinman, A. Sharma, F. C. MacKintosh, G. H. Koenderink, Molecular motors robustly drive active gels to a critically connected state, *Nature Physics* **2013**, *9*(9), 591–597.
- [230] D. Smith, F. Ziebert, D. Humphrey, C. Duggan, M. Steinbeck, W. Zimmermann, J. Käs, Molecular motor-induced instabilities and cross linkers determine biopolymer organization, *Biophysical Journal* **2007**, *93*(12), 4445–4452.
- [231] H. Ennomani, G. Letort, C. Guérin, J.-L. Martiel, W. Cao, F. Nédélec, M. Enrique, M. Théry, L. Blanchoin, Architecture and connectivity govern actin network contractility, *Current Biology* **2016**, *26*(5), 616–626.
- [232] A.-C. Reymann, R. Boujemaa-Paterski, J.-L. Martiel, C. Guérin, W. Cao, H. F. Chin, M. Enrique, M. Théry, L. Blanchoin, Actin network architecture can determine myosin motor activity, *Science* **2012**, *336*(6086), 1310–1314.
- [233] G. T. Charras, C.-K. Hu, M. Coughlin, T. J. Mitchison, Reassembly of contractile actin cortex in cell blebs, *The Journal of Cell Biology* **2006**, *175*(3), 477–490.

-
- [234] J. Sedzinski, M. Biro, A. Oswald, J.-Y. Tinevez, G. Salbreux, E. Paluch, Polar actomyosin contractility destabilizes the position of the cytokinetic furrow, *Nature* **2011**, *476*(7361), 462–466.
- [235] S. Stam, S. L. Freedman, S. Banerjee, K. L. Weirich, A. R. Dinner, M. L. Gardel, Filament rigidity and connectivity tune the deformation modes of active biopolymer networks, *Proceedings of the National Academy of Sciences* **2017**, *114*(47), E10037–E10045.
- [236] P. Bleicher, T. Nast-Kolb, A. Sciortino, Y. de la Trobe, T. Pokrant, J. Faix, A. Bausch, Intra-bundle contractions enable extensile properties of active actin networks, *Scientific Reports* **2021**, *11*(1), 1–12.
- [237] N. A. Medeiros, D. T. Burnette, P. Forscher, Myosin II functions in actin-bundle turnover in neuronal growth cones, *Nature Cell Biology* **2006**, *8*(3), 216–226.
- [238] E. Korkmazhan, A. R. Dunn, The membrane-actin linker ezrin acts as a sliding anchor, *bioRxiv* **2021**.
- [239] T. Ikawa, in *Atomic Force Microscopy Investigations into Biology-From Cell to Protein*, IntechOpen, **2012**.
- [240] J. D. Winkelman, C. Suarez, G. M. Hocky, A. J. Harker, A. N. Morganthaler, J. R. Christensen, G. A. Voth, J. R. Bartles, D. R. Kovar, Fascin-and α -actinin-bundled networks contain intrinsic structural features that drive protein sorting, *Current Biology* **2016**, *26*(20), 2697–2706.
- [241] S. Yang, F.-K. Huang, J. Huang, S. Chen, J. Jakoncic, A. Leo-Macias, R. Diaz-Avalos, L. Chen, J. J. Zhang, X.-Y. Huang, Molecular mechanism of fascin function in filopodial formation, *Journal of Biological Chemistry* **2013**, *288*(1), 274–284.
- [242] A. Bretscher, Fimbrin is a cytoskeletal protein that crosslinks F-actin in vitro, *Proceedings of the National Academy of Sciences* **1981**, *78*(11), 6849–6853.
- [243] K. L. Weirich, S. Stam, E. Munro, M. L. Gardel, Actin bundle architecture and mechanics regulate myosin II force generation, *Biophysical Journal* **2021**, *120*(10), 1957–1970.

- [244] B. Demé, D. Hess, M. Tristl, L.-T. Lee, E. Sackmann, Binding of actin filaments to charged lipid monolayers: Film balance experiments combined with neutron reflectivity, *The European Physical Journal E* **2000**, *2*(2), 125–136.
- [245] L. Danos, R. Greef, T. Markvart, Efficient fluorescence quenching near crystalline silicon from Langmuir–Blodgett dye films, *Thin Solid Films* **2008**, *516*(20), 7251–7255.
- [246] M. Kocun, T. D. Lazzara, C. Steinem, A. Janshoff, Preparation of solvent-free, pore-spanning lipid bilayers: modeling the low tension of plasma membranes, *Langmuir* **2011**, *27*(12), 7672–7680.
- [247] J. Sibold, V. E. Tewaag, T. Vagedes, I. Mey, C. Steinem, Phase separation in pore-spanning membranes induced by differences in surface adhesion, *Physical Chemistry Chemical Physics* **2020**, *22*(17), 9308–9315.
- [248] F.-C. Tsai, A. Bertin, H. Bousquet, J. Manzi, Y. Senju, M.-C. Tsai, L. Picas, S. Miserey-Lenkei, P. Lappalainen, E. Lemichez, et al., Ezrin enrichment on curved membranes requires a specific conformation or interaction with a curvature-sensitive partner, *Elife* **2018**, *7*, e37262.
- [249] A. Cordes, H. Witt, A. Gallemí-Pérez, B. Brückner, F. Grimm, M. Vache, T. Oswald, J. Bodenschatz, D. Flormann, F. Lautenschläger, et al., Prestress and area compressibility of actin cortices determine the viscoelastic response of living cells, *Physical Review Letters* **2020**, *125*(6), 068101.
- [250] M. Kelkar, P. Bohec, G. Charras, Mechanics of the cellular actin cortex: From signalling to shape change, *Current Opinion in Cell Biology* **2020**, *66*, 69–78.
- [251] P. Thevenaz, U. E. Ruttimann, M. Unser, A pyramid approach to subpixel registration based on intensity, *IEEE Transactions on Image Processing* **1998**, *7*(1), 27–41.
- [252] P. Mühlenbrock, K. Herwig, L. Vuong, I. Mey, C. Steinem, Fusion pore formation observed during SNARE-mediated vesicle fusion with pore-spanning membranes, *Biophysical Journal* **2020**, *119*(1), 151–161.

A Appendix

A.1 List of Figures

1.1	Schematic illustration of the cellular cytoskeleton.	1
1.2	Exemplary crystal structure of G-actin.	3
1.3	Schematic illustration of the time-dependent actin polymerization and F-actin structure.	4
1.4	Cellular actin localization and organization.	6
1.5	Schematic illustration of the ezrin domains and two-step activation.	8
1.6	Schematic illustration of different approaches for minimal actin cortices (MACs).	10
3.1	Chemical structure of PtdIns[4,5]P ₂	15
3.2	Exemplary SDS-PAGE of <i>N</i> -terminal His ₆ -tagged ezrin T567D	25
3.3	Schematic illustration of critical steps within skeletal rabbit muscle myosin II isolation	28
3.4	Reaction mechanism of an (NHS)-ester conjugated fluorescent probe with a primary amino group.	31
3.5	Schematic depiction of a GUV chamber.	36
3.6	Depiction of pore-spanning membranes on SiO _x functionalized substrates.	37
3.7	Schematic illustration of MAC preparation on solid supported and pore-spanning membranes.	40
3.8	RIFS setup and the light pathway during experiments.	43
3.9	Schematic illustration of a principle confocal laser scanning microscopy setup.	49
3.10	Exemplary representation of the point spread function.	50
3.11	Schematic illustration of the Airyscan detector and its principle.	52
3.12	Exemplary resolution comparison between an confocal and Airyscan image of a 3D F-actin network.	53
3.13	Schematic illustration of a typical FRAP measurement.	54
3.14	Schematic illustration of SNELL's law in terms of TIRF microscopy.	56
3.15	Schematic illustration of the evanescent field in TIRF microscopy.	57
3.16	Schematic illustration of a principle total internal reflection fluorescence microscopy setup.	59

3.17	Schematic illustration of the central modules of an atomic force microscope.	60
3.18	Depiction of an exemplary force distance curve.	62
3.19	Schematic illustration of AFM-CLSM correlation.	65
3.20	Exemplary illustration of the individual processing steps performed by the <i>tube-filter</i> analysis.	67
3.21	Exemplary skeletonization and node detection of a tube-filtered image.	68
3.22	Exemplary illustration of a director and nematic order field.	69
4.1	Fluorescence micrographs showing the specific binding of a minimal actin cortex to an ezrin T567D decorated membrane.	72
4.2	Fluorescence micrographs of the F-actin binding to lipid membranes lacking the receptor lipid or ezrin linkage.	73
4.3	Comparison of lipid diffusion in solid-supported bilayers with and without attached MAC.	74
4.4	Exemplary fluorescence micrographs showing the F-actin binding to SLBs containing 1-8 mol% PtdIns[4,5]P ₂	76
4.5	Box plots showing the actin network node density, skeleton network ratio and q_{mean} of membrane-bound MACs depending on PtdIns[4,5]P ₂ content.	77
4.6	Skeleton based actin intensity determination.	78
4.7	Exemplary fluorescence micrographs showing the F-actin binding to SLBs containing 2 mol% PtdIns[4,5]P ₂ depending on methyl cellulose (MC) concentration.	80
4.8	Exemplary fluorescence micrographs displaying the F-actin binding to SLBs containing 1-5 mol% PtdIns[4,5]P ₂ with and without 0.18 <i>w/v</i> % MC.	81
4.9	Box plots showing the actin network node- and skeleton network density of membrane-bound MACs depending on PtdIns[4,5]P ₂ content and MC treatment.	82
4.10	Fluorescence micrographs of 3-D F-actin gels polymerized in the absence or presence of Arp2/3.	84
4.11	Exemplary fluorescence micrographs showing the binding of Arp2/3 branched and unbranched F-actin networks to SLBs containing 1-8 mol% PtdIns[4,5]P ₂	85

4.12	Box plots showing the actin network node and skeleton network density of branched and unbranched membrane-bound MACs as a function of the PtdIns[4,5]P ₂ content.	86
4.13	Box plot showing the mean nematic order parameter (q_{mean}) and the mean actin intensity of branched and unbranched membrane-bound MACs as a function of the PtdIns[4,5]P ₂ content.	87
4.14	Exemplary RfS measurement displaying the specific binding of ezrin T567D to a PtdIns[4,5]P ₂ doped SLB.	89
4.15	Box plot showing the change in optical thickness for ezrin T567D adsorption on SLBs depending on PtdIns[4,5]P ₂ and POPS content.	90
4.16	Exemplary fluorescence micrographs showing the F-actin binding to SLBs containing 1-3 mol% PtdIns[4,5]P ₂ depending on POPS content.	91
4.17	Box plot showing the mean nematic order parameter (q_{mean}) and the mean actin intensity of membrane-bound MACs depending on PtdIns[4,5]P ₂ and POPS content.	92
4.18	Box plots showing the actin network node and skeleton network density of membrane-bound MACs depending on PtdIns[4,5]P ₂ and POPS content.	93
4.19	Exemplary time series displaying the single actin filament motion in dependence of the myosin II clusters.	96
4.20	Exemplary time series showing single actin filament tracking during myosin II induced motion.	97
4.21	Exemplary mean squared displacement and quantitative motion evaluation of membrane-bound single actin filaments.	98
4.22	Exemplary time series displaying the myosin II induced reorganization of membrane-bound minimal actin cortices as a function of the POPS content.	100
4.23	Exemplary quantification of the myosin II induced reorganization of the membrane-bound MACs shown in figure 4.22 B.	101
4.24	Comparison of the three general types of actin network contraction, observed in membrane-bound MACs.	103
4.25	Comparison of the contraction type dependent mean F-actin velocity magnitude probability distribution.	104
4.26	Dependence of actomyosin contractility on the F-actin network architecture and lipid membrane composition.	105

4.27	Exemplary fluorescence micrographs of MACs attached to PSLBs via the biomimetic ezrin-PtdIns[4,5]P ₂ -linkage.	108
4.28	Fluorescence and atomic force micrographs of PSMs prior to MAC attachment.	109
4.29	Fluorescence and atomic force micrographs of PSMs with a membrane-bound MAC.	110
4.30	Box plot of the lateral membrane tension (σ) with/without membrane-bound MAC and exemplary force distance curves.	111
5.1	Dependence of the F-actin bundling upon the receptor lipid content and skeleton network density.	115
5.2	Proposed modes of the ezrin T567D organization on solid supported membranes depending on the lipid composition.	119
5.3	Dependence of the F-actin bundling on POPS doped SLBs upon the receptor lipid content and skeleton network density.	121
5.4	Schematic illustration of the potential diffusion modes resulting from cortical actin.	123
5.5	Dependence of the F-actin bundling upon the receptor lipid content and Arp2/3 branching.	129
5.6	Illustration of the myosin II induced F-actin fragmentation and polar actomyosin aster structure.	132
A.1	Exemplary determination of the optimal window-size for the nematic order parameter.	170
A.2	Box plot showing the change in optical thickness for ezrin T567D adsorption on POPC/POPS SLBs.	171
A.3	Alexa Fluor TM 633 phalloidin fluorescence intensity on PSMs with and without membrane-bound F-actin.	173
A.4	Exemplary fluorescence micrographs of large actin filaments attached to PSLBs via the biomimetic ezrin-PtdIns[4,5]P ₂ -likage.	174

A.2 List of Tables

3.1	Chemical structure and properties of matrix lipids used for membrane preparation.	16
3.2	Chemical structure and molar mass of lipid coupled fluorescent probes used for membrane preparation.	18
3.3	NHS and phalloidin coupled fluorophores for protein staining.	20
3.4	Overview of the fluorophore-specific parameters used for concentration and <i>DOL</i> determination.	31
3.5	Final concentration of all reagents for the reorganization of membrane-bound minimal actin cortices by myosin II.	41
3.6	Parameter settings for FRAP experiments on SLBs.	55
A.1	Overview of the utilized parameters for the nematic order parameter determination according to SEARA et al. ^[146]	170
A.2	PIV parameters.	172
A.3	Overview of tested parameters for the PSM attachment of MACs on Fraunhofer substrates.	175
A.4	Overview of tested parameters for the PSM attachment of MACs on Fraunhofer substrates.	176
A.5	SOAX parameters.	177

A.3 Nematic order parameter: director field window-size determination and utilized parameters

Since the applied director field window-size has significant influence on the calculated nematic order parameter, the mean nematic order parameter (q_{mean}) has been calculated as a function of the window-size for each image in order to determine an optimal value. An example is given in figure A.1. For the F-actin network displayed in figure A.1 A, the corresponding window-size dependent q_{mean} -values in figure A.1 B reveal an optimal window-size of $1.3 \mu\text{m}$ ($q_{mean} = 0.6$).

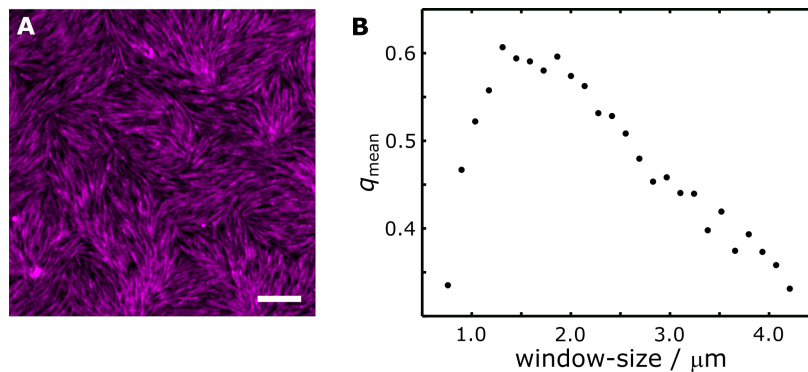


Figure A.1: Exemplary determination of the optimal window-size for the nematic order parameter. **A:** Fluorescence micrograph of an exemplary F-actin network (magenta). **B:** Mean nematic order parameter (q_{mean}) of the F-actin network shown in A as a function of the applied director field window-size. Scale bar: $5 \mu\text{m}$.

The optimal window-size used in this work ranged between $1 - 2 \mu\text{m}$ in dependence of the respective image.

An overview of the utilized parameters for the nematic order parameter determination according to SEARA et al., are displayed in table A.1.^[146]

Table A.1: Overview of the utilized parameters for the nematic order parameter determination according to SEARA et al.^[146]

parameter	
window-size	optimized per image
overlap	default (0.5)
spacing	default (2)
checkpoint	default (0)
mask method	local threshold

A.4 RfS control experiments for POPS

In order to exclude a non-specific adsorption of ezrin T567D to the negatively charged matrix lipid POPS, RfS experiments with POPC/POPS SLBs (83:17) were conducted. Sample preparation and RfS experiments were performed as described in the chapters 3.3.4.1 and 3.4.1.

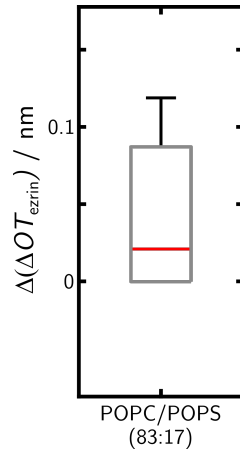


Figure A.2: Box plot showing the change in optical thickness for ezrin T567D adsorption on POPC/POPS SLBs. Change in optical thickness caused by irreversibly adsorbed ezrin T567D ($\Delta(\Delta OT_{ezrin})$) on POPC/POPS SLBs (83:17, $\Delta(\Delta OT_{ezrin}) = 0.04 \pm 0.06$ nm, $n = 4$). Data from n single experiments were analyzed. Boxes ranging from 25th to 75th percentiles of the sample, while whiskers represent to the most extreme data points not considered outliers. Medians are shown as red horizontals within the boxes

As shown in figure A.2, a low mean $\Delta(\Delta OT_{ezrin})$ of 0.04 ± 0.06 nm was detected for the interaction of ezrin T567D with POPC/POPS (83:17) SLBs, indicating no unspecific binding. As results of the detector noise obtained negative $\Delta(\Delta OT_{ezrin})$ -values were set to zero.

A.5 Particle image velocimetry analysis

The F-actin velocity in contractual actomyosin networks was analyzed by means of particle image velocimetry (PIV) using the MATLAB based *PIVlab* (version 2.53) from THIELICKE and SONNTAG.^[172] F-actin time series were pre-processed by first cropping the region of interest and subsequently reducing thermal drift via the ImageJ plugin StackReg (mode: rigid body) developed by THEVENAZ et al.^[251] Afterwards, each time series frame was saved individually. For the PIV analysis every tenth frame was loaded, with a final time difference of 10s between the analyzed frames. Utilized parameters are listed in table A.2.

Table A.2: PIV parameters.

parameter	
CLAHE window-size	50 pixel
PIV algorithm	FFT window deformation
Integration area:	
1. pass	64 , step 32
2. pass	32 , step 16
3. pass	16 , step 8
velocity limit	$1 \mu\text{m s}^{-1}$

A.6 Pore spanning membranes

A.6.1 Alexa Fluor™ 633 phalloidin control experiments

Since individual actin filaments could not be resolved for the f-PSM bound minimal actin cortices and the Alexa Fluor™ 633 phalloidin staining showed unspecifically adsorption to PSMs, blank experiments were conducted to verify a F-actin attachment. For this purpose GUVs (DPhPC/PtdIns[4,5]P₂/ATTO390-DPPE (91.6:8:0.4)) were prepared as described in chapter 3.3.1.2 and spreaded on SiO_x functionalized porous substrates ($\varnothing = 5 \mu\text{m}$) to generate PSMs (cf. chapter 3.3.2.2). To exclude the possibility that the measured actin fluorescence was completely caused by unspecifically adsorbed Alexa Fluor™ 633 phalloidin, minimal actin cortices were prepared as described in chapter 3.3.4.2 and attached via the ezrin-PtdIns[4,5]P₂ linkage. The blank samples were prepared in the same manner, however without G-actin in the polymerization solution. After rinsing the samples with F-buffer, CLSM micrographs of the PSMs were recorded. By comparing the averaged Alexa Fluor™ 633 fluorescence intensity on the f-PSMs between samples containing F-actin (112 ± 7.3 a.u., $n = 77$, $N = 2$) and blank samples (60 ± 3.7 a.u., $n = 46$, $N = 2$), lacking actin, it was revealed that F-actin containing samples exhibit a significantly enhanced Alexa Fluor™ 633 fluorescence intensity, indicating a F-actin membrane attachment.

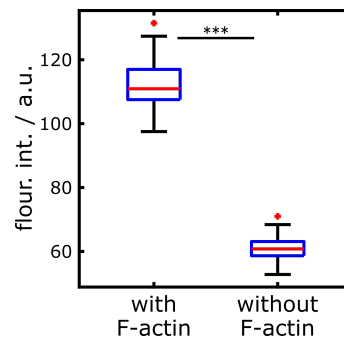


Figure A.3: Alexa Fluor™ 633 phalloidin fluorescence intensity on PSMs with and without membrane-bound F-actin. Comparison of the detectable fluorescence intensity of Alexa Fluor™ 633 phalloidin on PSMs for a preparation with (112 ± 7.3 a.u., $n = 77$, $N = 2$) and without (60 ± 3.7 a.u., $n = 46$, $N = 2$) F-actin. For the analysis n PSMs of N preparations were evaluated. Boxes ranging from 25th to 75th percentiles of the sample, while whiskers represents to the most extreme data points not considered outliers (red crosses). Medians are shown as red horizontals within the boxes. Statistical t -test: ***: $p \leq 0.001$.

A.6.2 Length-dependent binding of F-actin to pore-spanning membranes

Samples were prepared as described in chapter 4.3, however F-actin was stained via ATTO 594 labeled-G-actin as described in chapter 3.3.3.

The fluorescence micrographs in figure A.4 A1-2 display the generated PSMs with the f-PSMs identifiable as bright circular areas and the dimmer s-PSMs on the solid supported parts. Figure A.4 B1-2 illustrate the s-PSM attachment of the ATTO 594-labeled F-actin via the ezrin-PtdIns[4,5]P₂ linkage. The selective binding of long actin filaments on the s-PSMs but not on the f-PSMs is evident in the overlay of the membrane and F-actin fluorescence in figure A.4 C1-2.

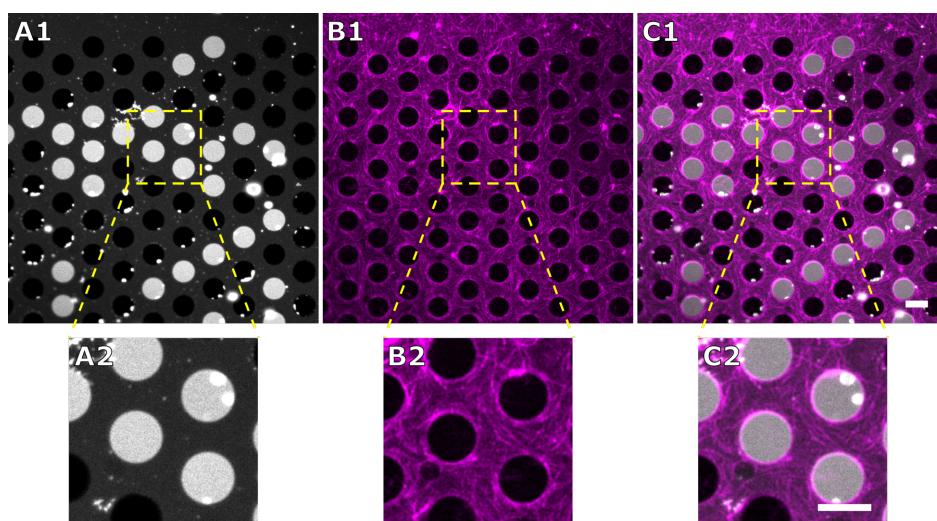


Figure A.4: Exemplary fluorescence micrographs of large actin filaments attached to PSLBs via the biomimetic ezrin-PtdIns[4,5]P₂-linkage A1-2: DPhPC/PtdIns[4,5]P₂/ATTO390-DPPE (91.6:8:0.4) PSMs (gray), with freestanding PSMs identifiable as bright circles and dimmer solid supported parts, as result of the surface quenching. **B1-2:** Corresponding fluorescence micrographs of the membrane-bound MAC (magenta), labeled with ATTO 594-G-actin. **C1-2:** PSMs (A1-2) and MAC (B1-2) overlay. Scale bars: 5 μ m.

A.6.3 Overview of tested parameters for the PSM attachment of minimal actin cortices

Parts of the measurements presented in this chapter were performed by Dominik Ruppelt and Kira Herwig as part of his master thesis and her laboratory internship.

Table A.3: Overview of tested parameters for the PSM attachment of MACs on Aquamarijn substrates. A: POPC/PtdIns[4,5]P₂, **B:** POPC/POPS/PtdIns[4,5]P₂, **C:** POPC/Chol/PtdIns[4,5]P₂, **D:** POPC/POPS/Chol/PtdIns[4,5]P₂, **E:** DPhPC/PtdIns[4,5]P₂. All lipid films were doped with 0.4 mol% ATTO390-DPPE.

Aquamarijn substrates $\varnothing = 5 \mu\text{m}$					
Funct.	Lipids	f-PSMs	F-actin binding		
			rim	s-PSM	f-PSM
6MH-Au [*]	A (94.6:5) ^{1,2}	✓	✓	✗	✗
6MH-Au ^{2,*}	A (94.6:5) ^{1,2}	✓	✓	✗	✗
6MH-Au ^{3,*}	A (94.6:5) ^{1,2}	✓	✓	✗	✗
SiO _x , 1 h 55°C **	A (94.6:5) ^{1,2}	✗	✓	✗	✗
SiO _x , 16 h 55°C **	A (91.6:8) ¹	✓	✓	✓	✗
SiO _x , 16 h 55°C **	B (74.6:17:8) ¹	✓	✓	✓	✗
SiO _x , 16 h 55°C **	C (76.6:15:8) ¹	✓	✓	✓	✗
SiO _x , 16 h 55°C **	D (59.6:17:15:8) ¹	✓	✓	✓	✗

¹ ITO GUVs, prepared as described in chapter 3.3.1.2.

² Pt GUVs, GUV electroformation on platinum wires (Pt, $\varnothing = 0.3 \text{ mm}$). Deposition of 0.2 mg lipid material on wires, dried in vacuum over night, electroformation over 2 h at 500 Hz, 125 mV_{pp} in Na-citrat buffer (+ 25 mM sucrose) to a final lipid concentration of 0.25 mg mL⁻¹.

³ BSA passivation, addition of 70 μM BSA after PSM formation, incubated 1 h at 20°C, 5 \times buffer replacement prior to ezrin addition.

⁴ LUV passivation, large unilamellar vesicles (LUVs, 0.8 mg mL⁻¹, POPC/POPS/ATTO488-DPPE, 94,6:5:0.4) were prepared by extrusion through a 200 nm polycarbonat membrane. After PSM formation 100 μL LUV suspension were added and incubated for 1 h at 20°C, 5 \times buffer replacement prior to ezrin addition.

*6MH-Au functionalization was conducted as described in ^[252]

**functionalization prepared as described in chapter 3.3.2.2, altered incubation times in water

Table A.4: Overview of tested parameters for the PSM attachment of MACs on Fraunhofer substrates. A: POPC/PtdIns[4,5]P₂, B: POPC/POPS/PtdIns[4,5]P₂. All lipid films were doped with 0.4 mol% ATTO390-DPPE.

Fraunhofer substrates (closed cavities) $\varnothing = 5 \mu\text{m}$					
Funct.	Lipids	f-PSMs	F-actin binding		
			rim	s-PSM	f-PSM
O ₂ plasma, 30 s, 30 %	A (94.6:5) ²	✗	✗	✗	✗
O ₂ plasma, 30 s, 60 %	A (94.6:5) ²	✗	✗	✗	✗
hydrophilized ⁵	A (94.6:5) ²	✗	✗	✗	✗
1 h 55°C *	A (94.6:5) ^{1,2}	✗	✗	✓	✗
1 h 55°C *	B (74.6:17:8) ¹	✗	✗	✓	✗
1-24 h 55°C *	A (94.6:5) ^{1,2}	✗	/	/	/
SiO _x , 1 h 55°C ^{3,**}	B (74.6:17:8) ¹	✗	✗	✓	✗
SiO _x , 1 h 55°C ^{3,**}	A (94.6:5) ¹	✗	✗	✓	✗
SiO _x , 2, 24 h 55°C **	A (94.6:5) ¹	lined pores	✓	✓	✓

¹ ITO GUVs, prepared as described in chapter 3.3.1.2.

² Pt GUVs, GUV electroformation on platinum wires (Pt, $\varnothing = 0.3 \text{ mm}$). Deposition of 0.2 mg lipid material on wires, dried in vacuum over night, electroformation over 2 h at 500 Hz, 125 mV_{pp} in Na-citrat buffer (+ 25 mM sucrose) to a final lipid concentration of 0.25 mg mL⁻¹.

³ BSA passivation, addition of 70 μM BSA after PSM formation, incubated 1 h at 20°C, 5 \times buffer replacement prior to ezrin addition.

⁴ LUV passivation, large unilamellar vesicles (LUVs, 0.8 mg mL⁻¹, POPC/POPS/ATTO488-DPPE, 94,6:5:0.4) were prepared by extrusion through a 200 nm polycarbonat membrane. After PSM formation 100 μL LUV suspension were added and incubated for 1 h at 20°C, 5 \times buffer replacement prior to ezrin addition.

⁵ hydrophilization conducted as described in chapter 3.3.2.1.

*substrate incubation in water

**functionalization prepared as described in chapter 3.3.2.2, altered incubation times in water

A.7 SOAX parameters

Used parameter set for the 3D network analysis of 8 bit tiff-images stacks.

Table A.5: SOAX parameters.

parameter		parameter	
intensity-scaling	0.01	gamma	2
gaussian-std	1	external-factor	1
ridge-threshold	0.05	stretch-factor	0.2
maximum-foreground	255	number-of-background- radial-sectors	8
minimum-foreground	0	background-z-xy-ratio	2.88
init-z	true	radial-near	4
snake-point-spacing	1	radial-far	8
minimum-snake-length	5	delta	4
maximum-iterations	10000	overlap-threshold	2
change-threshold	0.05	grouping- distance-threshold	8
check-period	100	grouping-delta	8
alpha	0.01	minimum-angle- for-soac-linking	2.1
beta	0.1	damp-z	false

A.8 Abbreviations and symbols

A_{max}	absorbance, fluorophore maximum
A_{280}	absorbance, at wavelength 280 nm
ABP	actin binding protein
ADP	adenosine diphosphate
AFM	atomic force microscopy
AFs	actin filaments
APS	ammonium peroxydisulfate
Arp2/3	actin-related-protein 2/3 complex
ATP	adenosine triphosphate
a.u.	arbitrary unit
AU	airy unit
BFP	back focal plane
BSA	bovine serum albumin
c	concentration
C-ERMAD	C-terminal ezrin-radixin-moesin associated domain
CF_{280}	correction factor at wavelength 280 nm
CK	creatine kinase
CLAHE	contrast-limited adaptive histogram equalization
CLSM	confocal laser scanning microscopy
CP	creatine phosphate
d	optical light path
D-loop	DNase I-binding loop
DMSO	dimethyl sulfoxide
DOGS-Ni-NTA	1,2-dioleoyl- <i>sn</i> -glycero-3-[(N-(5-amino-1-carboxypentyl)iminodiacetic acid)succinyl] (nickel salt)
DOL	degree of labeling
DOPC	1,2-dioleoyl- <i>sn</i> -glycero-3-phosphocholine
DPPE	1,2-dipalmitoyl- <i>sn</i> -glycero-3-phosphoethanolamine
DPhPC	1,2-diphytanoyl- <i>sn</i> -glycero-3-phosphocholine
DTT	dithiothreitol
<i>E. coli</i>	<i>Escherichia coli</i>
E1 buffer	ezrin buffer

E1-10	elution fractions 1-10
EDTA	ethylenediaminetetraacetic acid
EGTA	egtazic acid
EQ	equilibration buffer
F-actin	filamentous actin
f-PSM	freestanding pore-spanning membrane
FDC	force distance curves
FRAP	fluorescence recovery after photobleaching
FT	flow through
FWHM	full width at half maximum
G-actin	globular actin
GUV	giant unilamellar vesicles
His ₆ -tag	hexahistidine-tag
<i>I</i>	intensity, light
IFs	intermediate filaments
IMAC	immobilized metal ion affinity chromatography
IPTG	isopropyl β -D-thiogalactopyranoside
ITO	indium tin oxide
<i>lacI</i>	<i>lac</i> inhibitor
<i>lacO</i>	<i>lac</i> operon
LB	lysogeny broth
l_p	persistence length
LUV	large unilamellar vesicles
M buffer	myosin buffer
MAC	minimal actin cortex
MC	methyl cellulose
MHC	myosin heavy chain
min	minute
MLC	myosin light chain
MLV	multilamellar vesicles
MS buffer	myosin storage buffer
MSD	mean squared displacement
MTs	microtubules

MW	molecular weight, molecular weight marker
MWCO	molecular weight cut-off
n	refractive index
N-ERMAD	N-terminal ezrin-radixin-moesin associated domain
N-WASP	neural Wiskott-Aldrich syndrome protein
NA	numerical aperture
NPF	nucleation promoting factor
NHS	<i>N</i> -hydroxysuccinimide
Ni-NTA	nickel-nitrilotriacetic acid
nm actin	non-muscle actin
OD_{600}	optical density at wavelength 600 nm
OT	optical thickness
PDB	protein data bank
P_i	inorganic phosphate
PIV	particle image velocimetry
PM	plasma membrane
PS	phosphatidylserine
PSF	point spread function
PSD	position-sensitive photodiode
PSM	pore spanning membrane
PtdIns[4,5]P ₂	L- α -phosphatidylinositol-4,5-bisphosphate
POPC	1-palmitoyl-2-oleoyl- <i>sn</i> -glycero-3-phosphocholine
POPS	1-palmitoyl-2-oleoyl- <i>sn</i> -glycero-3-phospho-L-serine
q_{mean}	mean nematic order parameter
QI	quantitative imaging
RIfS	reflectometric interference spectroscopy
ROI	region of interest
RT	room temperature
s-PSM	solid supported pore-spanning membrane
SDS-PAGE	sodium dodecyl sulfate polyacrylamide gel electrophoresis
SLBs	solid supported lipid bilayers
SNR	signal to noise ratio
SOC	super optimal broth with catabolite repression

SUV	small unilamellar vesicles
t	time
TEMED	N,N,N',N' -tetramethyl ethylenediamine
TIRF	total internal reflection fluorescence
TxR	Texas Red [®]
UV	ultraviolet
v	volume
VCA	verprolin Homology/Cofilin/Acidic
w	weight
WI & WII	washing buffer I & II
WASP	Wiskott-Aldrich syndrome protein
γ	immobile fraction (FRAP)
δ	actin bundling factor
ε_{280}	molar attenuation coefficient at wavelength 280 nm
λ	wavelength
λ_{ex}	wavelength, excitation
λ_{em}	wavelength, emission
λ_{max}	wavelength, maximum absorption
σ	lateral membrane tension
χ	percentage
\varnothing	diameter

A.9 Chemicals and consumables

6-mercapto-1-hexanol	Sigma Aldrich, Taufkirchen, Germany
Acrylamid(AA)-mix	Sigma Aldrich, Taufkirchen, Germany
Alexa Fluor™ 488-phalloidin	Thermo Fisher Scientific Waltham, MA, USA
Alexa Fluor™ 633-phalloidin	Thermo Fisher Scientific Waltham, MA, USA
APS	Sigma Aldrich, Taufkirchen, Germany
argon	Air Liquide Deutschland GmbH, Düsseldorf, Germany
Arp2/3 protein complex	Cytoskeleton, Denver, CO, USA
ATP	Sigma Aldrich, Taufkirchen, Germany
ATTO 390-DPPE	Atto-tec, Siegen, Germany
ATTO 488-DPPE	Atto-tec, Siegen, Germany
ATTO 594-NHS-ester	Atto-tec, Siegen, Germany
Bio-Beads SM-2®	Bio-Rad Laboratories GmbH, München, Ger- many
bromophenol blue	VWR international, Darmstadt, Germany
CaCl ₂	Merck, Darmstadt, Germany
chloroform	VWR international, Darmstadt, Germany
cOmplete™	Roche, Mannheim, Germany
coomassie Brilliant Blue G- 250	Carl Roth GmbH, Karlsruhe, Germany
coverglass slides	Marienfeld GmbH & Co. KG, Lauda- Königshofen, Germany
coverglass (22 × 22 mm)	VWR international, Darmstadt, Germany
creatine kinase	Sigma Aldrich, Taufkirchen, Germany
creatine phosphate	Sigma Aldrich, Taufkirchen, Germany
DDM	Carl Roth GmbH, Karlsruhe, Germany
DPhPC	Avanti Polar Lipids, Alabaster, USA
DTT	Carl Roth GmbH, Karlsruhe, Germany
DyLight® 488-NHS-ester	Thermo Fisher Scientific Waltham, MA, USA
<i>E. coli</i> BL21(DE3)	Thermo Fisher Scientific Waltham, MA, USA
EDTA	Carl Roth GmbH, Karlsruhe, Germany
EGTA	Carl Roth GmbH, Karlsruhe, Germany

ethanol	VWR international, Darmstadt, Germany
G-actin protein	Cytoskeleton, Denver, CO, USA
glucose	Sigma Aldrich, Taufkirchen, Germany
glycerol	Merck, Darmstadt, Germany
glycine	Merck, Darmstadt, Germany
gold, 99.99%	Allg. Gold- und Silberscheideanstalt, Pforzheim, Germany
guanidine carbonate	Sigma Aldrich, Taufkirchen, Germany
H ₂ O ₂ (30%)	Merck, Darmstadt, Germany
HEPES	Carl Roth GmbH, Karlsruhe, Germany
imidazole	Sigma Aldrich, Taufkirchen, Germany
IPTG	Sigma Aldrich, Taufkirchen, Germany
isopropanol	Merck, Darmstadt, Germany
ITO slides	Präzision Glas and Optic GmbH, Iserlohn, Germany
kanamycin	Sigma Aldrich, Taufkirchen, Germany
KCl	Merck, Darmstadt, Germany
KH ₂ PO ₄	Sigma Aldrich, Taufkirchen, Germany
K ₂ HPO ₄	Sigma Aldrich, Taufkirchen, Germany
methanol	VWR international, Darmstadt, Germany
MgCl ₂	Merck, Darmstadt, Germany
microscopy slide	Thermo Fisher Scientific, Waltham, MA, USA
MLCT-cantilever	Bruker AFM Probes, Camarillo, USA
Mucaso [®]	Merck, Darmstadt, Germany
<i>n</i> -propanol	VWR international, Darmstadt, Germany
Na-citrate	Merck, Darmstadt, Germany
NaCl	Merck, Darmstadt, Germany
NaH ₂ PO ₄	Merck, Darmstadt, Germany
NaOH	Merck, Darmstadt, Germany
Na ₃ PO ₄	Merck, Darmstadt, Germany
NaN ₃	Merck, Darmstadt, Germany
Ni-NTA	Qiagen GmbH, Venlo, Netherlands
nitrogen	Air Liquide Deutschland GmbH,

NH ₃ (25 %)	Düsseldorf, Germany
oxygen	VWR international, Darmstadt, Germany Air Liquide Deutschland GmbH, Düsseldorf, Germany
PageRuler™ Plus	Thermo Fisher Scientific Waltham, MA, USA
phalloidin (untagged)	Sigma Aldrich, Taufkirchen, Germany
PtdIns[4,5]P ₂	Avanti Polar Lipids, Alabaster, USA
POPC, POPS	Avanti Polar Lipids, Alabaster, USA
porous substrates:	
closed cavities $\varnothing = 5 \mu\text{m}$	Fraunhofer-Institut für Mikrotechnik und Mikrosysteme IMM, Mainz, Germany
open cavities $\varnothing = 5 \mu\text{m}$	Aquamarijn, Zutphen, Netherlands
rabbit meat (myosin II)	Harlan Laboratories, Belton, Leicestershire, UK
SDS	AppliChem GmbH, Darmstadt, Germany
self adhesive copper stripe	Präzisions Glas & Optik GmbH, Iserlohn, Germany
SiO	Merck, Darmstadt, Germany
Slide-A-Lyzer MINI	Thermo Fisher Scientific, Waltham, USA
sucrose	Acros Organics, New Jersey, USA
TEMED	Sigma Aldrich, Taufkirchen, Germany
trolox	Sigma Aldrich, Taufkirchen, Germany
tryptone	Carl Roth GmbH, Karlsruhe, Germany
Tris	Carl Roth GmbH, Karlsruhe, Germany
TxR DHPE	Sigma Aldrich, Taufkirchen, Germany
VCA protein, N-WASP	Cytoskeleton, Denver, CO, USA
wafer (silicon)	Active Business Company GmbH, Brunnthal, Germany
yeast extract	Carl Roth GmbH, Karlsruhe, Germany
β -mercaptoethanol	Carl Roth GmbH, Karlsruhe, Germany

A.10 Devices and software

AFM

Nanowizard 4 JPK Instruments, Berlin, Germany

CLSM

FluoView 1200 Olympus, Tokyo, Japan

LUMFLN 60XW, NA 1.1 Olympus, Tokyo, Japan

LSM 880 Examiner Carl Zeiss Microscopy GmbH, Oberkochen, Germany

40X A Plan Apochromat, NA 1.0 Carl Zeiss Microscopy GmbH, Oberkochen, Germany

Protein isolation

Beckman L70 Ultra Centrifuge Beckman Coulter, Krefeld, Germany

centrifuge Allegra X22R Beckmann Coulter, Krefeld, Germany

centrifuge Sigma 3K30 Sigma GmbH, Osterode, Harz, Germany

gel imager c300 Azure Biosystems, Dublin, USA

incubator Shaker Innova 44 New Brunswick Scientific, Enfield, USA

Mini Protean gel system Bio Rad Lab. GmbH, München, Germany

Nanodrop 2000c Thermo Fisher Scientific, Waltham, USA

power supply Power Pac 200 Bio Rad Lab. GmbH, München, Germany

ThermoMix Compact Eppendorf AG, Hamburg, Germany

Preparation of vesicles

frequency generator Agilent 3220A Agilent Technologies, Santa Clara, USA

Varian Cary Scan 50 Varian, Darmstadt, Germany

RfS

Flame Spectrometer Ocean Optics, Dunedin, FL, USA

NanoCalc-2000, SD2000 spectrometer	Ocean Optics, Dunedin, FL, USA
Ismatec 795C peristaltic pump	IDEX Health & Science, Wertheim, Germany
HL-2000-LL Light source	Ocean Optics, Dunedin, FL, USA

Surface coating

Coating System MED020	Bal-Tec, Balzers, Lichtenstein
Sputtercoater 108 auto	Cressington Scientific Instruments, Watford, United Kingdom
Zepto plasma cleaner	Diener Electronics, Ebbhausen, Germany

TIRF

IXpolre TIRF	Olympus Deutschland GmbH, Hamburg, Germany
cellTIRF-4Line	Olympus Deutschland GmbH, Hamburg, Germany
Zyla 4.2 sCMOS	Andor Technology Ltd., Belfast, UK
100X, UPlanApo, NA 1.5	Olympus Deutschland GmbH, Hamburg, Germany
60X, ApoN oTIRF, NA 1.4	Olympus Deutschland GmbH, Hamburg, Germany

Software

FluoView 1200	Olympus, Tokyo, Japan
Gwyddion 2.45	http://gwyddion.net
ImageJ 1.52t	http://imagej.nih.gov/ij
JPK Data Processing	Instruments AG, Berlin, Germany
Matlab R2021a	Math Works, Natick, USA
Python™, 2.7 & 3.7	http://www.python.org
SOAX 3.7	https://www.lehigh.edu/div206/soax/
Spectra Suite	Ocean Optics Inc., Dunedin, FL, USA
Zen 2.3	Carl Zeiss Microscopy GmbH, Oberkochen, Germany

Miscellaneous

Osmomat 030	Gonotec, Berlin, Germany
pH meter Calimatic 766	Knick, Berlin, Germany
thermomixer compact	Eppendorf, Hamburg, Germany
Tip sonifier Sonoplus HD2070	Bandelin, Berlin, Germany
Ultrapure Water System, MilliQ Gradient A10	Merck Millipore, Darmstadt, Germany
Vacuum drying oven VD23	Binder GmbH, Tuttlingen, Germany